

Development of Antisense Oligonucleotide Combinatorial Therapies for Spinal Muscular Atrophy (SMA)



**Inaugural-Dissertation
zur
Erlangung des Doktorgrades
der Mathematisch-Naturwissenschaftlichen Fakultät
der Universität zu Köln**

**vorgelegt von
Anixa Muiños Bühl
Aus Redondela, Spanien**

**Köln
2022**

The Doctoral Thesis “Development of Antisense Oligonucleotide Combinatorial Therapies for Spinal Muscular Atrophy (SMA)” was performed at the Institute of Human Genetics and Center for Molecular Medicine Cologne (CMMC) of the University of Cologne from July 2017 to December 2022. The oral examination will take place in 2023.

Berichterstatter: Prof. Dr. Elena I. Rugarli

Prof. Dr. David Vilchez

Tag der mündlichen Prüfung: 24.02.2023

Para mis padres y mis abuelos

TABLE OF CONTENT

TABLE OF CONTENT	I
LIST OF FIGURES	VI
LIST OF TABLES	VIII
ABBREVIATIONS.....	IX
DECLARATION OF CONTRIBUTIONS	XI
1.1 Publications	XI
1.2 Methods	XII
1.2.1 Part I: Antisense oligonucleotide combinatorial therapy targeting SMN and CHP1.....	XII
1.2.1 Part II: Antisense oligonucleotide combinatorial therapy targeting SMN and NCALD: re-injections to assess long term therapeutic effect	XIII
SUMMARY	XV
ZUSAMMENFASSUNG.....	XVII
1. INTRODUCTION	1
1.1 Spinal Muscular Atrophy (SMA)	1
1.1.1 Autosomal recessive proximal SMA	1
1.1.2 SMA pathology and classification.....	1
1.1.3 Molecular genetics of SMA.....	5
1.2 SMN protein and function.....	6
1.3 Animal models for SMA.....	9
1.3.1 Severe SMA mouse models	10
1.3.2 Intermediate SMA mouse models.....	11
1.4 hiPSCs, cellular model for SMA	11
1.5 SMA therapies	14
1.5.1 SMN-dependent therapies	14
1.5.1.1 Antisense oligonucleotides (ASOs): Nusinersen	15
1.5.1.2 Small molecules: Risdiplam	16
1.5.1.3 Gene replacement: Onasemnogen abeparvovec-xioi.....	17
1.5.2 SMN-independent therapies for combinatorial strategies	17
1.6 Genetic modifiers of SMA.....	19
1.6.1 PLS3	20
1.6.2 CHP1	20
1.6.2.1 Regulation of gene transcription.....	21
1.6.2.2 Vesicular trafficking	21
1.6.2.3 Regulation of plasma membrane ion transporters	22
1.6.2.4 CHP1 role as SMA genetic modifier.....	22

1.6.3 NCALD.....	22
2. AIMS OF THE STUDY	25
2.1 Part I: Antisense oligonucleotide combinatorial therapy targeting SMN and CHP1.....	25
2.2 Part II: Antisense oligonucleotide combinatorial therapy targeting SMN and NCALD: re-injections to assess long term therapeutic effect	26
3. RESULTS	27
3.1 Part I: Antisense oligonucleotide combinatorial therapy targeting SMN and CHP1.....	27
3.1.1 Efficacy and tolerability of eight murine <i>Chp1</i> -ASOs leads in wild type adult mice.....	27
3.1.2 Efficacy and tolerability screening of four murine <i>Chp1</i> -ASO leads in neonatal wild type mice	29
3.1.2.1 Injection of 50ug <i>Chp1</i> -ASO leads in neonatal wild type mice.	29
3.1.2.2 <i>Chp1</i> -ASO3 dosage optimization.....	32
3.1.2.3 <i>Chp1</i> -ASO4	33
3.1.3 Combination of low-dose <i>SMN</i> -ASO and 30 µg <i>Chp1</i> -ASO4 in SMA mice at PND21.	37
3.1.3.1 Electrophysiological predictors: CMAP and MUNE	39
3.1.3.2 NMJ architecture.....	40
3.1.3.3 Muscle fiber size and spinal MNs proprioceptive inputs	41
3.1.4 Re-injection of <i>Chp1</i> -ASO4 at PND28	42
3.1.4.1 Efficacy and tolerability of <i>Chp1</i> -ASO4 i.c.v. bolus injection at PND28 in wild type mice	42
3.1.4.2 Analysis SMA hallmarks upon re-injection of <i>Chp1</i> -ASO4	45
3.1.5 hiPSCs derived MNs: in vitro model for drug testing	47
3.1.5.1 Healthy and SMA hiPSCs lines	47
3.1.5.2 Directed differentiation of hiPSC into MNs	49
3.1.5.3 <i>SMN</i> protein is reduced in SMA hiPSC derived MNs.....	51
3.1.5.4 hiPSC derived MNs exhibit synaptic machinery components	52
3.1.6 Human <i>CHP1</i> -ASO leads testing in hiPSCs derived MNs	53
3.2 Part II: Long-term antisense oligonucleotide combinatorial therapy targeting SMN and NCALD	59
3.2.1 Combinatorial therapy in SMA mouse model: Re-injections	59
3.2.1.1 Efficacy and tolerability of <i>Ncald</i> -ASO i.c.v. bolus injection at PND28 in wild type mice	60
3.2.1.2 NCALD protein levels 4-weeks after 500 µg <i>Ncald</i> -ASO injection in HET and SMA	61
3.2.1.3 Analysis of SMA hallmarks: electrophysiological predictors	62
3.2.1.4 Analysis of SMA hallmarks: NMJ area and innervation	64
3.2.1.5 Analysis of SMA hallmarks: muscle fiber size	65
3.2.2 Human NCALD-ASO treatment in MN derived from hiPSCs.....	66
3.2.2.1 Efficacy and tolerability of three human NCALD-ASO treatment.....	66
3.2.2.2 Efficacy of NCALD-ASO69 in other hiPSCs derived MN lines	71
3.2.2.3 Growth cone morphology analysis upon NCALD-ASO treatment.....	73
3.2.2.4 Multi-electrode array measurements upon NCALD-ASO treatment	76

4. DISCUSSION	81
4.1 Part I: Combinatorial therapy using <i>SMN</i> -ASO and <i>Chp1</i> -ASO.....	82
4.1.1 The importance of CHP1 reduction during development	84
4.1.2 Ubiquitous vs targeted CHP1 reduction	84
4.1.3 CHP1 levels, a matter of balance.....	85
4.1.4 Antisense oligonucleotide nature	85
4.2 Part II: Long-term combinatorial therapy using <i>SMN</i> -ASO and <i>Ncald</i> -ASO	87
4.2.1 <i>Ncald</i> -ASO re-injection prolongs amelioration of electrophysiological defects	89
4.2.2 <i>Ncald</i> -ASO reinjections prolong amelioration of NMJ pathology	89
4.2.3 <i>NCALD</i> -ASO in hiPSC derived MNs	90
4.2.3.1 <i>NCALD</i> -ASO69 has an impact in growth cone morphology.....	91
4.2.3.2 <i>NCALD</i> -ASO69 has an impact in neuronal activity	93
4.3 Future outlook.....	94
5. MATERIALS AND METHODS.....	97
5.1 Materials.....	97
5.1.1 Laboratory equipment.....	97
5.1.2 Mouse work equipment	98
5.1.3 Chemicals.....	99
5.1.4 Reagents	100
5.1.4.1 Reagents used for molecular biology	100
5.1.4.2 Cell culture reagents, media and plates.....	100
5.1.5 Kits	101
5.1.6 Enzymes.....	102
5.1.7 Primary antibodies and staining reagents.....	102
5.1.8 Secondary antibodies	102
5.1.9 Eukaryotic cell lines	103
5.1.9.1 <i>PC12</i> cells	103
5.1.9.2 Primary murine embryonic fibroblasts (MEFs).....	103
5.1.9.3 hiPSCs.....	103
5.1.10 Mouse inbred strains.....	104
5.1.11 Solutions and media	105
5.1.11.1 Routinely used solutions.....	105
5.1.11.2 Cell culture media.....	105
5.1.12 Primers for genotyping.....	106
5.1.13 Antisense oligonucleotides.....	106
5.1.13.1 Antisense oligonucleotides for <i>in vivo</i> injections.....	106
5.1.13.2 Antisense oligonucleotides for <i>in vitro</i> experiments	107

5.1.14 Software Packages and internet databases	108
5.2 Methods	108
5.2.1 Nucleic acid methods	108
5.2.1.1 Isolation of DNA from mouse tissue biopsies	108
5.2.1.2 Polymerase chain reaction (PCR)	109
5.2.1.3 Agarose gel electrophoresis	110
5.2.2 Protein biochemistry methods.....	110
5.2.2.1 Isolation of proteins from tissues	110
5.2.2.2 Isolation of proteins from cells.....	110
5.2.2.3 Determination of protein concentration with Bradford	111
5.2.2.4 Sodium dodecyl polyacrylamide gel electrophoresis (SDS-PAGE)	111
5.2.2.5 Western Blot.....	112
5.2.2.6 Detection of proteins on Western blot membranes	112
5.2.3 Cell culture.....	113
5.2.3.1 MEFs and PC12 cells.....	113
5.2.3.2 hiPSCs culture.....	113
5.2.3.3 hiPSCs differentiation into MNs	114
5.2.3.4 Cell counting.....	115
5.2.3.5 Cryo-conservation of cells	115
5.2.3.6 Antisense oligonucleotide treatments.....	115
5.2.3.7 Multielectrode array	116
5.2.4 Laboratory mice work.....	116
5.2.4.2 Subcutaneous injection of antisense oligonucleotides (ASOs)	117
5.2.4.3 i.c.v. injections of ASOs.....	117
5.2.4.4 Compound muscle action potential (CMAP) and motor unit number estimation (MUNE) measurements in mice	119
5.2.4.5 The beam-walking assay.....	120
5.2.4.6 Preparation of mouse tissue and organs	121
5.2.4.7 Transcardial perfusion of mice	121
5.2.5 Histological methods.....	122
5.2.5.1 Immunofluorescent staining of cells	122
5.2.5.2 Immunofluorescent staining of the TVA.....	122
5.2.5.3 Immunofluorescent staining of spinal cord sections.....	123
5.2.5.5 Hematoxylin and eosin staining of muscle paraffin sections	123
5.2.5.6 Immunostaining of cerebellum paraffin sections.....	124
5.2.6 Microscopic image acquisition and analysis.....	125
5.2.6.1 NMJ analysis.....	125
5.2.6.2 Proprioceptive inputs per MN soma.....	125
5.2.6.3 Muscle fiber size analysis	126

5.2.7 Experimental design	126
5.2.8 Statistical Analysis	126
5.3 Storage of materials and data	127
6. PUBLICATIONS AND SCIENTIFIC COMMUNICATIONS	129
Publications	129
Oral presentation	129
Poster presentations	130
Awards.....	130
7. REFERENCES	131
ACKNOWLEDGEMENTS	XVII
ERKLÄRUNG ZUM GESUCH UM ZULASSUNG ZUR PROMOTION	XIX
CURRICULUM VITAE	XXIII

LIST OF FIGURES

Figure 1. SMA hallmarks in the sensory-motor circuit	2
Figure 2. SMA disease classification	3
Figure 3. Schematic overview of <i>SMN1</i> and <i>SMN2</i> genes and the SMN protein each of them produce.	6
Figure 4. SMN general functions and localization in neurons	7
Figure 5. Overview FDA- and EMA-approved therapies for SMA	15
Figure 6. Activity and tolerability screening of eight ASOs targeting murine <i>Chp1</i> by i.c.v. bolus injection in adult wild type mice.	28
Figure 7. Activity and tolerability screening of four selected <i>Chp1</i> -ASOs in neonatal wild type mice.	30
Figure 8. CHP1 antibody is specific for Western blot but not for immunostaining.	31
Figure 9. Dosage optimization of <i>Chp1</i> -ASO3 in neonatal wild type mice.	33
Figure 10. Dosage optimization with 40 and 50 µg <i>Chp1</i> -ASO4 in neonatal wild type mice.	34
Figure 11. Dosage optimization 20 µg <i>Chp1</i> -ASO4 in neonatal wild type mice.	35
Figure 12. Dosage optimization 30 µg <i>Chp1</i> -ASO4 in neonatal wild type mice.	36
Figure 13. Breeding strategy and experimental scheme.	38
Figure 14. Survival and weight of <i>Chp1</i> -ASO-injected SMA mice on Mixed50 background	38
Figure 15. Electrophysiological analysis at PND21 of <i>Chp1</i> -ASO4-injected SMA mice.	39
Figure 16. NMJ analysis at PND21 of <i>Chp1</i> -ASO4-injected SMA mice.	40
Figure 17. Proprioceptive inputs and muscle fiber size analysis at PND21 of <i>Chp1</i> -ASO4 injected SMA mice.	41
Figure 18. Efficacy of various <i>Chp1</i> -ASO4 concentrations 2-weeks after i.c.v. bolus injection in adult wild type mice.	43
Figure 19. Efficacy of <i>Chp1</i> -ASO4 i.c.v. bolus re-injected mice at 2 months	44
Figure 20. Morphological and histological analysis of <i>Chp1</i> -ASO4 re-injected mice	46
Figure 21. hiPSCs staining of pluripotency markers OCT3/4 and SOX2.	48
Figure 22. SMN protein staining in hiPSCs lines.	49
Figure 23. Scheme of the MN differentiation protocol from hiPSCs.	50
Figure 24. MN differentiation protocol efficiency, ISL1+/DAPI.	51
Figure 25. SMN is reduced in MN soma and growth cone of SMA hiPSC derived MNs	52
Figure 26. Immunostaining for neurotransmission machinery components.	53
Figure 27. <i>CHP1</i> MOE-gapmer ASO leads.	54
Figure 28. Free uptake <i>CHP1</i> -ASO57 and <i>CHP1</i> -ASO59 in SMA type I MNs.	55
Figure 29. <i>CHP1</i> -ASOs administered using Lipofectamine in SMA type I MNs.	56
Figure 30. Experimental breeding and injection scheme.	60
Figure 31. <i>Ncald</i> -ASO efficiency 2-weeks after injection in wild type adult mice.	61
Figure 32. <i>Ncald</i> -ASO efficiency 4-weeks after injection in mixed ₅₀ HET and SMA mice.	62
Figure 33. 500 µg <i>Ncald</i> -ASO reinjection improves electrophysiological defects at 2 months.	63
Figure 34. NMJ area and innervation at 2 months of age after <i>Ncald</i> -ASO re-injection.	65
Figure 35. Gastrocnemius muscle fiber size distribution after <i>Ncald</i> -ASO re-injection at 2 months of age	66
Figure 36. NCALD MOE gapmer ASOs.....	67
Figure 37. Preliminary efficacy and tolerability study of <i>NCALD</i> -ASO leads in healthy MNs at day 15.	68
Figure 38. <i>NCALD</i> -ASO lead efficiency and tolerability 7 days after treatment in healthy MNs.	69
Figure 39. Healthy MNs 7days after 60nM <i>NCALD</i> -ASOs treatment show changes in growth cone morphology	70
Figure 40. 60 nM <i>NCALD</i> -ASO69 efficacy in healthy and SMA type I lines.	71

Figure 41. NCALD reduction in MNs upon treatment with <i>NCALD</i> -ASO69.....	72
Figure 42. Actin morphology at the growth cone upon <i>NCALD</i> -ASO69 treatment.	74
Figure 43. Microtubule morphology at the growth cone upon <i>NCALD</i> -ASO69 treatment.....	75
Figure 44. Spikes and burst of healthy and SMA hiPSC derived MNs upon <i>NCALD</i> -ASO69 treatment	77
Figure 45. Multielectrode array shows increase in neuronal firing upon <i>NCALD</i> -ASO69 treatment.....	79
Figure 46. Graphical summary of the combinatorial therapy targeting SMN and NCALD.....	88
Figure 47. Graphical scheme for neonatal i.c.v. injection.	118
Figure 48. Graphical representation of the i.c.v. bolus injection in adult animals.	119

LIST OF TABLES

Table 1. hiPSC lines.....	104
Table 2. Human and murine ASOs provided by Ionis Pharmaceuticals, for <i>in vivo</i> experiments.	107
Table 3. Human ASOs provided by Ionis Pharmaceuticals, for <i>in vitro</i> experiments.....	107
Table 4: Standard thermocycler PCR program.	109
Table 5: Components and volumes of genotyping PCR.....	109
Table 6. H&E staining protocol.....	124

ABBREVIATIONS

A	adenine
AChRs	acetylcholine receptors
ALS	amyotrophic lateral sclerosis
APS	ammonium persulfate
ASO	antisense oligonucleotide
a.u.	arbitrary unit
BDNF	brain-derived neurotrophic factor
BSA	bovine serum albumin
BTX	bungarotoxin
C	cytosine
Ca ²⁺	calcium
CMAP	compound muscle action potential
CME	clathrin-mediated endocytosis
CNS	central nervous system
CSF	cerebrospinal fluid
DMEM	dulbecco's modified eagle medium
DMSO	dimethyl sulfoxide
DNA	deoxyribonucleic acid
EMA	European Medicines Agency
ER	endoplasmatic reticulum
ESC	embryonic stem cell
ESE	exonic splicing enhancer
ESS	exonic splicing silencer
et al.	et alii
FCS	fetal calf serum
FDA	Food and Drug Administration of the USA
fw	forward
g	gravitational force
G	guanine
GDNF	glial cell line-derived neurotrophic factor
h	hours
HDACis	histone deacetylase inhibitors
hnRNP A1	heterogeneous nuclear ribonucleoprotein A1
hiPSC	human induced pluripotent stem cell
IC50	half maximum inhibitory concentration
IHC	immunohistochemistry
i.c.v.	intracerebroventricular
kb	kilobases
kDa	kilo Dalton
KO	knockout
IF	immunofluorescent
ISS	intronic splicing silencer
m	mili
μ	micro
M	molar
MEFs	murive embryonic fibroblasts
min	minutes

MN	motor neuron
MOE	2'-O-methoxyethyl
mRNA	messenger RNA
MUNE	motor unit number estimation
mV	mili volt
MW	molecular weight
N	number
NF	neurofilament
NMJ	neuromuscular junction
ns	not significant
p	probability
PBS	phosphate-buffered saline
PCR	polymerase chain reaction
PFA	paraformaldehyde
pH	power of hydrogen
pmol	picomol
PND	postnatal day
PS	phosphorothioate
rev	reverse
RNA	ribonucleic acid
RNP	ribonucleoprotein
rpm	rotations per minute
s.c.	subcutaneous
scAAV	self-complementary adeno-associated virus
SD	standard deviation
SDS	sodium dodecyl sulfate
SDS-PAGE	sodium dodecyl sulfate polyacrylamide gel electrophoresis
sec	seconds
SF2	splicing factor 2
SMA	spinal muscular atrophy
SMN1	survival of motor neuron 1
SMN2	survival of motor neuron 2
snRNP	small nuclear ribonucleoproteins
SV	synaptic vesicle
T	tyrosine
tg	transgene
TVA	transversus abdominis
Unrip	uNR-interacting protein
UTR	untranslated region
vac	<i>vacillator</i>
WB	western blot
WT	wild type

DECLARATION OF CONTRIBUTIONS

1.1 Publications

Parts of the data, tables, paragraphs and figures of this doctoral thesis have been adapted from the original research articles, which have been published or are under preparation:

2022: Scientific publication as first author

Muinos-Bühl A, Rombo R, Janzen E, Ling KK, Hupperich K, Rigo F, Bennet CF, Wirth B

Combinatorial ASO-mediated therapy with low dose SMN and the protective modifier Chp1 is not sufficient to ameliorate SMA pathology hallmarks

Neurobiology of disease. 2022 September; 171:105795. doi: 10.1016/j.nbd.2022.105795. Epub 2022 Jun 18.

2023: Scientific publication as first author (in preparation)

Muinos-Bühl A, Rombo R, Ling KK, Rigo F, Bennet CF, Wirth B

Long-term *SMN*- and *Ncald*-ASO combinatorial therapy in SMA mice and *NCALD*-ASO treatment in hiPSC-derived motoneurons

Manuscript in preparation

1.2 Methods

Anixa Muiños Bühl designed and statistically analyzed all the experiments under the supervision of Prof. Dr. Brunhilde Wirth. Contributions to the laboratory work are listed here.

1.2.1 Part I: Antisense oligonucleotide combinatorial therapy targeting SMN and CHP1

Method	Contributors
Murine and human antisense oligonucleotide design, preliminary test in A431 cell line, preliminary test in adult wild type mice, analysis	Ionis pharmaceuticals
Test <i>Chp1</i> -ASOs leads in neonatal wild type mice, injections, western blot and analysis	Anixa Muiños Bühl and Dr. Eva Janzen
Walking beam assay	Anixa Muiños Bühl and Dr. Eva Janzen
Brain sections for Purkinje neuron analysis and Purkinje neuron quantification	Kristina Hupperich
Combinatorial therapy <i>Chp1</i> -ASO, electrophysiology experiments, electrophysiology analysis, spinal cord sections, spinal cord section analysis, NMJ staining, NMJ imaging, NMJ analysis, muscle staining, muscle imaging, muscle analysis	Anixa Muiños Bühl and Dr. Eva Janzen
i.c.v. bolus injection of <i>Chp1</i> -ASO in adult wild type animals	Anixa Muiños Bühl and Roman Rombo
Re-injection <i>Chp1</i> -ASO in experimental animals	Anixa Muiños Bühl and Roman Rombo
NMJ staining, NMJ imaging, NMJ analysis and muscle staining, muscle imaging and muscle analysis	Anixa Muiños Bühl and Roman Rombo
CHP1 antibody stainings in MEFs and PC12 cells	Anixa Muiños Bühl
Figure preparation	Anixa Muiños Bühl supervised by Prof. Dr. Brunhilde Wirth
Write manuscript	Anixa Muiños Bühl supervised by Prof. Dr. Brunhilde Wirth
Generation of hiPSCs used in this work	Generated by former member of AG Wirth Purchase at Cedars Sinai iPSC core facility Huvec line is a gift from Prof. Dr. Kurian
Establishment of hiPSCs culture in the lab and the MN differentiation protocol from hiPSCs	Anixa Muiños Bühl
Test of human <i>CHP1</i> -ASOs in MNs, western blot and analysis	Anixa Muiños Bühl

1.2.1 Part II: Antisense oligonucleotide combinatorial therapy targeting SMN and NCALD: re-injections to assess long term therapeutic effect

Method	Contributors
Murine and human antisense oligonucleotide design, preliminary test in A431 cell lines	Ionis Pharmaceuticals
Test re-injection <i>Ncald</i> -ASO lead in adult wildtype mice, i.c.v. bolus injections, western blot and analysis	Anixa Muiños Bühl and Roman Rombo
Long-term Combinatorial therapy <i>Ncald</i> -ASO, i.c.v. bolus injections, electrophysiology experiments, electrophysiology analysis, NMJ staining, NMJ imaging, NMJ analysis, muscle staining, muscle imaging, muscle analysis	Anixa Muiños Bühl and Roman Rombo
Human <i>NCALD</i> -ASO leads testing in hiPSC derived MNs, differentiation, treatment, westernblot and analysis	Anixa Muiños Bühl
hiPSC and derived MNs stainings	Anixa Muiños Bühl
MN treatment with <i>NCALD</i> -ASO, growth cone staining, imaging, quantification and analysis	Anixa Muiños Bühl
Multielectrode array experiments, analysis	Anixa Muiños Bühl
Figure preparation	Anixa Muiños Bühl supervised by Prof. Dr. Brunhilde Wirth
Write manuscript (in preparation)	Anixa Muiños Bühl supervised by Prof. Dr. Brunhilde Wirth

SUMMARY

Spinal muscular atrophy (SMA) is a devastating genetically inherited neuromuscular disorder characterized by the progressive loss of α -motor neurons (MNs) in the anterior horn of the spinal cord, leading to muscle atrophy and weakness. Without treatment, SMA is the leading genetic cause of infant death. Although SMA is caused by homozygous mutations in *survival motor neuron 1 (SMN1)* gene, the disease severity is mainly determined by *SMN2* copy number, an almost identical gene that produces ~10% correctly spliced full length *SMN* transcripts. Recently, three FDA- and EMA-approved therapies that either increase correctly spliced *SMN2* transcripts (nusinersen - antisense oligonucleotide, ASO - and risdiplam - small molecule -) or replace *SMN1* gene (onasemnogen abeparvovec-xioi) have revolutionized the clinical outcome of SMA patients. However, clinical and scientific evidence emphasize the importance of a presymptomatic treatment in order to achieve a significant therapeutic outcome. Moreover, there is a significant number of patients that do not respond to the SMN-enhancing treatments. Indeed, for severely affected SMA individuals carrying only two *SMN2* copies even a presymptomatic therapy might be insufficient to fully counteract disease development. Therefore, SMN-independent compounds supporting SMN-dependent therapies represent a promising therapeutic approach. In this regard, genetic modifiers such as PLS3, NCALD or CHP1 have proved to act protective against SMA across species. Therefore, the aims of this work are the following: 1) To test a combinatorial therapy using *SMN*-ASO and *Chp1*-ASOs in SMA mice, 2) To develop an efficient MN differentiation protocol from healthy and SMA hiPSCs to use as a platform for compound screening (ASOs), 3) To test the long-term effect of the combinatorial therapy based on *SMN*-ASO and *Ncald*-ASO.

In the first part of this work, we focused on the combinatorial treatment enhancing SMN protein levels and reducing CHP1 protein amount. CHP1, calcineurin-like EF-hand protein 1, is an interacting partner of PLS3, a strong modifier of SMA, and acts as a negative regulator of neurite outgrowth and endocytosis. Importantly, a significant amelioration of SMA disease hallmarks was observed in a severely affected SMA mouse model carrying a mutant *Chp1* allele when combined with a suboptimal dose of *SMN*-ASO treatment. In this work, we aimed to pharmacologically reduce CHP1 levels in an ASO-based combinatorial therapy targeting *SMN* and *Chp1* in SMA mice. Notably, *Chp1* modulation represents a major challenge since its reduction to ~50% showed an amelioration of SMA pathology, while the downregulation below those levels is detrimental and prompts cerebellar ataxia characterized by Purkinje neuron loss. Hereby, efficacy and tolerability studies in neonatal wild type mice determined that a single injection of 30 μ g *Chp1*-ASO4 in the CNS is a safe dosage that significantly reduced CHP1 levels to about 50% at postnatal day (PND) 14 in the brain and the spinal cord. Unfortunately, neither electrophysiological predictors such as compound muscle action potential

(CMAP) or motor unit number estimation (MUNE) nor morphological properties of the neuromuscular junctions (NMJ), the spinal cord or the tibialis anterior muscle were ameliorated in SMA mice treated with *Chp1*-ASO4 compared to CTRL-ASO at PND21. Unexpectedly, CHP1 levels were not reduced at 4-weeks post injection, indicating a rather short-term effect and stability of the ASO. Next, we re-administered *Chp1*-ASO4 by i.c.v. bolus injection at PND28. However, no significant improvement of SMA hallmarks was observed at 2 month-of-age. Taken together, in contrast to the protective effect of the genetically-induced *Chp1* reduction on SMA, combinatorial therapy based on *Chp1*- and *SMN*-ASOs failed to significantly ameliorate the SMA pathology in mice. The short-term stability of *Chp1*-ASOs compared to *SMN*-ASO suggests that further optimization of the ASO may be required to fully explore the combination of treatments.

The second part of this work focused on the long-term combinatorial treatment targeting *SMN* upregulation and *Ncald* reduction. NCALD, neurocalcin delta, was identified as a SMA protective modifier in a SMA discordant family, where asymptomatic individuals exhibited a 4-5 fold NCALD reduction. NCALD is a calcium sensor protein that negatively regulates clathrin-mediated endocytosis and axonal outgrowth. NCALD reduction improves impaired endocytosis and ameliorates SMA pathology across species. Moreover, previous work carried out in our research group demonstrated that NCALD pharmacological reduction using *Ncald*-ASO in a low-dose *SMN*-ASO treated severe SMA mouse model, significantly improved electrophysiological and morphological pathology hallmarks at PND21. However, at 3 months of age, SMA mice exhibited amelioration of motoric abilities solely. In the present work, we aimed to study the long-term effect of *Ncald*-ASO by re-injecting it via i.c.v. bolus administration at PND28. In parallel, we aimed to test the therapeutic effect of human *NCALD*-ASOs in MNs differentiated from patient-derived hiPSCs. First, 500µg *Ncald*-ASO administered via i.c.v. bolus injection at PND28 in wild type mice showed a good tolerability of the procedure and a significant reduction of NCALD in the brain and the spinal cord after two weeks. Importantly, *Ncald*-ASO re-injection prolonged the amelioration of electrophysiological parameters and rescued denervation defects. Moreover, human *NCALD*-ASO69 significantly downregulated NCALD levels in hiPSC derived MNs from healthy and SMA type I individuals. In addition, growth cone morphology and spontaneous neuronal activity were improved upon *NCALD*-ASO69 treatment. These data strongly supports the therapeutic role of NCALD in SMA and the importance of maintaining its reduction in order to achieve better clinical outcomes.

ZUSAMMENFASSUNG

Spinale Muskelatrophie (SMA) ist eine verheerende genetisch vererbte neuromuskuläre Störung, die durch den fortschreitenden Verlust von Alpha-Motorneuronen im Vorderhorn des Rückenmarks gekennzeichnet ist und zu Muskelschwund und -schwäche führt. Ohne Behandlung ist SMA die häufigste genetisch bedingte Todesursache bei Kindern. Obwohl SMA durch homozygote Mutationen im *Survival Motor Neuron 1 (SMN1)*-Gen verursacht wird, wird die Schwere der Erkrankung hauptsächlich durch die Kopienzahl von *SMN2* bestimmt, fast identisch mit dem *SMN1* Gen, das ~10% korrekt gespleißte SMN-Transkripte in voller Länge produziert. In jüngster Zeit haben drei von der FDA und der EMA zugelassene Therapien, die entweder die Zahl der korrekt gespleißten *SMN2*-Transkripte erhöhen (Nusinersen - Antisense-Oligonukleotid, ASO - und Risdiplam - kleines Molekül -) oder das *SMN1*-Gen ersetzen (Onasemnogen abeparvovec-xioi), den klinischen Verlauf von SMA-Patienten revolutioniert. Klinische und wissenschaftliche Erkenntnisse unterstreichen jedoch, wie wichtig eine präsymptomatische Behandlung ist, um einen signifikanten therapeutischen Erfolg zu erzielen. Darüber hinaus gibt es eine beträchtliche Anzahl von Patienten, die nicht auf die SMN-erhöhenden Behandlungen ansprechen. Bei schwer betroffenen SMA-Patienten, die nur zwei *SMN2*-Kopien tragen, könnte sogar eine präsymptomatische Therapie unzureichend sein, um der Entwicklung der Krankheit vollständig entgegenzuwirken. Daher stellen SMN-unabhängige Substanzen, die SMN-abhängige Therapien unterstützen, einen vielversprechenden therapeutischen Ansatz dar. In dieser Hinsicht haben sich genetische Modifikatoren wie PLS3, NCALD oder CHP1 bei verschiedenen Spezies als schützend gegen SMA erwiesen. In diesem Zusammenhang sind die Ziele dieser Arbeit die folgenden: 1) Erprobung einer kombinatorischen Therapie unter Verwendung von *SMN*-ASO und *Chp1*-ASO in SMA-Mäusen, 2) Entwicklung eines effizienten MN-Differenzierungsprotokolls aus gesunden und SMA-hiPSCs als Plattform für das Screening von Wirkstoffen (ASOs), 3) Prüfung der Langzeitwirkung der kombinatorischen Therapie auf der Grundlage von *SMN*-ASO und *Ncald*-ASO.

Im ersten Teil dieser Arbeit konzentrierten wir uns auf die kombinatorische Behandlung, die den SMN-Proteinspiegel erhöht und die CHP1-Proteinmenge reduziert. CHP1, das Calcineurin-ähnliche EF-Hand-Protein 1, ist ein Interaktionspartner von PLS3, einem starken Modifikator von SMA, und wirkt als negativer Regulator des Neuritenauswuchses und der Endozytose. Bei einer schwer betroffenen SMA-Maus, die ein mutiertes *Chp1*-Allel trägt, wurde in Kombination mit einer suboptimalen *SMN*-ASO-Behandlung eine deutliche Verbesserung der SMA-Krankheitsmerkmale beobachtet. In dieser Arbeit haben wir versucht, die CHP1-Spiegel in einer ASO-basierten kombinatorischen Therapie, die auf *SMN* und *Chp1* in SMA-Mäusen abzielt, pharmakologisch zu reduzieren. Insbesondere die Modulation von *Chp1* stellt eine große Herausforderung dar, da eine Reduktion auf ca. 50 % eine Verbesserung der SMA-Pathologie zeigt, während eine Herabregulierung unter dieses Niveau nachteilig ist und eine

durch den Verlust von Purkinje-Neuronen gekennzeichnete zerebelläre Ataxie hervorruft. Wirksamkeits- und Verträglichkeitsstudien an neonatalen Wildtyp-Mäusen ergaben, dass eine einmalige Injektion von 30 µg *Chp1*-ASO4 in das ZNS eine sichere Dosis ist, die die CHP1-Konzentration am postnatalen Tag (PNT)14 signifikant auf etwa 50 % senkte. Leider waren weder elektrophysiologische Prädiktoren wie das zusammengesetzte Muskelaktionspotenzial (CMAP) oder die Schätzung der Anzahl der motorischen Einheiten (MUNE), noch die morphologischen Eigenschaften der neuromuskulären Verbindungen (NMJ), des Rückenmarks oder des Tibialis-anterior-Muskels bei SMA-Mäusen, die mit *Chp1*-ASO4 behandelt wurden, im Vergleich zu CTRL-ASO bei PNT21 verbessert. Unerwarteterweise waren die CHP1-Spiegel vier Wochen nach der Injektion nicht reduziert, was auf eine eher kurzfristige Wirkung und Stabilität des ASOs hinweist. Anschließend verabreichten wir *Chp1*-ASO4 als i.c.v.-Bolusinjektion an PNT28. Jedoch konnte im Alter von zwei Monaten keine signifikante Verbesserung der SMA-Merkmale festgestellt werden. Im Gegensatz zur schützenden Wirkung einer genetisch induzierten *Chp1*-Reduktion auf die SMA, konnte die kombinatorische Therapie auf der Basis von *Chp1*- und *SMN*-ASOs die SMA-Pathologie bei Mäusen nicht signifikant verbessern. Die Kurzzeitstabilität von *Chp1*-ASOs im Vergleich zu *SMN*-ASO deutet darauf hin, dass eine weitere Optimierung der ASOs erforderlich sein könnte, um die Kombination von Behandlungen vollständig zu erforschen.

Der zweite Teil dieser Arbeit konzentrierte sich auf die langfristige kombinatorische Behandlung, die auf die Hochregulierung von *SMN* und die Reduzierung von *Ncald* abzielt. *NCALD*, Neurocalcin delta, wurde in einer SMA-diskordanten Familie als ein SMA-Schutzfaktor identifiziert, wobei asymptotische Personen eine 4-5-fache *NCALD*-Reduktion aufwiesen. *NCALD* ist ein Kalzium-Sensorprotein und reguliert die Clathrin-vermittelte Endozytose negativ. Eine *NCALD*-Reduktion verbessert die gestörte Endozytose und führt zu einer Besserung der SMA-Pathologie bei allen Spezies. Darüber hinaus haben frühere Arbeiten unserer Forschungsgruppe gezeigt, dass die pharmakologische Reduktion von *NCALD* mit *Ncald*-ASO in einem mit niedrig dosiertem *SMN*-ASO behandelten schweren SMA-Mausmodell zu einer signifikanten Verbesserung der SMA-Pathologiemerkmale bei PNT21 führte. Im Alter von drei Monaten zeigten die SMA-Mäuse jedoch lediglich eine Verschlechterung der motorischen Fähigkeiten. In der vorliegenden Arbeit wollten wir die Langzeitwirkung von *Ncald*-ASO durch eine erneute i.c.v.-Bolusinjektion bei PNT28 untersuchen. Parallel dazu wollten wir die therapeutische Wirkung von humanem *NCALD*-ASO in MNs testen, die aus von Patienten stammenden hiPSCs differenziert wurden. Die Verabreichung von 500 µg *Ncald*-ASO als i.c.v.-Bolusinjektion bei PNT28 in Wildtyp-Mäusen zeigte zunächst eine gute Verträglichkeit des Verfahrens und eine signifikante Reduktion von *NCALD* im Gehirn und im Rückenmark nach zwei Wochen. Hierbei führte die erneute Injektion von *Ncald*-ASO zur Verbesserung der elektrophysiologischen Parameter und hob die Denervierungsdefekte auf. Darüber hinaus wurde durch humanes *NCALD*-ASO69 die *NCALD*-

Konzentration in hiPSC-abgeleiteten Nervenfasern von gesunden und SMA-Typ-I-Patienten signifikant herunterreguliert. Außerdem verbesserten sich die Morphologie der Wachstumskegel und die spontane neuronale Aktivität durch die Behandlung mit *NCALD*-ASO69. Diese Daten unterstreichen die therapeutische Rolle von *NCALD* bei SMA, und zeigen, wie wichtig eine Aufrechterhaltung der Reduktion ist, um bessere klinische Ergebnisse zu erzielen.

1. INTRODUCTION

1.1 Spinal Muscular Atrophy (SMA)

Spinal muscular atrophies (SMAs) refer to a heterogeneous group of inherited neuromuscular disorders characterized by muscle weakness, atrophy and hypotonia caused by the loss of spinal and in some cases bulbar motor neurons (Oskoui 2017). SMAs can be classified according to their inheritance pattern into autosomal recessive, autosomal dominant and recessive X-linked (Wirth, Brichta, and Hahnen 2006). The present work will focus on the most abundant form of SMAs: autosomal recessive proximal SMA linked to chromosome 5 (5q-SMA)(Melki et al. 1990), from now on referred to as SMA.

1.1.1 Autosomal recessive proximal SMA

In 1891, the physicians Guido Werdnig and Johann Hoffmann described for the first time “an early infantile progressive SMA” nowadays known as autosomal recessive proximal SMA (Oskoui 2017), although the underlying genetic cause of the disease was identified in 1995 (Lefebvre et al. 1995). After cystic fibrosis, autosomal recessive proximal SMA is the second most frequent autosomal recessive inherited disorder, with an incidence of 1 in 6,000 – 10,000 and a carrier frequency of 1:51 worldwide and 1:41 in the European population (Feldkotter et al. 2002; Sugarman et al. 2012; Wirth et al. 2020). Indeed, without treatment, SMA is the leading hereditary cause of infant death. Importantly, more countries are including SMN in newborn screening programs, which will help to better determine these numbers in the future (Vill et al. 2021).

SMA is caused by decreased levels of the ubiquitously expressed survival of motor neuron protein (SMN). The reduction of SMN protein levels is due to biallelic deletions (96% of the patients) or mutations in the *survival of motor neuron 1* gene (*SMN1*, [MIM:600354]), located at chromosome 5, and the presence of *survival of motor neuron 2* (*SMN2* [MIM: 601627]) gene copies that are alternatively spliced generating only ~10% functional SMN protein per copy (Lefebvre et al. 1995; Feldkotter et al. 2002; Wirth et al. 2020).

1.1.2 SMA pathology and classification

The major pathological hallmark of SMA is the progressive loss of α -motor neurons (MNs) in the ventral (anterior) horns of the spinal cord resulting in muscle weakness and atrophy (Figure 1) (Lunn and Wang

2008). Moreover, neuromuscular junction (NMJ) synapse impairment (Figure 1) is an early pathological feature observed in SMA patients (Swoboda et al. 2005; Martinez-Hernandez et al. 2009) and SMA animal models (Murray et al. 2008; Kariya et al. 2008; Chang et al. 2008; McWhorter et al. 2003), preceding MN death. In more detail, NMJ pathology in SMA is characterized by small endplate size, delayed maturation, denervation, impaired MN excitability and reduced synaptic transmission (Jablonka et al. 2007; Kariya et al. 2008; Ling et al. 2012; Ruiz et al. 2010; Torres-Benito et al. 2011). In addition, sensory-motor dysfunction has been described in SMA patients and mice (Shorrock, Gillingwater, and Groen 2019; Mentis et al. 2011; Ling et al. 2010), which is characterized by reduced proprioceptive synapses onto MNs (Figure 1). Furthermore, apart from the contribution of MN dysfunction to muscle atrophy (Greensmith and Vrbova 1997), skeletal muscles display intrinsic defects due to reduced SMN levels that add to the overall disease pathogenesis (Figure 1) (Cifuentes-Diaz et al. 2001). Indeed, muscles from severely affected individuals exhibit small atrophic fibers (Lunn and Wang 2008).

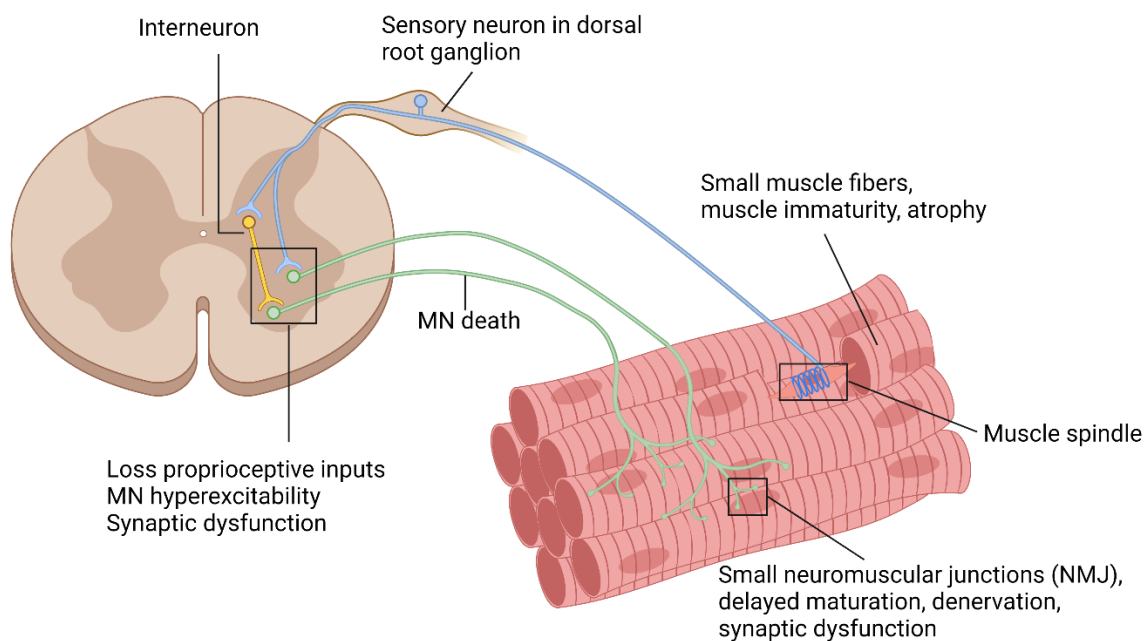


Figure 1. SMA hallmarks in the sensory-motor circuit

Scheme representing the main morphological and functional impairments of the sensory-motor circuit upon loss of SMN. NMJ pathology is characterized by denervation, delayed maturation, reduced size and impairment of the synaptic transmission. MNs are hyperexcitable and there is a loss of synaptic transmission preceding MN death. Skeletal muscles of SMA individuals are characterized by atrophic fibers, smaller in size. In addition, there is a marked reduction of proprioceptive inputs from sensory neurons into MNs. Figure created with BioRender.com.

Despite SMA being considered a “lower motor neuron disorder”, in severe forms of the disease other neuronal regions have been reported to be affected, including the cerebral cortex, brain stem, cerebellum and basal ganglia (Towfighi, Young, and Ward 1985; Harding et al. 2015; Tharaneetharan et al. 2021). Moreover, functional impairment of other tissues, including the heart, liver, vasculature, intestine, bone, and pancreas have been observed in severely affected patients and disease models (Rudnik-Schoneborn et al. 2008; Hamilton and Gillingwater 2013; Yeo and Darras 2021; Shababi, Lorson, and Rudnik-Schoneborn 2014). For instance, SMN deficiency impairs murine and hiPSC derived cardiomyocyte function by dysregulating intracellular Ca^{2+} signaling (Khayrullina et al. 2020). The multisystemic aspect of SMA in its severe forms emphasize the importance of targeting non-neuronal tissues with SMN-enhancing therapies.

Although SMA is a monogenic disease caused by deletions or mutations of *SMN1* leading to the reduction of SMN protein, the clinical spectrum ranges from early onset severe weakness with respiratory insufficiency to mild proximal limb weakness in ambulatory adults.

The widely used disease classification is based on age of onset and motor abilities, established at the International SMA consortium meeting in 1992 (Munsat and Davies 1992). A graphical representation of SMA classification is depicted in Figure 2.

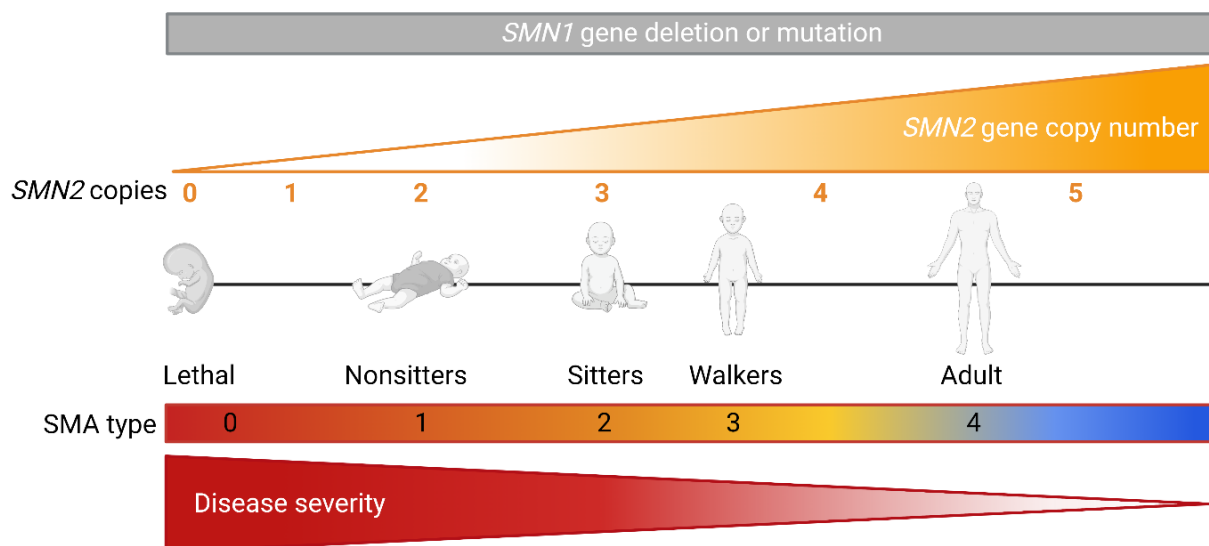


Figure 2. SMA disease classification

Schematic overview of the disease classification based on *SMN2* copy numbers and motor milestones. All patients exhibit mutations of deletions of *SMN1* gene (grey). Disease severity inversely correlates with *SMN2* copy number, from zero copies being embryonically lethal, to five copies displaying mild symptoms in adulthood. Figure created with BioRender.com.

Noteworthy, absence of *SMN1* and *SMN2* gene copies is incompatible with life and leads to embryonic lethality. Type 0 SMA or type 1A is the most severe form of the disease, with most infants carrying one copy of *SMN2*. Onset of symptoms can be noted prenatally by reduced intrauterine movements or in the first week after birth, and patients die within the first month of life (Al Dakhoul 2017; Singh et al. 2018).

Type 1 SMA (MIM: 253300), also referred to as Werdnig-Hoffmann disease, is the most prevalent form of SMA with onset of symptoms in the first 6 months of life, and death occurring within the first two years if treatment is not administered. Patients typically carry two copies of *SMN2*, with some individuals with three copies. Infants cannot roll over or sit, thus are also classified as “nonsitters”. Observed symptoms include muscle weakness and hypotonia, respiratory insufficiency due to deformations of the thoracic cage, progressive bulbar weakness, feeding difficulties and in some infants, cardiac abnormalities (Lunn and Wang 2008; Shababi, Lorson, and Rudnik-Schoneborn 2014; Rudnik-Schoneborn et al. 2010).

Type 2 SMA (MIM: 253550) is also referred to as intermediate SMA or Dubowitz disease. Symptoms onset spans between 6 and 18 months of age, patients survive more than two years and 68.5% of individuals reach 25 years of age with nutritional and respiratory support. The majority of the children carry three *SMN2* copies. Without receiving SMN-enhancing treatments, infants can sit independently (“sitters”) but this ability can be lost over time, and they are never able to walk. Symptoms include proximal weakness mainly affecting the lower limbs, kyphoscoliosis and intercostal muscle weakness leading to respiratory insufficiency (Lunn and Wang 2008; Oskoui 2017).

Type 3 SMA (MIM: 253400) or Kugelberg-Welander disease, is considered a mild form of SMA. Generally, affected children are diagnosed after 18 months of age and have an average life expectancy. Individuals carry three or four copies of *SMN2*, with some patients that can walk independently (“walkers”) their entire life, and some that lose the ability over time due to the progressive weakness. (Lunn and Wang 2008; Oskoui 2017).

Type 4 SMA (MIM: 271150), is considered the adult manifestation of the disease, and the less prevalent. Typically, individuals carry four or five copies of *SMN2*, are usually diagnosed in the third decade of their life and have an average life expectancy. Individuals might lose independent ambulation years after diagnosis (Lunn and Wang 2008; Oskoui 2017).

1.1.3 Molecular genetics of SMA

In 1990, two independent groups performed linkage analysis and mapped the gene responsible for SMA in a highly unstable chromosomal region of 500 Kb, region 5q12-14 (Melki et al. 1990; Gilliam et al. 1990). Five years later, *survival of motor neuron 1 (SMN1, [MIM: 600354])*, which encodes for SMN protein, was identified as the disease-causing gene located in region 5q13.2, (Lefebvre et al. 1995). Moreover, SMN protein is also encoded by *survival of motor neuron 2 (SMN2, [MIM: 601627])*, a paralog of *SMN1* present only in *H. sapiens* (Rochette, Gilbert, and Simard 2001). Generally, healthy individuals carry two *SMN1* copies and one or two *SMN2* copies, but the copy number of both genes can vary between null and four per chromosome (Wirth 2017). SMA is caused by the homozygous loss of the telomeric gene copy, *SMN1*, and the disease severity inversely correlates with the number of copies of the centromeric gene, *SMN2*, considered the most potent SMA genetic modifier (Lefebvre et al. 1995; Lefebvre et al. 1997; Lorson et al. 1999; Feldkotter et al. 2002).

In more detail, *SMN1* and *SMN2* are comprised of nine exons with similar size but differ in five exonic and intronic mutations (Figure 3). While *SMN1* is correctly spliced, the translationally silent C to T mutation at the sixth nucleotide of exon 7 in *SMN2* gene (c.840C>T) is responsible of exon 7 skipping during splicing by abrogating an exonic splicing enhancer (ESE), thus preventing splicing factor 2 (SF2) binding (Cartegni and Krainer 2002; Lorson et al. 1999). In addition, this mutation creates a new exonic splicing silencer (ESS) site which is recognized by the heterogeneous nuclear ribonucleoprotein A1 (hnRNP A1) and promotes exon 7 skipping during splicing (Figure 3) (Kashima and Manley 2003). Hence, about 90% of *SMN2* pre-mRNA undergoes alternative splicing with skipping of exon 7, leading to production of an unstable truncated protein referred to as SMN Δ 7 that is rapidly degraded through the ubiquitin-proteasome pathway (Lorson et al. 1999; Lorson and Androphy 2000). Interestingly, about 10% of *SMN2* is correctly spliced, producing a small amount of functional SMN protein (Figure 3). For instance, SMA type I individuals carrying two *SMN2* copies are predicted to produce only 20% of functional SMN and to develop this devastating disease, whereas harboring more than 50% of functional SMN protein is enough to be asymptomatic (Mailman et al. 2002). Noteworthy, homozygous loss of *Smn1* in any other species leads to embryonic lethality (Schrank et al. 1997; Rochette, Gilbert, and Simard 2001), while in humans the presence of one to five *SMN2* gene copies is responsible for the development of SMA when *SMN1* gene is absent.

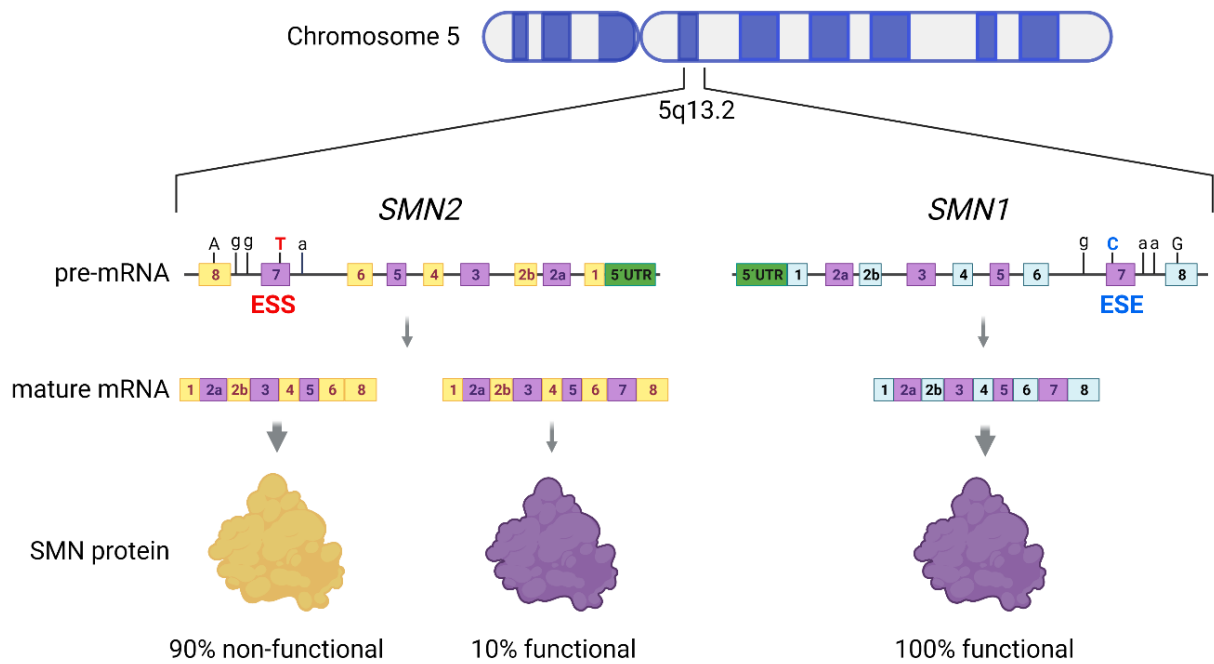


Figure 3. Schematic overview of *SMN1* and *SMN2* genes and the SMN protein each of them produce.

SMN2 and *SMN1* localize in the chromosomal region 5q13.2. *SMN2* differs from *SMN1* in 5 nucleotides. In *SMN2*, the silent C>T transition at position 6 of the exon 7, disrupts a exonic splicing silencer (ESE, blue) and creates an exonic splicing silencer (ESS, red), promoting exon 7 skipping in ~90% of the transcripts, which will produce truncated protein that will be rapidly degraded. In comparison to *SMN1*, which produces 100% of functional protein, *SMN2* produces only 10% functional SMN. Figure created with BioRender.com

1.2 SMN protein and function

SMN is a ubiquitously expressed protein of 38 kDa with variable expression patterns in different tissues (Groen et al. 2018), but especially abundant in the lower spinal cord MNs (Battaglia et al. 1997; Coover et al. 1997). SMN protein housekeeping functions and subcellular localizations are summarized in Figure 4 and reviewed in (Chaytow et al. 2018).

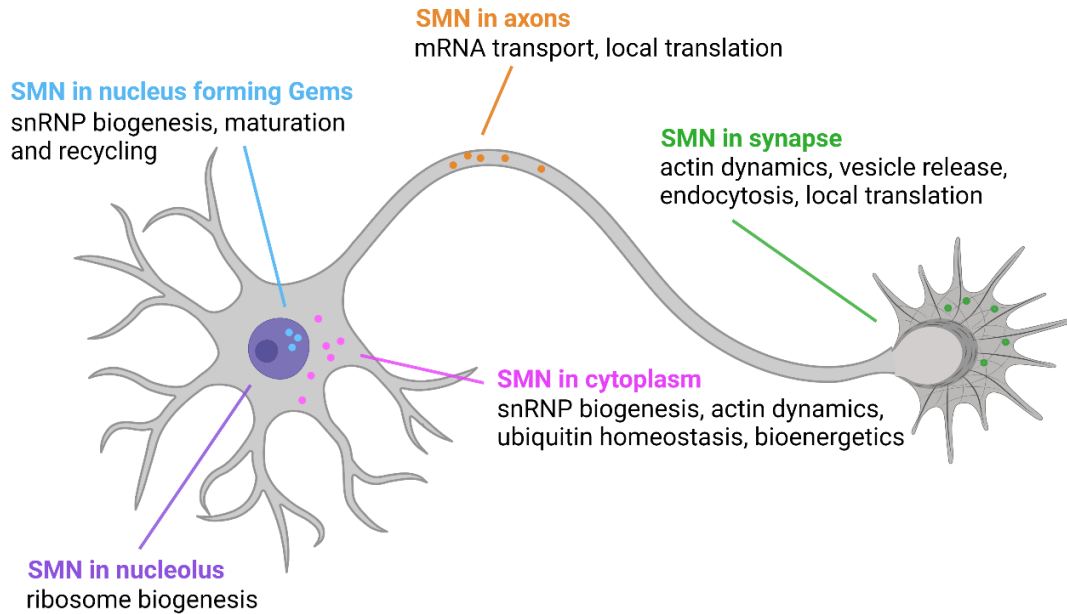


Figure 4. SMN general functions and localization in neurons

In the nucleus, SMN is found in Gems where is involved in small nuclear ribonucleoprotein (snRNP) biogenesis, maturation and recycling. In the nucleolus participates in ribosome biogenesis. In the cytoplasm is involved in snRNP biogenesis, actin dynamics, and ubiquitin homeostasis and bioenergetics pathways. In the axons takes part in mRNA transport and local translation. In the nerve terminals is involved in actin dynamics, vesicle release, endocytosis and local translation. Adapted from (Bowerman et al. 2017). Figure created with BioRender.com

SMN protein localizes in the cytoplasm and the nucleus of the cells. In the nucleus it is concentrated in nuclear Gems (Gemin of coiled) (Liu et al. 1997) that share components with the Cajal bodies, which are essential for ribonucleoprotein (RNP) complexes maturation including small nuclear RNPs (snRNPs) (Singh et al. 2017). snRNPs consist of small nuclear uridine-rich noncoding RNAs forming complexes with several proteins that play critical roles in nuclear posttranscriptional gene expression, including pre-mRNA splicing (Liu et al. 1997; Pellizzoni, Charroux, and Dreyfuss 1999). SMN forms part of a large complex together with Gemins 2-8 and UNR-interacting protein (Unrip), known as the SMN-complex, which ensures snRNP assembly (the key components of the spliceosome) (Meister, Eggert, and Fischer 2002). snRNP biogenesis occurs in the nucleus and cytoplasm of higher eukaryotes, and the role of SMN complex is to mediate the assembly of the Sm core in the cytoplasm (Pellizzoni 2007). Consistent with this critical function, SMN loss results in splicing alterations (Zhang et al. 2008; Gabanella et al. 2007) of genes involved in synaptogenesis, including *Agrin* (critical for NMJ function, maintenance and structure) and *Etv1/ER81* (formation of the sensory-motor circuit) (Zhang et al. 2013). Indeed, a recent study found that SMN plays an essential role in U7 snRNP assembly and histone mRNA processing, required for *Agrin* expression and NMJ integrity (Tisdale et al. 2022). In addition, SMN is involved in other processes related to RNA metabolism, including stress granule formation (Hua and Zhou 2004), regulation of translation (Sanchez et al. 2013) and mRNA trafficking along the axons (Fallini, Bassell,

and Rossoll 2012). Interestingly, a recent study demonstrated that reduction of SMN has a strong impact in reprogramming efficiency and pluripotency, and that SMN is upregulated during preimplantation of the mouse embryo, suggesting that SMN might play a role in the expression of pluripotency genes (Chang et al. 2022).

SMN is also present at the neurites and growth cones of MNs in ribonucleoprotein granules (Fan and Simard 2002; Zhang et al. 2006), where is involved in mRNA transport and local translation along the axon to the NMJ (Rossoll et al. 2003; Rossoll et al. 2002; Fallini, Bassell, and Rossoll 2012). Indeed, SMN reduction leads to decreased levels of β -actin mRNA in the axon and growth cones, resulting in an impairment of actin dynamics that affect axonal outgrowth (Rossoll et al. 2003; Jablonka et al. 2006). Moreover, mRNA of *growth-associated protein 43 (Gap43)*, abundant in developing growth cones, was also found to be reduced in SMA MNs, further supporting the critical role of SMN in mRNA axonal transport (Fallini et al. 2016). In general, if there is an impairment of the axonal transport, proteins required for synaptic transmission would not reach the end terminal, resulting in a deficient synapse at the NMJ. Besides defective mRNA transport, local mRNA translation has been described to be altered upon SMN reduction (Saal et al. 2014; Fallini et al. 2016; Bernabo et al. 2017). In fact, SMN binds to ribosomes *in vitro* and *in vivo* and modulates the translation of specific mRNAs subsets crucial for several pathways described to be impaired in SMA, including cytoskeleton dynamics, synaptic vesicle, translation, ubiquitination or chromatin/histones (Lauria et al. 2020). Furthermore, SMN interacts with hnRNP-R, HuD, and IMP1, which are mRNA-binding proteins necessary for mRNA trafficking and local protein synthesis found to be reduced in SMA axons (Rossoll et al. 2003; Fallini et al. 2011; Fallini et al. 2014). Interestingly, overexpression of HuD and IMP1 mRNA-binding proteins increased *Gap43* mRNA levels in growth cones of murine primary MNs and ameliorated axonal outgrowth defects in SMA (Fallini et al. 2016).

Moreover, there is evidence of the role of SMN in the regulation of cytoskeleton dynamics, particularly actin dynamics, which is perturbed in SMA. Indeed, SMN binds to the actin-binding protein profilin Ila (Sharma et al. 2005). *Smn* loss in PC12 cells induces upregulation of profilin Ila, which then interacts with ROCK, thus activating the RhoA/ROCK pathway, essential for actin dynamics regulation (Bowerman, Shafey, and Kothary 2007). Remarkably, RhoA/ROCK pathway pharmacological inhibition by Fasudil or Y-27632 resulted in amelioration of NMJ pathology, muscle fiber size and prolonged survival of an intermediate SMA mouse (Bowerman et al. 2010; Bowerman, Murray, Boyer, et al. 2012). In addition, key processes like synaptic vesicle trafficking or endocytosis are driven by cytoskeleton dynamics and are dysregulated in SMA (Hosseini-barkooie et al. 2016; Kong et al. 2009; Ling et al. 2010). Interestingly, overexpression of the F-actin-binding and bundling protein PLS3, which is downstream the RhoA/ROCK pathway (Bowerman et al. 2009), rescues endocytosis and acts protective against SMA

across species independently of SMN (Dimitriadi et al. 2010; Oprea et al. 2008; Ackermann et al. 2013; Hao le et al. 2012; Hosseinibarkooie et al. 2016).

The housekeeping functions of SMN can explain why SMA is considered a multiorgan disease in its severe forms, when SMN levels are reduced below a certain threshold (Hamilton and Gillingwater 2013). However, why MNs are predominantly vulnerable to the loss of ubiquitously expressed SMN protein remains unclear. SMN expression levels vary between tissues and stages of development (Groen et al. 2018). Indeed, during NMJ maturation, SMN expression is increased (Kariya et al. 2014). Therefore, a reduction of SMN would be detrimental for the development and function of NMJs. Moreover, SMN binding to ribosomes and polysomes occurs in a tissue-specific manner *in vivo* (Lauria et al. 2020) and its deficiency leads to tissue-specific splicing defects that might contribute to MN particular vulnerability (Zhang et al. 2008). Altogether, these findings point towards differential requirements of SMN in each tissue and developmental time points, which could explain MN vulnerability.

1.3 Animal models for SMA

Animal models are an indispensable tool used in preclinical research that help us to better understand the molecular mechanisms underlying diseases, since they can mimic altered biological processes similar to what happens in humans. Moreover, they can be used to develop novel therapies before translating to the clinic.

There are important considerations to take into account when working with SMA animal models. SMN duplication happened during evolution and only humans and higher primates carry it. Other species have only the *Smn1* gene, and its loss leads to embryonic lethality (Schrank et al. 1997). This means that SMA is caused by reduced SMN levels below a certain threshold and not by its complete depletion. Several groups have succeeded in the generation of SMA animal models of different species that resemble features of the human pathology, including *C. elegans*, *D. melanogaster*, *D. rerio*, *M. musculus* and *S. scrofa* (Briese et al. 2009; Sleight et al. 2011; Rajendra et al. 2007; Chan et al. 2003; McWhorter et al. 2003; Monani, Coover, and Burghes 2000; Le et al. 2005; Hsieh-Li et al. 2000; Duque et al. 2015). In mouse models, there is no perfect correlation between *SMN2* copy number and SMA severity. A small increase in SMN levels has a stronger rescue potential in mice compared to humans (Burghes 2017). In the following sections, the commonly used mouse models will be introduced, including the model used in the present work: the Taiwanese mouse model in its intermediate form.

1.3.1 Severe SMA mouse models

The first severe SMA mouse model was generated by incorporating two copies of the human *SMN2* transgene to *Smn* null (*Smn*^{2A/2A}) background to rescue embryonic lethality (Monani, Coover, and Burghes 2000). The resultant *Smn*^{2A/2A}; *SMN2*^{+/+} mice survived for less than a week (5.2 days), which resembled the severe form of SMA in humans. Moreover, the addition of more *SMN2* transgene copies reduced the severity of the disease; in particular, eight copies of the transgene fully rescued the phenotype of the mice. Furthermore, integration of the *SMNΔ7* transgene lacking exon 7 (section 1.1.3) into the *Smn*^{ko/ko}; *SMN2*, (*Smn*^{ko/ko}; *SMN2*; *SMNΔ7*) mouse further increased life span of the animals to 13.3 days (Le et al. 2005). These mice, commonly referred to as “delta 7 mice” showed reduced levels of SMN, NMJ pathology with MN death and muscle weakness. Interestingly, animals exhibit differences in survival depending on the background of the mice, being more severe in C57BL/6 than in FVB/N or the mixed background, which lived the longest (Burghes 2017).

A second severe SMA mouse model commonly referred to as the “Taiwanese SMA mouse” was generated two decades ago (Hsieh-Li et al. 2000). In this case, *Smn* deletion was achieved by replacing *Smn* exon 7 with the hypoxanthine-guanine phosphoribosyltransferase (HPRT) selection cassette. In this situation, a transcript lacking exon 7 can still be produced. In addition, a transgenic mouse was created by introducing a bacterial artificial chromosome (BAC) with a 115 kb DNA fragment with the coding region and flanking sequence of two human *SMN2* tandem copies (two copies per allele). When combined in a *Smn*^{ko/ko} background (*Smn*^{ko/ko}; *SMN2*), animals exhibited high phenotypic variability: from early death before PND10 to mild symptoms. Moreover, *Smn*^{ko/ko}; *SMN2*^{tg/tg} mice which carry four *SMN2* copies are fertile and do not exhibit a strong phenotype apart from ear and tail necrosis.

Our research group routinely uses the Taiwanese mouse model and established a new breeding scheme by crossing homozygous *Smn* knockout mice *Smn*^{ko/ko}; *SMN2*^{tg/tg} with heterozygous *Smn*^{ko/wt} mice (Riessland et al. 2010). The resulting offspring has only one *SMN2* transgene (*SMN2*^{tg/0}, two *SMN2* copies), and 50% of the animals develop severe SMA (*Smn*^{ko/ko}; *SMN2*^{tg/0}) and the other 50% are healthy (HET: *Smn*^{ko/wt}; *SMN2*^{tg/0}) and serve as littermate controls. These SMA mice recapitulate SMA type I disease hallmarks such NMJ impairment, muscle atrophy, and loss of spinal MNs. In addition, these mice exhibit severe peripheral organ impairments (Schreml et al. 2013). As already mentioned, the genetic background of the mouse line strongly influences life span and disease severity. In our hands, these severe SMA mice on FVB/N background display an median lifespan of about 10 days (Riessland et al. 2010) whereas on congenic C57BL6/N background the median survival is extended to 15.5 days (Ackermann et al. 2013). Moreover, crossing SMA mice on mixed genetic background (50% FVB/N and 50% C57BL6/N) increases average lifespan up to 19.2 days (Ackermann et al. 2013).

1.3.2 Intermediate SMA mouse models

Mouse models exhibiting intermediate degrees of disease severity help researchers to study SMA pathology in its entire spectrum. In this regard, one of the most commonly used models is the *Smn*^{2B}, developed by Kothary's Lab. This mouse model exhibits a 3-nucleotide substitution (GGA to TTT) in exon 7 of *Smn* that alters an exonic splicing enhancer element that normally recruits the transcription factor TRA2B (Hofmann et al. 2000). Disruption of the enhancer sequence promotes exon 7 skipping and the production of truncated SMN Δ 7 protein. The combination of *Smn*^{2B} allele with *Smn*^{ko/ko} background leads to functional SMN production of about 15% and a median survival of the animals of 28 days in a mixed background. Before PND10 animals exhibit a healthy phenotype, but after that time point animals develop characteristics of SMA pathology including muscle weakness, atrophy, loss of lower MNs and NMJ impairments (Bowerman et al. 2010; Bowerman, Murray, Beauvais, et al. 2012). Moreover, disease severity can be altered depending on the genetic background of the animals: *Smn*^{2B/-} mice have a shorter life span in FVB background (median of 19 days) compared to animals on C57BL/6 genetic background (median of 25 days) (Eshraghi et al. 2016).

Our laboratory established a different approach to generate an intermediate mouse model, based on elevation of SMN levels in the peripheral organs by systemic administration of a suboptimal dose of *SMN*-ASO in animals carrying the human *SMN2*. Low-dose *SMN*-ASO administration ameliorates the severe organ impairments of the severe SMA mouse, thus prolonging the median survival from 16 days to about 28 days (Hosseinibarkooie et al. 2016).

In the present study, in order to generate a mild SMA mouse model, a suboptimal dose of *SMN*-ASO (30 μ g) can be administered subcutaneously to severe SMA mice at PND1 on mixed genetic background (Riessland et al. 2017; Torres-Benito et al. 2019; Muinos-Buhl et al. 2022).

1.4 hiPSCs, cellular model for SMA

The development of several SMA animal models provided us with a better understanding of the disease. Nevertheless, their intrinsic differences from humans such as the existence of *SMN2* only in humans do not facilitate a direct translation of the findings to the clinic. In this regard, patient skin fibroblasts have been widely used to model diseases *in vitro* and screen therapeutic compounds with great success (Makhortova et al. 2011; Cherry et al. 2013; Naryshkin et al. 2014). However, the main disadvantage of using non-MN cells is that key features of the most vulnerable cell type in SMA cannot be studied from fibroblasts.

Human induced pluripotent stem cells (hiPSCs) were first developed in 2007, and have the capacity to differentiate into cells belonging to all three germ layers (Yu et al. 2007; Takahashi et al. 2007), broadening the research possibilities and applications in the fields of regenerative medicine, disease modeling, drug discovery, and stem cell biology. In more detail, the group of Yamanaka discovered that the overexpression of four transcriptional factors - called “Yamanaka factors”- (Oct4, Sox2, c-Myc and Klf4) was sufficient to reprogram murine and human somatic cells and induce a pluripotent ESC-like identity (Takahashi and Yamanaka 2006; Takahashi et al. 2007). An additional study showed that Lin28 and Nanog could substitute c-Myc and Klf4, respectively (Yu et al. 2007). hiPSCs offer advantages compared to hESCs: 1) hiPSCs can be obtained from human biopsy instead of a fertilized embryo and 2) hiPSCs are obtained from independent individuals, which allows the *in vitro* modeling of the entire disease spectrum and preservation of the donor genetic background. In neuroscience, hiPSCs are especially relevant since there is limited access to human primary neuronal cells from the CNS and peripheral nervous system. These cells provide a valuable resource to study pathological mechanisms involved in neurodegeneration and model various degrees of the disease, as well as represent a powerful platform for drug screening and personalized medicine. Indeed, hiPSCs are frequently used in drug discovery to test efficacy and toxicity (Okano et al. 2020; Mullard 2015), supporting the preclinical and clinical data in order to better determine the therapeutic potential of a treatment. Moreover, genome editing technologies can be applied to introduce genetic modifications and generate isogenic hiPSCs lines to understand if a particular mutation is causative for the observed phenotype (Valadez-Barba et al. 2020; Delle Vedove et al. 2022). Furthermore, to improve hiPSC-based disease modeling, researchers developed various techniques, including the co-culture of different cell types to study them as functional units (Shi et al. 2017), grow 3D organoids which resemble the structural organization in the organs (Andrews and Kriegstein 2022) or humanized animal models which are hybridized with hiPSC-derived tissues (Sharma et al. 2020).

In 2009, Ebert and collaborators derived one of the first SMA hiPSC lines from fibroblast of a 3 year old patient affected with SMA type I using lentivirus coding for the transcription factors Oct4, Nanog, Sox2 and Lin28 (Ebert et al. 2009). This study demonstrated that SMA hiPSC lines exhibited significant reduction of SMN transcripts containing the 9 exons (full-length *SMN*) and SMN protein, compared to healthy hiPSCs. Importantly, pluripotency profiles were comparable between SMA hiPSCs and control lines. Moreover, SMA hiPSCs were differentiated into MNs without significant differences in efficiency or morphology after 4 weeks when compared to the healthy lines. However, after 6 weeks in culture, a drastic decrease of positive cells for the MN marker ChAT and reduction of the soma area was observed in neuronal cultures from the SMA lines (Ebert et al. 2009). In addition, as a proof-of-principle, Ebert and collaborators treated patient hiPSCs with two SMN-enhancing compounds, valproic acid and tobramycin, and showed elevation of SMN protein levels and increased Gems per

nuclei. Since then, several hiPSCs derived from SMA patients have been generated and other phenotypes have been described, including decreased axonal length (Corti et al. 2012; Lin et al. 2017), endoplasmic reticulum (ER) stress activation (Ng et al. 2015), MN hyperexcitability in SMA type I MNs but not in SMA type III (Liu et al. 2015; Lin et al. 2017), and altered proteome (Varderidou-Minasian et al. 2021). In addition, researchers are using this important platform to test therapeutic compounds (Ando et al. 2019; Ando et al. 2017). Moreover, hiPSCs derived MNs from asymptomatic individuals of the PLS3 SMA discordant families (Oprea et al. 2008) exhibited PLS3 up-regulation in comparison to their affected siblings, predominantly at the growth cones (Heesen et al. 2016). This study supports the evidence observed in humans and mice about the protective role of PLS3 against SMA, and serves as an example of the potential that hiPSCs derived cells have to resemble human phenotypes.

Additionally, other cell types that contribute to SMA can be differentiated from SMA hiPSCs and help to better understand disease pathology. Astrocytes play a pivotal role in MN health and CNS homeostasis by secreting trophic factors like glial cell line-derived neurotrophic factor (GDNF). Moreover, SMN reduction induces astrocytes reactivity and decreased GDNF secretion (Rindt et al. 2015; Patitucci and Ebert 2016) and monocyte chemoattractant protein 1 (MCP1) (Martin et al. 2017), which might influence MN loss. This cell model confirmed the role of astrocytes in SMA pathology, recapitulating the increase in astrocyte activation observed in murine spinal cords (Rindt et al. 2015). Furthermore, hiPSC-derived SMA microglia adopt a reactive profile and increased inflammatory response as already described in murine models (Khayrullina et al. 2022). SMA myogenic progenitors have been generated already (Hosoyama et al. 2014). In addition, SMA murine and hiPSCs-derived cardiomyocytes exhibit dysregulation of intracellular Ca^{2+} signaling and function (Khayrullina et al. 2020).

NMJ impairment is regarded to be an important hallmark of SMA that precedes MN loss. Human NMJs can be generated *in vitro* by co-culturing hiPSC-derived MNs with hiPSCs-derived myotubes using microfluidic devices. Microfluidic chambers permit cell-specific microenvironment maintenance while allowing cell-cell contact through microgrooves crossed by the MNs to the myotube compartment (Stoklund Dittlau et al. 2021a), and can be used to test therapeutic compounds (Stoklund Dittlau et al. 2021b). Importantly, this model could provide a valuable tool to test the impact of drugs in the major functional unit impaired in SMA. Indeed, Yoshida and collaborators established a hybrid co-culture using hiPSC-derived MNs and C2C12 myotubes and succeeded to generate NMJs exhibiting reduced acetylcholine receptors (AChRs) clusters in SMA cultures. Moreover, this platform was used to test the therapeutic potential of SMN elevation using Valproic acid or *SMN* morpholinos. Notably, number of AChRs cluster improved upon *SMN* morpholino treatment (Yoshida et al. 2015). Nevertheless, up to now, there are no studies where SMA hiPSCs derived MNs and myotubes were used to generate SMA NMJs.

1.5 SMA therapies

1.5.1 SMN-dependent therapies

Since the identification of mutations or deletions of *SMN1* as the genetic cause of SMA, most treatment strategies have focused on SMN level restoration and are generally referred to as SMN-dependent therapies. Importantly, disease duration prior to treatment is a crucial parameter: the earlier the patients receive the treatment (ideally pre-symptomatically), the higher the probability that they will respond to SMN-enhancing therapies (Ramos et al. 2019; Vill et al. 2021; Baranello, Gorni, et al. 2021). Several strategies have been tested in order to increase SMN protein levels, three of which have been approved by the Food and Drug Administration (FDA) and the European Medicines Agency (EMA).

Histone deacetylase inhibitors (HDACis) have the potential to increase gene transcription by allowing histone acetylation, an epigenetic modification that promotes chromatin relaxation. Until now, various HDACis have been described to increase *FL-SMN2* transcripts *in vitro* and *in vivo*, including sodium butyrate, valproic acid (VPA), phenylbutyrate, trichostatin A, LBH589, and the hydroxamic acids suberoylanilide hydroxamic acid (SAHA)(Chang et al. 2001; Sumner et al. 2003; Brichta et al. 2003) (Andreassi et al. 2004; Avila et al. 2007; Garbes et al. 2009; Riessland et al. 2010). Despite the promising results obtained in pre-clinical trials for some HDACis, translation to the clinics did not have the same effect. In the case of VPA, non-responsiveness was explained by an increased expression of the fatty acid translocase CD36, preventing two-thirds of the treated SMA patients from responding to the treatment (Garbes et al. 2013).

Another therapeutic approach focused on preventing SMN degradation via the ubiquitin proteasome pathway. The proteasome inhibitor bortezomib increased SMN levels *in vitro* and *in vivo* (Chang et al. 2004; Kwon et al. 2011; Foran et al. 2016). In addition, a synergistic effect was observed by the combination of proteasomal degradation blocking and HDAC inhibitors (Kwon et al. 2011).

Excitingly, in past years several breakthroughs have led to the FDA and EMA approval of three SMN-dependent treatments that reduce disease severity, although they do not offer a cure for SMA. A graphical summary of the mechanism of action of the approved therapies is depicted in Figure 5, and a detailed explanation will be given in the following sections.

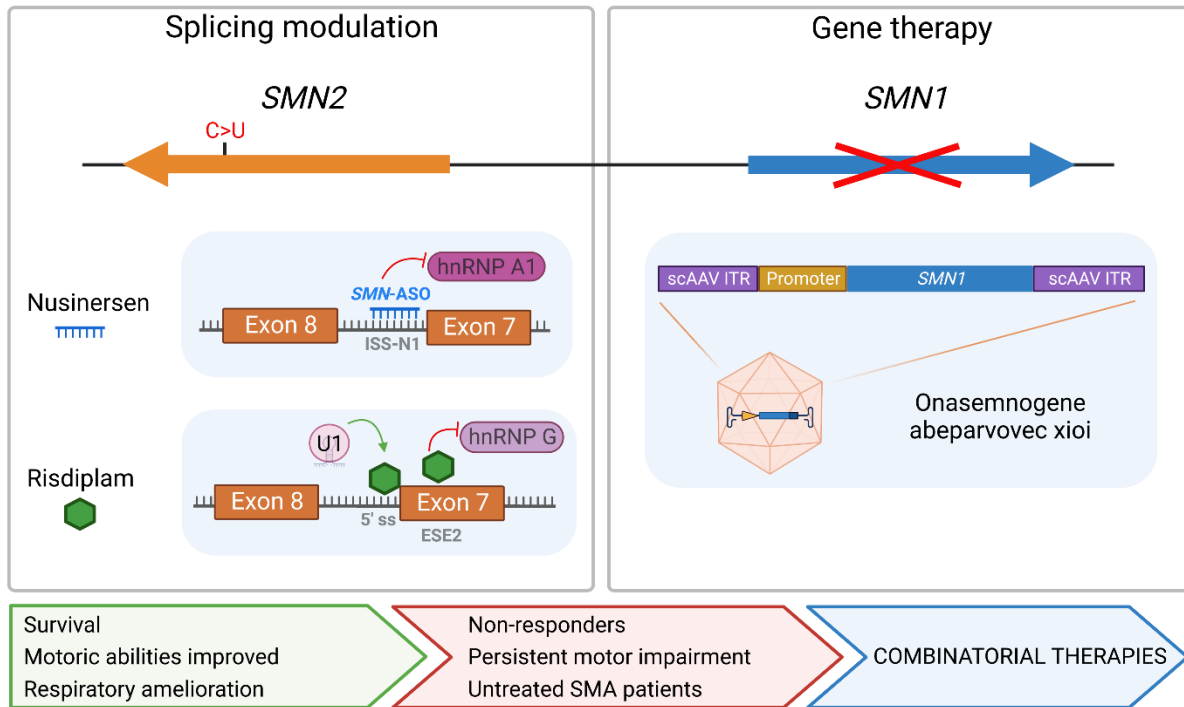


Figure 5. Overview FDA- and EMA-approved therapies for SMA

FDA- and EMA-approved SMA therapies aim to increase SMN protein levels by modulating the splicing of *SMN2* gene (nusinersen and risdiplam) or replacing *SMN1* gene (onasemnogene ABEAV075). Nusinersen (blue schematic oligo) is an antisense oligonucleotide that binds to the intronic splicing silencer N1 (ISS-N1, gray) in intron 7 of *SMN2*, thus preventing hnRNP A1 to bind and promoting exon 7 inclusion. Risdiplam is a small molecule that binds to the 5' splice site (5'ss) of intron 7, thus increasing U1 snRNP recognition and inclusion of exon 7. Moreover, risdiplam (green hexagone) also binds to an exonic splicing enhancer 2 (ESE2, gray) in exon 7 avoiding hnRNP G binding, therefore facilitating inclusion of exon 7. Onasemnogene ABEAV075 is a scAAV9 based gene therapy that aims to replace the mutated or deleted *SMN1* gene. *SMN1* new gene sequence is flanked by inverted terminal repeats (ITRs, purple) and uses the CMV promoter (yellow). In the bottom part of the figure, the green arrow shows the advantages of the available SMN-enhancing compounds, the red arrow the disadvantages and the blue arrow suggest the combinatorial therapies as an opportunity to overcome such disadvantages. Figure created with BioRender.com

1.5.1.1 Antisense oligonucleotides (ASOs): Nusinersen

Chemically, antisense oligonucleotides are synthetic single-stranded sequences of 15-25 modified nucleotides that target complementary RNA. This specific binding allows gene expression regulation using different mechanisms, including splicing modulation, RNase H1 or RISC recruitment to promote mRNA degradation, or blocking of protein binding disrupting secondary and tertiary RNA structures. A detailed overview of antisense technology can be found in (Crooke et al. 2021). In December 2016, nusinersen (*SMN*-ASO, commercial name Spinraza, from Biogen) was the first FDA-approved therapy for SMA, followed by EMA approval in June 2017. Nusinersen is an 18-mer modified 2'-O-methoxyethyl (2'-MOE) phosphorothioate ASO that binds to the intronic splicing silencer N1 element (ISS-N1) located in intron 7 of *SMN2* transcript and blocks the recruitment of hnRNP A1 to the ISS-N1, promoting exon 7 inclusion and functional SMN protein production (Figure 5) (Hua et al. 2008).

Clinical trials in presymptomatic SMA type I and early-onset SMA patients with two *SMN2* copies showed encouraging improvements in motor function and prolonged survival (Finkel et al. 2017; Vill et al. 2021). Notably, presymptomatic treatment leads to better clinical outcomes, stressing the importance of newborn screenings. For type II and III SMA, nusinersen improved motor function (Mercuri et al. 2018), and its administration for about 3 years resulted in disease stabilization (Darras, Chiriboga, et al. 2019). However, since ASOs are unable to cross the blood-brain barrier (BBB), lumbar intrathecal administration is necessary to target affected tissues in the CNS. After four initial loading dosages, nusinersen has to be administered every four months since it does not sustain long-term activity as seen by the decreased production of SMN after 3-4 months (Luu et al. 2017). Nevertheless, distribution within the CNS is not uniform (Ramos et al. 2019), which could explain reduced degrees of amelioration in bulbar and respiratory function in early onset SMA patients (Pechmann et al. 2022). Since its approval, more than 11,000 patients (until September 2021) have been treated with nusinersen, which has proven to be a game changer for all types of SMA. However, for severe forms of the disease, the number of *SMN2* copies that can be targeted by *SMN*-ASO are low and nusinersen treatment might be insufficient to counteract the disease life-long.

1.5.1.2 Small molecules: Risdiplam

Risdiplam (commercially called Evrysdi, from Roche), a small molecule administered orally that corrects *SMN2* splicing, was approved in 2020 by the FDA and in 2021 by the EMA. Mechanistically, risdiplam binds to the 5 splice site in intron 7 of *SMN2*, where the U1 small nuclear RNA (U1 snRNA) binds to form the quaternary U1 snRNP complex involved in exon 7 retention, and increases U1 snRNA binding affinity (El Marabti and Abdel-Wahab 2021). In addition, risdiplam binding to the exonic splicing enhancer 2 (ESE2) is predicted to dislocate the heterogeneous nuclear RNP G (hnRNP G) binding and promote exon 7 inclusion (Sivaramakrishnan et al. 2017).

Risdiplam has a short-term stability, thus requires daily oral administration (Ratni et al. 2018). As of May 2022, more than 1,800 patients are taking risdiplam. Treatment of SMA type I patients with risdiplam starting at the age of 1-7 months, showed an increase of full-length SMN protein in the blood. Moreover, about 30% of patients were able to sit at the end of the study. However, amelioration of motoric function was not comparable to the achieved motor milestones with presymptomatic administration of ASO and gene therapy (Darras et al. 2021; Baranello, Darras, et al. 2021), suggesting that treatment of symptomatic SMA patients, even with a systemically acting drug is not enough, emphasizing the requirement for presymptomatic and/or combinatorial treatments. Nevertheless, a recent study treating SMA type II and non-ambulant SMA type III found significant motoric improvements (Mercuri et al. 2022).

1.5.1.3 Gene replacement: Onasemnogen abeparvovec-xioi

SMN2 has been the predominant target of many therapeutic approaches, since all SMA patients harbor *SMN1* deletions or mutations. For monogenic disorders like SMA, gene replacement therapies represent a promising therapeutic strategy. The first gene replacement therapy for SMA, onasemnogene abeparvovec-xioi (commercial name Zolgensma, from Novartis), was first approved by the FDA in 2019 and by the EMA in 2020. It is based on a non-replicating self-complementary derivative of the recombinant adeno-associated virus (scAAV) of serotype 9, which effectively transduces the CNS and delivers functional *SMN1* (Figure 5). Transgene expression is driven by the constitutively active and hybrid cytomegalovirus enhancer/chicken β -actin promoter (Foust et al. 2010; Foust et al. 2009).

As of March 2022, more than 2,000 SMA patients have been treated with onasemnogene abeparvovec-xioi. The scAAV9 is administered only one time by intravenous infusion, since it can penetrate the BBB and effectively transduce spinal MNs (Duque et al. 2009). Moreover, presymptomatic administration of scAAV9-SMN had a stronger amelioration of SMA pathology in a porcine SMA model (Duque et al. 2015). Clinical trials in SMA type I patients showed prolongation of survival and motoric improvement, especially in patients treated before 8 months of age (Mendell et al. 2017; Day et al. 2021). Results from a phase III clinical trial (SPR1NT) in presymptomatic SMA type I with two or three *SMN2* copies, where patients were treated before 6 weeks of age, show survival of all patients without nutritional or respiratory support. Moreover, about 30% of patients with two *SMN2* copies gained the ability to walk before 18 months of age (Strauss, Farrar, Muntoni, Saito, Mendell, Servais, McMillan, Finkel, Swoboda, Kwon, Zaidman, Chiriboga, Iannaccone, Krueger, Parsons, Shieh, Kavanagh, Wigderson, et al. 2022; Strauss, Farrar, Muntoni, Saito, Mendell, Servais, McMillan, Finkel, Swoboda, Kwon, Zaidman, Chiriboga, Iannaccone, Krueger, Parsons, Shieh, Kavanagh, Tauscher-Wisniewski, et al. 2022). This study corroborates the importance of presymptomatic treatment to maximize the therapeutic effect, and stresses the need for the implementation of newborn screenings programs in the countries where SMA therapies are available. Noteworthy, while one-time delivery of the vector can presumably supply non-proliferative cells like MNs with sufficient levels of SMN, peripheral organs and proliferative cells might not maintain those protein levels life-long. In addition, a recent study demonstrated that long-term overexpression of SMN leads to SMN aggregates in the cytoplasm and splicing defects prompting neurotoxicity in the sensory-motor circuit (Van Alstyne et al. 2021).

1.5.2 SMN-independent therapies for combinatorial strategies

Currently, with three treatments available for the patients, there is a strong interest in the SMA community to assess if the combination of therapeutic compounds could lead to better patient outcomes. The term combinatorial therapy refers to two or more compounds that work through the

same or different mechanisms of action that can be administered simultaneously or in short temporal proximity. In SMA, combinatorial treatments may lead to synergistic benefits either by increasing SMN levels using different mechanisms of action (combination of two SMN-dependent therapies) or by addressing multiple aspects of the disease (combining SMN-dependent and independent therapies).

In the first approach, the combination of two SMN-dependent therapies, it is important to keep in mind that using more than one drug to increase SMN levels may not have an additional benefit if a single compound can achieve the required threshold for maximal SMN impact alone. In mice, SMN levels decrease with age (Groen et al. 2018) and in humans, the critical time point for SMN upregulation is the perinatal period (Ramos et al. 2019). Nevertheless, SMN-enhancing treatments are required throughout life in order to prevent the appearance of symptoms (Zhao et al. 2021). Moreover, it has been widely assumed that increased SMN levels above physiological requirements would not be harmful, but recent studies have demonstrated that overexpression of SMN via the scAAV9 leads to neurotoxicity of the sensory-motor circuit in the long term (Van Alstyne et al. 2021). The first retrospective study combining nusinersen and onasemnogene abeparvovec-xioi showed no adverse effects (Harada et al. 2020), although a second study in SMA type I patients did not demonstrate a synergistic amelioration in the patients (Mirea et al. 2021). Enhancing SMN levels is the logical therapeutic approach and showed impressive results in some patients, however, there are significant numbers of non-responders, which emphasizes the complexity of treating SMA and the need for alternative therapies that could compensate for SMN-irreversible degenerative processes.

The second therapeutic approach aims to combine SMN-enhancing compounds with SMN-independent drugs to target pathways disturbed in SMA that might ameliorate functions or symptoms that cannot be improved by the increase of SMN solely. These combinatorial therapies might play critical roles when SMN-enhancing therapies are administered in symptomatic stages, when severe SMA individuals do not respond to SMN-dependent treatments, or for mild SMA patients that are symptomatic for a long time until they receive the first treatment.

Various SMN-independent approaches focused on enhancing MN survival and muscle integrity using neuro- and muscle protector compounds. Olesoxime (TRO19622) exerts its neuroprotective effect by decreasing mitochondrial membrane permeability, thereby preserving essential functions. Despite its protective effect having been demonstrated *in vitro* and *in vivo* (Bordet et al. 2010), clinical trials in SMA type II and III showed no amelioration of the disease progression upon Olesoxime administration (Muntoni et al. 2020). Muscle protection focuses on enhancing muscle functionality or increasing muscle mass. Reldesemtiv (formerly known as CK-2127107) is a second-generation fast skeletal muscle troponin activator (FSTA) that reduces Ca²⁺ release from the regulatory troponin complex, thus increasing muscle calcium sensitivity. Indeed, clinical trials in SMA type II-IV patients showed

improvement in motor performance upon Reldesemtiv treatment alone (Rudnicki et al. 2021). Moreover, a promising compound that acts at the muscle level is GYM329, an antibody that specifically binds to the inactive form of myostatin in plasma and tissue, reducing the amount of active myostatin generated, thus enhancing muscle growth (Muramatsu et al. 2021), is being tested by Roche in combination with risdiplam in ambulant pediatric patients (NCT05115110). A similar compound has been developed and clinically tested by Scholar Rock in combination with nusinersen, SRK-015, with similar results (NCT03921528) (Abati et al. 2022).

Moreover, SMA protective modifiers represent a unique opportunity to further ameliorate or rescue SMA independently of SMN upregulation, which will be further introduced in the following section.

1.6 Genetic modifiers of SMA

In monogenic disorders, different individuals carrying the same genetic variant can exhibit phenotypic variety, from no clinical symptoms to severely affected, even among relatives (Kingdom and Wright 2022). This phenomenon is called incomplete penetrance and is caused by several factors, including epigenetic regulation, variants in regulatory regions, environmental factors, or genetic modifiers. In this work, we will focus on the role of genetic modifiers in protecting from SMA and how we can use them as targets for SMN-independent approaches in combination with SMN-enhancing drugs.

By definition, a genetic modifier is a genetic locus that can ameliorate or exacerbate the phenotypic outcome of the primary disease-causing variant but may not be the disease-causing gene itself (Rahit and Tarailo-Graovac 2020). Genetic modifiers can act on the disease-causing gene or proteins involved in the same or common pathways (Wirth, Garbes, and Riessland 2013). SMA is a well-known example of a monogenic disorder in which the severity of the disease is strongly determined by genetic modifiers. The first identified SMA genetic modifier was *SMN2* gene copy numbers, which inversely correlate with the severity of the disease (Feldkotter et al. 2002). Indeed, splicing modulator therapeutic approaches aiming to enhance SMN protein target *SMN2* transcripts (section 1.5.1). In this work, we focus on SMN-independent genetic modifiers identified via screening of human discordant families (PLS3 and NCALD) or by biochemical screening (CHP1), and their potential as therapeutic targets. Notably, the discovery of several disease modifiers has unraveled key molecular pathways that contribute to disease progression downstream SMN, like cytoskeleton dynamics, endocytosis, synaptic vesicle trafficking, neurotransmission, axonal transport, and local translation, extensively reviewed in (Wirth 2017).

1.6.1 PLS3

Transcriptome-wide differential expression analysis of lymphoblastoid cells RNA from individuals of six unrelated SMA discordant families led to the discovery of the first described SMN-independent protective modifier, *Plastin 3* (PLS3) (Oprea et al. 2008). Unaffected siblings carried a genotypic combination of *SMN1* and *SMN2* that would normally cause SMA type II-III. However, unlike their affected siblings, asymptomatic individuals exhibited a 40-fold upregulation of *PLS3* transcripts, preventing them from developing SMA. PLS3 is a calcium dependent F-actin and bundling protein that stabilizes F-actin filaments (Lin et al. 1994; Giganti et al. 2005). Moreover, increased levels of PLS3 were found in hiPSC derived MNs from the asymptomatic individuals but not in the MNs derived from the affected siblings (Heesen et al. 2016). PLS3 overexpression rescued axonal length in SMA MNs and neuropathology in *Smn*-deficient zebrafish (Oprea et al. 2008), and SMA hallmarks in a SMA severe mouse model, including MN soma size, NMJ area, muscle fiber size, proprioceptive inputs per MN soma and neurotransmission, but failed to prolong survival (Ackermann et al. 2013). An explanation for the lack of survival improvement is the importance of harboring a certain amount of SMN in order for a modifier to exert its therapeutic potential. Indeed, asymptomatic individuals of discordant SMA families have three to four *SMN2* copies, resembling an intermediate SMA phenotype, but never a SMA type I genotypic combination (Oprea et al. 2008; Riessland et al. 2017). Importantly, various studies showed that PLS3 overexpression, together with subcutaneous low-dose *SMN*-ASO injected animals (resembling an intermediate phenotype), further prolonged the survival of SMA mice (Hosseinibarkooie et al. 2016; Kaifer et al. 2017). Altogether, these results demonstrate the protective role of PLS3 overexpression in intermediate SMA mouse models, resembling the situation in the discordant families.

In addition, the discovery of PLS3 as genetic modifier unraveled endocytosis as a key molecular mechanism altered in SMA pathology, and its upregulation was proven to ameliorate endocytic defects in an F-actin dependent manner (Hosseinibarkooie et al. 2016).

1.6.2 CHP1

Calcineurin-like EF-hand protein 1 (CHP1) is a calcineurin inhibitor (Lin et al. 1999) that directly interacts with PLS3 and its reduction acts protective against SMA (Janzen et al. 2018). CHP1 is a member of the conserved Ca²⁺ binding CHP subfamily, composed also of CHP2 and CHP3. CHP1 is ubiquitously expressed, whereas CHP2 and CHP3 are restricted to specific tissues (Di Sole et al. 2012). In the cell, CHPs localize in the cytoplasm, around the nucleus and in the plasma membrane (Di Sole et al. 2012). CHP1 [MIM: 606988] coding gene in human is located in chromosome 15 and in mice in

chromosome 2. CHP1 is a 22 kDa protein composed of two globular domains, the N- and C-lobe, each of them harboring two Ca²⁺-binding EF hand motifs. Interestingly, only the EF3 and EF4 hands of the C-lobe bind Ca²⁺. In addition, CHP1 has two nuclear export signals responsible for its export to the cytosol, and a N-terminal myristoylation signal involved in its Ca²⁺-induced conformational change (Naoe et al. 2005; Pang et al. 2004).

Among CHP1 functions are: 1) regulation of gene transcription (Jimenez-Vidal et al. 2010), 2) vesicular trafficking from organelles to the plasma membrane (Barroso et al. 1996; Andrade et al. 2004; Nakamura et al. 2002) and 3) plasma membrane ion transporter regulator (Lin and Barber 1996; Liu et al. 2013; Pang et al. 2004).

1.6.2.1 Regulation of gene transcription

CHP1 shares high homology with the phosphatase calcineurin, and when overexpressed acts as a calcineurin inhibitor (Lin et al. 1999). Calcineurin activation dephosphorylates and translocates to the nucleus the transcription factor *nuclear factor of activated T-cells* (NFAT), responsible for gene transcription, including *interleukine IL2* and *IL4*. Indeed, CHP1 overexpression impairs the transcriptional activity of NFAT (Lin et al. 1999). On the contrary, CHP1 reduction increases calcineurin phosphatase activity and NFAT translocation to the nucleus. Importantly, NFAT transcriptional activity has been found to mediate axonal growth (Graef et al. 2003). Furthermore, in the nucleus, ribosomal RNA synthesis is inhibited by CHP1 association with upstream binding factors (UBFs) (Jimenez-Vidal et al. 2010).

1.6.2.2 Vesicular trafficking

CHP1 is required for the fusion of transcytotic vesicles (TCV) with the plasma membrane. Moreover, CHP1 N-myristoylation signal is necessary for exocytic trafficking (Barroso et al. 1996). EF-hand Ca²⁺ binding proteins, like CHP1, function as Ca²⁺ sensors and transducers of Ca²⁺ signals to proteins involved in vesicle exocytosis (Barroso et al. 1996; Di Sole et al. 2012). Microtubule cytoskeleton is involved in vesicle trafficking to the plasma membrane (Cui et al. 2022). Importantly, CHP1 associates with microtubules and membrane-bound organelles mediating their interaction and the targeting/fusion of exocytotic vesicles to the plasma membrane (Di Sole et al. 2012). This function is most likely facilitated by CHP1 interaction with other microtubule-binding proteins, such as GAPDH and kinesin KIF1Bβ2. Indeed, KIF1Bβ2 play a crucial role in synaptic vesicle transport to the neuronal end terminals, thus KIF1Bβ2-CHP1 interaction most probably modulates synaptic vesicle transport in neurons (Di Sole et al. 2012).

1.6.2.3 Regulation of plasma membrane ion transporters

CHP1 interacts with the Na⁺/H⁺ exchanger NHE1 (Lin and Barber 1996). NHE family proteins regulate pH homeostasis, cell volume, cell proliferation apoptosis and differentiation by catalyzing the exchange of Na⁺ for H⁺ (Di Sole et al. 2012; Casey, Grinstein, and Orlowski 2010). CHP1 interaction with NHE1 is required for pH sensing by the NHE1 (Liu et al. 2013; Pang et al. 2004). Noteworthy, pH homeostasis is crucial for neuronal activity and neurotransmission. Interestingly, loss of function mutations in NHE1 are associated with Lichtenstein-Knorr syndrome (LINKS [MIM:616291]) characterized by progressive cerebellar ataxia. In the same line, mutations in CHP1 are described to cause autosomal recessive cerebellar ataxia (Mendoza-Ferreira et al. 2018; Saito et al. 2020). These data strongly suggest that NHE1-CHP1 interaction is essential for optimal NHE1 activity.

1.6.2.4 CHP1 role as SMA genetic modifier

A study carried out in our research group by Janzen and collaborators identified CHP1 reduction to about 50% to act as a protective modifier against SMA (Janzen et al. 2018). CHP1 levels were found to be elevated in the spinal cord and brain of severe SMA mice, functioning as a negative regulator of axonal outgrowth most probably due to decrease of NFAT translocation to the nucleus. Indeed, it has been proven that CHP1 downregulation increases motor axonal length in *Smn*-depleted MN-like cells. In addition, CHP1 reduction counteracts impaired bulk endocytosis *in vitro* by inducing calcineurin phosphatase activity and DNM1 dephosphorylation (Janzen et al. 2018). Furthermore, severely-affected SMA mice carrying a heterozygous *Chp1* deficient mice, the so called *vacillator* mutation (Liu et al. 2013), in addition to a systemic administration of low-dose *SMN*-ASO immediately after birth, prolonged survival by 1.6 fold and significantly improved SMA pathology hallmarks such as electrophysiology predictors, neuromuscular junction (NMJ) size and maturity and reduced number of proprioceptive synapses per MN soma (Janzen et al. 2018). These results suggest CHP1 reduction as an attractive SMN-independent therapeutic target.

1.6.3 NCALD

Neurocalcin delta (NCALD) was identified as a SMN-independent protective modifier after Genome-wide linkage and transcriptome-wide differential expressions analysis was performed in a four-generation discordant family from Utah (USA) (Riessland et al. 2017). Seven members of the family carried *SMN1* deletions; two of them developed SMA type I (two *SMN2* copies) and five of them carried four *SMN2* copies, which would correspond to SMA type III, but were asymptomatic except for increased photosensitivity (Riessland et al. 2017). Genome-wide linkage analysis with 14 family

members identified eight regions with positive LOD scores (logarithm of the odds, probability that two loci are located near each other, and thus inherited together). Moreover, transcriptome-wide differential expression led to the identification of 17 transcripts differentially regulated in asymptomatic individuals. Among them, *NCALD* transcript was found to be downregulated 4-5 fold in the asymptomatic individuals but not in the relatives with SMA type I or in unrelated SMA type III patients. Importantly, *NCALD* was the only transcript localized in one of the eight positive LOD regions, making it an interesting genetic modifier candidate (Riessland et al. 2017). *NCALD* [MIM: 606722] coding gene in humans is located in chromosome 8 and has seven exons that produce 30 splice variants. In mice, the *Ncald* gene is on chromosome 15, and has seven exons that generate 12 alternatively spliced transcripts. *NCALD* encodes for a 22 kDa protein that belongs to the neuronal calcium sensor (NCS) family together with NCS-1, hippocalcin, VILIP1-3, GCAP1-3 and KCHIP1-4 (Burgoyne and Haynes 2012). This group of proteins are abundantly expressed in the CNS and are involved in neuronal function regulation (Paterlini et al. 2000). Interestingly, a recent study found that *NCALD* expression in peripheral blood from SMA I-III and healthy subjects exhibits similar expression patterns (Zhuri et al. 2022).

NCALD, like all NCS protein family members, harbors four EF hand domains, three of them have the ability to bind Ca^{2+} (EF2, EF3, and EF4) (Burgoyne 2007). Moreover, *NCALD* has an N-terminal myristoylation group that facilitates its binding to the membranes in a Ca^{2+} dependent manner. At resting Ca^{2+} concentrations, *NCALD* localizes in the cytoplasm with the myristoylation signal hidden in a hydrophobic pocket. Elevated calcium levels induce a conformational change that exposes the *NCALD* myristoyl chain and allows protein-protein interactions and binding to membranes (Ivings et al. 2002), including outer mitochondrial membrane and the endoplasmic reticulum (ER) (Braunewell and Klein-Szanto 2009; Ames and Lim 2012). At the ER membrane, *NCALD* interacts with the microsomal cytochrome b5 (Cyb5) and modulates NADH-dependent electron transport (Oikawa et al. 2004; Oikawa et al. 2016).

In neurons, Ca^{2+} enters the cell mainly by voltage-gated channels, and plays a role as secondary messenger in processes such neurite outgrowth and neurotransmission (Burgoyne 2007). Moreover, dysregulation of Ca^{2+} signaling can trigger apoptotic processes leading to cell death and development of neurodegenerative disorders (Pchitskaya, Popugaeva, and Bezprozvanny 2018). NCS proteins, like *NCALD*, respond to changes in calcium levels and regulate signaling targets (Baksheeva et al. 2022). *NCALD* is abundant in retinal neurons, where is involved in the cyclic guanosine phosphate (cGMP) signaling pathway by binding to guanylate cyclase (GC) and promoting its activation, suggesting *NCALD* implication in cell-specific generation of the second-messenger cyclic GMP (Krishnan et al. 2004). *NCALD* role in the retinal neurons might explain the increased photosensitivity observed in asymptomatic patients of the SMA discordant family (Riessland et al. 2017). Interestingly, soluble GC

is associated with depression and NCALD reduction using helcid (a drug used to treat headaches) was proven to alleviate depression-like behaviors in a rat model by reducing hippocampal apoptosis (reduced levels of caspase-3) and sGC/cGMP/PKG pathway (Zhang et al. 2021). Moreover, NCALD is abundant in CA3 and dentate gyrus (DG) of the hippocampus (Girard et al. 2015; Upadhyay et al. 2019), and its knock-out impacts DG morphology and adult neurogenesis in mice, whereas its reduction to half does not exert pathological defects (Upadhyay et al. 2019). In addition, NCALD in the brain acts as a Ca^{2+} sensor and increases the sensitivity for the slow afterhyperpolarization current (sAHP) (Villalobos and Andrade 2010), which is considered as one of the largest inhibitory responses in the brain crucial for synaptic plasticity (Sahu and Turner 2021).

Mass spectrometry studies and co-immunoprecipitation assays revealed that NCALD in its myristoylated state directly interacts with clathrin heavy chain, α - and β -tubulin, and actin (Ivings et al. 2002). Moreover, clathrin-mediated endocytosis is assisted by actin cytoskeleton dynamics (Loebrich 2014), and NCALD directly binds to clathrin and actin, both important proteins involved in endocytosis and synaptic vesicle recycling. In addition, NCALD binding to actin and tubulin might suggest a functional role in cytoskeleton dynamics. Indeed, NCALD overexpression inhibits neurite outgrowth (Yamatani et al. 2010).

Previous work from our research group demonstrated that SMN deficiency impairs CME, which was completely rescued upon NCALD reduction. In SMA, low SMN levels reduce voltage-dependent Ca^{2+} influx. Interestingly, NCALD binds clathrin at low Ca^{2+} levels and acts as an inhibitor of endocytosis, by sequestering clathrin and preventing endocytic vesicle coating (Riessland et al. 2017). Moreover, NCALD reduction enhances MN differentiation and neurite outgrowth in NSC34 cells and restores axonal growth and NMJ function in zebrafish *Smn*-morphans. Unexpectedly, *Ncald* reduction was insufficient to prolong life span of intermediate SMA mice. However, heterozygous *Ncald* knockout (*Ncald*^{ko/wt}) in a mild SMA mouse model without life span impairment, significantly improved SMA pathology hallmarks such as NMJ area and maturity and motoric abilities (Riessland et al. 2017). Furthermore, *Ncald* pharmacological reduction using *Ncald*-ASO together with low-dose *SMN*-ASO significantly improved SMA hallmarks at PND21 in SMA mice but failed to do so in the long-term (Torres-Benito et al. 2019).

2. AIMS OF THE STUDY

The recent FDA- and EMA-approved therapies that either increase correctly spliced *SMN2* transcripts (nusinersen and risdiplam) or replace *SMN1* (onasemnogen abeparvovec-xioi) have revolutionized the clinical outcome of SMA patients (Finkel et al. 2017; Mercuri et al. 2018; Mendell et al. 2017; Day et al. 2021; Darras et al. 2021; Baranello, Darras, et al. 2021). However, for severely affected SMA individuals even a presymptomatic therapeutic intervention might be insufficient to fully counteract disease progression. Thus, there is an urgent need to identify SMN-independent compounds that could be used in a combinatorial therapy supporting SMN-dependent approaches. Importantly, genetic modifiers represent promising targets for such therapeutic strategies as they have already been proven to be protective across species (Oprea et al. 2008; Hosseinibarkooie et al. 2016; Riessland et al. 2017; Janzen et al. 2018; Torres-Benito et al. 2019).

2.1 Part I: Antisense oligonucleotide combinatorial therapy targeting SMN and CHP1

The genetic reduction resulting from the *vacillator* mutation of calcineurin like EF-hand protein 1 (CHP1) further prolonged the survival by 1.6-fold and SMA hallmarks of low-dose *SMN*-ASO treated SMA mice (Janzen et al. 2018). These results highlight the attractive therapeutic potential of CHP1 reduction, and encouraged us to test an antisense oligonucleotide-based combinatorial therapy aiming to upregulate SMN systemically and downregulate CHP1 in the CNS. Hereby, the six main aims of this study are the following:

1. Design, synthesize and test *Chp1*-ASOs leads in wild type adult animals.
2. Test for efficacy and tolerability of the top leads in neonatal wild type mice to select the best candidate.
3. Pre-symptomatic double-blinded preclinical study of *Chp1* + *SMN*-ASOs versus control (CTRL) + *SMN*-ASOs in SMA mice, measuring SMA hallmarks at PND21.
4. i.c.v. bolus *Chp1*-ASO re-injection at PND28 to prolong CHP1 downregulation and measure SMA hallmarks at 2 months of age.
5. To establish an efficient MN differentiation protocol using hiPSCs of healthy and SMA individuals.
6. To test *CHP1*-ASOs in hiPSCs-derived MNs for efficacy and tolerability.

2.2 Part II: Antisense oligonucleotide combinatorial therapy targeting SMN and NCALD: re-injections to assess long term therapeutic effect

NCALD reduction is proven to be a protective modifier of SMA not only in humans but also across species including worm, zebrafish and mice (Riessland et al. 2017). Furthermore, its pharmacological reduction using *Ncald*-ASO in combination with low-dose *SMN*-ASO injected in neonatal SMA mice significantly ameliorated electrophysiological and histological disease hallmarks at PND21. However, analysis of these pathological features at 3 months of age showed that a single *Ncald*-ASO injection at PND2, only improved motoric abilities but was not sufficient to rescue disease phenotype in a long term compared to *SMN*-ASO solely (Torres-Benito et al. 2019).

Therefore, the main goal of this study is to assess the long-term beneficial effect of *Ncald*-ASO re-injection in SMA mice, in combination with a single low-dose *SMN*-ASO administered pre-symptomatically at PND1. More precisely, we intend to:

1. To Assess *Ncald*-ASO i.c.v. injection efficacy and tolerability in adult wild type mice.
2. Pre-symptomatic double-blinded preclinical study of *Ncald* + *SMN*-ASOs versus control (CTRL) + *SMN*-ASOs in SMA mice, with re-injection of *Ncald*-ASO or CTRL-ASO at PND28, measuring SMA hallmarks at 2 months of age.
3. To test *NCALD*-ASOs in hiPSCs derived MNs for efficacy and tolerability
4. To perform morphological and functional analysis of patient hiPSCs-derived MNs upon antisense oligonucleotide treatment.

3. RESULTS

3.1 Part I: Antisense oligonucleotide combinatorial therapy targeting SMN and CHP1

A previous study carried out by Janzen and collaborators showed that severely-affected SMA mice carrying the heterozygous deficient *Chp1* allele, the *vacillator* mutation (Liu et al. 2013), in addition to a systemic low-dose *SMN*-ASO administration, lived longer and exhibited amelioration of SMA hallmarks such as electrophysiological markers, neuromuscular junction (NMJ) size and maturity and reduced number of proprioceptive synapses per MN soma (Janzen et al. 2018). Here, we aim to investigate if pharmacological *Chp1* downregulation, by *Chp1*-ASO administration, in a combinatorial approach together with low-dose *SMN*-ASO in a SMA mouse model is a promising therapeutic strategy. In addition, we aim to test human *CHP1*-ASOs in hiPSCs derived MNs from healthy and SMA patients. Noteworthy, results presented in the following sections 3.1.1 to 3.1.4 have been published in September 2022 in the journal *Neurobiology of disease* under: Muinos-Buhl A. Combinatorial ASO-mediated therapy with low dose SMN and the protective modifier Chp1 is not sufficient to ameliorate SMA pathology hallmarks (Muinos-Buhl et al. 2022).

3.1.1 Efficacy and tolerability of eight murine *Chp1*-ASOs leads in wild type adult mice

In the frame of a collaboration with Ionis Pharmaceuticals, multiple 5-10-5 MOE gapmer ASOs on a mixed backbone targeting murine *Chp1* were designed and tested in order to downregulate *Chp1* efficiently. The best eight leads from the cell culture screen were tested in 7-9-week-old wild-type mice for preliminary efficacy and tolerability studies. At first, 500 µg of the respective *Chp1*-ASO was administered by intracerebroventricular (i.c.v) bolus injection, and PBS was used as injection control. After two weeks, the efficacy of the different *Chp1*-ASOs was variable, ranging between 20-80% knockdown of *Chp1* mRNA levels in both cortex and spinal cord (Figure 6A and B). Except for animals treated with ASOs #1113745 and #1114001, all mice continued to gain weight (Figure 6C).

Next, we performed an 8-week tolerability study of the four most efficient *Chp1*-ASOs (> 60% reduction in the cortex), injecting 700 µg of the respective *Chp1*-ASO. Only ASO #1113751 (later referred to as *Chp1*-ASO2) and #1113816 (later *Chp1*-ASO3) showed a significant reduction in the cortex and in the spinal cord (Figure 6D and E) 8 weeks after injection. After 8 weeks, ASO #1113816 was the only ASO lead that maintained similar knockdown levels as in the 2-week efficacy study, exhibiting the strongest effect with a knockdown of 83% in the cortex and 64% in the spinal cord (Figure 6E and D) and elevated inflammatory markers such as *Gfap* and *Cd68* (Figure 6F). Moreover, histological analysis revealed that

all four of the tested *Chp1*-ASOs caused severe Purkinje neuron loss in the cerebellum (Figure 6F), which is driven by Purkinje axon degeneration, eventually leading to the loss of the soma. These results not only indicate that the designed *Chp1*-ASOs are highly specific since previous publications report Purkinje neuron loss upon CHP1 reduction, but also confirm that the CHP1 level cannot fall below a certain threshold since it is otherwise detrimental for Purkinje neurons (Liu et al. 2013; Mendoza-Ferreira et al. 2018).

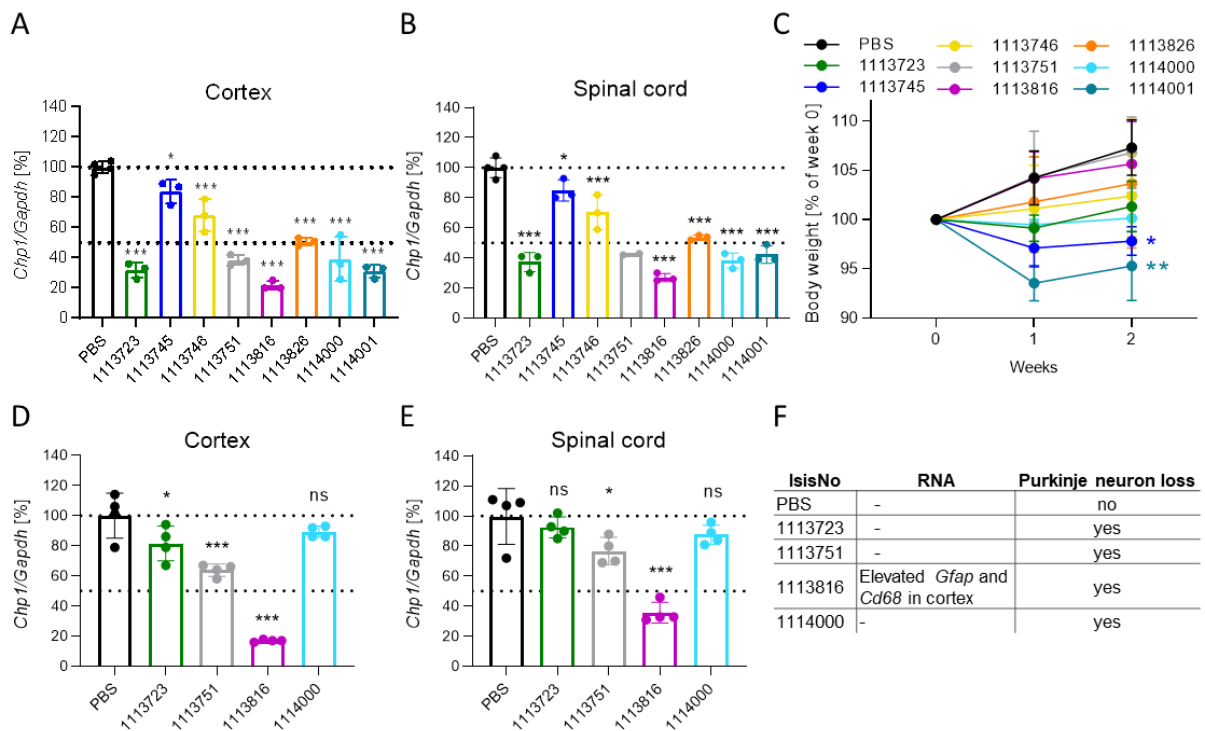


Figure 6. Activity and tolerability screening of eight ASOs targeting murine *Chp1* by i.c.v. bolus injection in adult wild type mice.

A-C) Wild type adult mice were i.c.v. bolus injected with 500 μ g *Chp1*-ASO and sacrificed 2 weeks post injection. *Chp1* knockdown in cortex (A) and spinal cord (B) was evaluated by qRT-PCR. Dots in the graph represent number of animals. One-way ANOVA with Tukey posthoc test for multiple comparisons was applied. * $p \leq 0.05$, *** $p \leq 0.001$. (C) Body weight of *Chp1*-ASO injected mice. N = 4 (PBS) and N = 3 for the *Chp1*-ASOs. One-way ANOVA with Tukey posthoc test for multiple comparisons was applied. * $p \leq 0.05$, ** $p \leq 0.01$.

D-E) The four most efficient ASOs were selected for 8-week *Chp1* expression studies. Wild type adult mice were i.c.v. bolus injected with 700 μ g *Chp1*-ASO and sacrificed 8-weeks post injection. *Chp1* knockdown in cortex (D) and spinal cord (E) was evaluated by qRT-PCR. Dots in the graph represent number of animals. One-way ANOVA with Tukey posthoc test for multiple comparisons was applied. * $p \leq 0.05$, *** $p \leq 0.001$. (F) Summary of biochemical and histological findings. N = 4 for all *Chp1*-ASOs.

Due to these results and previous studies showing that, a reduction of CHP1 of about 50% is well tolerated *in vivo*, for our combinatorial studies we aimed to achieve a CHP1 reduction of about 50% (Janzen et al. 2018; Mendoza-Ferreira et al. 2018).

3.1.2 Efficacy and tolerability screening of four murine *Chp1*-ASO leads in neonatal wild type mice

It is important to emphasize that we were not interested in the most efficient *Chp1*-ASO regarding knockdown levels but in pharmacologically reduce CHP1 levels to ~50%. Based on the previous data from the ASO leads in adult wild-type mice (Figure 6), we selected for further testing in neonatal wild-type mice four out of the eight tested *Chp1*-ASOs.

3.1.2.1 Injection of 50ug *Chp1*-ASO leads in neonatal wild type mice.

The four *Chp1*-ASO leads selected (Figure 7A) displayed various efficacies when injected in adult wild-type mice (Figure 6A). Here we want to assess the efficacy and tolerability of these leads in neonatal wild-type mice to find the best candidate for our combinatorial therapy preclinical trial. First, we i.c.v.-injected mice at PND1 with an initial dose of 50 µg of the respective *Chp1*-ASO and collected brain and spinal cord samples at PND14. Surprisingly, survival analysis revealed that only 25% of animals injected with *Chp1*-ASO1 and about 54% injected with *Chp1*-ASO2 survived until PND14 (Figure 7B). In case of death, mice usually died within the first 48h post-injection, suggesting toxicity of both ASOs in neonatal mice. Instead, 100% of mice injected with *Chp1*-ASO3, and 95% injected with *Chp1*-ASO4 survived, revealing good tolerability in neonatal animals, comparable to animals injected with CTRL-ASO (Figure 7B).

Next, we investigated the knockdown efficacy of the *Chp1*-ASOs in the brain and spinal cord on protein level by Western Blot (Figure 7C-J). In the animals that survived the injection, 50 µg of *Chp1*-ASO1 led to an average CHP1 reduction to about 66% in the brain and 76% in the spinal cord (Figure 7C and D), none of them reaching the desired ~50% reduction. *Chp1*-ASO2 led to variable reduction of the CHP1 levels, on average to about 67% in the brain and no reduction in the spinal cord (Figure 7E and F). Injection of 50 µg *Chp1*-ASO3 resulted in a highly significant CHP1 reduction to about 22% in the brain and 24% in the spinal cord (Figure 7G and H), which aligns with the results observed in adult wild-type mice demonstrating the high efficacy of this ASO. Finally, *Chp1*-ASO4 also led to a significant CHP1 reduction to about 63% in the brain and 53% in the spinal cord (Figure 7I and J), closer to the desired reduction levels.

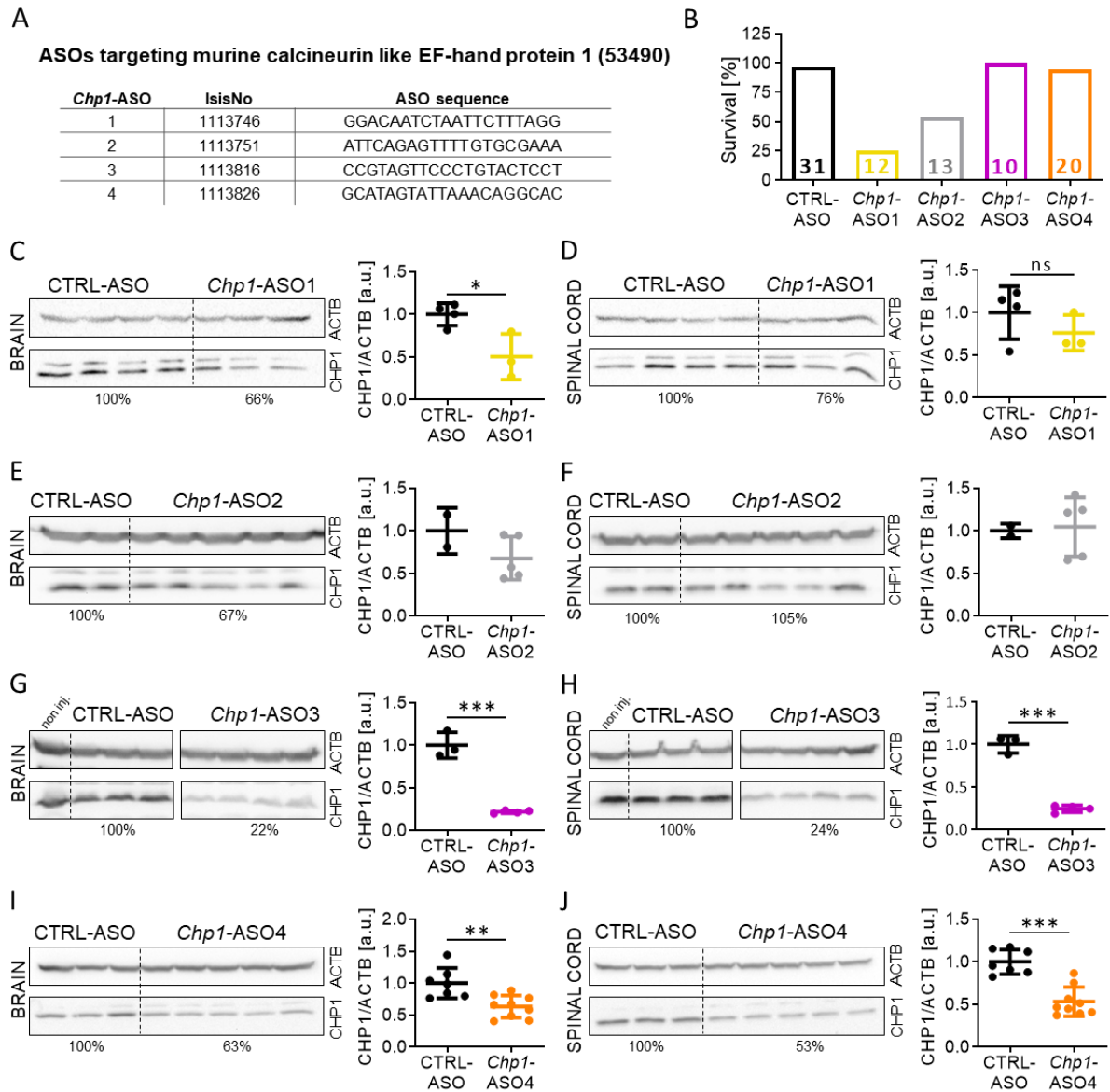


Figure 7. Activity and tolerability screening of four selected *Chp1*-ASOs in neonatal wild type mice.

A) Summary of the four selected *Chp1*-ASOs for testing in neonatal mice.

B) Survival analysis of ASO injected animals until PND14. Numbers in graph indicate N of injected mice per condition. Survival rate is 25% for *Chp1*-ASO1, 53.8% for *Chp1*-ASO2, 100% for *Chp1*-ASO3 and 95% for *Chp1*-ASO4.

C-J) Western blot analysis and quantification of *CHP1* level in brain and spinal cord lysates from ASO injected mice. *Chp1*-ASO1 injection led to a *Chp1* knockdown of 34% in brain (C) and 24% in spinal cord (D). *Chp1*-ASO2 injection led to a *Chp1* knockdown of 33% in brain (E) and no reduction in spinal cord (F). *Chp1*-ASO3 injection led to a *Chp1* knockdown of 78% in brain (G) and 76% in spinal cord (H). *Chp1*-ASO4 injection led to a *Chp1* knockdown of 37% in brain (I) and 47% in spinal cord (J). All mice were i.c.v. injected at PND1 with 50 μ g of the respective ASO and sacrificed at PND14. ACTB: loading control. Unpaired two-tailed Student's t test. All values reported as mean and error bars represent \pm SD. * $p \leq 0.05$, ** $p \leq 0.01$, *** $p \leq 0.001$. Each dot in the bar graphs represents an independent animal.

Unfortunately, assessment of CHP1 reduction in MNs of spinal cord cross sections was not possible, since the CHP1 antibodies give unspecific signals by immunostainings as shown in *Chp1* KO PC12 cells (Figure 8A) and MEFs derived from the *vacillator* mice, carrying *Chp1* homozygous mutations (Figure 8B). On the contrary, the available CHP1 antibody gives a specific signal on Western blot (Figure 8C), thus western blot was the technique used to determine CHP1 reduction in the tissues. We even tested newly generated CHP1 antibodies in collaboration with Dr. Koch Lab with similar results (data not shown).

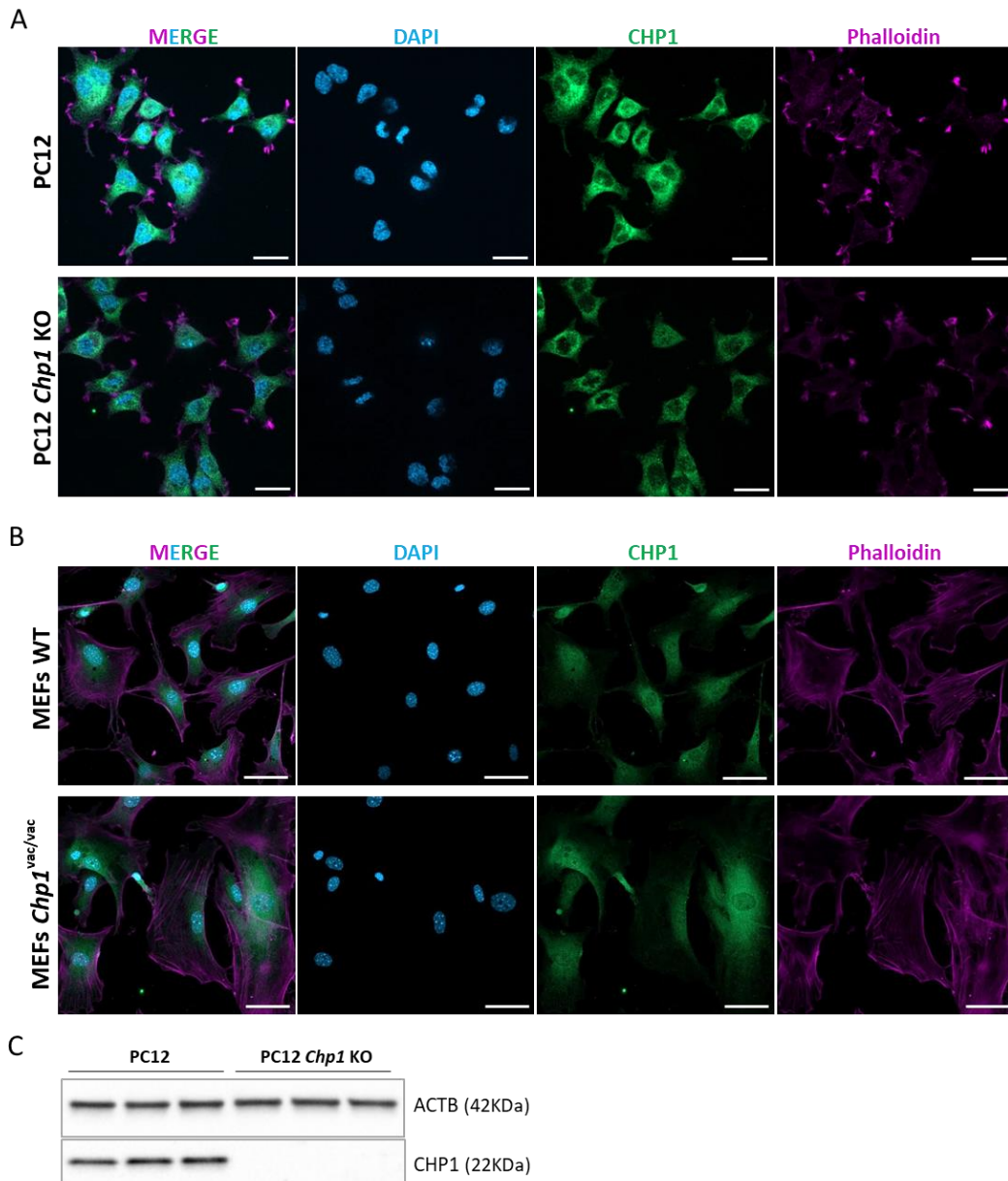


Figure 8. CHP1 antibody is specific for Western blot but not for immunostaining.

A) Immunostaining of PC12 cells and *Chp1* KO PC12 cells generated using CRISPR/Cas9 show unspecific CHP1 antibody staining (green). F-actin was stained with Phalloidin (magenta) and the nucleus with DAPI (blue). Scale bar: 20 μ m.

B) Immunostaining of WT murine embryonic fibroblasts (MEFs) and *Chp1*^{vac/vac} MEFs from the *vacillator* mouse model, with homozygous mutations on *Chp1*. CHP1 (green), Phalloidin stains F-actin (magenta) and DAPI for the nucleus (blue). Scale bar: 50 μ m.

C) Western blot from PC12 cells and *Chp1* KO PC12 cells. CHP1 antibody specifically binds to CHP1 in the PC12 cells and no bands were detected for the PC12 cells with *Chp1* KO. ACTB as loading control. Each band correspond to a technical repetition.

After the results obtained in this preliminary neonatal screen, we decided to discontinue with *Chp1*-ASO1 and ASO2 due to their toxicity observed by the reduction of the survival and their inconsistent efficacy. However, *Chp1*-ASO3 and ASO4 represent promising candidates, thus we further proceed with the dosage optimization.

3.1.2.2 *Chp1*-ASO3 dosage optimization

Chp1-ASO3 led to a strong CHP1 reduction in comparison to the other ASO leads. To decrease CHP1 amount to about 50-60% in the CNS, we further reduced the concentration of *Chp1*-ASO3. Remarkably, 20 µg of *Chp1*-ASO3 led to an average CHP1 reduction to 45% in brain and 42% in spinal cord 2-weeks after injection (Figure 9A and B) more similar to the desired therapeutic concentration, but still below the safety levels of ~50%. Further decrease of *Chp1*-ASO3 concentration to 10 µg led to an average CHP1 reduction to 44% in brain and 80% in spinal cord (Figure 9C and D). In this situation, CHP1 levels in brain were below ~50% increasing the risk of ataxic gait development. In addition, low dosages of *Chp1*-ASO3 injected by i.c.v. showed poor distribution in the CNS, since CHP1 reduction in spinal cord is only 20%. An explanation to this irregular CHP1 reduction between brain and spinal cord can be explained by the ASOs tendency to accumulate in the cortex, hippocampus and cerebellum (Bennett, Krainer, and Cleveland 2019; Jafar-Nejad et al. 2021). Moreover, 6-weeks brains exhibited reduced cerebellar size upon *Chp1*-ASO3 injection, for both tested concentrations (Figure 9E and F), which could be a consequence of Purkinje cell degeneration in the cerebellum due to CHP1 reduction. Taken together, these results lead us to discard *Chp1*-ASO3 as candidate for the preclinical trial.

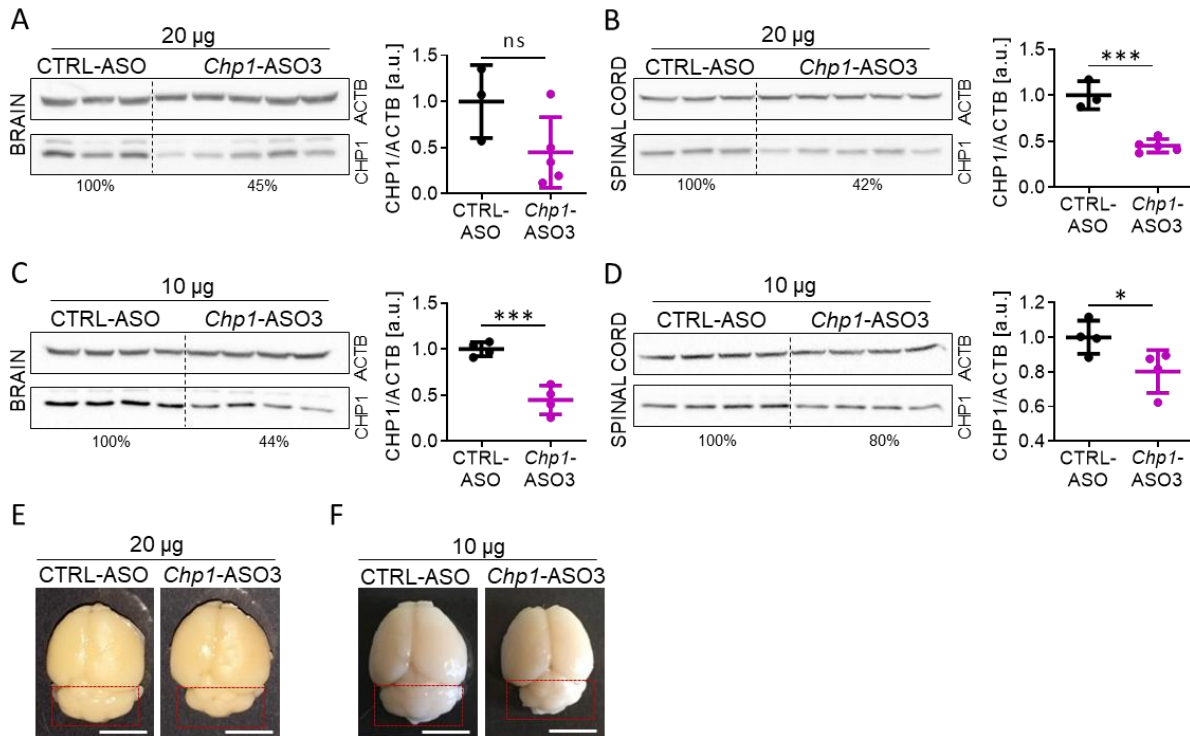


Figure 9. Dosage optimization of *Chp1*-ASO3 in neonatal wild type mice.

A-D) Western blot analysis and quantification of CHP1 level in brain and spinal cord lysates of ASO injected mice at PND14. 20 µg of *Chp1*-ASO3 led to a 55% reduction of CHP1 levels in brain (A) and 58% reduction in spinal cord (B). 10 µg of *Chp1*-ASO3 led to a 56% reduction of CHP1 level in brain (C) and 20% reduction in spinal cord (D). All mice were i.c.v. injected at PND1 with the respective *Chp1*-ASO3 concentration. ACTB: loading control. Unpaired two-tailed Student's t test. All values reported as mean and error bars represent \pm SD. * $p \leq 0.05$, *** $p \leq 0.001$. Each dot in the bar graphs represents an independent animal.

(E-F) Morphological analysis of brains from *Chp1*-ASO3 injected mice at 6-weeks. Injection showing severe reduction of cerebellar size (scale bar: 5 mm).

3.1.2.3 *Chp1*-ASO4

For dosage optimization of *Chp1*-ASO4, we reduced the initial concentration to 40, 30 and 20 µg, respectively, to avoid CHP1 reduction in the brain below safety levels as observed in some experimental animals after 50 µg of *Chp1*-ASO4 administration.

First, 40 µg of *Chp1*-ASO4 led to a significant average CHP1 reduction to 53% in brain, which is within the safety therapeutic window, and 42% in spinal cord (Figure 10A and B). Morphological analysis of brains at 6-weeks of age showed a mildly reduced cerebellar size upon 50 µg, but also after 40 µg *Chp1*-ASO4 injection in comparison to CTRL-ASO injected animals (Figure 10C and D). Next, we investigated the effect of 40 µg *Chp1*-ASO4 on cerebellar morphology and motoric behavior in more detail, in order to determine if 40 µg *Chp1*-ASO4 had an effect in Purkinje neuron population or prompted cerebellar ataxia. For this purpose, we performed sagittal brain sections 6-weeks after i.c.v. injection of 50 and 40 µg *Chp1*-ASO4 and specifically detected the Purkinje neurons in the cerebellum by calbindin-D28k

staining. Strikingly, strong Purkinje neuron loss was identified in mice injected with 50 μg and less severe reduction when injected with 40 μg of *Chp1*-ASO4 (Figure 10E), however Purkinje neuron population was not conserved in neither situation as in CTRL-ASO injected animals. Importantly, motoric analysis by beam-walking assay did not reveal any significant difference in average performance of mice injected with 40 μg *Chp1*-ASO4 versus control treated mice at 3- and 6-weeks of age (Figure 10F and G). However, out of eight mice injected with 40 μg *Chp1*-ASO4, one developed a mild ataxic gait at 3-weeks of age (Figure 10F). Furthermore, a trend towards reduced motor performance was perceived at 6-weeks of age in comparison to CTRL-ASO treated animals (Figure 10G).

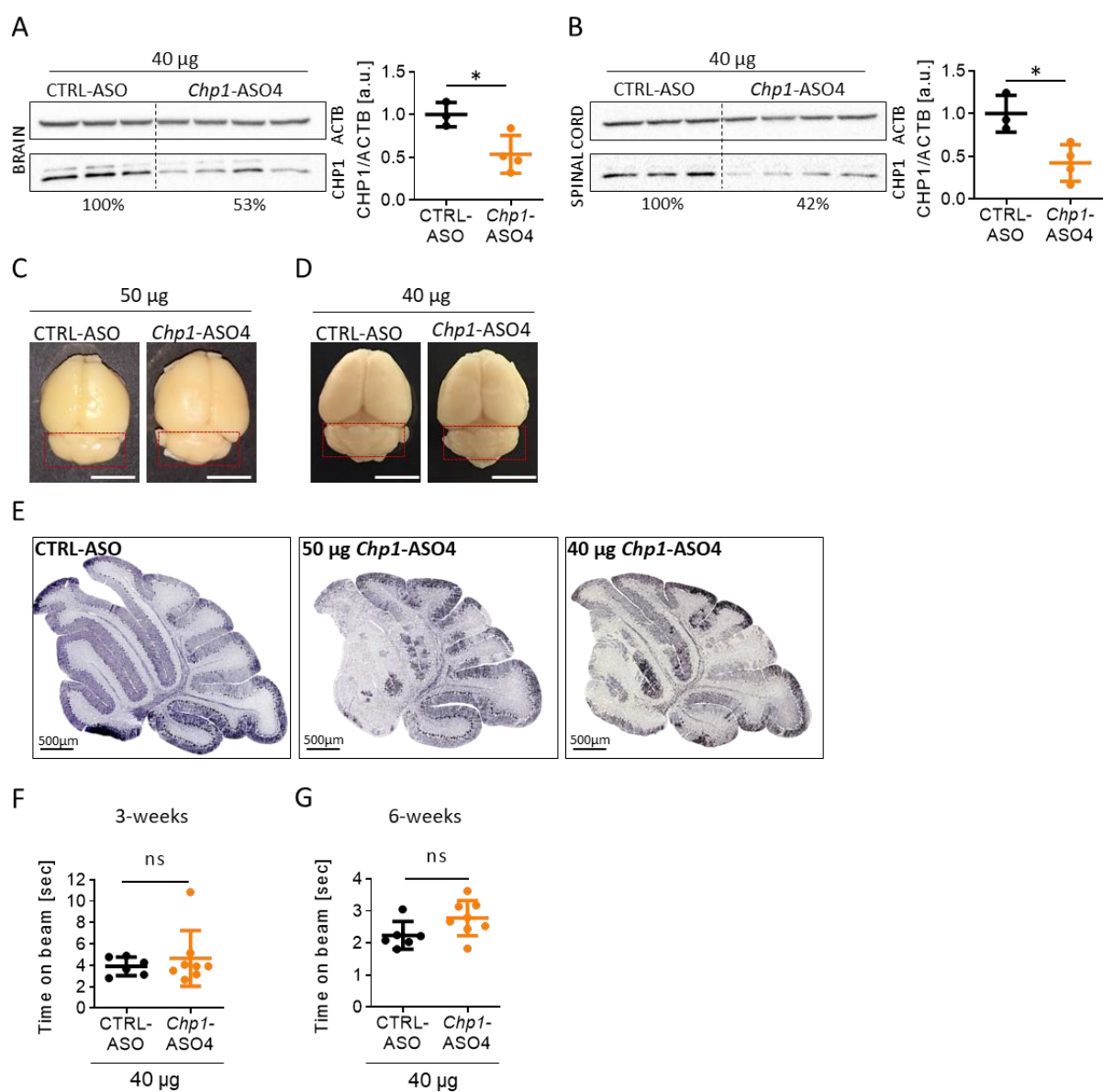


Figure 10. Dosage optimization with 40 and 50 μg *Chp1*-ASO4 in neonatal wild type mice.

A-B) Western blot analysis and quantification of CHP1 levels in brain and spinal cord lysates of ASO injected mice at PND14. 40 μg of *Chp1*-ASO4 led to a 47% reduction of CHP1 levels in brain (A) and 58% reduction in spinal cord (B). ACTB: loading control.

C-D) Morphological analysis of brains from ASO injected mice at 6-weeks. 50 μg *Chp1*-ASO4 (C) caused a reduction of cerebellar size, whereas 40 μg *Chp1*-ASO4 (D) caused a milder reduction. (Scale bar: 5 mm).

E) Representative pictures of sagittal paraffin sections of cerebellum of *Chp1*-ASO4 injected mice at 6-weeks. A dose dependent loss of Purkinje neurons and axon degeneration was detected for 50 and 40 μg *Chp1*-ASO4. Purkinje cells were immunostained with anti-calbindin-D-28k antibody.

F-G) Beam-walking assay of 40 μg *Chp1*-ASO4 injected mice at 3- and 6-weeks, respectively. The time to cross the beam was measured for quantification. 40 μg administration of *Chp1*-ASO4 did not significantly affect the performance at 3-weeks (F) and 6-weeks (G).

All mice were i.c.v. injected at PND1 with 40 μg *Chp1*-ASO4. Unpaired two-tailed Student's t test was performed. All values reported as mean and error bars represent \pm SD. Each dot in the bar graphs represents an independent animal.

The initial knock down data suggested that 40 μg of *Chp1*-ASO4 could represent a valuable option for our therapeutic approach. However, Purkinje neuron population of the cerebellum did not resemble the one in the CTRL-ASO injected mice and one of the animals developed an ataxic gate three weeks after injection. Therefore, in order to avoid secondary effects 40 μg of *Chp1*-ASO4 was discarded as a therapeutic dosage option.

Next, the administration of 20 μg *Chp1*-ASO4 led to CHP1 reduction to 60% in brain (Figure 11A) and 85% in spinal cord (Figure 11B), similar to the effect observed for 10 μg *Chp1*-ASO3, with poor ASO distribution in the CSF towards the spinal cord (Figure 9C and D). In addition, morphological analysis of brains at 6-weeks did not reveal reduction of cerebellum size (Figure 11C), but this concentration was dropped off for not reaching the desired CHP1 reduction in spinal cord.

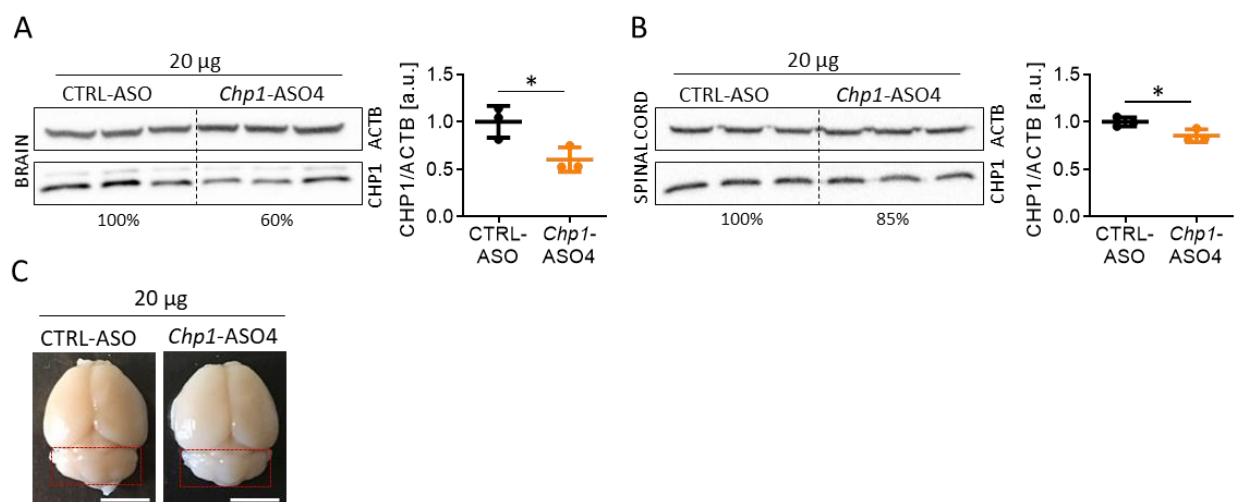


Figure 11. Dosage optimization 20 μg *Chp1*-ASO4 in neonatal wild type mice.

A-B) Western blot analysis and quantification of CHP1 levels in brain and spinal cord lysates of ASO injected mice at PND14. 20 μg of *Chp1*-ASO4 led to a 40% reduction of CHP1 levels in brain (A) and 15% reduction in spinal cord (B). ACTB: loading control.

C) Morphological analysis of brains from ASO injected mice at 6-weeks. 20 μg *Chp1*-ASO4 did not affect the cerebellar size (Scale bar: 5 mm).

Finally, we tested 30 μg of *Chp1*-ASO4, which led to an average CHP1 reduction to 47% in brain and 53% in spinal cord (Figure 12A and B). Notably, brain morphological analysis at 6-weeks of age did not show cerebellar size reduction upon 30 μg of *Chp1*-ASO4 i.c.v. injection (Figure 12C). In addition, no Purkinje neuron degeneration was detected in any of the analyzed mice (Figure 12D). Most importantly, no mice injected with 30 μg *Chp1*-ASO4 displayed at any time point an ataxic gait or reduced performance in comparison to CTRL-ASO treated mice (Figure 12E and F). Strikingly, CHP1 levels detected by western blot in the brain and spinal cord at PND28 were the same as in CTRL-ASO injected animals, indicating a short-term effect of *Chp1*-ASO4 (Figure 12G). Previous work by Torres-Benito and collaborators already showed short-term stability of a gap-MOE ASO targeting *Ncald*, although the therapeutic potential was maintained for some weeks (Torres-Benito et al. 2019).

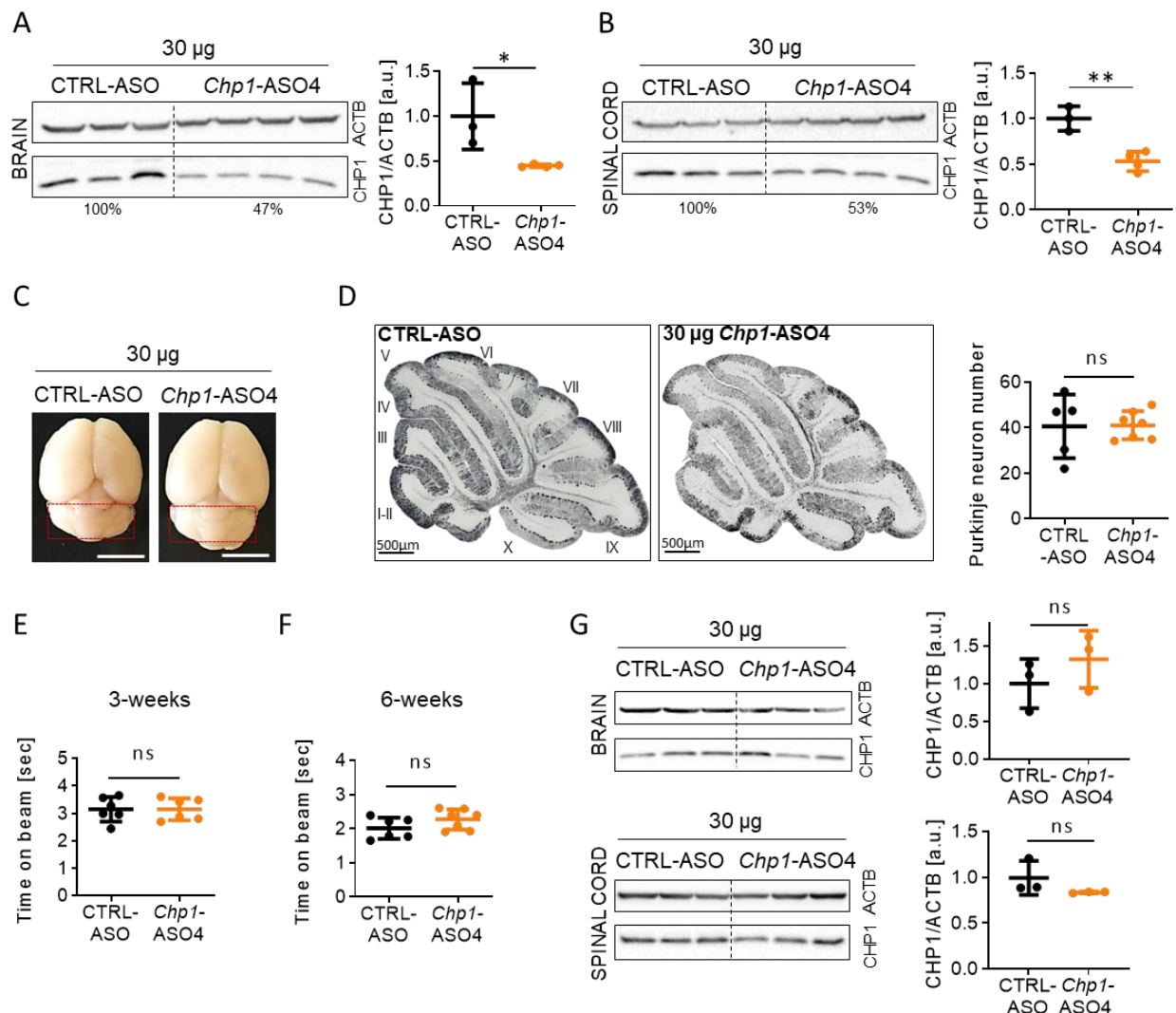


Figure 12. Dosage optimization 30 μg *Chp1*-ASO4 in neonatal wild type mice.

A-B) Western blot analysis and quantification of CHP1 levels in brain and spinal cord lysates of ASO injected mice at PND1 and analyzed at PND14. I.c.v. injection of 30 μg *Chp1*-ASO4 led to a 53% reduction of CHP1 level in brain (A) and 47% reduction in spinal cord (B). * $p \leq 0.05$, ** $p \leq 0.01$.

C) Morphological analysis of brains from ASO injected mice at 6-weeks. 30 μg *Chp1*-ASO4 did not affect the cerebellar size (scale bar: 5 mm), $N = 2$ (CTRL-ASO), $N = 5$ (30 μg *Chp1*-ASO4).

D) Representative pictures of sagittal paraffin sections and quantification of Purkinje neuron number in lobe I-II of the cerebellum of *Chp1*-ASO4 injected mice at 6-weeks. No Purkinje neuron loss and axon degeneration was detected for 30 µg *Chp1*-ASO4. Purkinje cells were immunostained with anti-calbindin-D-28k antibody (Scale bar: 500 µm).

E-F) Beam-walking assay of *Chp1*-ASO4 injected mice at 3-weeks and 6-weeks. The time to cross the beam was measured for quantification. 30 µg *Chp1*-ASO4 did not significantly affect the performance at 3-weeks (E) and 6-weeks (F).

G) Western blot analysis and quantification of CHP1 level in brain and spinal cord for 4-weeks post-injection efficacy study of 30 µg *Chp1*-ASO4. No significant difference was detected.

All mice were i.c.v. injected at PND1 with the 30 µg *Chp1*-ASO4 concentration. Unpaired two-tailed Student's t test was performed. All values reported as mean and error bars represent ± SD. Each dot in the bar graphs represents an independent animal.

The data obtained from the *Chp1*-ASO leads screening in adult and neonatal wild type mice led us to conclude that 30 µg *Chp1*-ASO4 did not promote Purkinje neuronal loss neither animals developed an ataxic gait, meaning that the dosage is safe. Moreover, it leads to CHP1 reduction to the desired therapeutic levels at PND14 of ~50% in brain and most importantly, in spinal cord. However, *Chp1*-ASO4 did not display a long-term reduction effect four weeks after the administration, similar to the observations with *Ncald*-ASO (Torres-Benito et al. 2019). Nevertheless, the positive results obtained by Torres-Benito and collaborators encouraged us to test the combinatorial therapy using 30 µg *Chp1*-ASO4 and low-dose *SMN*-ASO in an intermediate SMA mouse model.

3.1.3 Combination of low-dose *SMN*-ASO and 30 µg *Chp1*-ASO4 in SMA mice at PND21.

Here, we aimed to analyze the therapeutic effect of *Chp1*-ASO4 injection in a double-blinded, randomized preclinical study in a well-established pharmacologically-induced mildly affected SMA mouse model. A suboptimal dose of 30 µg *SMN*-ASO was administered systemically at PND1 in order to slightly elevate *SMN* protein levels in the peripheral organs, thereby, mimicking the asymptomatic patient's condition where gene modifiers exert their protective function.

For the preclinical trial, SMA and heterozygous control (HET) mice on mixed₅₀ background (50% C57BL6/N and 50% FVB/N) were first injected on PND1 with low-dose *SMN*-ASO (30 µg) subcutaneously (s.c.) and subsequently on PND2 with 30 µg CTRL- or *Chp1*-ASO4 i.c.v. respectively (Figure 13). In the present study, HET (*Smn*^{ko/wt}; *SMN2*^{tg/0}) littermates were used as controls.

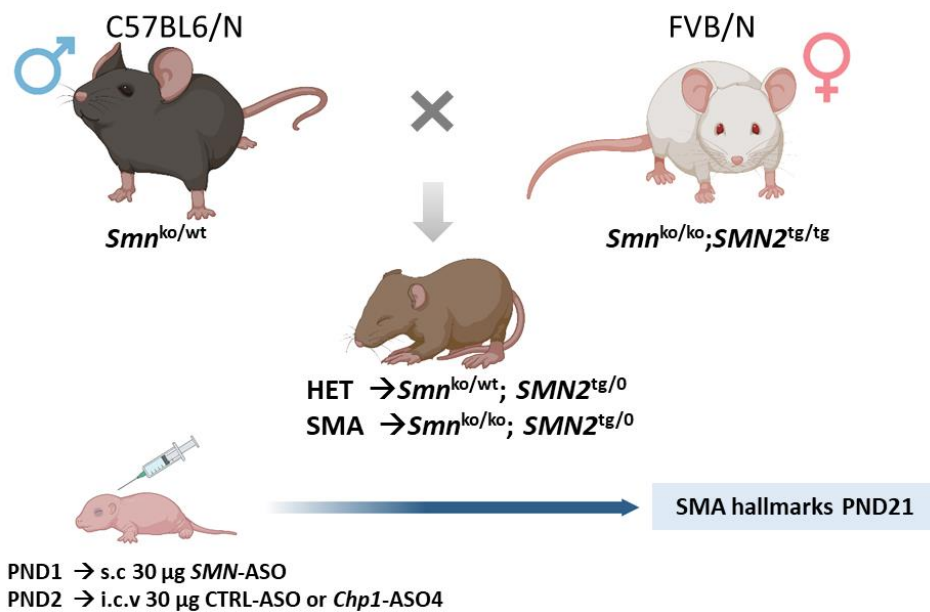


Figure 13. Breeding strategy and experimental scheme.

Breeding strategy to generate a mild SMA mouse model by injecting mixed background mice with low-dose (30 μ g) of *SMN*-ASO at PND1. For the combinatorial therapy, neonatal mice were injected at PND2 with 30 μ g of CTRL-ASO or *Chp1*-ASO4, and SMA hallmarks were analyzed at PND21. Figure generated with BioRender.

Survival of the animals was monitored until PND21, with no reduction observed for any of the four studied groups (Figure 14A), implying a rescue of the multiorgan failure by suboptimal *SMN*-ASO administration. Still, the body weight of SMA mice was reduced in comparison to HET mice (Figure 14B). Surprisingly, we detected that the mean body weight of SMA+*Chp1*-ASO4 injected animals was more variable and presented a trend towards reduced body weight compared to SMA+CTRL-ASO treated mice after PND12.

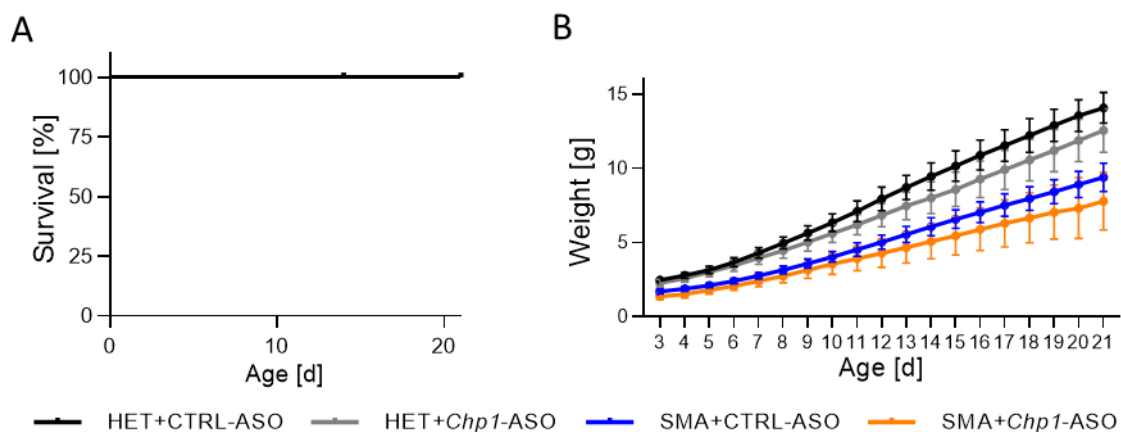


Figure 14. Survival and weight of *Chp1*-ASO-injected SMA mice on Mixed50 background

A) Kaplan-Meier curve until PND21 did not show any difference in survival.

B) Weight progression curve. N = 10 (HET-CTRL-ASO), N = 11 (HET-*Chp1*-ASO4), N = 16 (SMA-CTRL-ASO), N = 8 (SMA-*Chp1*-ASO4). All mice were s.c. injected with 30 μ g *SMN*-ASO at PND1 and i.c.v. injected at PND2 with 30 μ g *Chp1*-ASO4 or CTRL-ASO respectively.

3.1.3.1 Electrophysiological predictors: CMAP and MUNE

Previous studies reported electrophysiological deficits in SMA patients and mice, including reduction of the compound muscle action potential (CMAP) and the motor unit number estimation (MUNE) (Arnold et al. 2014; Bogdanik et al. 2015), relevant electrophysiological predictors of muscle-nerve functionality. In addition, in SMA mice harboring heterozygous *Chp1* reduction via the *vacillator* mutation in combination with low-dose *SMN*-ASO, a significant amelioration of both electrophysiological parameters was achieved in the gastrocnemius muscle, emphasizing the role of CHP1 reduction in motor unit functionality and preservation (Janzen et al. 2018).

Hereby, in order to assess if the combinatorial therapy using *Chp1*-ASO4 has a similar effect in muscle-nerve functionality to the one observed by Janzen and collaborators, we analyzed these electrophysiological predictors in the gastrocnemius muscle at PND21. As previously described, SMA animals exhibited a marked reduction of both parameters in comparison to HET mice (Figure 15A and B). Surprisingly, nor CMAP nor MUNE revealed a significant motor amelioration in SMA+*Chp1*-ASO4 injected mice when compared to SMA+CTRL-ASO-treated animals (Figure 15A and B), which contrast with the results obtained with *Chp1* genetic reduction, suggesting that 30 μ g *Chp1*-ASO4 administered pre-symptomatically had no therapeutic effect at electrophysiological level.

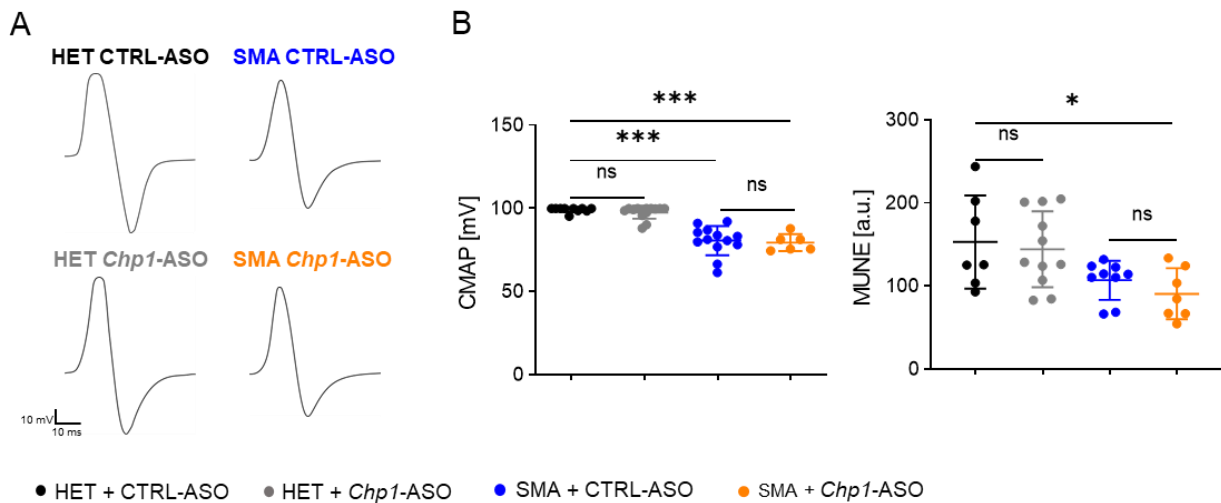


Figure 15. Electrophysiological analysis at PND21 of *Chp1*-ASO4-injected SMA mice.

A) Representative traces of sciatic CMAP response of gastrocnemius muscle at PND21.

B) Dot plots of CMAP and MUNE values at PND21 in HET and SMA mice on mixed₅₀ background with mean \pm SD. Number of animals used for CMAP: N = 10 (HET+CTRL-ASO); N = 14 (HET+*Chp1*-ASO4); N = 13 (SMA+CTRL-ASO); N = 6 (SMA+*Chp1*-ASO4). MUNE: N = 7 (HET+CTRL-ASO); N = 11 (HET+*Chp1*-ASO4); N = 9 (SMA+CTRL-ASO); N = 7 (SMA+*Chp1*-ASO4). For analyses, ordinary one-way ANOVA with Tukey posthoc test for multiple comparisons was applied. * $p \leq 0.05$, *** $p \leq 0.001$.

3.1.3.2 NMJ architecture

NMJ defects have been described as an early pathological feature in SMA, characterized by reduced acetylcholine receptors positive area and delayed maturation (Gogliotti et al. 2012) that precede MN death (Ling et al. 2012). For this reason, we evaluated their architecture in the vulnerable transversus abdominis (TVA) muscle upon 30 μg *Chp1*-ASO4 treatment (Murray et al. 2008). For NMJ quantification, the postsynaptic acetylcholine receptors (AChRs) were stained with α -bungarotoxin (BTX), and the presynaptic terminals with neurofilament-specific antibody (NF) (Figure 16). First, we measured α -BTX-positive endplates area. As expected, NMJ area was reduced in SMA+CTRL-ASO compared with HET+CTRL-ASO at PND21. However, there was no significant improvement in the size of SMA NMJs upon *Chp1*-ASO4 treatment compared to CTRL-ASO. The lack of NMJ amelioration upon *Chp1*-ASO4 treatment go in line and explain the results obtained from the electrophysiological predictors (section 3.1.3.1): pharmacological reduction of CHP1 by i.c.v. injection of 30 μg *Chp1*-ASO4 is not enough to ameliorate NMJ pathology in PND21 SMA mice.

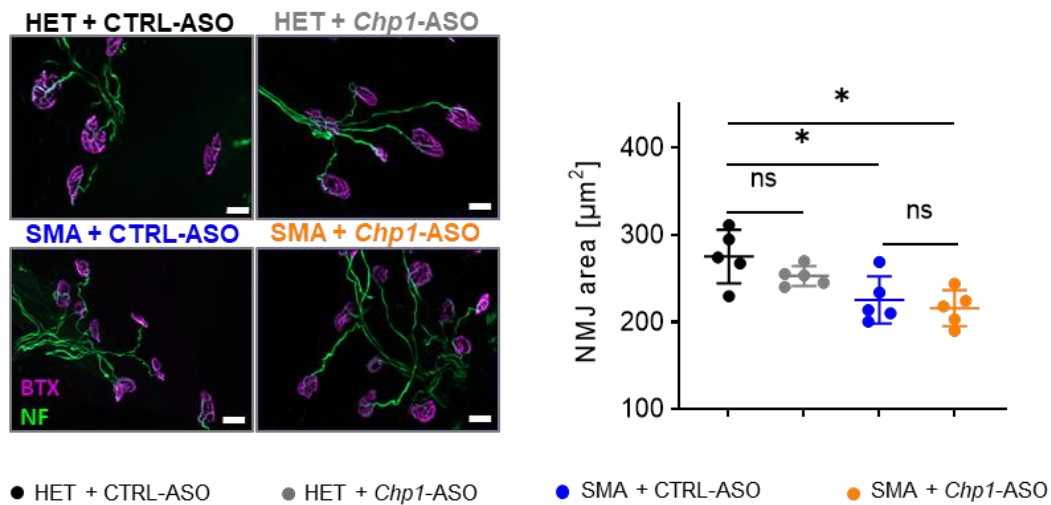


Figure 16. NMJ analysis at PND21 of *Chp1*-ASO4-injected SMA mice.

Representative images and quantification of NMJ area and maturity in TVA muscle at PND21, showing postsynaptic NMJ region (BTX, magenta) and presynaptic nerve (NF, green) (scale bar: 20 μm). NMJ area was analyzed with ImageJ (N=5, n= 100 NMJs/mouse). Statistics were performed with mean values of animals per group. Ordinary one-way ANOVA with Tukey posthoc test for multiple comparisons, * $p \leq 0.05$.

3.1.3.3 Muscle fiber size and spinal MNs proprioceptive inputs

In the sensory-motor circuit, proprioceptive neurons localized in the dorsal root ganglia convey information coming from the muscles and tendons to the MNs, thus allowing fine control of the movements. Sensory-motor connectivity, the proprioceptive inputs in the MNs, have been reported to be impaired in SMA mouse models (Mentis et al. 2011; Shorrock, Gillingwater, and Groen 2019), thus we next quantified the number of glutamatergic inputs per MN soma in sections of the spinal cord lumbar region which is vulnerable to degeneration. In this case, we compared two groups, SMA+CTRL-ASO and SMA+*Chp1*-ASO4 treated animals, in order to assess if CHP1 downregulation has an effect on the number of proprioceptive inputs and, therefore in the functionality of sensory synapsis. However, in contrast with the observations obtained by Janzen and collaborators showing an increase in the number of VGLUT1⁺ inputs upon CHP1 reduction, we did not detect differences in the number of proprioceptive synapses per MN soma between the groups (Figure 17A).

Even though MNs are the most affected cells in SMA and their dysfunction contributes to skeletal muscle atrophy, it is likely that SMN-depleted muscles exert intrinsic defects that can be directly involved in SMA pathology. In the previous work performed by Janzen and collaborators, tibialis anterior fiber analysis revealed a clear size difference between HET and SMA animals (Janzen et al. 2018). Moreover, a significant increase in average fiber size was observed in heterozygous *Chp1* mutant SMA animals. Since CHP1 reduction might have a positive effect on muscle pathology, we quantified the area of muscle fibers from the tibialis anterior muscle at PND21, which is known to be affected in SMA. The results showed no significant positive effect of *Chp1* reduction in the mean muscle fiber area in PND21 SMA animals (Figure 17B).

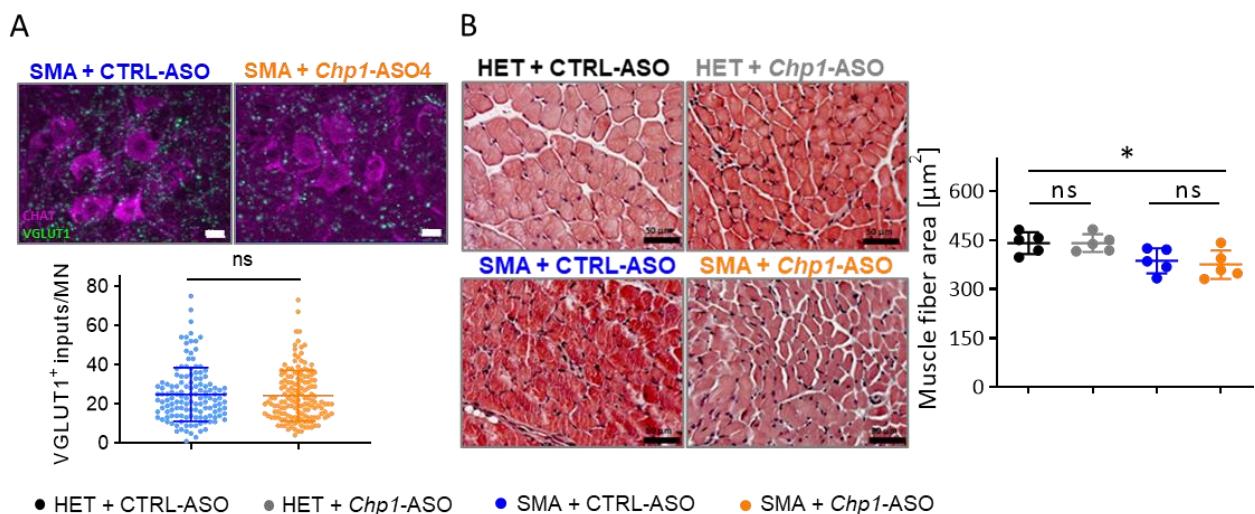


Figure 17. Proprioceptive inputs and muscle fiber size analysis at PND21 of *Chp1*-ASO4 injected SMA mice.

A) Representative images and quantification of proprioceptive inputs per MN soma in SMA mice. MN were stained with CHAT (magenta, MN) and VGLUT1 (green, for glutamatergic synapses) (Scale bar: 20 μm). Mean

input number within 5 μm of MN soma was analyzed with ImageJ. $N = 3$ for both groups, $n = 30\text{-}50$ MNs/animal. Unpaired two-tailed Student's t test was performed.

B) Representative H&E staining and quantification of muscle fiber area of tibialis anterior muscle at PND21. (Scale bar: $50\mu\text{m}$). $N = 5$ for all groups, $n=100$ fibers/animal). Ordinary one-way ANOVA with Tukey posthoc test for multiple comparisons. Error bars represent \pm SD. $*p \leq 0.05$.

In conclusion, these results contrast with the data obtained by Janzen and collaborators and can be explained by apparent short-term effect of *Chp1*-ASO4, which does not maintain CHP1 levels of about 50% for a prolonged period as shown in Figure 12G. Consequently, the time CHP1 protein amount fluctuates between therapeutic and non-therapeutic levels is not sufficient to improve SMA hallmarks at PND21.

3.1.4 Re-injection of *Chp1*-ASO4 at PND28

Next, we wanted to assess if the re-injection of *Chp1*-ASO4 at PND28 could maintain *Chp1* at therapeutic levels and lead to an improvement in SMA hallmarks as previously observed in the *Chp1* heterozygous genetic model (Janzen et al. 2018).

3.1.4.1 Efficacy and tolerability of *Chp1*-ASO4 i.c.v. bolus injection at PND28 in wild type mice

First, we tested the efficacy and tolerability of various *Chp1*-ASO4 dosages in PND28 wild type mice. All tested concentrations (15, 20 and 25 $\mu\text{g/g}$ of animal) succeeded to downregulate CHP1 levels in brain and spinal cord in comparison to PBS injected animals. Moreover, injection of 20 $\mu\text{g/g}$ *Chp1*-ASO4 achieved a CHP1 reduction to about $\sim 45\%$ in brain (Figure 18A) and $\sim 60\%$ in spinal cord (Figure 18B) 2-weeks after injection. Importantly, none of the animals developed an ataxic gait (data not shown). Following the same strategy used for the treatment of SMA patients with nusinersen, we decided to inject a fixed amount of *Chp1*-ASO4 (400 μg) independently of the body weight of the animals.

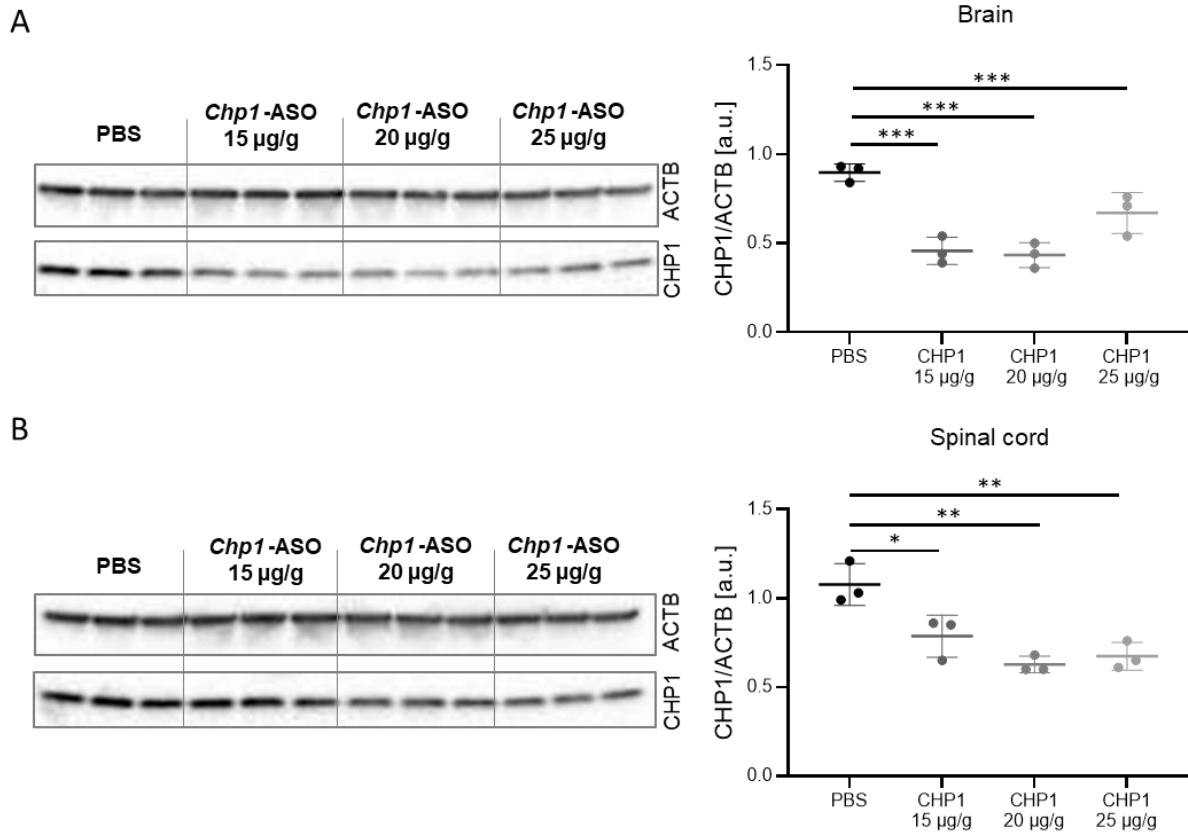


Figure 18. Efficacy of various *Chp1*-ASO4 concentrations 2-weeks after i.c.v. bolus injection in adult wild type mice.

A-B) *Chp1*-ASO4 efficacy at different concentrations in brain (A) and spinal cord (B) 2-weeks after injection via i.c.v. bolus at PND28 in wild type mice, in comparison to PBS injected animals. ACTB: loading control. Ordinary one-way ANOVA with Tukey posthoc test for multiple comparisons. Error bars represent \pm SD. * $p \leq 0.05$, ** $p \leq 0.01$, *** $p \leq 0.001$. Each dot in the bar graphs represents an independent animal.

Next, we followed a similar experimental scheme as in the first part of the study, with an additional administration of 400 μ g *Chp1*-ASO4 at PND28 by i.c.v. bolus injection, and SMA hallmarks were analyzed at 2 months of age (Figure 19A). Western blot analysis performed on brain samples at 2 months revealed a significant downregulation of CHP1 in HET and SMA animals re-injected with *Chp1*-ASO4 when compared to their respective CTRL-ASO group (Figure 19B). In contrast, in spinal cord of HET animals no significant reduction was observed upon *Chp1*-ASO4 treatment after 2 months (Figure 19C). Although, there was a significant reduction between SMA CTRL-ASO and SMA *Chp1*-ASO groups (Figure 19C).

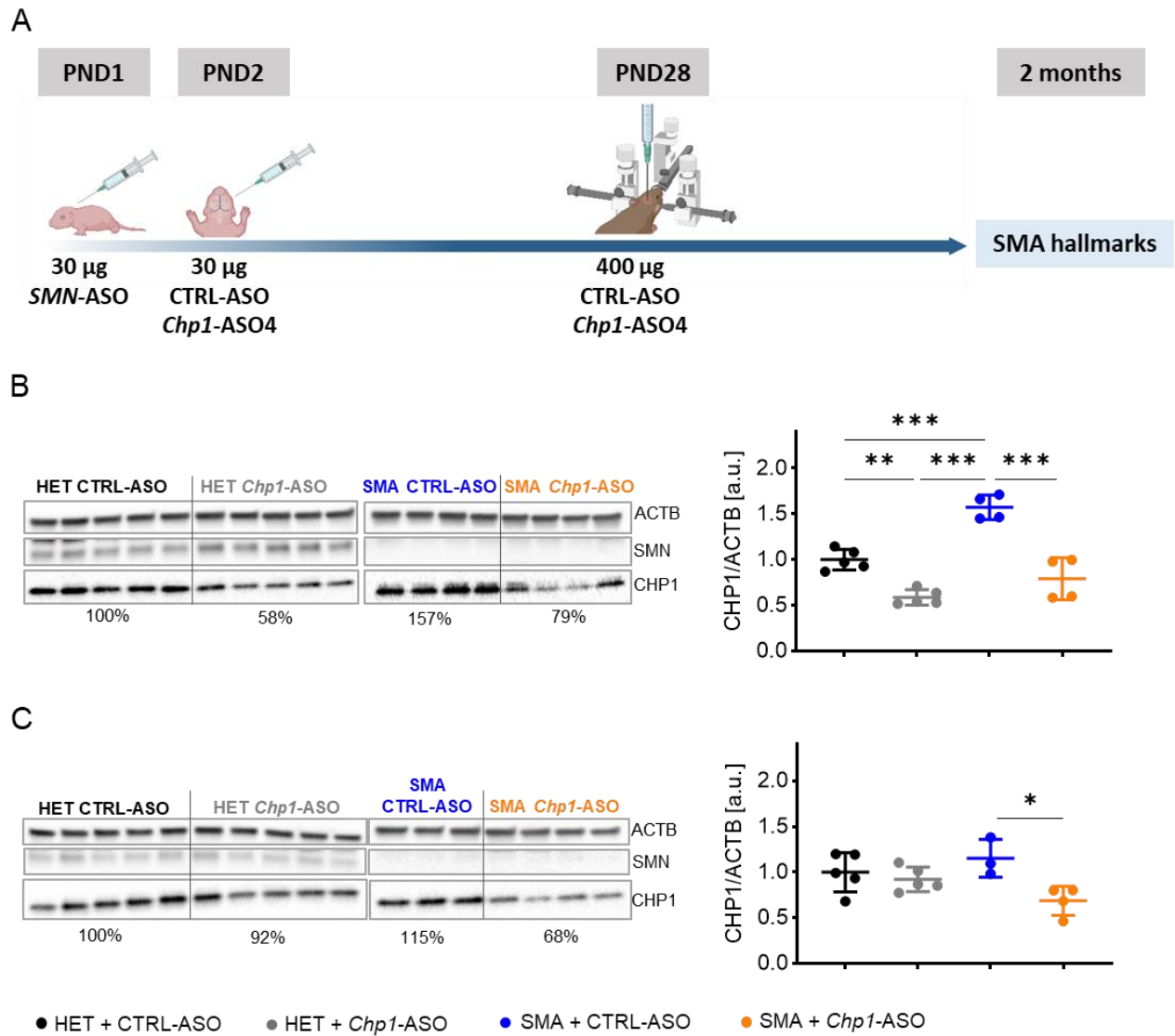


Figure 19. Efficacy of *Chp1*-ASO4 i.c.v. bolus re-injected mice at 2 months

A) Treatment injection scheme. Figure generated with BioRender.

B-C) Western blot analysis and quantification of CHP1 levels in brain (B) and spinal cord (C) lysates from ASO injected mice. B) 4-weeks post i.c.v. bolus injection with 400 µg *Chp1*-ASO4 shows significant reduction between *Chp1*-ASO4 and CTRL-ASO injected animals in brain. C) 4-weeks post i.c.v. bolus injection with 400 µg *Chp1*-ASO4 only shows significant reduction in spinal cord in SMA animals when compared to 400 µg SMA-CTRL-ASO, but not between HET groups. ACTB: loading control. Ordinary one-way ANOVA with Tukey posthoc test for multiple comparisons. Error bars represent \pm SD. All mice were s.c. injected with 30 µg *SMN*-ASO at PND1 and i.c.v. injected at PND2 and PND28 with 30 µg/400µg *Chp1*-ASO4 or CTRL-ASO respectively. * $p \leq 0.05$, ** $p \leq 0.01$, *** $p \leq 0.001$. Each dot in the bar graphs represents an independent animal

3.1.4.2 Analysis SMA hallmarks upon re-injection of *Chp1*-ASO4

SMA hallmarks were analyzed at two months of age after *Chp1*-ASO4 or CTRL-ASO re-administration to assess if the pharmacological reduction of CHP1 could have beneficial therapeutic effects over time.

As previously performed, we determined the NMJ area from the transversus abdominis muscle. Re-injection with *Chp1*-ASO4 had no enhancing effect on NMJ area in SMA compared to CTRL-ASO injected animals (Figure 20A). Moreover, SMA pathology at the NMJ level is characterized by denervation leading to the loss of motor functionality. Thus, we wanted to assess if *Chp1*-ASO4 treatment could exert a protective influence. Innervation degree was categorized as fully, partially innervated or denervated. Importantly, mild SMA animals injected with CTRL-ASO showed a higher degree of NMJ denervation at the TVA muscle than the HET mice. However, *Chp1*-ASO4 re-injection did not rescue the denervation in SMA adult mice (Figure 20B).

Finally, we studied muscle pathology by analyzing fiber size from the gastrocnemius muscle. Interestingly, analysis of size-grouped gastrocnemius muscle fibers exhibited a trend towards an increase in fibers with larger diameter (300 - 400 μm) in SMA *Chp1*-ASO4 injected animals compared to CTRL-ASO treated SMA mice (Figure 20C).

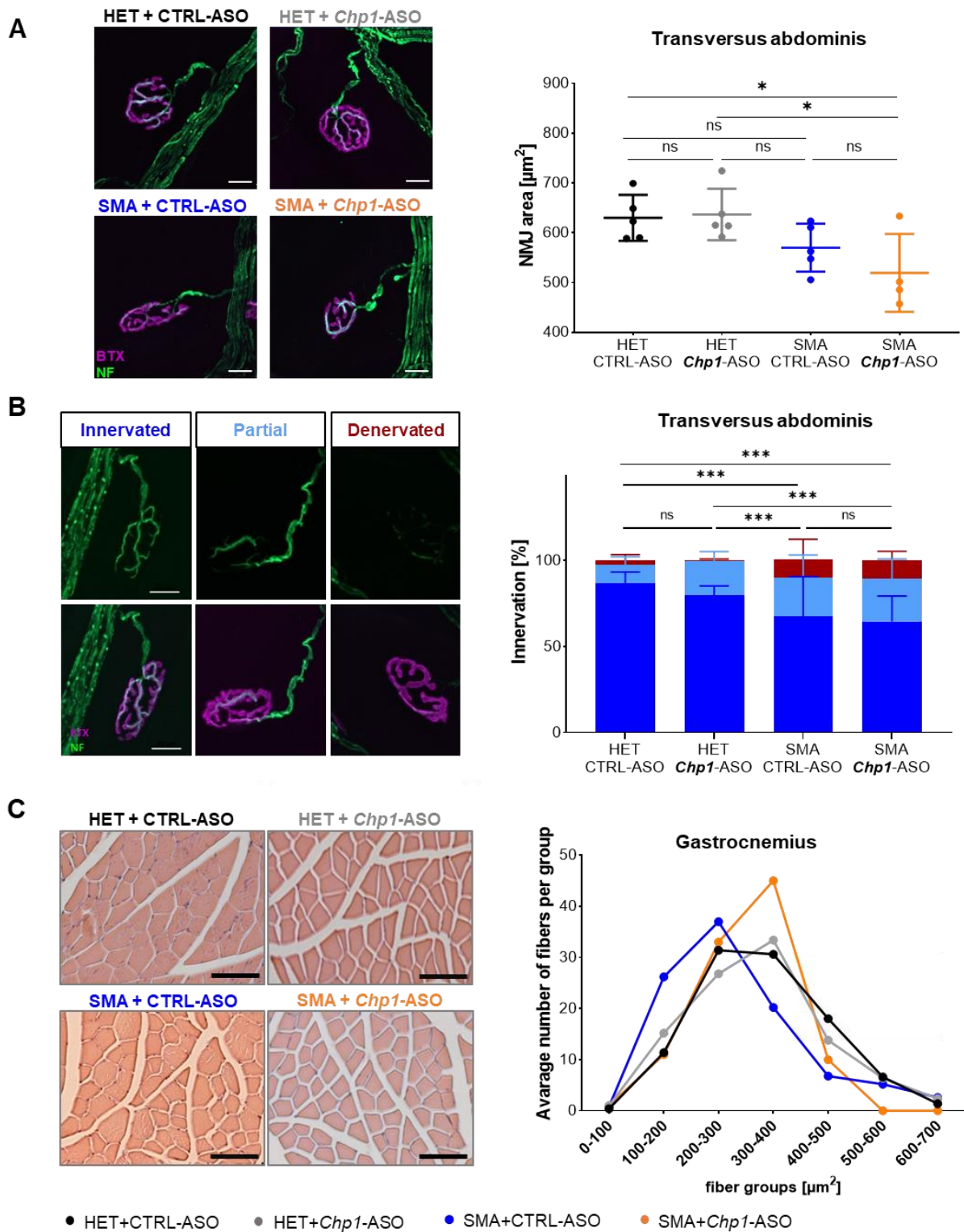


Figure 20. Morphological and histological analysis of *Chp1*-ASO4 re-injected mice

A) Representative images and quantification of NMJ area in TVA muscle, showing postsynaptic NMJ region (BTX, magenta) and presynaptic nerve (NF, green) (scale bar: 20 μm). Each dot in the bar graphs represents an independent animal. For each animal, 50 NMJs were analyzed. Statistics were performed with mean values of animals per group. Ordinary one-way ANOVA with Tukey posthoc test for multiple comparisons. * $p < 0.05$.

B) NMJ innervation analysis from TVA muscle, showing postsynaptic region (BTX, magenta) and presynaptic nerve (NF, green). NMJ innervation was classified in three categories: Innervated when more than 80% of the AChRs was covered by the nerve terminals, partially innervated when the innervation was between 15 – 80%, and denervated when the nerve terminals covered less than 15% of the endplate. (Scale bar: 20 μm). N = 4 for

all groups, n = 40-60 NMJs/animal. Results are presented in percentages from n ≥ 150 representing 4 independent experiments. *** denotes statistical significance $p \leq 0.001$ (χ^2 test).

C) Representative H&E staining and grouping of gastrocnemius muscle fibers according to the area (μm^2) at 2 months of age. (Scale bar: 50 μm). N = 5 for all groups, n = 100 fibers/animal).

Altogether, we demonstrated that the *Chp1*-ASO4 used in this preclinical study specifically downregulates *Chp1*. Moreover, injection with 30 μg and 400 μg *Chp1*-ASO4 in neonatal and adult animals, respectively, is well tolerated and do not produce toxic effects. However, even though 30 μg of *Chp1*-ASO4 is safe and does not induce an ataxic phenotype, it is not enough to counteract the SMA pathology at PND21 when combined with low-dose *SMN*-ASO. Unfortunately, during *Chp1*-ASOs screening and dosage optimization, we observed that administration of doses above 40 μg led to ataxic defects, excluding the possibility of increasing the dosage. In addition, re-injections with 400 μg *Chp1*-ASO4 at PND28 failed to improve SMA hallmarks in a long term.

3.1.5 hiPSCs derived MNs: in vitro model for drug testing

The discovery of hiPSCs allowed researchers to model diseases *in vitro* and perform drug screenings in the targeted cell type. In the present study, we aimed to determine the therapeutic potential of *Chp1* or *Ncald* (section 3.2.2) pharmacological reduction using human ASOs targeting the respective mRNAs in MNs derived from hiPSC lines. For this reason, we first had to establish a MN differentiation protocol in our lab that could provide us with high yield functional MNs.

As an important side note, all the experiments, images, graphs, statistics and text presented from this point on are unpublished or under preparation for a future manuscript.

3.1.5.1 Healthy and SMA hiPSCs lines

In our lab we have several hiPSC lines derived from healthy and SMA patients from type I to type III that were previously validated (Table 1).

For maintenance and expansion, hiPSCs were cultured in feeder-free conditions using the commercial pluripotent media mTeSR™1 and matrigel coated plates. All cell lines exhibited typical hESC-like appearance consisting in small cell body with a high nucleus/cytoplasm ratio and a characteristic flat colony shape with rounded borders and dense centre. First, prior to our drug testing, we wanted to determine if the hiPSC lines expressed pluripotency markers essential for stemness maintenance. All

hiPSC lines expressed pluripotent stem cell markers as OCT4 (Figure 21A) and SOX2 (Figure 21B), determined by immunostaining.

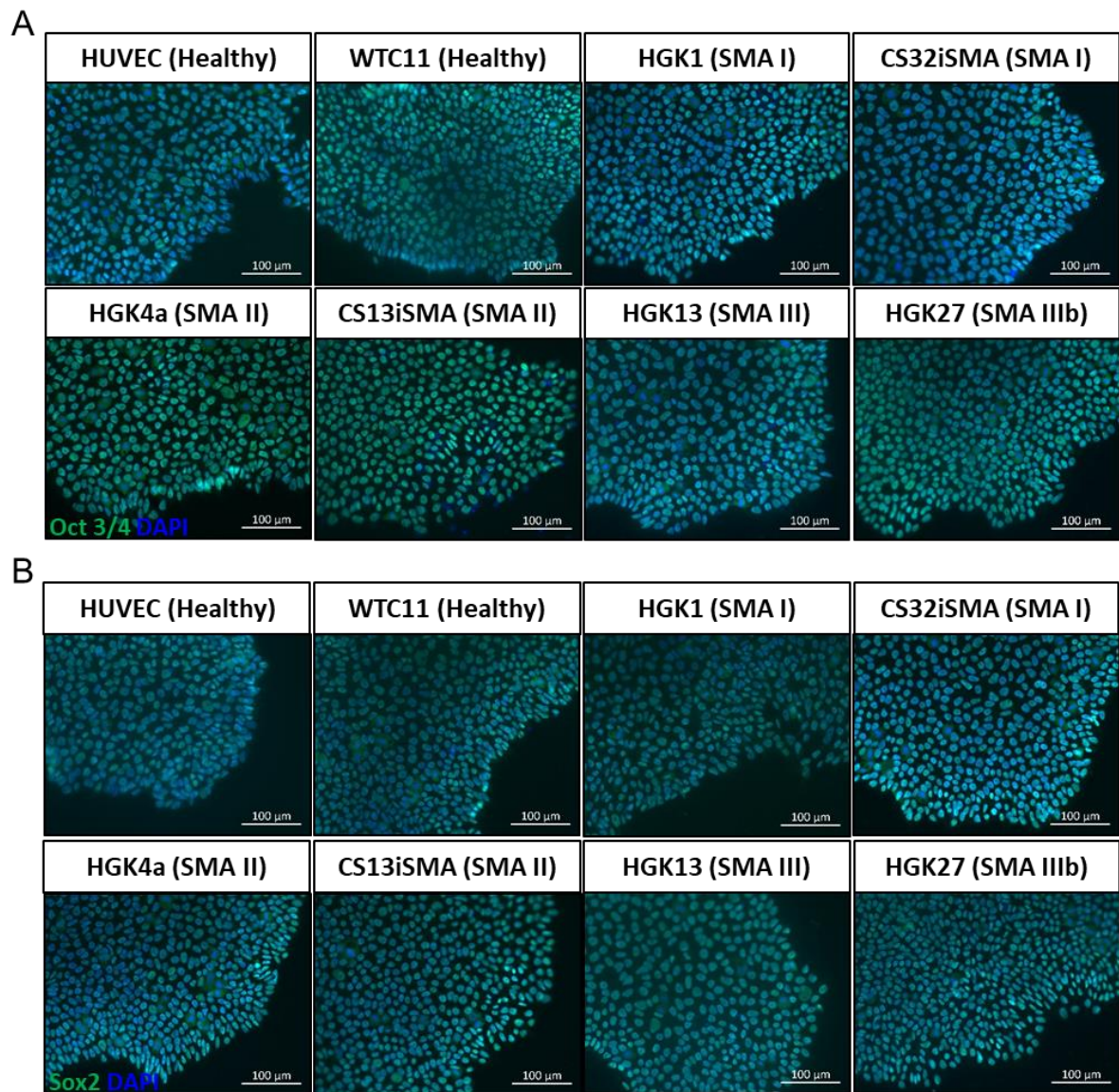


Figure 21. hiPSCs staining of pluripotency markers OCT3/4 and SOX2.

A-B) Representative pictures of typical flat colony morphology in all hiPSC lines.

A) Cells were immunostained for the pluripotency marker OCT 3/4 (green). Nuclei were counterstained with DAPI (blue).

B) Cells were stained with SOX2 marker (green) and nuclei were counterstained with DAPI (blue). Scale bar 100 μm .

In addition, SMN staining was performed in order to detect the number of SMN gems in the nucleus. As expected, healthy hiPSC lines exhibited characteristic SMN dot-like gems marked with the white arrows, which were absent in all SMA type I or type II cells (Figure 22). Few small gems were observed

in both SMA type III lines. Furthermore, SMN was also detected in the cytosol of the healthy and SMA type III hiPSC lines, but markedly reduced in SMA type I and II lines.

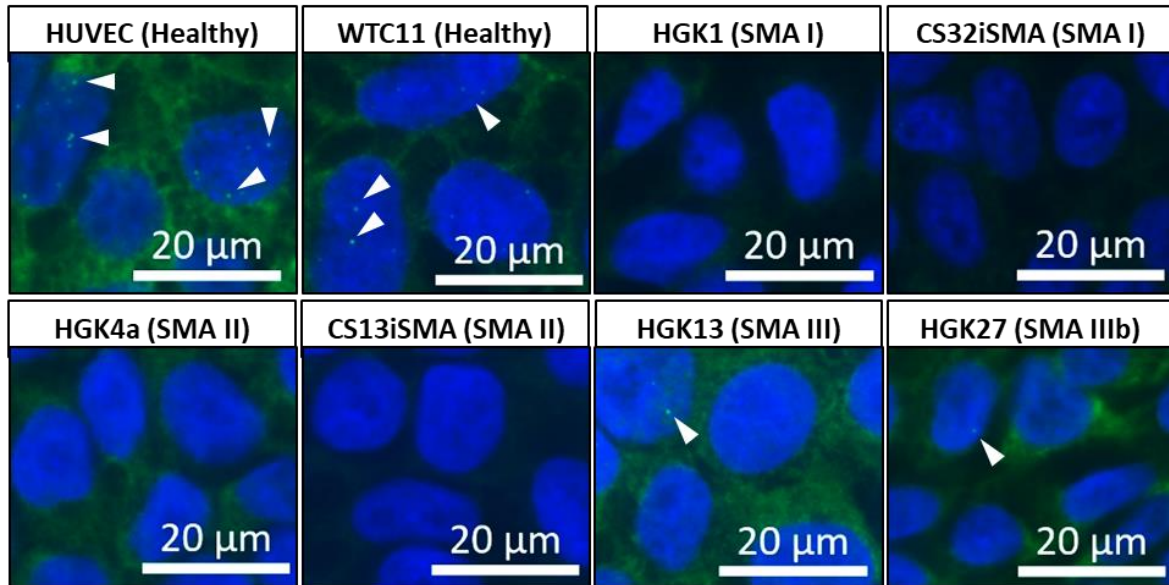


Figure 22. SMN protein staining in hiPSCs lines.

SMN staining (green) showed the characteristic dots in the nuclei (blue, DAPI) that represents the gems (marked with white arrows) in both HUVEC and WTC11 healthy lines, and presence of SMN in the cytosol. SMN gems were not observed in SMA type I (HGK1 and CS32iSMA) and SMA type II (HGK4a and CS13iSMA) and a visible reduction of SMN staining in the cytosol. Few gems were detected in some of the nuclei of the SMA type III individual and an increase in SMN protein present in the cytosol.

3.1.5.2 Directed differentiation of hiPSC into MNs

To obtain MNs from hiPSC lines, we selected the high-efficiency MN differentiation protocol used in (Guo et al. 2017), to which we applied some modifications. The protocol (Figure 23) begins with the generation of embryoid bodies (EBs), which resemble the 3D conformation of embryos and facilitate spontaneous differentiation of the uncommitted stem cells (Odorico, Kaufman, and Thomson 2001). On the first days of the differentiation, induction into the neuroectodermal lineage (neuralization) was achieved with SB431542 (which inhibits the transforming growth factor beta mediated activation of SMAD proteins) and LDN193189 (inhibits the bone morphogenic protein signaling pathway), in what is commonly known as dual SMAD inhibition, and by activating Wtn signaling using CHIR99021 (inhibits Glycogen synthase kinase 3, GSK3). Next, in the patterning phase of the neural progenitors, caudalization was accomplished with retinoic acid (RA) and ventralization with Smoothed agonist (SAG) responsible for sonic hedgehog signaling pathway activation. The strong inhibitor of the γ secretase, DAPT, was later added to the MN progenitors to hamper Notch pathway, that will further enhance the differentiation towards MNs (Ben-Shushan, Feldman, and Reubinoff 2015). Finally,

maturation of the spinal MNs was achieved by administration of three neurotrophic factors: brain-derived neurotrophic factor (BDNF), glial cell-derived neurotrophic factor (GDNF) and ciliary neurotrophic factor.

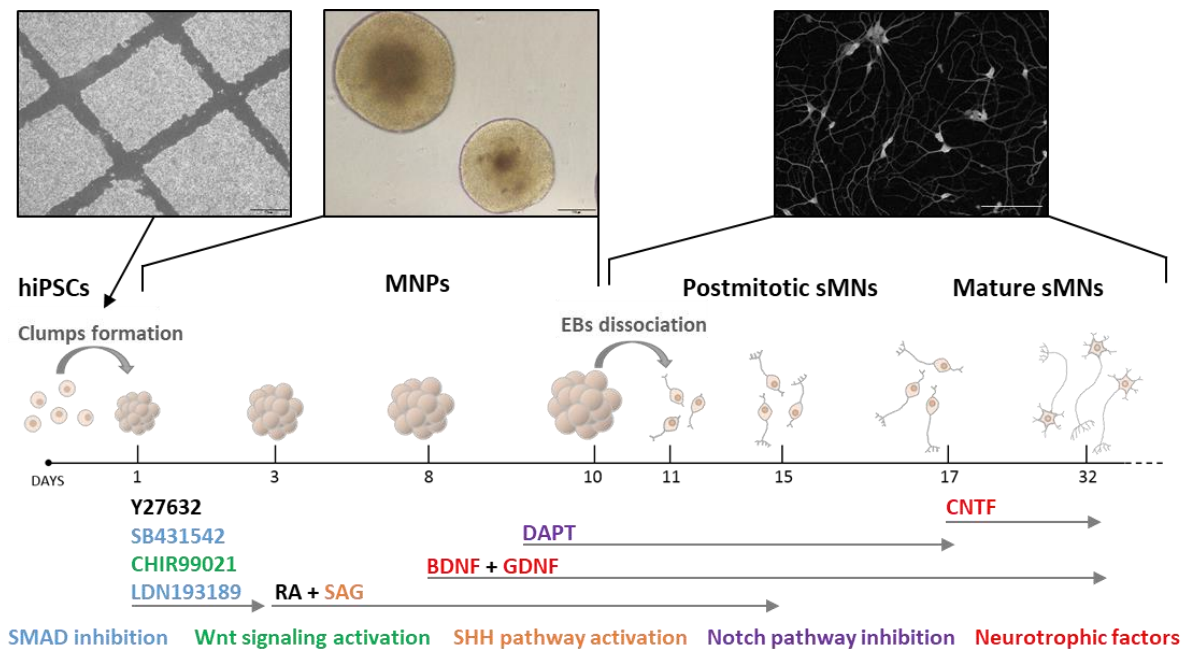


Figure 23. Scheme of the MN differentiation protocol from hiPSCs.

Left image shows the similar-sized squares manually made to help in the formation of the clumps (Scale bar: 500 μm). Central image shows aspheric embryoid bodies from the WTC11 hiPSC line at day 7 (Scale bar: 200 μm). Right image is a representative picture of a MN culture derived from healthy HUVEC hiPSCs at d15 of the differentiation (Scale bar: 100 μm). Above of the gray arrows are the abbreviation of the cytokines used in the respective days during the differentiation, and below, following the color code, their role. MNPs refers to MN progenitors.

To determine the efficiency of the differentiation protocol in our hands, for each cell line, MNs were fixed at day 15 of the differentiation and immunostained for LIM Homodomain factor Islet1 (ISL1), one of the first MN transcription factor expressed in post mitotic MNs (Liang et al. 2011). The ratio between ISL1⁺ cells and DAPI was quantified from three independent differentiations (Figure 24). MN differentiation protocol efficiency ranged from 50 to 75% of ISL1⁺ cells between cell lines. SMA lines harboring different *SMN2* copies did not differ morphologically at this time point in comparison with MNs from healthy individuals. Following this differentiation protocol, SMA type II (CS13iSMA) and SMA type III (HGK27) lines exhibited a reduced number of ISL1⁺ cells compared to SMA type II line HGK4, which reached the highest percentage of ISL⁺ MNs. We can conclude that in general, the established protocol enables the direct differentiation of hiPSCs into MNs expressing ISL1. However, despite of the SMA background, some lines differentiate more efficiently than others do.

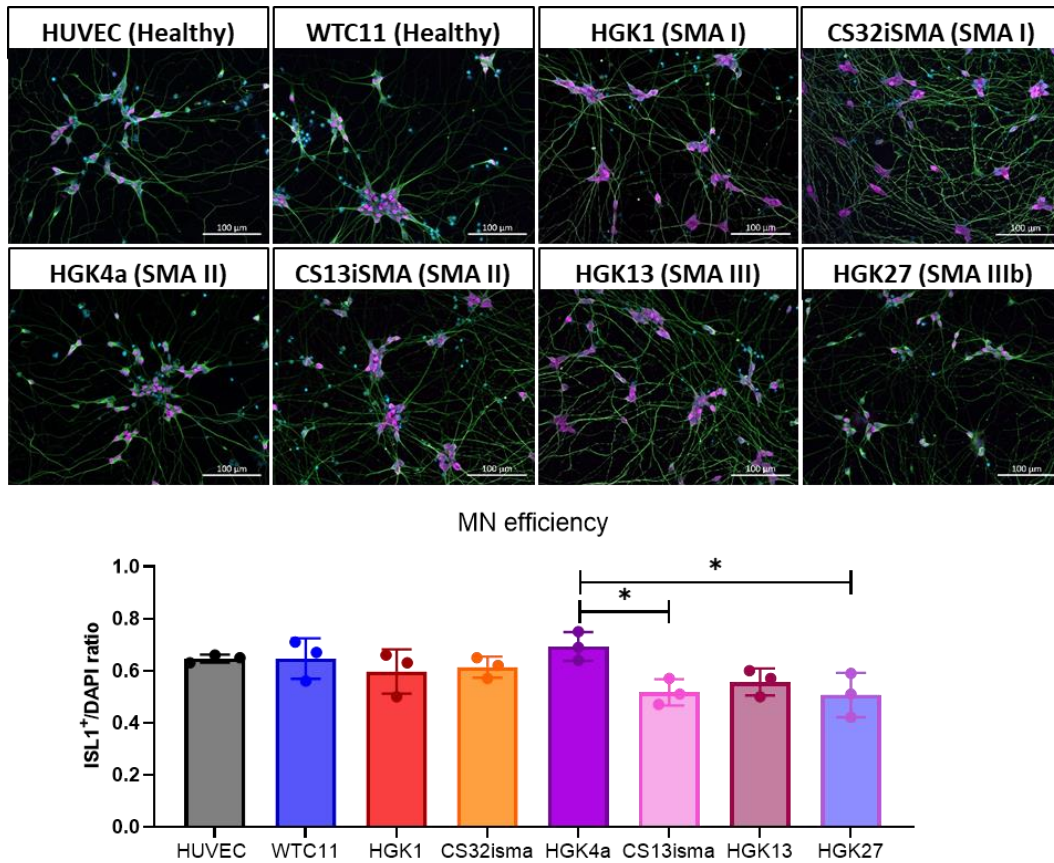


Figure 24. MN differentiation protocol efficiency, ISL1⁺/DAPI.

All hiPSCs were differentiated into MNs following the same protocol previously described, and MNs were fixed and immunostained at day 15. MN specification was determined by the presence of ISL1 positive staining (magenta), axons were counterstained with β -III-tubulin (green), and nuclei with DAPI (blue). Scale bar: 100 μ m for all images. Ordinary one-way ANOVA with Tukey posthoc test for multiple comparisons. Error bars represent \pm SD. * $p \leq 0,05$. Each dot represents the average ratio of ISL1⁺/DAPI of each independent differentiation, N=3 for all hiPSC lines. Total number of cells counted per line is: HUVEC = 1461, WTC11 = 1534, HGK1 = 1466, CS32iSMA = 1289, HGK4 = 759, CS13iSMA = 1011, HGK13 = 460, HGK27 = 350.

3.1.5.3 SMN protein is reduced in SMA hiPSC derived MNs

Next we wanted to validate SMN loss in SMA hiPSCs derived MNs. SMN can be found in the nucleus (Gubitz, Feng, and Dreyfuss 2004), cytoplasm (Liu and Dreyfuss 1996), along the axon and the growth cone (Fan and Simard 2002; Fallini, Bassell, and Rossoll 2010), where it exerts a plethora of functions (section 1.2). We differentiated MNs from the healthy line HUVEC and a SMA type I, CS32iSMA line. Immunostaining was performed at day 20 of the differentiation. As expected, SMN was detected in the neuronal soma and along the axons of healthy derived MNs, whereas a marked reduction was observed in the SMA type I MNs (Figure 25A). Moreover, a clear SMN reduction was detected at the growth cones of the MNs (Figure 25B) compared to healthy MNs.

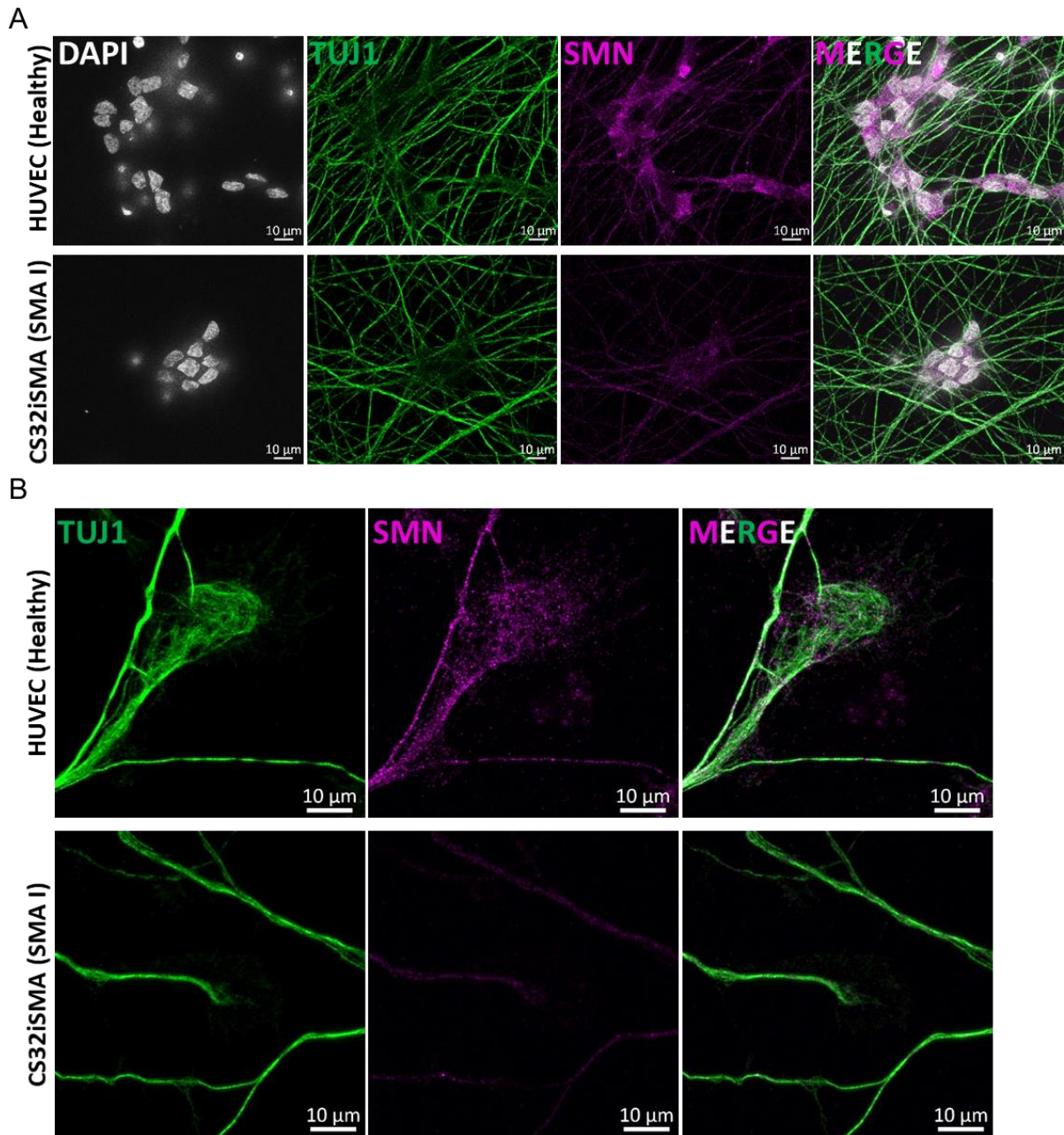


Figure 25. SMN is reduced in MN soma and growth cone of SMA hiPSC derived MNs

SMN staining (magenta) of healthy and SMA type I MNs derived from hiPSCs.

A) SMN localizes at the nucleus (white, DAPI), cytoplasm and axons (green, TUJ1) of healthy MNs, whereas a strong reduction of the signal was observed in SMA type I MNs. Scale bar 10 μm.

B) SMN (magenta) accumulates at the presynaptic terminal, the growth cone. Axons are counter stained with TUJ1 (green), a microtubule marker. Scale bar 10 μm.

3.1.5.4 hiPSC derived MNs exhibit synaptic machinery components

In order to assess if the derived MNs express relevant proteins involved in the synaptic machinery, mature neuronal cells were fixed and immunostained at day 20 with PSD95, Synaptophysin and Bassoon (Figure 26). Postsynaptic density protein 95 (PSD95) is a scaffolding protein that orchestrates

the localization of receptors, channels and signaling proteins involved in synapses of excitatory neurons (Jeong et al. 2019). Synaptophysin is a presynaptic vesicular protein that regulates vesicle endocytosis during and after neuronal stimulation (Kwon and Chapman 2011). Bassoon is a protein localized at the active zone of the presynaptic terminals. At day 20, after three days in culture under maturation conditions MNs expressed PSD95, synaptophysin and bassoon, key components involved in synaptic transmission.

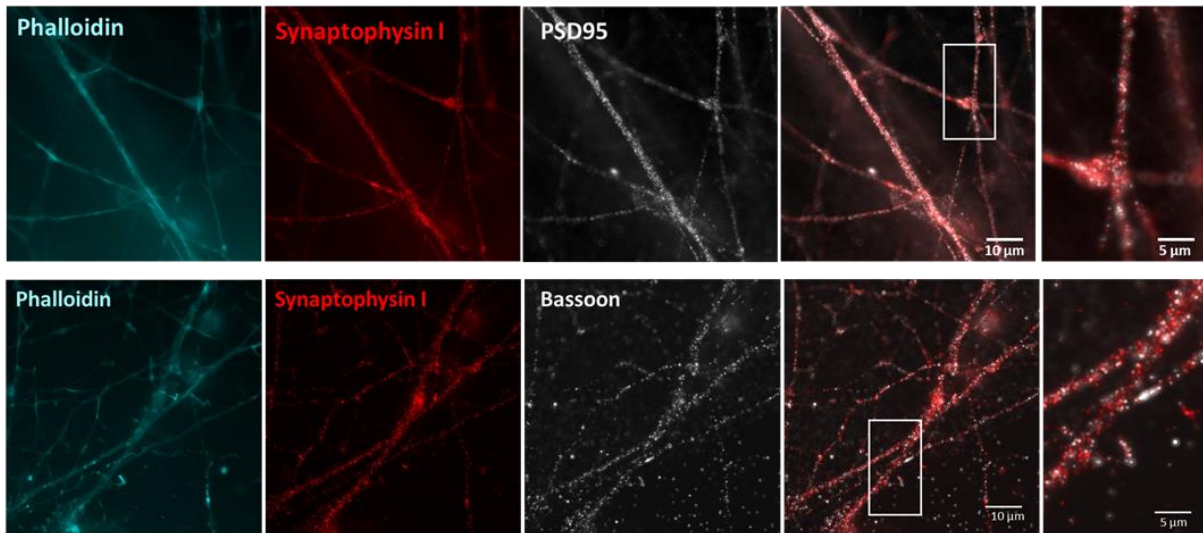


Figure 26. Immunostaining for neurotransmission machinery components.

Mature HUVEC hiPSC derived MNs were stained at day 20 with phalloidin (light blue) synaptophysin I (red), PSD95 (upper image, white) and bassoon (lower image, white). MNs exhibit relevant components required for neurotransmission. Scale bar 10 μm .

3.1.6 Human *CHP1*-ASO leads testing in hiPSCs derived MNs

In parallel to our preclinical studies on *SMN*-ASO and *Chp1*-ASO combinatorial therapy, we tested the delivery method and efficacy of three MOE-gapmer ASOs targeting human *CHP1* in hiPSC derived MNs (Figure 27A). *CHP1*-ASO57 and *CHP1*-ASO59 bind to a region located in intron 1, whereas *CHP1*-ASO84 binds to a region in exon 7 (Figure 27C). The MOE gapmer ASOs used in this study regulate *CHP1* translation by recruiting RNase H, which will induce the cleavage of the targeted mRNA. The mechanism of action of ASO gapmers rely on their special structure: chemically modified RNA bases, in this case three, are flanking a central domain of DNA referred to as the gap, here 10 bases (kkk-10- kkk). The RNA flanking sequences enhance affinity to complementary sequences while the central DNA domain serve as a substrate for RNase H, thus inhibiting translation of the targeted protein (Shen and Corey 2018).

First, Ionis Pharmaceuticals tested the *CHP1*-ASO leads in A431 squamous carcinoma cell line by delivering the ASO via free uptake. After 48h, *CHP1* mRNA levels were quantified to determine the

half-maximal inhibitory concentration (IC₅₀) of each ASO (Figure 27B). Via free uptake, 60 nM *CHP1*-ASO59 was enough to downregulate mRNA levels to 50% whereas *CHP1*-ASO57 needed 90 nM. *CHP1*-ASO84 had the highest IC₅₀ of the three tested ASOs, 240 nM were needed in order to reduce *CHP1* mRNA to half.

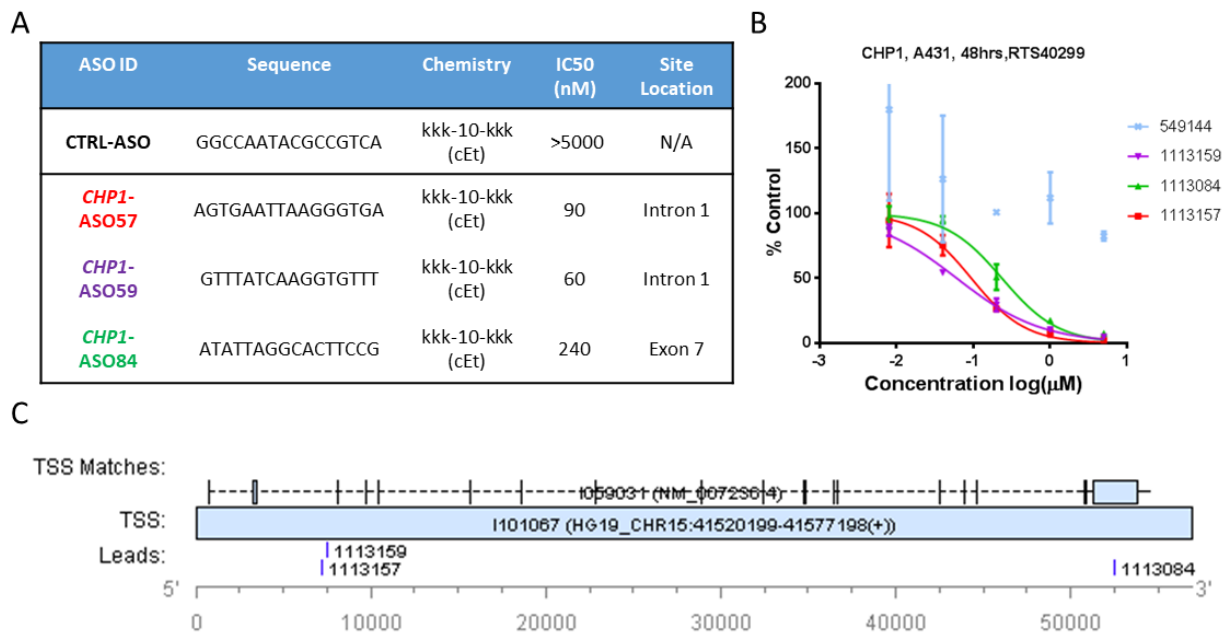


Figure 27. *CHP1* MOE-gapmer ASO leads.

- A) Table with relevant information about the best three human *CHP1*-ASOs designed for the study.
 B) Dose response curve to determine the IC₅₀ of each human *CHP1*-ASO tested in A431 cells 48 hours after free up take treatment quantified by real-time PCR.
 C) Location of the respective target site of each *CHP1*-ASO along *CHP1*.

Next, we tested the *CHP1*-ASO leads in hiPSCs derived MNs by free uptake administration, to assess *CHP1* protein levels after 7 days. We decided to test our ASOs via free uptake using type I SMA HGK1 MNs since antisense oligonucleotides enter in the cells by endocytosis (Crooke et al. 2017), a pathway that is affected in SMA (Hosseini-barkooie et al. 2016), and wanted to confirm that the cells uptake the compounds. MNs were treated at day 17 of the differentiation and proteins were collected at day 24. Before differentiation day 17, media exchange occurs daily, thus in order to avoid ASO removal from the media the day after treatment, we decided to treat the cells on day 17, when maturation media exchange occurs every other day. The only limitation of free uptake in our case is that cells would not be treated before the maturation phase begins. Based on the IC₅₀ of each ASO (Figure 28A and B), we first tested increasing concentrations of the most efficient leads, *CHP1*-ASO57 and *CHP1*-ASO59.

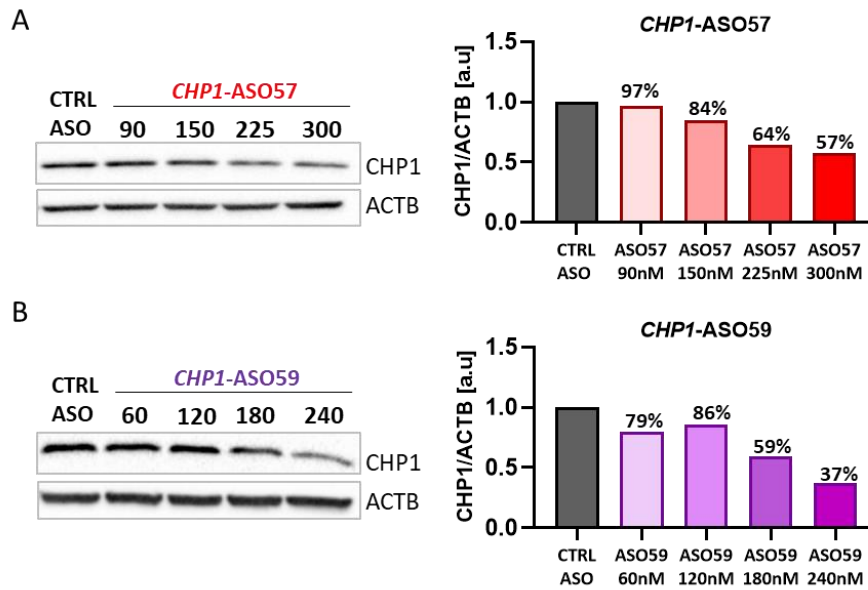


Figure 28. Free uptake *CHP1-ASO57* and *CHP1-ASO59* in SMA type I MNs.

A) SMA type I (HGK1) MNs were treated on day 17 with 90, 150, 225 and 300 nM of *CHP1-ASO57* via free uptake, and proteins were collected on day 24 of the differentiation for western blot. As control, MNs were treated with 300 nM of CTRL-ASO. ACTB was used as loading control. N=1 for each condition.

B) SMA type I (HGK1) MNs were treated on day 17 with 60, 120, 180 and 240 nM of *CHP1-ASO59* via free uptake, and proteins were collected on day 24 of the differentiation for western blot. As control, MNs were treated with 240 nM of CTRL-ASO. ACTB was used as loading control. N=1 for each condition.

Surprisingly, SMA type I MNs treated with 90 nM *CHP1-ASO57*, the IC₅₀ determined by Ionis Pharmaceuticals, did not exert reduction of CHP1 protein levels in comparison to CTRL-ASO treated cells after 7 days (Figure 28A). A dose dependent reduction was observed upon increase of *CHP1-ASO57* administration. Indeed, in order to decrease CHP1 levels down to 57%, cells had to be treated with 300 nM. Mild decreases of CHP1 levels were obtained after 60 nM and 120 nM treatment with *CHP1-ASO59* (Figure 28B). However in this case, 180 nM of the ASO reduced CHP1 levels almost to half, and 240 nM further decreased CHP1 protein down to 37%.

In parallel, we tested the ASOs using Lipofectamine™ as delivery method since it is considered the “gold-standard” for safe delivery of exogenous oligonucleotides. In this case, we treated the cells even earlier, at day 13 of the differentiation and collected proteins at day 15, 48h after administration. SMA type I MNs were treated with various ASO concentrations, and wash out of the media was performed 2h after. *CHP1-ASO57* treatment with different concentrations led to similar knock down efficiencies ~40-50% (Figure 29A). Interestingly, MNs treated with 90 nM *CHP1-ASO57* or CTRL-ASO exhibited axonal swelling, which was not detected when treated via free uptake, suggesting ASO neurotoxicity when administered in high doses using Lipofectamine™ (Figure 29B). After this observation, for the other *CHP1-ASOs* we decided to discard the treatment with 90nM, and tested lower concentrations, ranging from 15 to 60 nM. Surprisingly, *CHP1-ASO59*, which was the most efficient candidate when

administered via free uptake (down to 37% of CHP1), only reached a maximum CHP1 reduction down to 61% after 60 nM of treatment when administered using Lipofectamine™ (Figure 29C). Moreover, 30nM of *CHP1*-ASO84 exerted the strongest reduction bringing CHP1 protein levels down to 55% (Figure 29D). In general, treatment using Lipofectamine™ required less amount of ASO to reach similar knockdown efficiencies as compared to free uptake. Finally, we selected 30nM of *CHP1*-ASO57 as a promising candidate to be tested in triplicates for knock down efficiency. As a result, 30 nM of *CHP1*-ASO57 led to a significant reduction of 69% CHP1 protein levels in SMA type I MNs (Figure 29E).

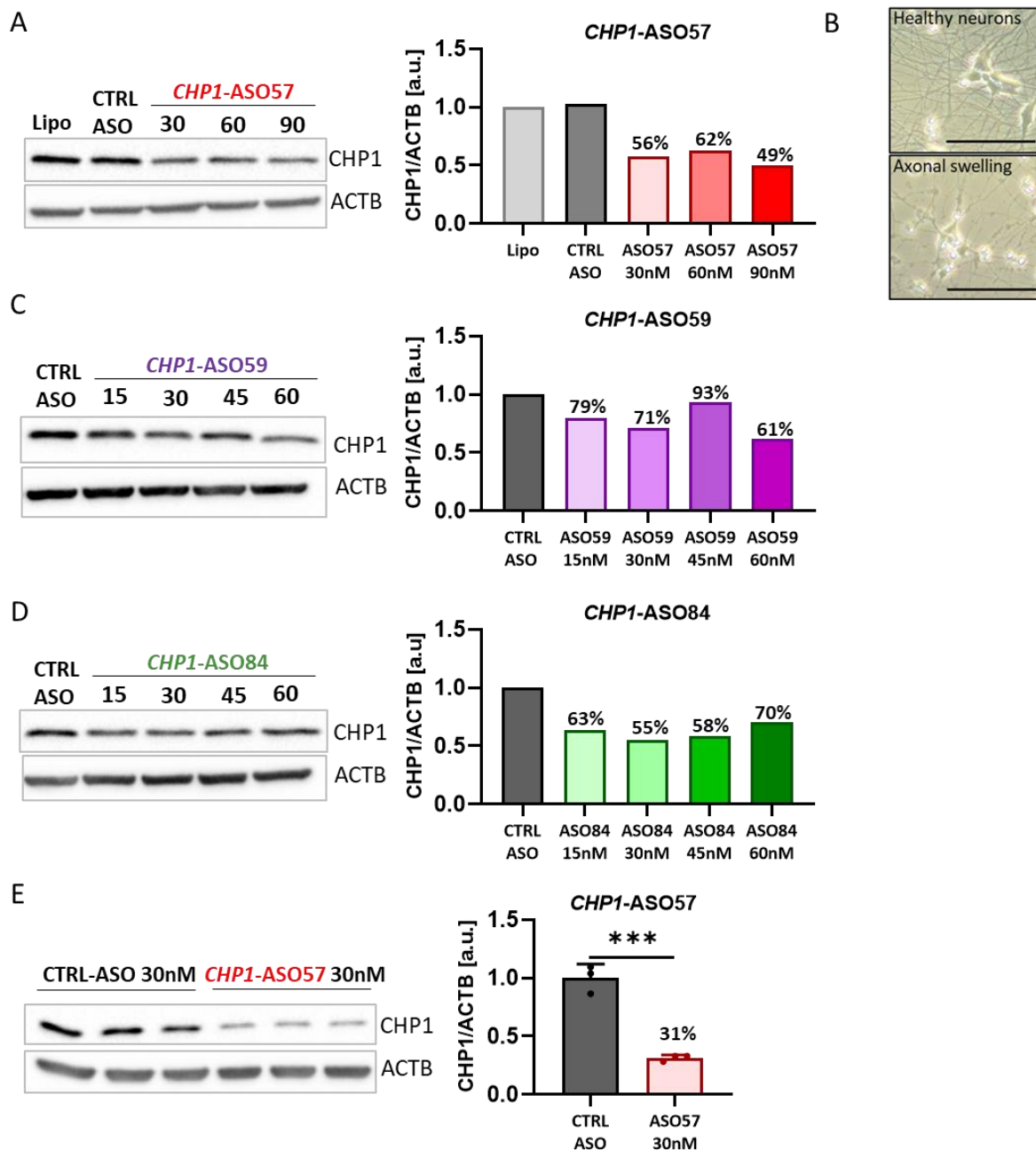


Figure 29. *CHP1*-ASOs administered using Lipofectamine in SMA type I MNs.

A) SMA type I (HGK1) MNs were treated on day 13 with 30, 60 and 90nM of *CHP1*-ASO57 using Lipofectamine™, and proteins were collected on day 15 of the differentiation for western blot. As control, MNs were treated

with 90 nM of CTRL-ASO. Lipo refers to cells treated with Lipofectamine alone. ACTB was used as loading control. N=1 for each condition.

B) Representative images of healthy MNs, and MNs showing signs of axonal swelling when treated with more than 90 nM of either CTRL-ASO or CHP1-ASO57 administered using Lipofectamine™. Scale bar 100 µm.

C) SMA type I (HGK1) MNs were treated on day 13 with 15, 30, 45 and 60nM of *CHP1*-ASO59 using Lipofectamine™, and proteins were collected on day 15 of the differentiation for western blot analysis. As control, MNs were treated with 90 nM of CTRL-ASO. ACTB was used as loading control. N=1 for each condition.

D) SMA type I (HGK1) MNs were treated on day 13 with 15, 30, 45 and 60nM of *CHP1*-ASO84 using Lipofectamine™, and proteins were collected on day 15 of the differentiation for western blot analysis. As control, MNs were treated with 90 nM of CTRL-ASO. ACTB was used as loading control. N=1 for each condition.

E) SMA type I (HGK1) MNs were treated on day 13 with 30nM of *CHP1*-ASO57 or CTRL-ASO using Lipofectamine™, and proteins were collected on day 15 of the differentiation for western blot analysis. ACTB was used as loading control. Unpaired two-tailed Student's t test. All values reported as mean and error bars represent ± SD. ***p≤0.001. N=3, each dot in the bar graphs represents an independent well.

In conclusion, all human *CHP1*-ASOs efficiently downregulated *CHP1* levels in hiPSCs derived MNs. Even though ASOs are uptaken by the cells via endocytosis, a pathway that is impaired in SMA (Hosseinibarkoie et al. 2016), *CHP1*-ASOs were successfully internalized by SMA type I MNs when administered without any lipid-based reagent. Nevertheless, the amount of ASO needed in order to reduce to half (IC50) was 3 times higher the amount used by Ionis Pharmaceuticals in A431 cells. ASOs delivered with Lipofectamine™ efficiently reduced *CHP1* levels 2 days after treatment. In addition, Lipofectamine™ delivery allowed us to treat earlier in the differentiation, which resembled pre-symptomatic stages. Finally, we selected 30 nM of *CHP1*-ASO57 administered via Lipofectamine™ as an interesting option for therapeutic testing in SMA MNs. However, due to the results obtained in the double-blinded preclinical study, where combinatorial therapy using 30 µg *Chp1*-ASO4 and low-dose *SMN*-ASO is not sufficient to ameliorate SMA phenotype in mice, we decided to discontinue the testing in hiPSCs derived MNs for human *CHP1*-ASO57.

3.2 Part II: Long-term antisense oligonucleotide combinatorial therapy targeting SMN and NCALD

Previous studies have unraveled the reduction of the calcium sensor NCALD to act protective against SMA not only in human discordant families but also across species (Riessland et al. 2017). Moreover, NCALD reduction improved endocytosis in *in vitro* and *in vivo* SMA models. Indeed, low-dose *SMN*-ASO injected severe SMA mice carrying heterozygous *Ncald* (*Ncald*^{ko/wt}) in mixed background (50% FVB/N, 50% C57BL/6N), resembling mild SMA phenotype, exhibited synergistic improvements of SMA hallmarks (Riessland et al. 2017). Moreover, combinatorial treatment using antisense oligonucleotides to pharmacologically upregulate *SMN* and reduce *Ncald* in a mild SMA mouse model significantly improved SMA hallmarks such as electrophysiological properties, NMJs area and maturity and muscle fiber size at PND21 (Torres-Benito et al. 2019). Surprisingly, only motoric abilities were improved 3 months after the treatment, suggesting a short-term effect of the *Ncald*-ASO. Here, we aim to test the long-term therapeutic effect of the combinatorial therapy *SMN*-ASO and *Ncald*-ASO by re-injecting *Ncald*-ASO in adult mice.

3.2.1 Combinatorial therapy in SMA mouse model: Re-injections

In order to assess the long-term therapeutic effect of *Ncald*-ASO, we applied the same experimental breeding scheme used in previous studies, which resembles a mild SMA mouse model (Figure 30A) (Riessland et al. 2017; Torres-Benito et al. 2019; Muinos-Buhl et al. 2022). In addition, the similar experimental program used for *Chp1*-ASO re-injections was followed (section 3.1.4.2) (Figure 30B). First, animals were injected s.c at PND1 with a suboptimal dose of 30 µg *SMN*-ASO in order to rescue the multiorgan impairment. The next day, animals received i.c.v. injection of 100 µg CTRL-ASO or *Ncald*-ASO as determined in (Torres-Benito et al. 2019). At PND28, experimental animals were anesthetized and fixed in a stereotaxic equipment in order to perform an i.c.v. bolus injection of CTRL-ASO or *Ncald*-ASO. Finally, at 2 months of age we analyzed various SMA hallmarks to determine if *Ncald*-ASO re-injection can prolong the therapeutic effect of NCALD reduction in SMA.

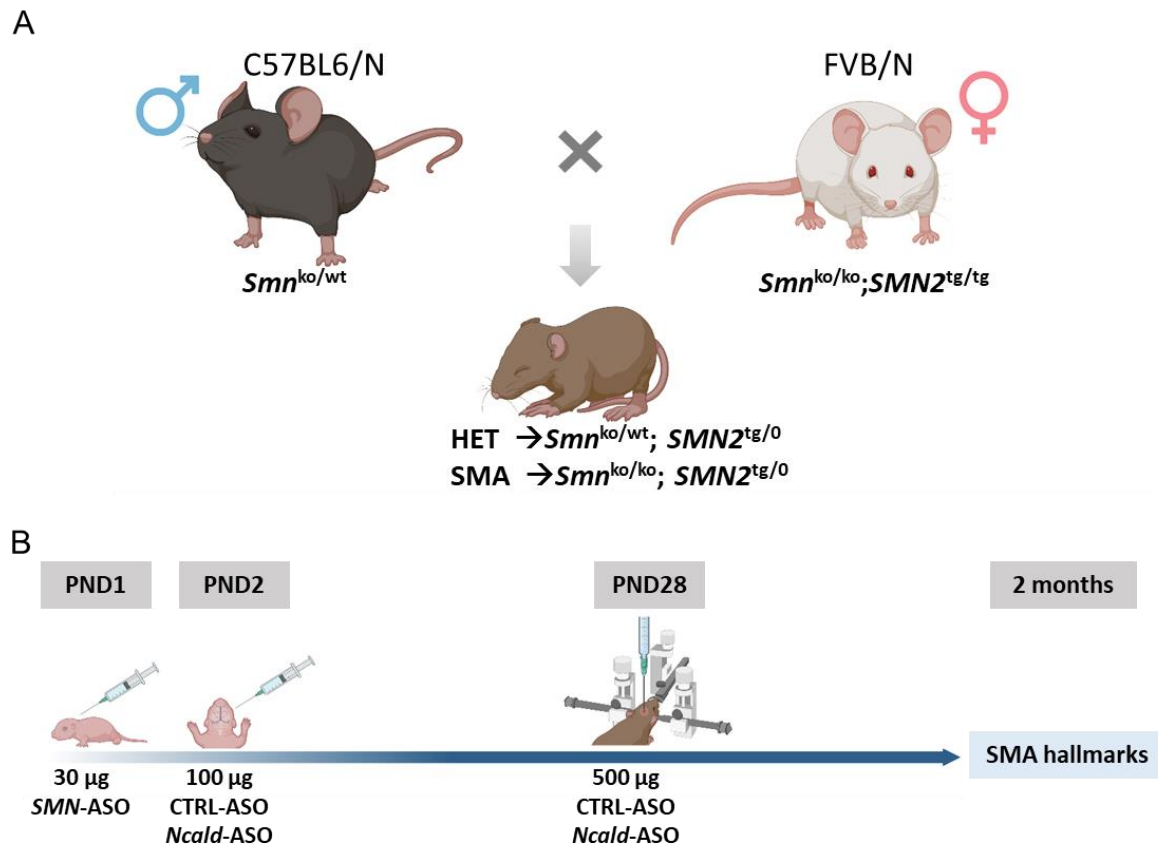


Figure 30. Experimental breeding and injection scheme.

A) Experimental SMA breeding on mixed₅₀ background.

B) Injection scheme to test long-term *Ncald*-ASO therapeutic effect. At PND1, pups were injected s.c. with low-dose *SMN*-ASO. At PND2, either CTRL-ASO or *Ncald*-ASO were injected i.c.v. At PND28, all animals were injected with their respective treatment, CTRL-ASO or *Ncald*-ASO. SMA hallmarks were evaluated at 2 months of age. Figure created with BioRender.

3.2.1.1 Efficacy and tolerability of *Ncald*-ASO i.c.v. bolus injection at PND28 in wild type mice

First, we tested the efficacy and tolerability of i.c.v. bolus injection of 500 µg of CTRL-ASO and *Ncald*-ASO in adult wild type mice. For this purpose, animals were injected at PND28 and brain and spinal cord tissues were collected 2-weeks after injection for western blot analysis. In brain lysates, upon 500 µg of *Ncald*-ASO injection, NCALD protein levels were reduced to 43% compared to CTRL-ASO injected animals (Figure 31A). In the spinal cord, a significant reduction of NCALD protein to 63% was observed in comparison to CTRL-ASO injected animals (Figure 31B). As previously observed, NCALD reduction in the spinal cord is less pronounced than in the brain, since i.c.v. injected ASOs have to be distributed in the CNS through the CSF. Importantly, 500 µg of CTRL and *Ncald*-ASO were well tolerated by the animals and no adverse effects were observed. In summary, 500 µg of *Ncald*-ASO was sufficient to significantly reduce NCALD levels in brain and spinal cord 2-weeks after injection in wild type mice.

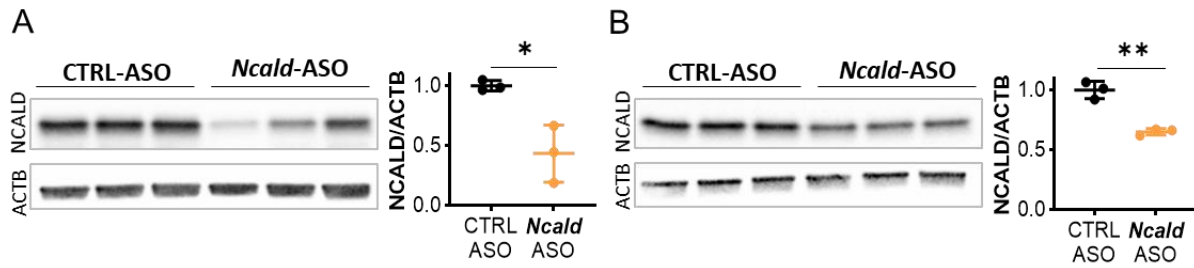


Figure 31. *Ncald*-ASO efficiency 2-weeks after injection in wild type adult mice.

A) Western blot analysis and quantification of NCALD levels in brain lysates from i.c.v. bolus injected wild type mice at PND28, samples collected 2-weeks after injection. Injection with 500 μ g *Ncald*-ASO or CTRL-ASO showed significant reduction of NCALD protein levels compared to CTRL-ASO injected animals.

B) Western blot analysis and quantification of NCALD levels in spinal cord lysates from i.c.v. bolus injected wild type mice at PND28. Injections with 500 μ g *Ncald*-ASO or CTRL-ASO show significant reduction of NCALD levels in the spinal cord.

Unpaired two-tailed Student's *t*-test. All values reported as mean and error bars represent \pm SD. * $p \leq 0.05$, ** $p \leq 0.01$. Each dot in the bar graphs represents an independent animal.

3.2.1.2 NCALD protein levels 4-weeks after 500 μ g *Ncald*-ASO injection in HET and SMA

Ncald-ASO long-term stability has been reported to be rather short (Torres-Benito et al. 2019), and a similar effect was observed with *Chp1*-ASO4 (Figure 12G and (Muinos-Buhl et al. 2022)). Hereby, we wanted to determine NCALD downregulation at 2 months, 4-weeks after 500 μ g CTRL-ASO or *Ncald*-ASO i.c.v. bolus re-injection at PND28 in HET and SMA animals. One month after CTRL-ASO or *Ncald*-ASO re-injection, brain lysates of HET *Ncald*-ASO (Figure 32A and B) and SMA *Ncald*-ASO (Figure 32A and C) animals exhibited a significant reduction of NCALD levels in brain when compared to their respective control groups. Moreover, NCALD was significantly reduced in the spinal cord of HET animals 4-weeks after receiving *Ncald*-ASO re-injection compared to mice treated with CTRL-ASO (Figure 32D and E). Notably, NCALD reduction in the spinal cord of SMA animals was highly variable, ranging between 50% reduction to absence of reduction (Figure 32D and F).

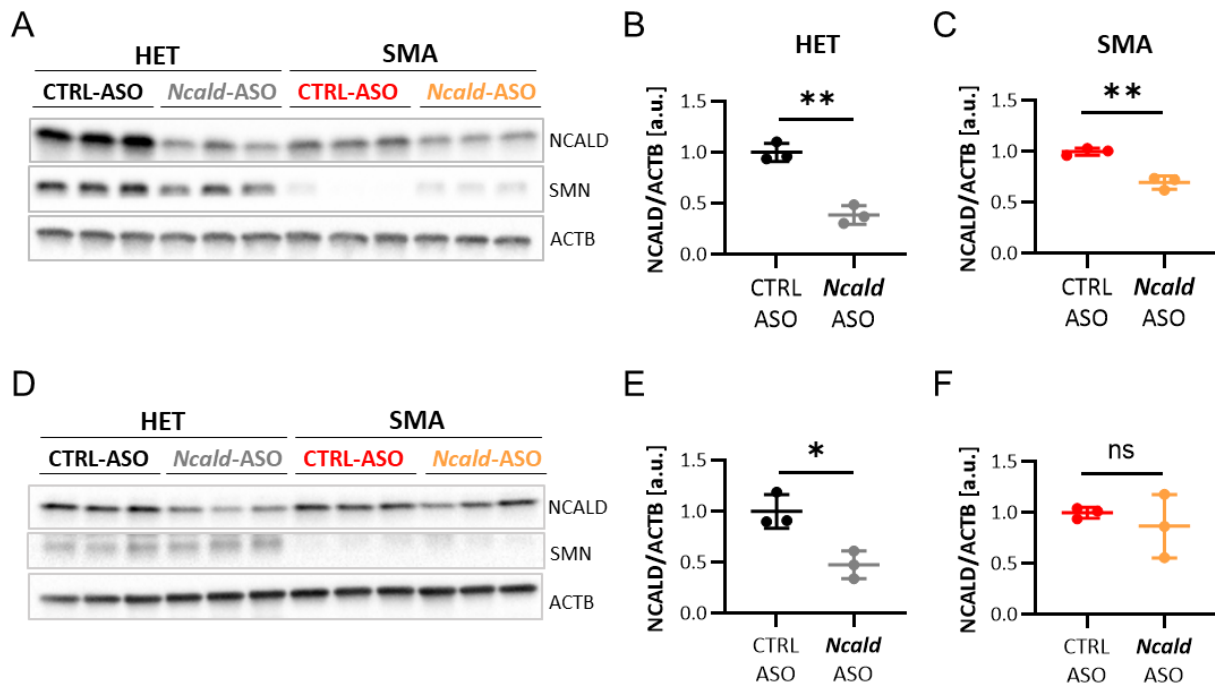


Figure 32. *Ncald*-ASO efficiency 4-weeks after injection in mixed₅₀ HET and SMA mice.

A) Western blot analysis of NCALD levels in the brain of HET and SMA mixed background animals at 2 months of age, 4-weeks after i.c.v. bolus re-injection.

B) Quantification of NCALD reduction in brain of HET animals re-injected with CTRL-ASO in black or *Ncald*-ASO in grey. Unpaired two-tailed Student's t test was performed. All values reported as mean and error bars represent \pm SD. Each dot in the bar graphs represents an independent animal. ** $p \leq 0.01$

C) Quantification of NCALD protein levels in brain of SMA animals re-injected with CTRL-ASO in red or *Ncald*-ASO in orange. Unpaired two-tailed Student's t test was performed. All values reported as mean and error bars represent \pm SD. Each dot in the bar graphs represents an independent animal. ** $p \leq 0.01$

D) Western blot analysis of NCALD levels in the spinal cord of HET and SMA mixed background animals at 2 months of age, 4-weeks after i.c.v. bolus re-injection.

E) Quantification of NCALD reduction in the spinal cord of HET animals re-injected with CTRL-ASO in black or *Ncald*-ASO in grey. Unpaired two-tailed Student's t test was performed. All values reported as mean and error bars represent \pm SD. Each dot in the bar graphs represents an independent animal. * $p \leq 0.05$

F) Quantification of NCALD protein levels in the spinal cord of SMA animals re-injected with CTRL-ASO in red or *Ncald*-ASO in orange. Unpaired two-tailed Student's t test was performed. All values reported as mean and error bars represent \pm SD. Each dot in the bar graphs represents an independent animal.

3.2.1.3 Analysis of SMA hallmarks: electrophysiological predictors

Electrophysiological defects have been described in SMA patients and animal models, including reduction of CMAP and MUNE (Lewelt et al. 2010; Arnold et al. 2014; Torres-Benito et al. 2019). One single injection of *Ncald*-ASO at PND2 significantly increased both electrophysiological parameters of the gastrocnemius muscle in SMA mice at PND21, but was not sufficient to prolong the effect over time (Torres-Benito et al. 2019). In this study, we aimed to assess the long-term effect of *Ncald*-ASO reinjection in both CMAP and MUNE measurements of the gastrocnemius muscle upon sciatic nerve stimulation. For that purpose, we determined the CMAP response and the MUNE at 2 months of age,

after re-injection of 500 μg *Ncald*-ASO at PND28. In order to assess the CMAP response, supramaximal stimulation of the sciatic nerve was applied. As previously reported, SMA mice injected with CTRL-ASO and low-dose *SMN*-ASO exhibited reduced CMAP responses compared to healthy HET animals (Figure 33A and B). On the contrary, intermediate SMA mice re-injected with *Ncald*-ASO showed a significant amelioration of the CMAP response, indicating that prolonged NCALD reduction has a beneficial effect on the functionality of the motor units (Figure 33A and B). Moreover, MUNE analysis confirmed reduced motor unit numbers in SMA CTRL-ASO animals compared to HET animals, a parameter that was rescued upon *Ncald*-ASO re-injection (Figure 33C). This data strongly supports that 500 μg *Ncald*-ASO re-injection in combination with a single low-dose *SMN*-ASO administration not only prolongs the motor unit function but also prevents the loss of motor unit numbers in SMA mice over time, thus protecting from neurodegeneration.

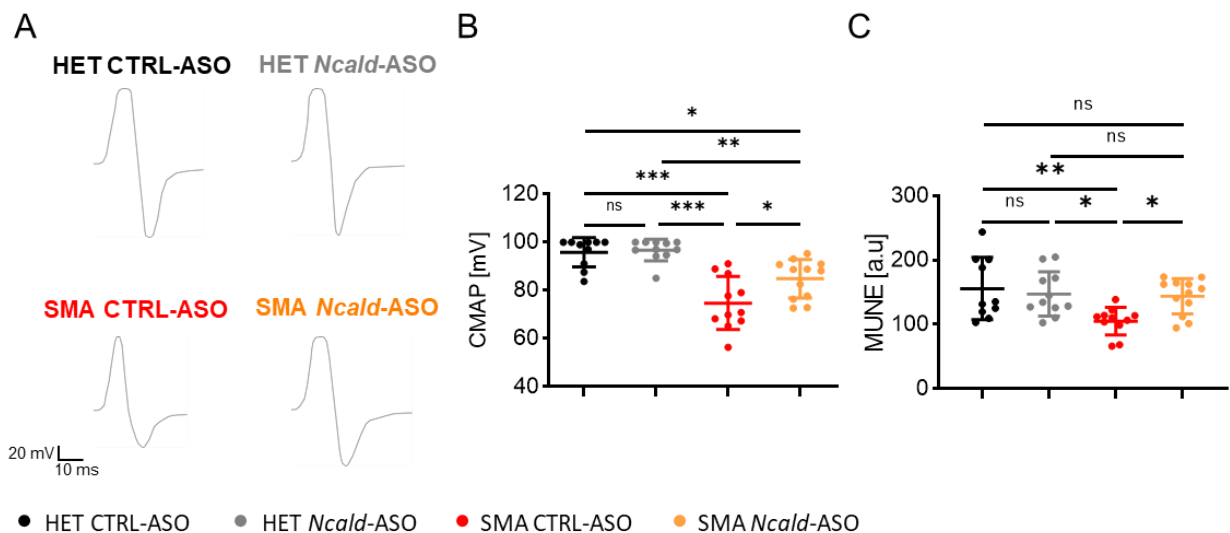


Figure 33. 500 μg *Ncald*-ASO reinjection improves electrophysiological defects at 2 months.

A) Representative traces of CMAP response in the gastrocnemius muscle from HET CTRL-ASO, HET *Ncald*-ASO, SMA CTRL-ASO and SMA *Ncald*-ASO at 2 months of age, 4-weeks after re-injection.

B) Quantification of sciatic CMAP response of the gastrocnemius muscle in the four analyzed experimental groups. For CMAP response, peak-to-peak amplitude was quantified. Each dot in the graph represents one animal, N=10-12. Ordinary one-way ANOVA with Tukey posthoc test for multiple comparisons. Error bars represent \pm SD. * $p \leq 0.05$, ** $p \leq 0.01$, *** $p \leq 0.001$.

C) Quantification of the motor unit number estimation (MUNE) of the gastrocnemius muscle in the four analyzed experimental groups. Each dot in the graph represents one animal, N=10-12. Ordinary one-way ANOVA with Tukey posthoc test for multiple comparisons. Error bars represent \pm SD. * $p \leq 0.05$, ** $p \leq 0.01$.

3.2.1.4 Analysis of SMA hallmarks: NMJ area and innervation

Previous work has shown that one single injection of *Ncald*-ASO administered at PND2 was able to improve NMJ area and maturation at PND21 in a severe SMA mouse model when combined with low dose *SMN*-ASO, however this effect was not observed after 3 months (Torres-Benito et al. 2019).

In order to test the long-term effect of *Ncald*-ASO re-injection in the pathological features of the NMJ, we selected the TVA muscle which is proven to be affected in SMA (Murray et al. 2008). To quantify the NMJ area, the size of BTX-positive endplates was measured. To analyze NMJ innervation, NMJs were categorized according to the percentage of nerve terminal that overlaid with the AChRs as fully innervated (>80%), partially innervated (>15% - 79%) and non-innervated (< 15%). In line with the results obtained in the combinatorial therapy with *Chp1*-ASO4, NMJ area and innervation were affected in the intermediate SMA mouse compared to HET littermates, both injected with low-dose *SMN*-ASO. Despite previous results showing an amelioration of NMJ area in TVA muscle at PND1 after one single injection of 100 µg *Ncald*-ASO, re-injection with 500 µg *Ncald*-ASO did not increase NMJ area in SMA animals compared to CTRL-ASO injected SMA mice at 2 months of age (Figure 34A). Remarkably, denervation of NMJs was rescued upon *Ncald*-ASO re-injection in SMA animals (Figure 34B), emphasizing the key role of NCALD reduction in preventing the progressive retraction of the nerve terminal from its target muscle fiber, hence delaying neurodegeneration.

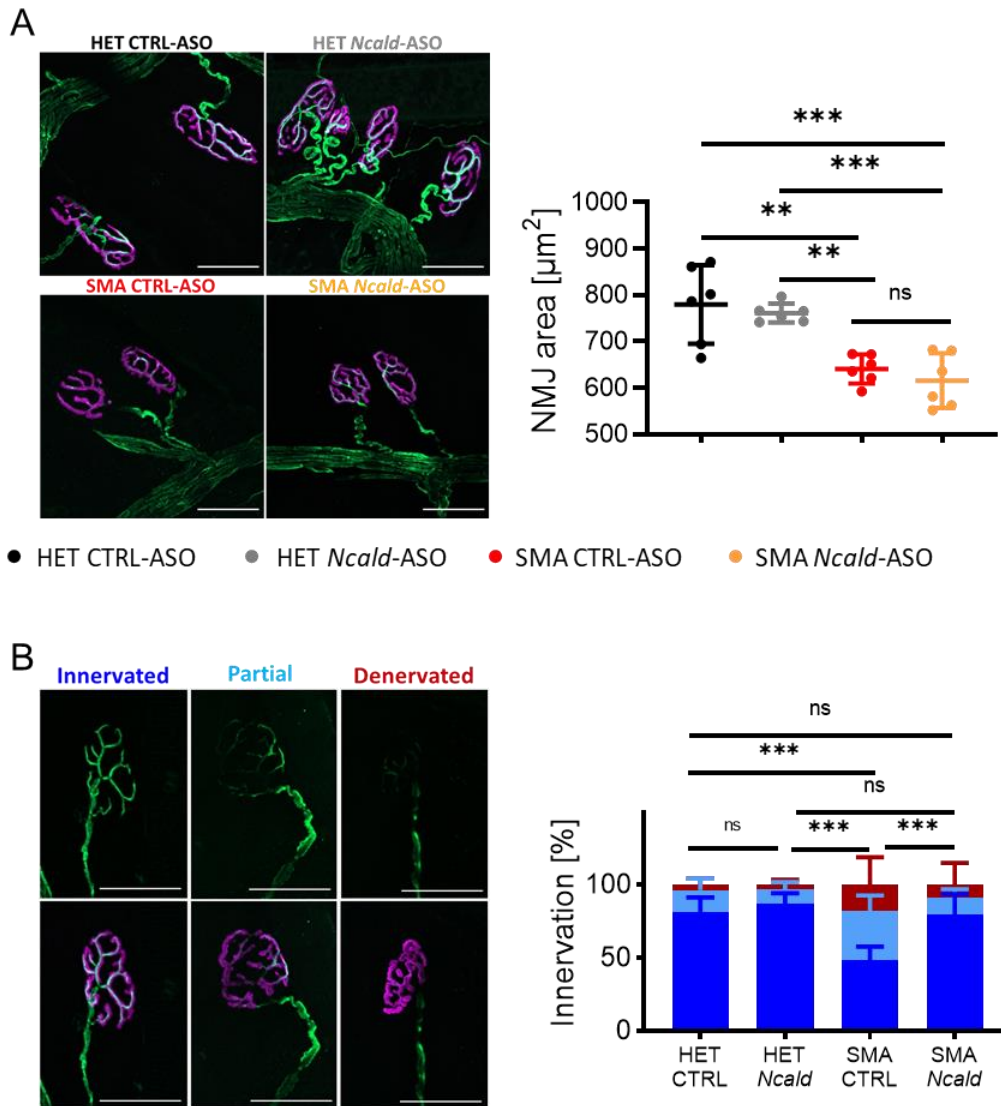


Figure 34. NMJ area and innervation at 2 months of age after *Ncald*-ASO re-injection.

A) Transversus abdominis NMJ area. Representative images and quantification of NMJ area at 2 months of age, showing postsynaptic NMJ region (BTX, magenta) and presynaptic nerve (NF, green) (Scale bar: 50 μ m). NMJ area was analyzed with ImageJ (N = 6, n = 100 NMJs/mouse). Statistics were performed with mean values of animals per group. Ordinary one-way ANOVA with Tukey posthoc test for multiple comparisons, ** $p \leq 0.01$, *** $p \leq 0.001$.

B) Transversus abdominis NMJ innervation. Representative images of TVA NMJ innervation in each category, showing the postsynaptic region (BTX, magenta) and presynaptic nerve (NF, green). NMJ innervation was classified in three categories according to the degree of innervation. HET CTRL-ASO (N=5, n=272), HET *Ncald*-ASO (N=5, n=270), SMA CTRL-ASO (N=5, n=259), SMA *Ncald*-ASO (N=6, n=322). Results are presented in percentages. *** denotes statistical significance $p \leq 0.001$ (χ^2 test).

3.2.1.5 Analysis of SMA hallmarks: muscle fiber size

In SMA, muscle pathology is characterized by small atrophic fibers that occur as a response to MN denervation. Previously, one single dose of 100 μ g *Ncald*-ASO at PND2 was sufficient to increase gastrocnemius muscle fiber size at PND21, but not in the long term (Torres-Benito et al. 2019). Here, we aim to determine if 500 μ g *Ncald*-ASO re-injection at PND28 can ameliorate this pathological

feature over time. For this reason, we analyzed muscle fiber size from gastrocnemius muscles at 2 months of age (Figure 35A and B). Muscle fiber size grouping did not reveal an improvement of the phenotype upon 500 μg *Ncald*-ASO reinjection in SMA animals compared to CTRL-ASO SMA mice (Figure 35B).

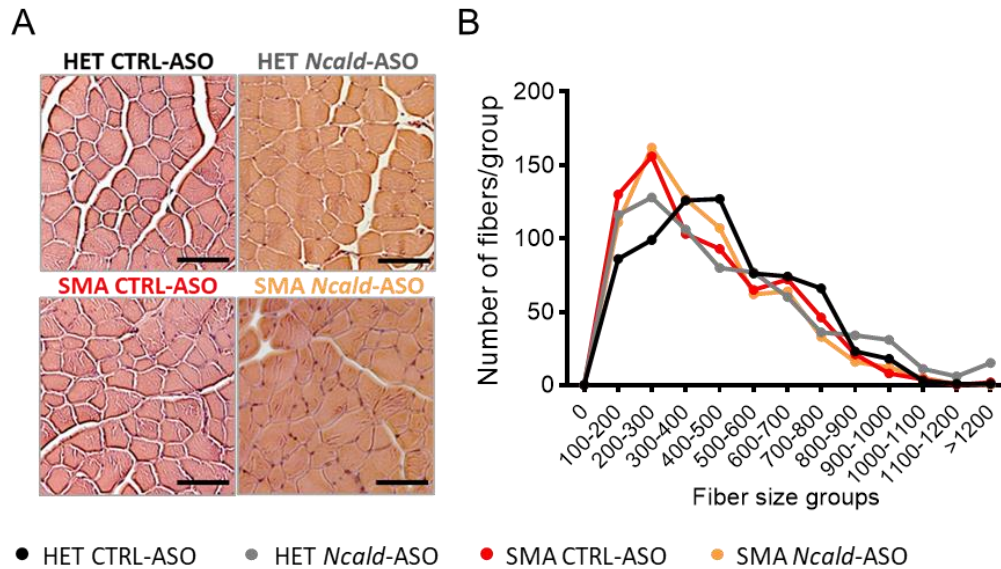


Figure 35. Gastrocnemius muscle fiber size distribution after *Ncald*-ASO re-injection at 2 months of age.

A) Representative images of H&E staining of gastrocnemius muscle fibers from HET and SMA animals at 2 months of age. Scale bar 50 μm .

B) Gastrocnemius muscle size categorization according to area intervals of 100 μm^2 . In total, five animals were analyzed per genotype, and 100 muscle fibers per animal.

3.2.2 Human *NCALD*-ASO treatment in MN derived from hiPSCs

In parallel to our preclinical studies on *SMN*-ASO and *Ncald*-ASO combinatorial therapy in SMA mice, we tested the efficacy and tolerability of three human *NCALD*-ASOs in hiPSC derived MNs from healthy and SMA type I individuals. Moreover, functional and morphological analysis were performed to determine the therapeutic effect of the best *NCALD*-ASO leads.

3.2.2.1 Efficacy and tolerability of three human *NCALD*-ASO treatment

Several human MOE-gapmer on mixed backbone *NCALD*-ASOs were designed and tested in A431 carcinoma cells by Ionis Pharmaceuticals. The three best *NCALD*-ASO leads were sent to us for further validation in hiPSCs derived MNs (Figure 36A). All *NCALD*-ASOs bind to regions located in exon 6 (Figure 36C). Similarly to human *CHP1*-ASOs (section 3.1.6), the MOE gapmer backbone structure of *NCALD*-ASOs allows the RNase H-mediated cleavage of *NCALD* mRNA.

First, Ionis Pharmaceuticals tested the free uptake of various *NCALD*-ASO leads in the A431 cell line. After 48h, *CHP1* mRNA levels were quantified to determine the half-maximal inhibitory concentration (IC₅₀) of each ASO (Figure 36B). Via free uptake, 60 nM *NCALD*-ASO55 and *NCALD*-ASO89 were enough to decrease *NCALD* mRNA levels to 50% whereas *NCALD*-ASO69 needed 90 nM.

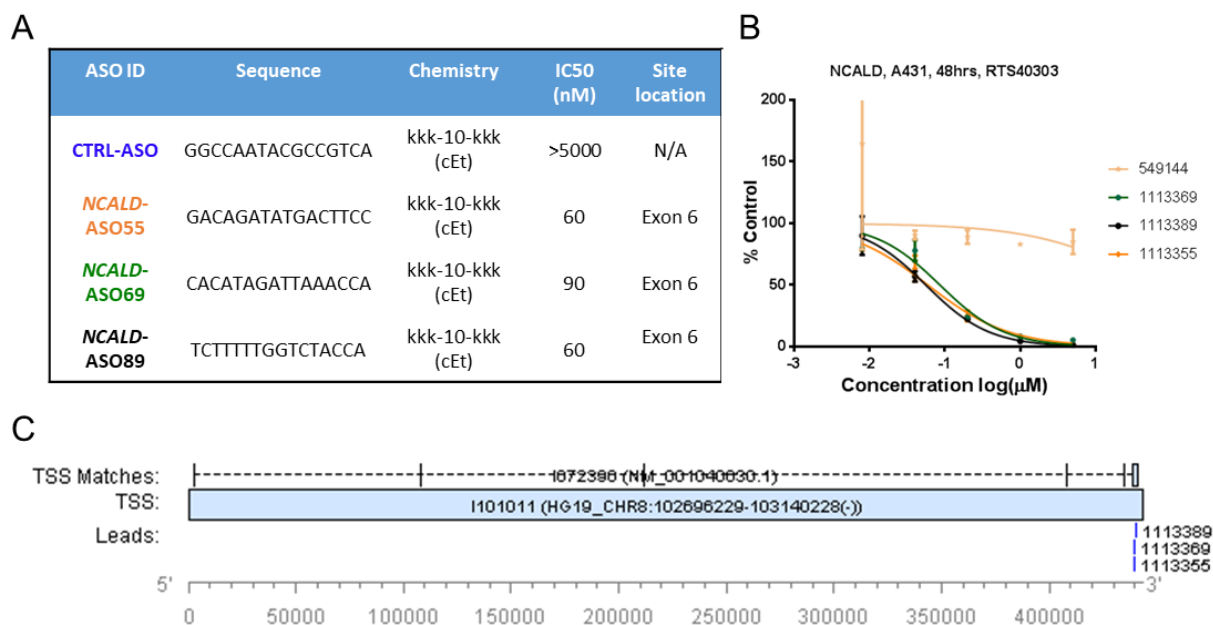


Figure 36. *NCALD* MOE gapmer ASOs.

- A) Table with relevant information about the best three human *NCALD*-ASOs designed for the study.
 B) Dose response curve to determine the IC₅₀ of each human *NCALD*-ASO tested in A431 cells 48 hours after free up take treatment quantified by real-time PCR.
 C) Location of the respective target site of each *NCALD*-ASO along *NCALD*.

Next, to test the efficacy and tolerability of *NCALD*-ASO leads in hiPSC derived MNs we used Lipofectamine 3000 as described in section 5.2.3.4.2. As a preliminary experiment, we wanted to test the efficacy and tolerability of various concentrations (20 nM – 60 nM) of the three *NCALD*-ASOs in a healthy line, the HUVEC MNs (Figure 37). To avoid axonal swelling as detected when treating with 90 nM of *CHP1*-ASOs or CTRL-ASO (section 3.1.6), the maximum concentration used for *NCALD*-ASO candidate testing was 60 nM. Similarly, as performed for human *CHP1*-ASOs (section 3.1.6), MN cultures were treated at day 13 of the differentiation and proteins were collected at day 15 to determine *NCALD* reduction by western blot. Noteworthy, *NCALD*-ASOs were tested simultaneously in MNs derived from the same differentiation, in order to detect possible side effects of the ASOs. Interestingly, in comparison to *CHP1*-ASOs, treated MNs with maximum concentration of *NCALD*-ASO55 and *NCALD*-ASO69 did not show a decrease of *NCALD* levels compared to CTRL-ASO treated cells. *NCALD*-ASO89 was the most efficient ASO in comparison to the other candidates, reducing *NCALD*

levels to 75% when treated with 60nM. Importantly, no axonal swelling was detected upon *NCALD*-ASOs treatment. This was a preliminary test, with only one sample per condition.

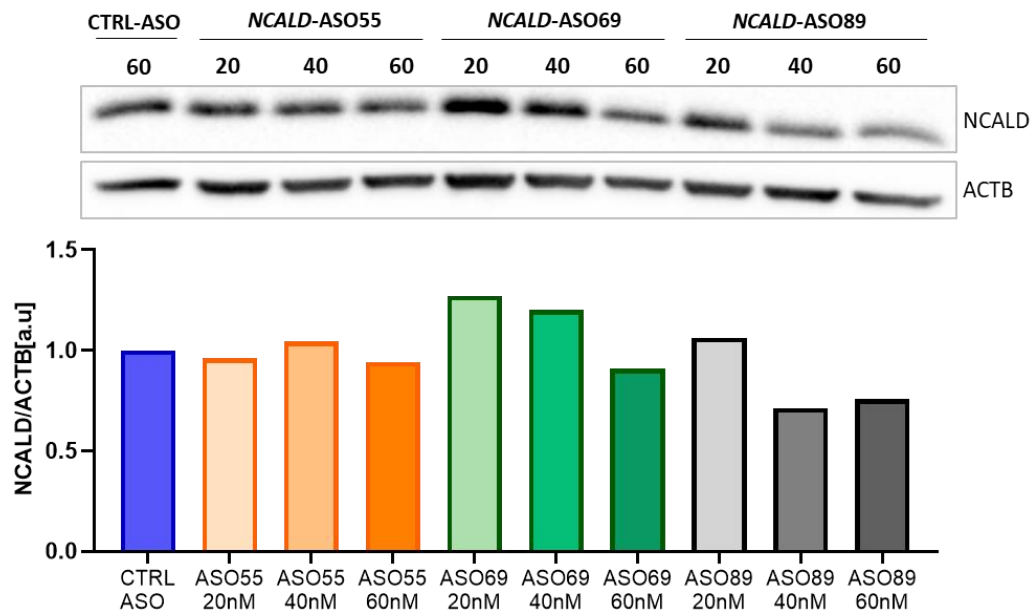


Figure 37. Preliminary efficacy and tolerability study of *NCALD*-ASO leads in healthy MNs at day 15.

hiPSCs derived MNs from the healthy cell line HUVEC were treated at day 13 with various concentrations of *NCALD*-ASOs (20 nM – 60 nM). As control, MNs were treated with 60 nM of CTRL-ASO. Proteins were collected at day 15 of the differentiation and processed for western blot analysis. ACTB was used as loading control.

Next, we decided to perform the experiment by simultaneously treating HUVEC derived MNs belonging to the same differentiation with 60 nM of each *NCALD*-ASO lead and to collect the proteins at day 20 (7 days after treatment) in order to assess if *NCALD*-ASOs efficiency increases over time. At day 20 of the differentiation, all *NCALD*-ASO leads significantly downregulated *NCALD* protein levels in healthy MNs determined by western blot (Figure 38A and B). Treatment with 60 nM of *NCALD*-ASO55 and *NCALD*-ASO69 had comparable knockdown efficiencies, reducing *NCALD* protein levels to 51% and 46%, respectively (Figure 32B). Moreover, 60nM of *NCALD*-ASO89 further reduced *NCALD* levels down to 30% in healthy derived MNs (Figure 38B). Surprisingly, the protein amount of the MN marker ISL1 was significantly reduced upon treatment with 60 nM of *NCALD*-ASO55 and *NCALD*-ASO89 in comparison to CTRL-ASO and *NCALD*-ASO69 treated MNs (Figure 38A and C). Moreover, SMN levels were also reduced after *NCALD*-ASO55 and *NCALD*-ASO89 treatment when compared to SMN levels in CTRL-ASO or *NCALD*-ASO69 treated MNs (Figure 38A and D). Strikingly, no axonal swelling or signs of degeneration were observable in the MNs treated with *NCALD*-ASO55 or *NCALD*-ASO89 in comparison to CTRL-ASO treated cells. These unexpected results suggest that *NCALD*-ASO55 and *NCALD*-ASO89

might have some *off-target* effects that produce toxicity in the neurons, which were not detected in the first screen performed by Ionis Pharmaceuticals on the A431 cells.

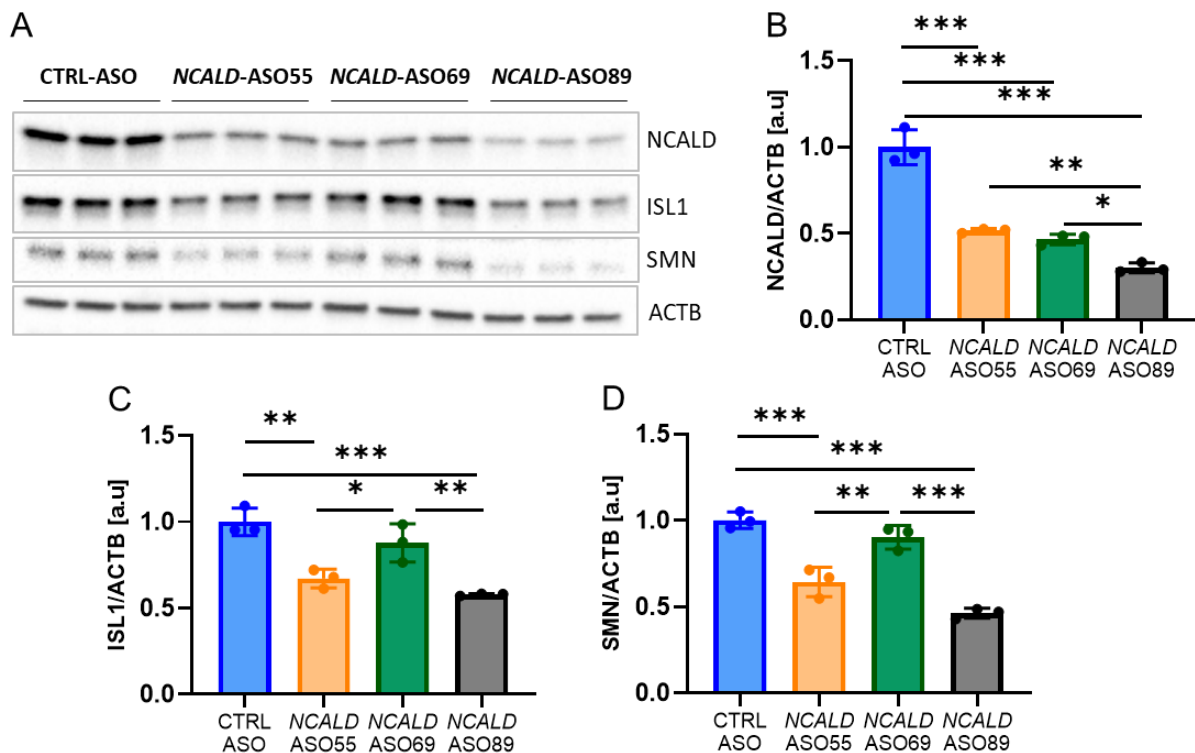


Figure 38. NCALD-ASO lead efficiency and tolerability 7 days after treatment in healthy MNs.

A) Western blot of HUVEC hiPSCs derived MNs treated with 60 nM of CTRL-ASO or the respective *NCALD*-ASO lead using Lipofectamine™ at day 13, proteins collected at day 20 of the differentiation. ACTB used as loading control.

B) *NCALD* levels quantification at day 20 after treatment with each *NCALD*-ASOs. Ordinary one-way ANOVA with Tukey posthoc test for multiple comparisons. Error bars represent \pm SD. * $p \leq 0.05$, ** $p \leq 0.01$, *** $p \leq 0.001$. All values reported as mean and error bars represent \pm SD. N=3, each dot in the bar graphs represents an independent well.

C) *ISL1* levels quantification at day 20 after treatment with each *NCALD*-ASOs. Ordinary one-way ANOVA with Tukey posthoc test for multiple comparisons. Error bars represent \pm SD. * $p \leq 0.05$, ** $p \leq 0.01$, *** $p \leq 0.001$. All values reported as mean and error bars represent \pm SD. N=3, each dot in the bar graphs represents an independent well.

D) *SMN* levels quantification at day 20 after treatment with each *NCALD*-ASOs. Ordinary one-way ANOVA with Tukey posthoc test for multiple comparisons. Error bars represent \pm SD. ** $p \leq 0.01$, *** $p \leq 0.001$. All values reported as mean and error bars represent \pm SD. N=3, each dot in the bar graphs represents an independent well.

Next, we wanted to assess morphological changes in the MNs upon treatment with 60 nM *NCALD*-ASO69 or *NCALD*-ASO89 in comparison with CTRL-ASO. For that, treated MNs were immunostained at day 20 of the differentiation with anti- β -III-tubulin, to mark microtubules, and Phalloidin for F-actin filaments (Figure 39). *NCALD*-ASO69 treated cells displayed the typical morphology of MNs with long axons similar to CTRL-ASO treated cultures, and no axonal swelling was detected. However, MNs treated with 60 nM *NCALD*-ASO89 displayed an altered morphology characterized by shorter axons

compared to CTRL-ASO or *NCALD*-ASO69 treated cells (Figure 39). Remarkably, both MN HUVEC cultures treated with *NCALD*-ASOs seemed to have actin filaments displaying filopodial and lamellipodial conformations in the growth cones in comparison to CTRL-ASO treated cells (Figure 39).

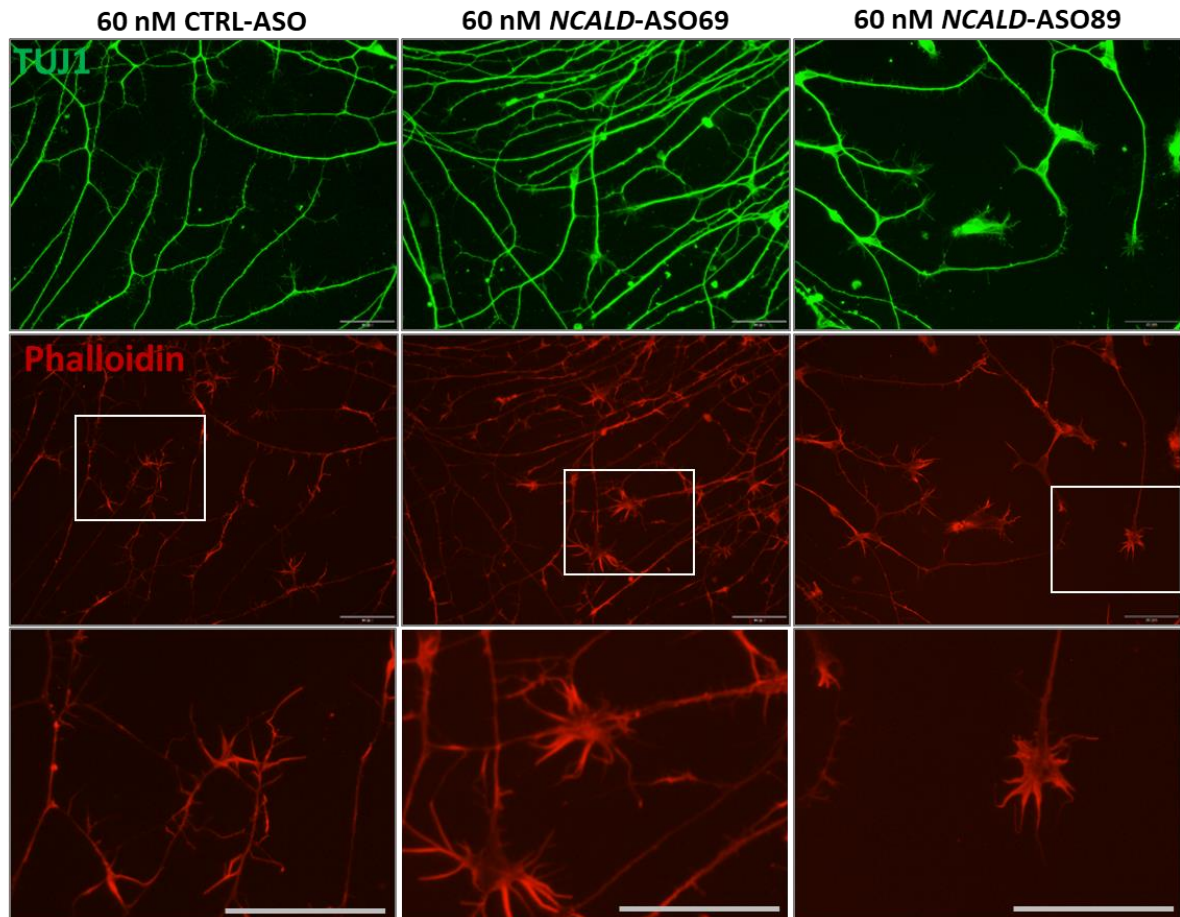


Figure 39. Healthy MNs 7 days after 60nM *NCALD*-ASOs treatment show changes in growth cone morphology Healthy MNs derived from the HUVEC hiPSC line were treated at day 13 with 60 nM of CTRL-ASO or *NCALD*-ASO using Lipofectamine. Images were taken 7 days after transfection, at day 20 of the differentiation. Scale bar: 50 μ m

In summary, 60 nM *NCALD*-ASO69 significantly downregulated *NCALD* protein levels in healthy MNs derived from the HUVEC hiPSC line, and did not show reduction of MN number determined by ISL1 protein levels, neither reduction of SMN levels in comparison to CTRL-ASO treated cells. Interestingly, immunostaining of *NCALD*-ASO69 treated MNs showed normal morphology similar to the one exhibited by CTRL-ASO treated cells. Moreover, *NCALD*-ASO69 treatment seems to have an impact in growth cone morphology, which was later investigated in section 3.2.2.2.

3.2.2.2 Efficacy of *NCALD*-ASO69 in other hiPSCs derived MN lines

For *NCALD*-ASO69 therapy testing, to assess the therapeutic effect of *NCALD* reduction in SMA we decided to use another healthy hiPSC line to have a second control (line WTC11) and two hiPSC lines derived from SMA type I patient fibroblasts, HGK1 and CS32iSMA (Table 1). First, efficiency of 60nM *NCALD*-ASO69 treatment was corroborated in each hiPSC line derived MNs, and *NCALD* and *ISL1* protein levels were estimated by western blot (Figure 40). Noteworthy, none of the lines exhibited axonal swelling or signs of ASO toxicity.

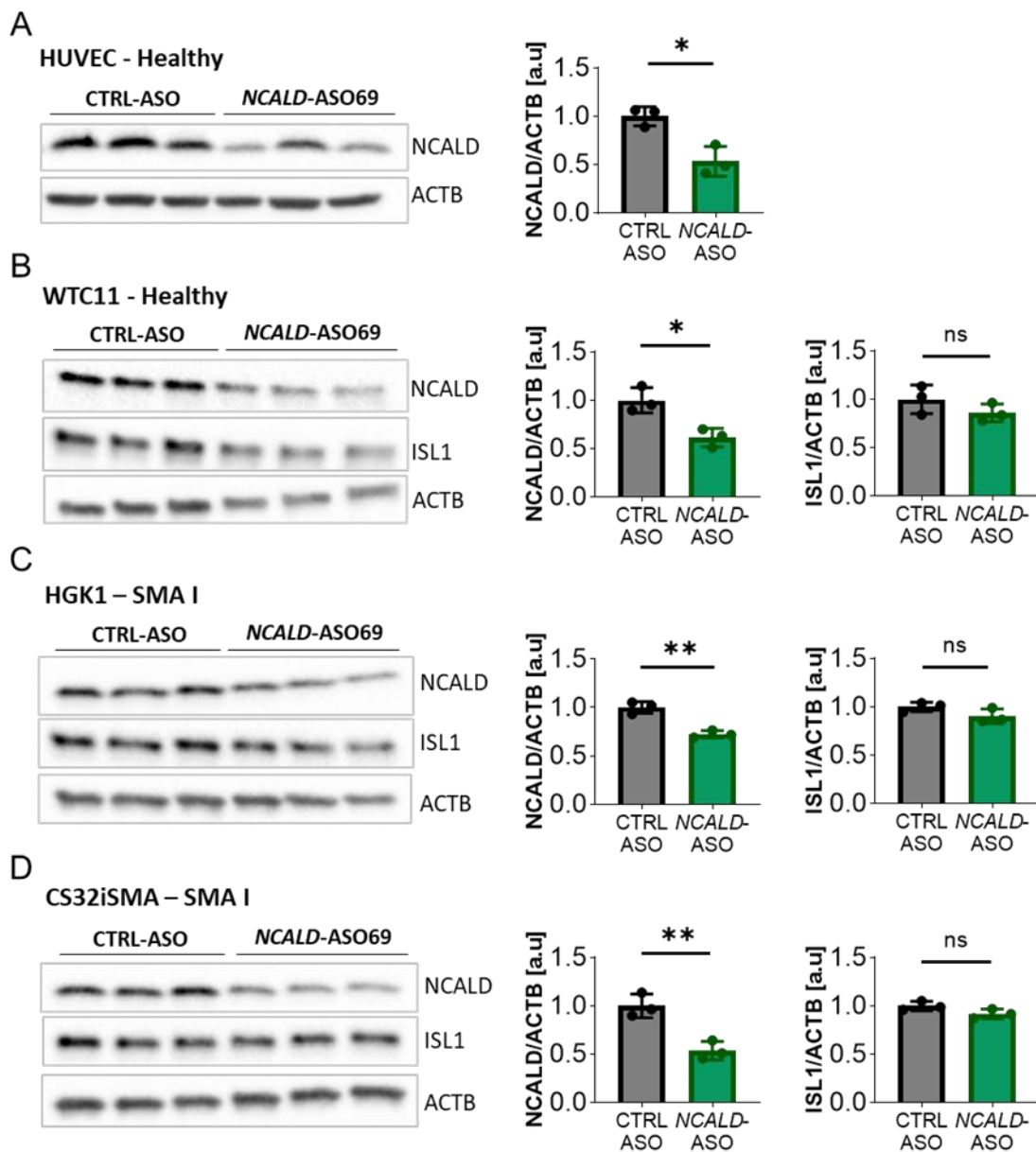


Figure 40. 60 nM *NCALD*-ASO69 efficacy in healthy and SMA type I lines.

hiPSC derived MNs from healthy HUVEC (A) and WTC11 (B) lines and SMA type I lines HGK1 (C) and CS32iSMA (D) were treated at day 13 of the differentiation with 60 nM of CTRL-ASO or *NCALD*-ASO69 using Lipofectamine™, and proteins were collected at day 20 of the differentiation for western blot analysis. Each

dot in the graphs represent one well of treated MNs. Unpaired two-tailed Student's t test was performed. All values reported as mean and error bars represent \pm SD. * $p \leq 0.05$, ** $p \leq 0.01$.

Next, WTC11 MNs treated with 60nM CTRL-ASO or *NCALD*-ASO69 were fixed and immunostained at day 20 in order to verify *NCALD* reduction (Figure 41). *NCALD* is highly abundant in the soma of the neurons (Figure 41A) and localizes at the growth cones (Figure 41B), which are a SMA relevant site. In SMA, voltage-dependent Ca^{2+} influx is reduced prompting the binding of *NCALD* to clathrin, thus preventing clathrin from coating the synaptic vesicles at the presynaptic terminal (Riessland et al. 2017). Thus, *NCALD* reduction allows clathrin to mediate endocytosis, even at low intracellular Ca^{2+} levels. Upon 60 nM *NCALD*-ASO69 treatment, *NCALD* levels detected by immunostaining were drastically reduced in the soma (Figure 41A) but also at the presynaptic terminal, in the growth cones (Figure 41B) when compared to CTRL-ASO treated MNs, which support the results obtained by western blot (Figure 40B).

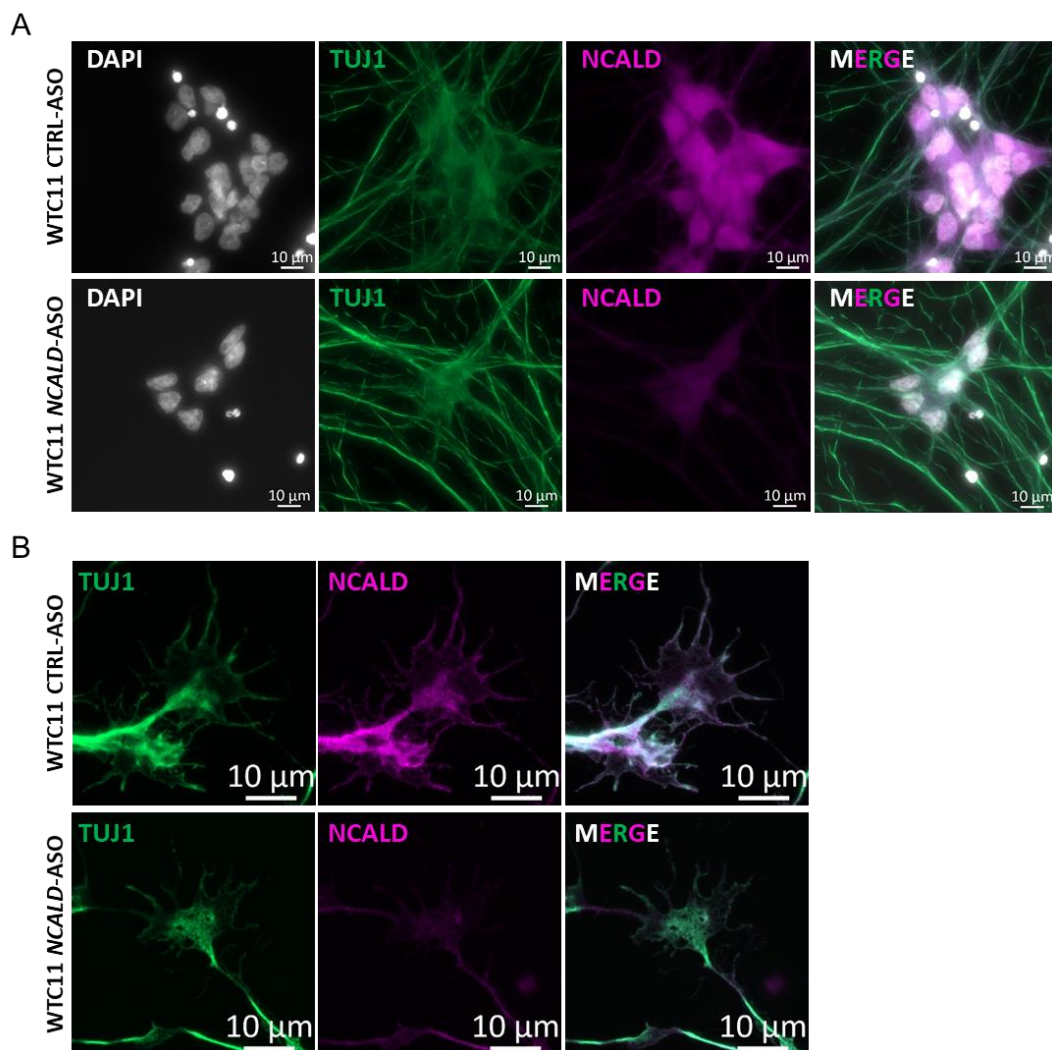


Figure 41. *NCALD* reduction in MNs upon treatment with *NCALD*-ASO69.

NCALD staining (magenta) of healthy WTC11 MNs derived from hiPSCs, treated with 60 nM CTRL-ASO or *NCALD*-ASO69 at day 13, immunostaining performed at day 20 of the differentiation.

- A) NCALD localizes at the cytosol of MNs, and it is markedly reduced upon *NCALD*-ASO69 treatment. Nuclei were counter stained DAPI (white) and axons are stained with TUJ1 (green). Scale bar 10 μ m.
- B) NCALD localizes in the growth cones, and is reduced upon treatment with *NCALD*-ASO69. Axons were counter stained with TUJ1 (green), a microtubule marker. Scale bar 10 μ m.

To sum up, we identified *NCALD*-ASO69 as an efficient and non-toxic ASO that enables NCALD reduction in the four tested hiPSCs derived MNs. Moreover, NCALD downregulation can be detected at the growth cones of the MNs, which are SMA relevant sites. To test the therapeutic potential of NCALD reduction in SMA MNs derived from hiPSCs, we decided to treat the neuronal cultures with 60 nM of *NCALD*-ASO69 at day 13, and perform the functional and morphological experiments at day 20 of the differentiation.

3.2.2.3 Growth cone morphology analysis upon *NCALD*-ASO treatment

In the present work, upon *NCALD*-ASO69 treatment we appreciated a change in neuronal terminal ends (Figure 39). Therefore, we decided to quantify if *NCALD* downregulation using 60 nM *NCALD*-ASO69 could have an impact in growth cone morphology. MNs were treated at day 13 with 60nM of *NCALD*-ASO69 or CTRL-ASO, and growth cone morphology analysis was performed at day 20 by immunostaining. Actin filaments were labeled using Phalloidin and microtubules were stained using anti- β -III-tubulin (TUJ1).

First, growth cone structure was classified based on actin morphology in three categories: blunt, filopodia and lamellipodia (Figure 42) (Khazaei et al. 2014). SMA type I MNs (HGK1 and CS32iSMA) had more growth cones with blunt actin filaments compared to the healthy lines (Figure 42). This number was reduced upon *NCALD*-ASO69 treatment and more growth cones displayed filopodial and lamellipodial actin morphologies. Surprisingly, *NCALD*-ASO69 also had an effect in growth cone morphology in one of the healthy lines (HUVEC), suggesting the NCALD might have a role in actin dynamics independent of the SMA background. Interestingly, no effect was detected in MNs derived from the WTC11 hiPSC line, suggesting that the effect of NCALD in actin dynamics might differ between individuals.

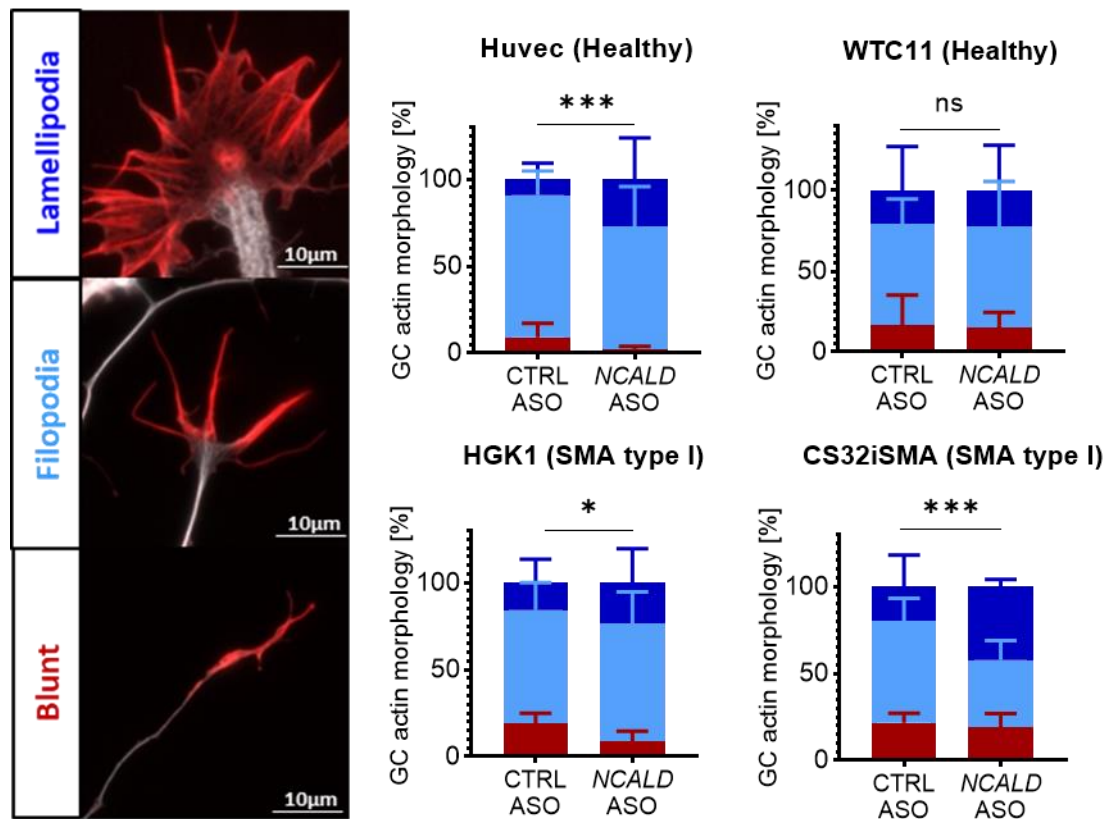


Figure 42. Actin morphology at the growth cone upon *NCALD*-ASO69 treatment.

Actin was stained using Phalloidin (red) and microtubules were stained using TUJ1 (white). Actin morphology was categorized as blunt ended, filopodia or lamellipodia based on the morphology of the filaments. Scale bar 10 μ m. In total, three independent experiments coming from independent differentiation were performed per cell line. HUVEC (N=3; CTRL-ASO n=141, *NCALD*-ASO69 n=103), WTC11 (N=3; CTRL-ASO n=84, *NCALD*-ASO n=85), HGK1 (N=3; CTRL-ASO n=138, *NCALD*-ASO69 n=149), CS32isma (N=3; CTRL-ASO n=154, *NCALD*-ASO69 n=146). Error bars show \pm SD. Graphs represent percentages. * $p \leq 0.05$, *** $p \leq 0.001$ (Chi-square test).

Next, microtubule morphology was categorized based on whether the microtubules of the central domain displayed a bundled, spread or looped conformation (Figure 43) (Berghuis et al. 2007). Analysis of the microtubule conformation resulted in marked presence of bundled microtubules in the SMA type I lines compared to the healthy MNs treated with CTRL-ASO. The amount of bundled microtubules was drastically reduced in the SMA lines upon *NCALD*-ASO69 treatment and a significant increase in spread and looped categories was observed. In this case, 60 nM *NCALD*-ASO69 treatment had a positive effect in growth cone morphology of MNs derived from both healthy lines.

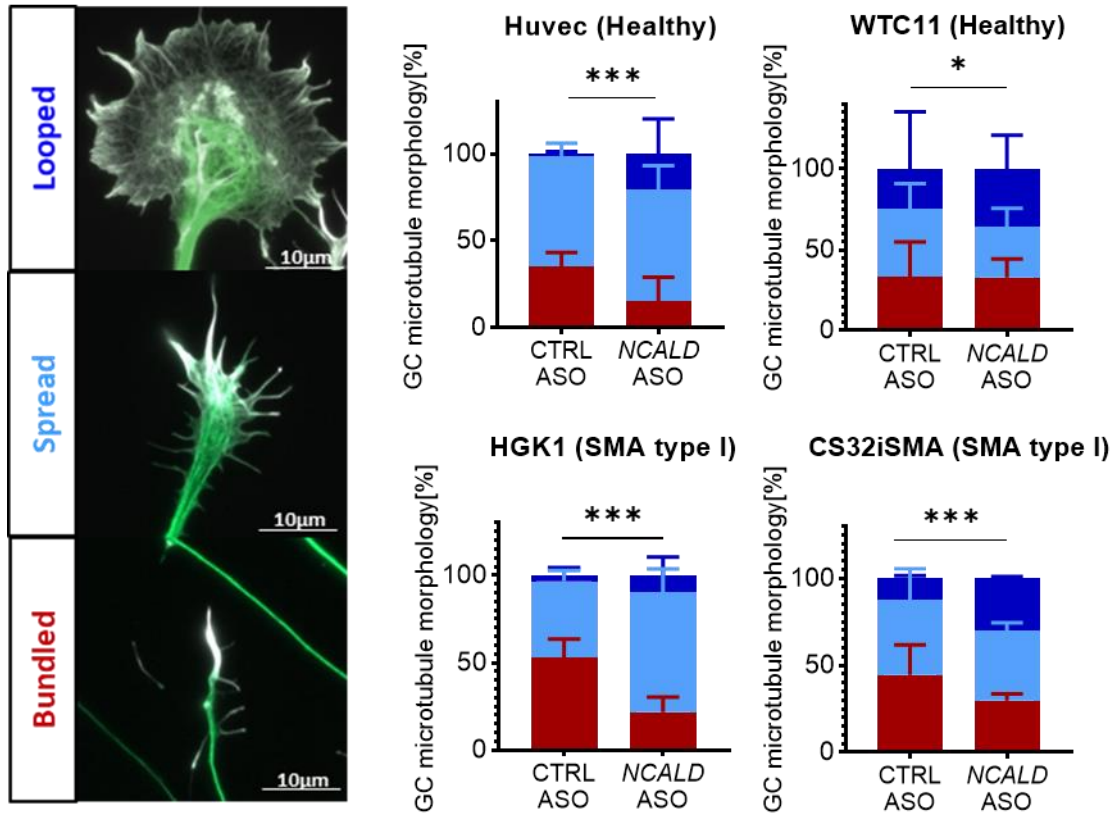


Figure 43. Microtubule morphology at the growth cone upon *NCALD*-ASO69 treatment.

Microtubules were stained using anti- β -III-tubulin (TUJ1, green), and actin was counterstained using Phalloidin (white). Microtubule morphology was categorized as bundled, spread or looped. Scale bar 10 μ m. In total, three independent experiments coming from three independent differentiations were performed per cell line. HUVEC (N=3; CTRL-ASO n=141, *NCALD*-ASO69 n=103), WTC11 (N=3; CTRL-ASO n=84, *NCALD*-ASO n=85), HGK1 (N=3; CTRL-ASO n=138, *NCALD*-ASO69 n=149), CS32iSMA (N=3; CTRL-ASO n=154, *NCALD*-ASO69 n=146). Error bars show \pm SD. Graphs represent percentages. * $p \leq 0.05$, *** $p \leq 0.001$ (Chi-square test).

These results strongly support the role of *NCALD* reduction on actin and microtubule cytoskeleton modulation and therefore, growth cone dynamics, which is crucial for neurite outgrowth and NMJ maturation and function. Indeed, *NCALD* directly binds to α - and β -tubulin, and actin (Ivings et al. 2002), which are essential component of the cytoskeleton. These results go in line with our findings on the improvement of NMJ innervation upon *Ncald*-ASO treatment in SMA mice (section 3.2.1.4), emphasizing once again the potential of *NCALD* reduction as a promising therapeutic approach that targets one of the key pathological features in SMA, the NMJ.

3.2.2.4 Multi-electrode array measurements upon *NCALD*-ASO treatment

Multi-electrode arrays (MEA) facilitate the recording of large populations of neurons and their network activity by detecting the extracellular voltages, which reflect the firing activity of the surrounding neuronal population. This type of electrophysiological measurements are particularly relevant for drug testing, since it gives important information of the impact a drug might have on the neuronal network, more similar to what would happen on a specific tissue *in vivo*. Whole-cell patch clamp recordings from muscle cells of *smn*-depleted zebrafish showed an improvement of neuronal circuit function upon *Ncald* reduction (Riessland et al. 2017). Moreover, *Ncald*-ASO in combination with low-dose *SMN*-ASO ameliorates electrophysiological properties (CMAP and MUNE) in SMA mice at PND21 (Torres-Benito et al. 2019) and at 2 months of age after *Ncald*-ASO re-injection (section 3.2.1.3).

To assess the therapeutic potential of 60 nM *NCALD*-ASO69 treatment in hiPSC derived MNs from SMA patients, spontaneous firing of treated healthy and SMA type I hiPSC derived MNs were recorded at day 20 of the differentiation using a multi-electrode array system. As expected, spontaneous neuronal activity was reduced in SMA type I MNs compared to healthy MNs when treated with CTRL-ASO, determined by the number of spikes (Figure 44A). Importantly, MN cultures treated with *NCALD*-ASO69 exhibited an increase in number of spikes. In addition, SMA MN cultures had less active electrodes than the healthy MN lines, a parameter that was improved after *NCALD*-ASO69 treatment (Figure 44). Moreover, the number of bursts (group of spikes in close succession followed by a period of silence) were markedly reduced in SMA MNs compared to the healthy lines (Figure 44B), a parameter that was ameliorated upon *NCALD*-ASO69 transfection.

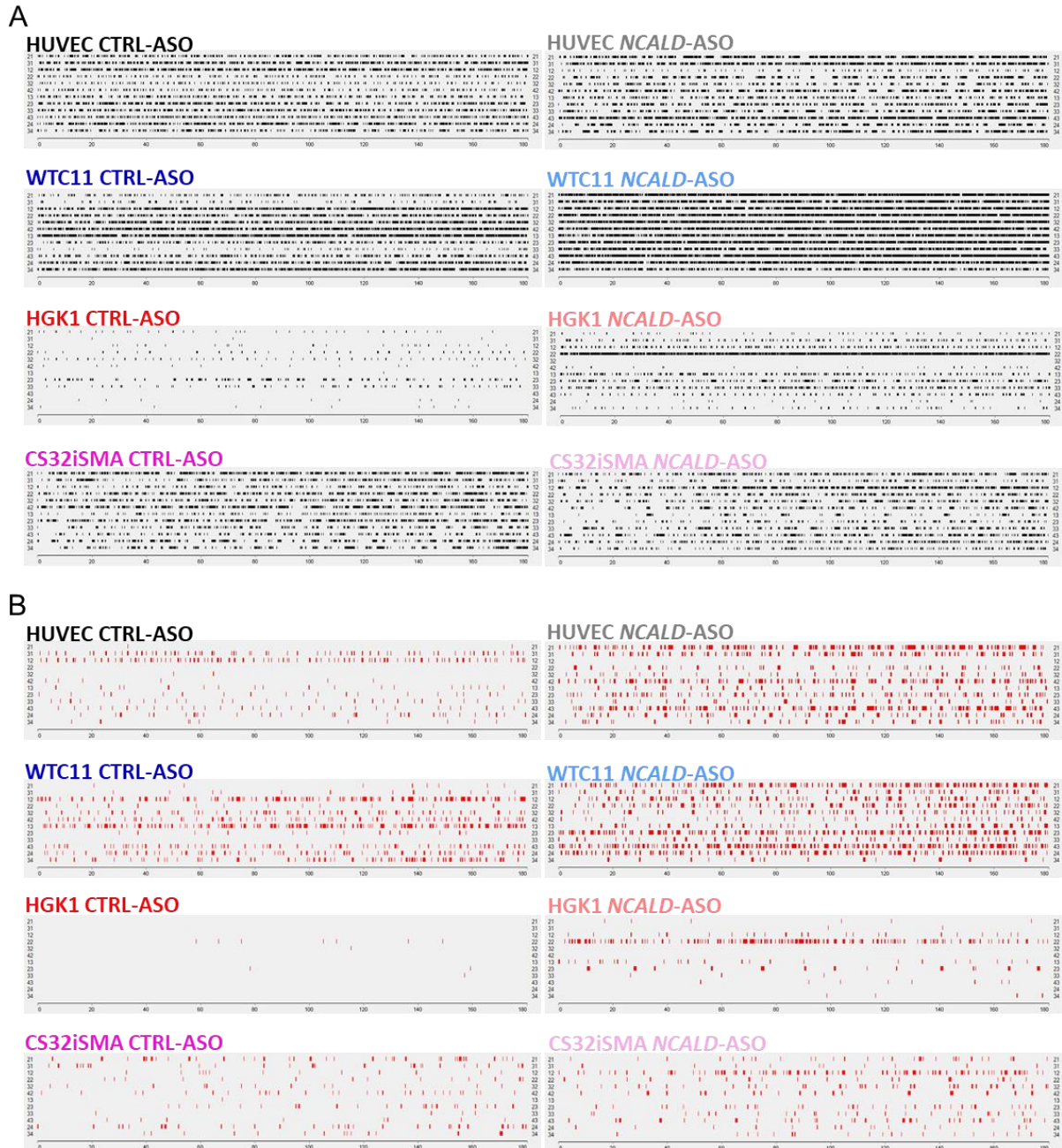


Figure 44. Spikes and burst of healthy and SMA hiPC derived MNs upon *NCALD-ASO69* treatment

A) MEA analysis at day 20 of CTRL-ASO or *NCALD-ASO69* treated MNs. Each image represents spikes (black) detected in 1 well, recorded for 3 minutes. Each line represents the activity detected by one electrode (in total 12 electrodes per well).

B) MEA analysis at day 20 of CTRL-ASO or *NCALD-ASO69* treated MNs. Each image represents burst (red) detected in 1 well, recorded for 3 minutes. Each line represents the activity detected by one electrode (in total 12 electrodes per well).

In total, three independent experiments from three independent MN differentiations were recorded.

Interestingly, an increase in active hiPSC derived MNs was observed after *NCALD*-ASO69 treatment independently of the genotype, as determined by the parameters evaluated: spike count, burst count, burst spike count and percentage of spikes in bursts (Figure 44 and Figure 45). In general, it seems that *NCALD* reduction increased the spike height in all MN lines (Figure 45A). The healthy MN line, WTC11 and two SMA type I hiPSC derived MNs exhibited a significant increase of spike numbers upon *NCALD*-ASO69 treatment (Figure 44A and 45B). Moreover, the healthy line WTC11 and the SMA type I HGK1 exhibited a marked increase in burst numbers when treated with *NCALD*-ASO69 in comparison to MNs treated with CTRL-ASO (Figure 44A and 45B). *NCALD* reduction does not have an impact in the overall number of burst spike counts (Figure 45B). Furthermore, the healthy HUVEC line and the SMA type I line exhibited an increase in the percentage of spikes that are present in a burst when treated with 60 nM *NCALD*-ASO69. Finally, *NCALD*-ASO69 had a strong impact in the reduction of the interval between neuronal bursts in the SMA type I line HGK1 (Figure 45B).

In conclusion, the multielectrode array allowed us to analyze the effect of *NCALD* downregulation in the neuronal network activity of SMA type I and healthy hiPSC derived MNs, demonstrating its role in increasing neuronal firing. These results further support the relevant role of *NCALD* in neuronal activity and synaptic connectivity, and go in line with our previous data from section 3.2.1.3 showing amelioration of the electrophysiological properties of the gastrocnemius muscle in SMA mice upon *Ncald*-ASO re-injection treatment. Notably, SMA type I line HGK1 seems to be more sensitive to *NCALD* reduction than SMA type I line CS32iSMA, and a similar phenomenon is observed between the healthy MNs, HUVEC and WTC11. These data emphasize the importance of testing compounds in hiPSC derived MNs, which better resemble the human genetic diversity, in order to provide a better understanding of which patients might respond to a treatment and which ones will not. Overall, the effect of *NCALD* reduction in neuronal activity was observed in all lines, suggesting that *NCALD* downregulation has an impact in neuronal activity independently of the SMA context and therefore could be beneficial in other neurodegenerative disorders where neuronal transmission is altered, for example in ALS.

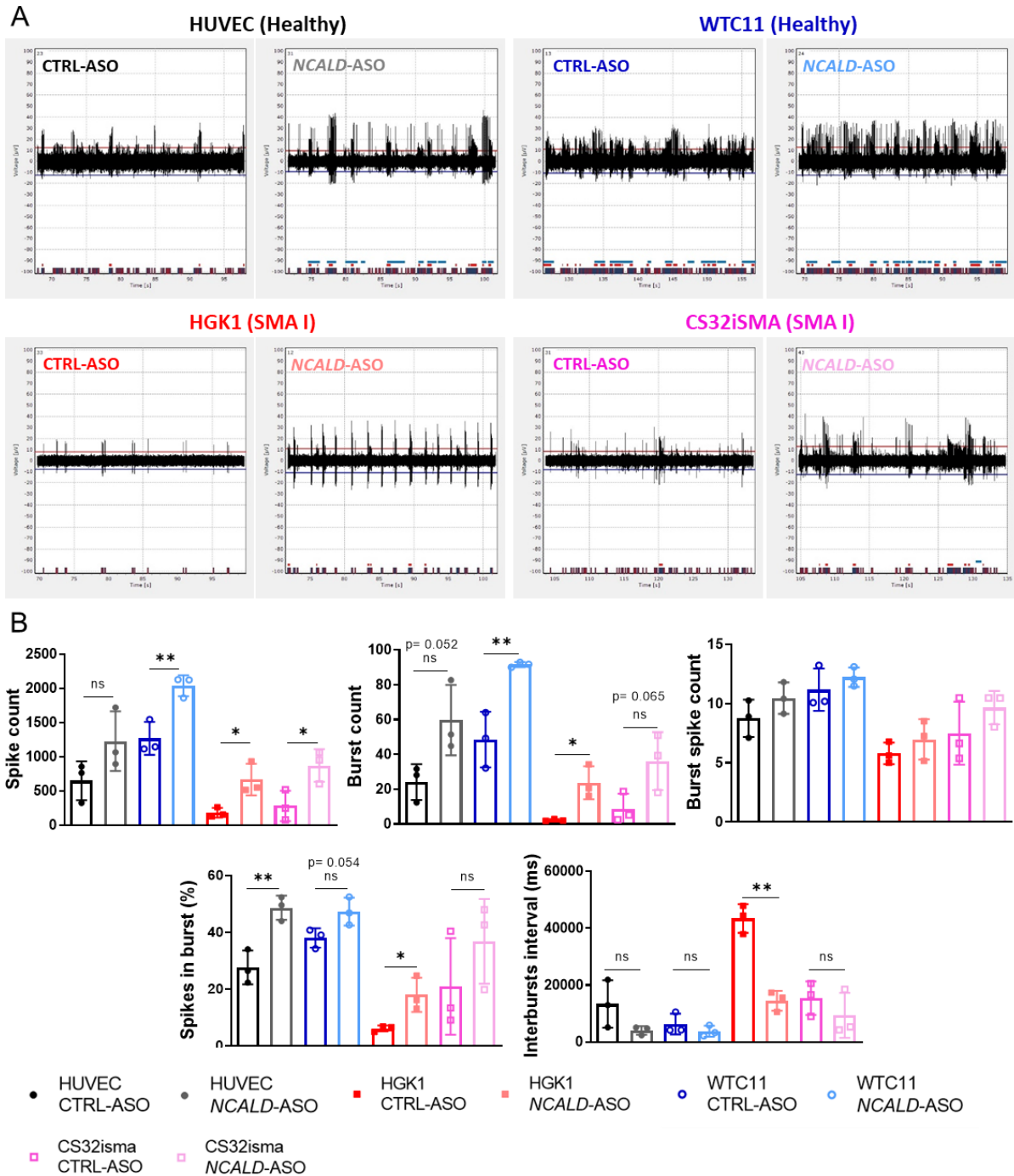


Figure 45. Multi-electrode array shows increase in neuronal firing upon *NCALD-ASO69* treatment.

A) Representative images of the activity detected by one electrode for 30 seconds per condition.

B) MEA analysis of various parameter measured at day 20 of CTRL-ASO or *NCALD-ASO69* treated MNs.

Dots in the graphs represent the average values of the technical replicates of each independent replicate, in total three independent replicates corresponding to three independent MN differentiations (N=3, n=3-4). Unpaired two-tailed Student's t test was performed in each line to compare CTRL-ASO versus *NCALD-ASO* treatment. All values reported as mean and error bars represent \pm SD. * $p \leq 0.05$, ** $p \leq 0.01$.

4. DISCUSSION

Since the discovery of the SMA disease-causing gene in 1995, there have been significant advances in the understanding of the complex pathomechanisms underlying SMA. Most importantly, all the efforts facilitated the development of FDA- and EMA-approved therapies for SMA that changed the natural history of the disease. Since SMA is caused by a decrease of functional SMN levels, the primary therapeutic goal of the translational programs was to develop drugs that increase full length SMN protein. Currently, there are three different FDA- and EMA-approved SMN-dependent drugs available on the market, which enhance functional, full-length SMN protein levels using different strategies. The first approved drug was nusinersen, an intrathecally injected antisense oligonucleotide that modifies the alternative splicing of *SMN2* pre-mRNA prompting the inclusion of exon 7 of the transcript, thus increasing the amount of functional SMN protein in the CNS. Next, the AAV9-based gene therapy, onasemnogene abeparvovec, is based on *SMN1* gene replacement. Finally, risdiplam is an orally available small molecule that modulates splicing and promotes exon 7 inclusion in different tissues of the body not only in the CNS (Finkel et al. 2016; Finkel et al. 2017; Mercuri et al. 2018; Darras, Chiriboga, et al. 2019; Mendell et al. 2017; Mendell et al. 2021; Darras et al. 2021; Baranello, Darras, et al. 2021).

Development of drugs that enhance SMN levels are without any doubt the most straightforward therapeutic strategy for SMA, and have shown impressive results in patients. However, in many cases, even when the therapy is administered at pre-symptomatic stages, there is still a considerable number of SMA patients that do not show significant improvements upon the SMN-enhancing treatments (De Vivo et al. 2019; Vill et al. 2021). Furthermore, a recent study demonstrated that long-term overexpression of AAV9-*SMN1* in a SMA mouse model induces a dose-dependent late-onset motor dysfunction characterized by loss of proprioceptive synaptic transmission and neurodegeneration. These observations highlight how crucial it is to understand the temporal requirements of SMN life long: highest during neonatal life while NMJs undergo maturation and lower during adulthood (Van Alstyne et al. 2021; Kariya et al. 2014). Although SMA is primarily characterized by MN dysfunction, SMN reduction below a certain threshold has an impact on several molecular and cellular pathways that lead to multiorgan impairment in severely affected individuals, which in some cases cannot be ameliorated with the available SMN enhancing therapies solely. Moreover, the finding of SMA discordant families with individuals carrying homozygous *SMN1* deletions and three to four *SMN2* copies but are fully asymptomatic (Oprea et al. 2008; Riessland et al. 2017), led to the discovery of SMA genetic modifiers independent from SMN. These findings opened the doors to a better understanding of crucial molecular pathways disturbed in SMA. PLS3 overexpression and NCALD

reduction protect individuals from developing SMA type II-IV by rescuing impaired endocytosis, a key pathway that contributes to SMA pathology (Hosseinibarkooie et al. 2016; Riessland et al. 2017). In addition, CHP1, an interacting partner of PLS3, ameliorates SMA pathology in an intermediate mouse model when it is downregulated (Janzen et al. 2018). Importantly, none of the SMN independent modifiers alone was able to prolong survival of severe SMA mice, most probably due to the multiorgan impairment caused by the disturbance of SMN housekeeping functions (Fallini et al. 2016; Hosseinibarkooie et al. 2016; Ackermann et al. 2013). In the discordant families, asymptomatic individuals carry at least three *SMN2* copies, suggesting that a certain level of SMN is required for a genetic modifier in order to exert its protective effect. Indeed, combinatorial treatments using PLS3 overexpression, NCALD reduction or CHP1 reduction together with *SMN*-ASO, efficiently improved SMA phenotype in mice (Hosseinibarkooie et al. 2016; Riessland et al. 2017; Kaifer et al. 2017; Torres-Benito et al. 2019; Janzen et al. 2018). Taking all of these into account, since genetic modifiers play such a critical role, it is of great interest to develop drugs that target those SMN-independent processes, and administer them in combination with SMN-dependent compounds for lifelong protection of SMA patients.

The present study consists of two preclinical trials testing combinatorial therapies based on independent antisense oligonucleotides targeting SMA genetic modifiers. The first part of the study (section 3.1) focused on the combinatorial therapy using *SMN*-ASO, which enhances SMN levels, and *Chp1*-ASO, which reduces CHP1 protein, in SMA mice. Part of this work has been published (Muinos-Buhl et al. 2022). The second study (section 3.2) tested the long-term effect of NCALD reduction via *Ncald*-ASO re-injection in adult SMA mice pre-symptomatically treated with low-dose *SMN*-ASO and *Ncald*-ASO. In addition, in order to have an approximation of the *NCALD*-ASO therapeutic effect in humans, we analyzed morphological and electrophysiological properties of SMA hiPSC derived MNs upon treatment. The following sections will focus on the discussion of the results from both studies.

4.1 Part I: Combinatorial therapy using *SMN*-ASO and *Chp1*-ASO

Previous work carried out in our research group tried to unravel the underlying molecular mechanism responsible for the PLS3 rescuing effect by screening for interacting partners that could also serve as therapeutic targets (Janzen et al. 2018). After a yeast-two-hybrid screen, CHP1 was identified as the only putative direct interacting partner of PLS3. CHP1 protein is ubiquitously expressed, but particularly abundant in the CNS. Interestingly, in SMA, CHP1 levels were found to be elevated in the CNS of severely affected SMA mice, but not in the TVA muscle, suggesting that CHP1 dysregulation upon SMN deficiency is particularly relevant in the neuronal tissue. In addition, CHP1 acts as an

endogenous calcineurin inhibitor (Lin et al. 1999) and its reduction improves impaired endocytosis by counteracting the decrease of calcineurin activity and DNM1 hyperphosphorylation in SMA, thus triggering bulk endocytosis (Janzen et al. 2018). Moreover, *CHP1* reduction in a severe SMA mouse model with a mutant *Chp1* allele, the *vacillator* mutation, in combination with low-dose *SMN*-ASO to increase *SMN* significantly improved SMA pathology hallmarks (Janzen et al. 2018).

These promising findings encouraged us to establish a collaboration with Ionis Pharmaceuticals to further analyze the therapeutic potential of the novel SMA genetic modifier, *Chp1*, by antisense oligonucleotide pharmacological downregulation in combination with low-dose of *SMN*-ASO in an intermediate affected SMA mouse model. In addition, we also wanted to establish an efficient MN differentiation protocol from healthy and SMA patient hiPSCs in order to test human *CHP1*-ASO leads in the MNs.

As a brief summary of the main findings of this work, we demonstrated:

- 1) All designed *Chp1*-ASOs efficiently downregulate *Chp1* in the CNS, however the long-term effect of the ASOs is variable.
- 2) Injection of 30 µg *Chp1*-ASO4 efficiently downregulates *CHP1* levels at PND14 to about 50% and is a safe dosage that does not cause Purkinje neuronal loss or an ataxic gait in the wild type mouse.
- 3) A single i.c.v. administration of 30 µg *Chp1*-ASO4 at PND2 is not sufficient to maintain *CHP1* levels at ~50% 4-weeks after the injection, suggesting that *Chp1*-ASO4 is not stable in a long-term.
- 4) Combinatorial therapy injecting 30 µg *Chp1*-ASO4 and low-dose *SMN*-ASO pre-symptomatically is insufficient to counteract SMA hallmarks at PND21 in comparison to *SMN*-ASO alone.
- 5) I.c.v. bolus re-injection of 400 µg *Chp1*-ASO4 in adult mice was not sufficient to ameliorate the disease pathology in a long-term.
- 6) hiPSCs from healthy individuals and SMA patient efficiently differentiate into MNs.
- 7) The designed human *CHP1*-ASOs efficiently reduce *CHP1* in hiPSCs derived MNs, via free up-take and using Lipofectamine™.

Our findings are surprising in light of the previous study showing SMA pathology amelioration in the intermediate SMA mouse model carrying the genetic *Chp1* mutant allele (Janzen et al. 2018), including prolongation of the survival, improvement of electrophysiological defects, increase of proprioceptive synapses per MN soma, and NMJ size and maturation. Moreover, preceding work testing a similar combinatorial therapeutic approach, targeting in that case the genetic modifier *Ncald* with a single i.c.v. dose of *Ncald*-ASO together with low-dose *SMN*-ASO, significantly ameliorated SMA pathology at

PND21 and motoric abilities at 3 months even though no significant reduction of NCALD was detected four weeks after administration (Torres-Benito et al. 2019). Since we did not obtain the therapeutic outcome expected given previous studies (Janzen et al. 2018), together with our findings, I will discuss possible differences and limitations of our investigation as compared to other therapeutic approaches.

4.1.1 The importance of CHP1 reduction during development

In the previous study carried out by Janzen and collaborators, *Chp1* reduction to about 50% was achieved by crossing *Smn*^{ko/ko}; *SMN2*^{tg/tg} animals with mice carrying the heterozygous *vacillator* mutation in *Chp1*, *Smn*^{ko/wt}; *Chp1*^{vac/wt} (Janzen et al. 2018). As a result, half of the offspring (in both HET and SMA groups) had a constant reduction of about 50% CHP1 protein levels from the time of conception to the finalization of the experiments. This means that CHP1 downregulation could exert its protective effect during pre-symptomatic and post-symptomatic stages of the disease. Importantly, a clinical study found increased levels of NF, a biomarker for axonal injury and neurodegeneration, in plasma samples from SMA type I patients with less than one year of age (Darras, Crawford, et al. 2019). These results suggest that MN degeneration most probably starts at perinatal stages, and that an effective therapeutic intervention might require prenatal administration of the treatment. Moreover, endocytosis, which is defective in SMA, is essential not only at the NMJ level - which undergoes complex postnatal maturation - but also for MN development and function (Hosseinibarkooie et al. 2016; Riessland et al. 2017; Janzen et al. 2018). Importantly, it has been proven that CHP1 protein reduction ameliorates altered bulk endocytosis in SMA; therefore the prenatal protective effect of *Chp1* reduction might have had an additional beneficial impact in the SMA-*Chp1*^{vac/wt} mouse model (Janzen et al. 2018). In contrast, our study pharmacologically reduced CHP1 levels with 30 µg *Chp1*-ASO from PND2, which might be too late to counteract the disease phenotype at PND21. Furthermore, CHP1 therapeutic levels were maintained only for a short period until they reached untreated levels 4-weeks after the injection.

4.1.2 Ubiquitous vs targeted CHP1 reduction

CHP1 protein is ubiquitously expressed and particularly abundant in the CNS. In the previous work, SMA mice carrying heterozygous *vacillator* mutation in *Chp1* had ubiquitous CHP1 reduction in all organs (Janzen et al. 2018). In contrast, in the present work, we i.c.v. injected *Chp1*-ASOs in order to pharmacologically induce *Chp1* reduction only in the CNS, since MNs are particularly vulnerable in SMA (Ling et al. 2012; Boyd 2017), and to mimic the administration route of the FDA- and EMA-approved *SMN*-ASO in SMA patients. However, from our results, it seems evident that ubiquitous *Chp1* downregulation might have a protective role also in other affected peripheral organs, and therefore contributes to the amelioration of SMA multiorgan defects. Surprisingly, our research showed a

positive trend in the gastrocnemius muscle after re-injections, with an increase in the number of fibers with higher size (300 – 400 μm^2) upon *Chp1*-ASO4 treatment compared to CTRL-ASO injected animals. This tendency goes in line with the observations obtained from the tibialis anterior muscle in the SMA heterozygous *Chp1* animals (Janzen et al. 2018).

4.1.3 CHP1 levels, a matter of balance

CHP1 functions as an essential cofactor of NHE1, regulating pH sensitivity of NHE1, maturation and membrane targeting (Liu et al. 2013; Pang et al. 2004). Remarkably, CHP1 reduction below a certain threshold leads to altered NHE1 maturation and causes Purkinje cell degeneration and ataxia in mice (Liu et al. 2013). Congruently, in humans, homozygous mutations in *CHP1* cause autosomal recessive cerebellar ataxia (Mendoza-Ferreira et al. 2018; Saito et al. 2020). However, individuals with heterozygous *CHP1* mutations have been reported to be asymptomatic, similar to the mice carrying heterozygous *Chp1* mutations. In the present work, we faced a great challenge: to find the safe dosage in which the amount of *Chp1*-ASO was not detrimental for the Purkinje neurons and at the same time was sufficient to ameliorate SMA pathology. The injection of 40 μg *Chp1*-ASO4 led to a comparable CHP1 reduction in the brain and the spinal cord in comparison to 30 μg . However, despite no significant differences in motor coordination, one out of eight animals injected with 40 μg *Chp1*-ASO4 developed a clear ataxic phenotype at 3-weeks after the injection. In addition, 6-weeks after injection the animals exhibited a trend towards decreased motor performance. In conclusion, it is possible that injection of 40 μg *Chp1*-ASO4 in SMA animals might lead to better therapeutic outcomes compared to 30 μg *Chp1*-ASO4, but we cannot disregard the potential risk of some animals developing ataxic side effects.

4.1.4 Antisense oligonucleotide nature

ASOs are synthetic oligonucleotides usually between 15 to 25 nucleotides in length that bind complementary RNA by Watson-Crick base pairing, thus modulating the expression of the targeted RNA by different mechanisms (Bennett, Krainer, and Cleveland 2019; Crooke et al. 2018). The mechanism of action, the efficiency and the long-term/short-term stability of each ASO is determined by the sequence, chemical modifications and their position, the structure, and the region where the ASO binds (Crooke et al. 2018). In the present study, we used murine chimeric 5-10-5 MOE ASOs with a central region of 10 nucleotides referred to as “gapmer”, which recruit the RNase H1 and mediate the cleavage of *Chp1* mRNA. Injection of 50 μg *Chp1*-ASO3 or *Chp1*-ASO4 was well tolerated by the neonatal wild type mice and significantly reduced CHP1 protein levels in brain and spinal cord. A single dose of 30 μg *Chp1*-ASO4 efficiently downregulated CHP1 levels to about 50% in the CNS 2-weeks after i.c.v. injection. Unexpectedly, stability of *Chp1*-ASO4 was rather low and CHP1 protein amount returned to untreated levels after 4-weeks. Moreover, the treatment failed to ameliorate SMA

phenotype at PND21. Interestingly, independent research studies using similar structured ASOs (5-10-5 MOE gapmer ASOs) to target huntingtin (*Htt*) or superoxide dismutase 1 (*Sod1*) proteins, administered the compounds in adult rodents via i.c.v. infusion for a period of 14-28 days (Smith et al. 2006; Kordasiewicz et al. 2012). As a result, both studies were able to reduce the respective protein levels up to 16 weeks, prolong survival and ameliorate the respective disease phenotype. In contrast, the effect of a single injection of *SMN*-ASO - a second generation uniform MOE PS splice-switching ASO - has been reported to last more than 6 months (Hua et al. 2010) and to act more efficiently when administered via i.c.v. injection than i.c.v. infusion (Rigo et al. 2014). In humans, *SMN*-ASO increases SMN protein production for 3-4 months before levels start to decrease (Luu et al. 2017). Congruently, SMA patients treated with nusinersen (*SMN*-ASO) receive a dose of 12 mg by intrathecal injection every 4 months. Altogether, these evidences suggest that in the case of 2' MOE gapmer ASOs (like the *Chp1*-ASOs used in part I of the study) with short half-life, long-term infusion in the CNS or repeated administrations in short time periods should be considered in order for the compound to act efficiently on its target and to achieve and maintain the therapeutic level over time. Nonetheless, a single injection of 2' MOE gapmer ASOs can exert a prolonged therapeutic effect despite the short-term stability of the ASO, as shown by *Ncald*-ASO (Torres-Benito et al. 2019). In the present study, pre-symptomatic administration in neonatal mice was essential, therefore the use of an implantable infusion pump was not considered. Importantly, i.c.v. injections/infusions distribute the drugs all over the CNS, but not uniformly. Indeed, higher concentrations of the compounds are found in cortex, hippocampus, and Purkinje cells of the cerebellum (Bennett, Krainer, and Cleveland 2019; Jafar-Nejad et al. 2021). Therefore, since it is well known that CHP1 protein levels below a certain threshold lead to Purkinje neuron loss and cerebellar ataxia (Janzen et al. 2018; Mendoza-Ferreira et al. 2018; Liu et al. 2013), long-term infusion of *Chp1*-ASO in the brain of adult mice would have been an unsafe approach.

In conclusion, in the first part of this thesis, our main aim was to ameliorate SMA pathology applying a combinatorial ASO-based therapeutic strategy, targeting two well-known SMA genetic modifiers: *SMN2* splicing modulation using *SMN*-ASO and *Chp1* downregulation via *Chp1*-ASO. The narrow therapeutic window in which *Chp1* exerts its protective effect and the critical balance between CHP1 reduction acting in a therapeutic or detrimental manner, made the development of a combinatorial therapy extremely challenging. Consistently, combination of low-dose *SMN*-ASO together with i.c.v. administration of 30 ug *Chp1*-ASO4 at presymptomatic stages was not sufficient to counteract SMA pathology in SMA mice. Nonetheless, we cannot discard the important role of the genetic modifiers in helping researchers decipher molecular mechanisms altered in SMA. Moreover, genetic modifiers still represent promising therapeutic targets when successfully modulated.

4.2 Part II: Long-term combinatorial therapy using *SMN*-ASO and *Ncald*-ASO

In 2017, our group reported the discovery of a new protective genetic modifier for SMA found in a four-generation SMA discordant family. While two out of seven family members carrying *SMN1* deletions developed SMA type I, five *SMN1*-deleted individuals with four *SMN2* copies were asymptomatic (which normally would correspond to SMA type III). Combination of genome-wide linkage analysis and transcriptome-wide differential expression studies led to the identification of neurocalcin delta (NCALD), a neuronal Ca^{2+} sensor protein, as a promising candidate to act protective in the asymptomatic individuals when downregulated (Riessland et al. 2017). In order to confirm this hypothesis, multiple *in vitro* and *in vivo* experiments were performed to corroborate the protective role of NCALD reduction across species. Importantly, severe SMA mice carrying heterozygous *Ncald* knockout and injected with low-dose *SMN*-ASO at PND1, exhibited a significant amelioration of the disease hallmarks. In addition, NCALD reduction had a major impact in rescuing defective endocytosis. In SMA, Ca^{2+} levels are low prompting the interaction of NCALD with clathrin, disturbing endocytosis by preventing vesicle coating. Thus, reduction of NCALD levels enhances clathrin-mediated endocytosis (Riessland et al. 2017). Notably, while homozygous *Ncald* knockout affects brain adult neurogenesis, heterozygous *Ncald* knockout is asymptomatic and acts protective against SMA (Upadhyay et al. 2019). In 2019, our research group carried out a randomized-blinded preclinical study in SMA mice: a single subcutaneous dose of 30 μg *SMN*-ASO injection together with a single i.c.v. injection of 100 μg *Ncald*-ASO3 or CTRL-ASO at PND1 and PND2, respectively. Low-dose *SMN*-ASO administered systemically rescued the multiorgan impairment, generating a mild SMA mouse model, which resembles the human situation in the asymptomatic discordant families. Additional NCALD reduction via *Ncald*-ASO, further ameliorated SMA pathology such as electrophysiological and morphological properties of NMJs and muscles at PND21. However, a single injection of *Ncald*-ASO at PND2 was not sufficient to maintain the amelioration of various disease hallmarks over time, only motoric abilities. In addition, *Ncald*-ASO stability was rather low, similarly to *Chp1*-ASO (Muinos-Buhl et al. 2022) and the NCALD knockdown effect was not detected at 3 months of age (Torres-Benito et al. 2019).

In the present work, our main goal was to determine if *Ncald*-ASO re-injections could prolong the therapeutic effect observed at PND21 in SMA mice. For that reason, we applied a similar experimental approach used by Torres-Benito and collaborators (Torres-Benito et al. 2019), and treated animals at PND2 with 100 μg *Ncald*-ASO and at PND28 with 500 μg of *Ncald*-ASO or CTRL-ASO via i.c.v. bolus injection and analyzed various SMA hallmarks at 2 months of age. In parallel, we established an efficient MN differentiation protocol for hiPSC lines from healthy and SMA type I-III patients, to use it as a tool to study SMA pathology in human cells and as platform for drug screening. In addition, Ionis Pharmaceuticals designed multiple human *NCALD*-ASOs for us to test in hiPSCs derived MNs. Finally,

we performed functional and morphological analysis of healthy and SMA hiPSC derived MNs upon *Ncald*-ASO treatment to assess the therapeutic potential of NCALD reduction in a human cell model. The main results obtained in this part of the study are summarized in Figure 46 and will be discussed in the following sections.

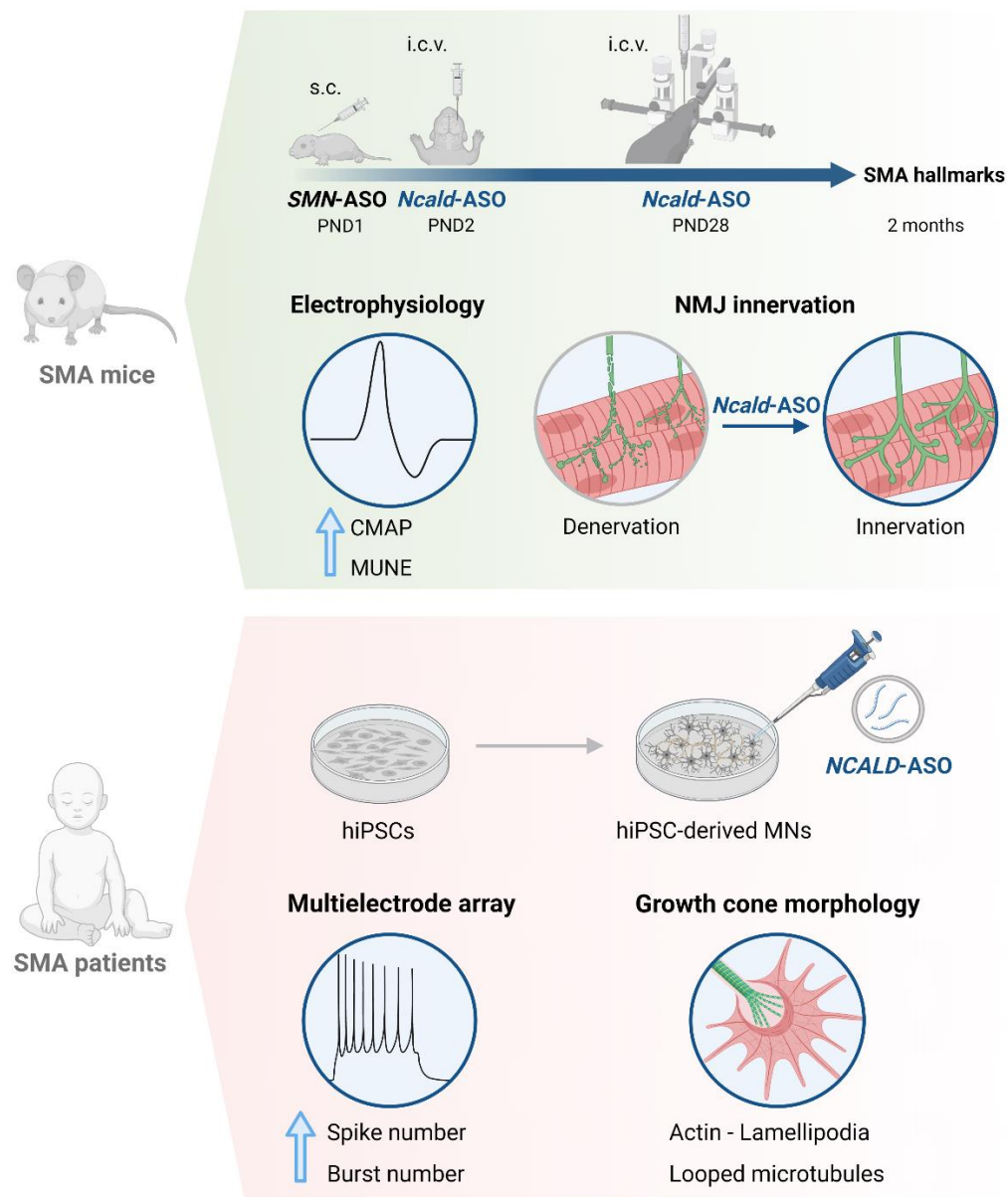


Figure 46. Graphical summary of the combinatorial therapy targeting SMN and NCALD

Long-term combinatorial therapy approach using ASOs to target SMN upregulation and NCALD reduction in SMA mouse, showed an amelioration of electrophysiological parameters and NMJ integrity at 2 months of age. Treatment of SMA hiPSC derived MNs with *NCALD*-ASO increased neuronal activity and ameliorated growth cone morphology. Figure created with BioRender.com.

4.2.1 *Ncald*-ASO re-injection prolongs amelioration of electrophysiological defects

Electrophysiological defects, such as decreased CMAP and MUNE, are described in SMA patients and mouse models and can be used as biomarkers for disease progression and treatment response (Arnold et al. 2014; Bogdanik et al. 2015; Lewelt et al. 2010). CMAP and MUNE measurements provide information about the functionality and the number of motor units. Moreover, electrophysiological recordings in patients have demonstrated that nusinersen treatment can increase the number of active motor units, which translates in gain of motor functionality (Kariyawasam et al. 2020). In this work, we carried out the electrophysiological characterization of the gastrocnemius muscle, one of the most common muscles studied in SMA mouse models for this parameter (Arnold et al. 2015). In line with results previously obtained for this mild SMA animal model (Torres-Benito et al. 2019; Muinos-Buhl et al. 2022), low-dose *SMN*-ASO injected SMA mice showed about 30% reduction in CMAP response, which implies a decreased motor functionality. In addition, animals exhibit a significant decrease in the number of functional motor units, as determined by the MUNE. In the previous combinatorial therapy approach, using *Ncald*-ASO and low-dose *SMN*-ASO, one single injection of *Ncald*-ASO at PND2 was not sufficient to ameliorate electrophysiological defects long-term (Torres-Benito et al. 2019). Importantly, here we demonstrated that NCALD reduction achieved by re-injections of *Ncald*-ASO at PND28, significantly increased CMAP amplitude and motor unit numbers (MUNE) in a long-term fashion. These results indicate that long-term NCALD reduction not only improves the functionality and number of motor units, but also prevents MNs from degeneration. Consequently, preserving neuromuscular function over time most probably halts the progression of the disease, alleviates muscle atrophy and improves muscle function (Boyd 2017). Mechanistically, we speculate that NCALD reduction ameliorates impaired neurotransmission by restoring clathrin-mediated endocytosis as previously described (Riessland et al. 2017).

Interestingly, *SMN* reduction leads to selective vulnerability of MN pools and muscles (Woschitz et al. 2022). Therefore, it would be essential to investigate the effect of NCALD reduction by analyzing electrophysiological parameters of other affected muscles, for example, the proximal muscle quadratus lumborum.

4.2.2 *Ncald*-ASO reinjections prolong amelioration of NMJ pathology

The NMJ is an essential synapse that controls motor behaviors and is comprised of the pre-synaptic motor nerve terminal and the post-synaptic skeletal muscle fiber. NMJ denervation and loss of function are key hallmarks of SMA and other neuromuscular disorders such, ALS (Gromova and La Spada 2020)

or Myasthenia gravis (Gilhus et al. 2019), that lead to skeletal muscle atrophy. NMJs form during embryonic development and undergo complex maturation steps even following birth (Boyd 2017). In SMA, MNs and NMJs show early pathological defects, including altered morphology and function that precede MN death. Importantly, MN loss is an irreversible pathogenic event. Consequently, development of therapies that protect NMJ integrity has important clinical implications to counteract the progression of the disease and prevent MN death. In the present work we analysed NMJ area and degree of innervation from the transversus abdominis muscle after re-injection with *Ncald*-ASO at 2 months of age. Torres-Benito and collaborators reported a significant amelioration of the NMJ area at PND21 upon one single injection of *Ncald*-ASO administered at PND2, but not at 3 months of age (Torres-Benito et al. 2019). Noteworthy, the degree of innervation was not analyzed in the work by Torres-Benito and collaborators despite being a key hallmark of the pathology. In the present work, NMJ area from the TVA muscle was not increased after re-injection with *Ncald*-ASO compared to NMJ area of animals injected with CTRL-ASO. Instead, long-term treatment of SMA animals with *Ncald*-ASO showed a significant rescue of the NMJ denervation when compared to animals treated with CTRL-ASO. These results further suggest that the observed amelioration in the electrophysiological parameter CMAP is probably due to an increase of NMJs that are fully innervated and functional. Moreover, the MUNE results indicate that NCALD reduction seems to protect against denervation of the MN from the NMJ (the dying-backwards phenomenon), which allows the maintenance of motor unit numbers over time. These evidences strongly emphasize the therapeutic role of NCALD reduction in the NMJ pathology, and the importance of re-injections to prolong the beneficial effect. Remarkably, similar to SMN protein, NCALD protein levels in the spinal cord of mice decrease with age, reaching about 50% reduction in HET and SMA animals at 6 months of age compared to protein levels at PND4 (Torres-Benito et al. 2019). This data suggests that pharmacological reduction of NCALD might be crucial at early stages of the disease, during formation and maturation of the NMJs until they reach a stabilization phase later in adulthood, when NCALD levels are naturally reduced. In the future, it would be interesting to test this hypothesis by administering *Ncald*-ASO for a longer period to determine the temporal requirements for the treatment.

4.2.3 NCALD-ASO in hiPSC derived MNs

The discovery and development of hiPSCs have led to massive progress in the understanding of disease mechanisms and served as a platform for the development of therapeutic compounds. Importantly, hiPSCs represent an unlimited source with the capacity to differentiate into all cell types that recapitulate a full array of disease features. Moreover, the possibility to obtain hiPSCs from somatic cells of patients gives the opportunity to study the disease from perspectives that other disease models

cannot offer, for example to study developmental defects. Together, the combination of animal models and hiPSC derived models represent an efficient and cost-effective strategy to gain insights in the human disease and drug development.

In the present work, our aim was to test human ASOs targeting *CHP1* and *NCALD*, to support the data obtained in the preclinical studies of each combinatorial therapy performed in SMA mice. For this reason, we successfully implemented in our laboratory an efficient MN differentiation protocol from SMA and healthy hiPSC lines (Guo et al. 2017). All hiPSC lines were able to differentiate into MNs, with efficiency ranging between 50-70% of ISL1+ cells (MN marker), quantified by immunostaining. SMN protein localizes to MN axons and growth cones (Figure 25) (Fan and Simard 2002), where its RNP assembly function is critical for proper neuromuscular junction development and maturation (Kariya et al. 2014). Here, SMA MNs exhibited reduced levels of SMN in axons and growth cones compared to MNs from healthy lines.

Next, we tested in the hiPSC derived MNs the efficacy and tolerability of the human *NCALD*-ASOs designed by Ionis Pharmaceuticals. Surprisingly, protein lysates of MNs treated with *NCALD*-ASO55 and *NCALD*-ASO89 exhibited a significant reduction of ISL1 and SMN protein, whereas CTRL-ASO and *NCALD*-ASO69 treated MNs showed no significant change. These results suggest that *NCALD*-ASO55 and *NCALD*-ASO89 have some off-target effects that were not spotted in the preliminary screening performed by Ionis Pharmaceuticals. This screening was carried out on the A431 cell line derived from squamous carcinoma. Therefore, these data emphasize the importance of compound testing in cells from the final target tissue, in this case MNs.

4.2.3.1 *NCALD*-ASO69 has an impact in growth cone morphology

Growth cones are highly plastic and constantly changing structures dependent of cytoskeleton dynamics that during neuronal development respond to intra- and extracellular cues and are the driving force of neurite outgrowth towards the target (Fan and Simard 2002; Nolle et al. 2011). Remarkably, defective cytoskeleton dynamics is a hallmark of SMA (Sharma et al. 2005; Bowerman, Shafey, and Kothary 2007). In SMA, SMN deficiency leads to axonal outgrowth defects, smaller growth cones and defects in local translation of different actin isoforms, resulting in impaired actin dynamics that affect the presynaptic terminal (Rossoll et al. 2003; Moradi et al. 2017). Moreover, several proteins have been described to be altered and produce cytoskeletal aberrations in SMA, such as Stathmin (Wen et al. 2013) and the RhoA/ROCK pathway, or that act as a protective modifier by modulating actin cytoskeleton dynamics like PLS3 (Ackermann et al. 2013). Actin cytoskeleton dynamics plays an important role in neurodegeneration through involvement in axonal functions and

synapse maintenance (Hensel and Claus 2018). Therefore, it seems of high relevance to develop SMN-independent therapies that target the defects in cytoskeleton dynamic processes involved in maturation and function of the presynaptic terminal to counteract SMA pathology. In this regard, NCALD is highly abundant in spinal MNs (Iino, Kobayashi, and Hidaka 1998) and its reduction promotes neurite outgrowth in *Smn*-deficient neuronal cells even in the absence of retinoic acid, and axonal growth in *smn*-depleted zebrafish (Riessland et al. 2017). In addition, NCALD directly binds to actin and tubulin, two major components of the cytoskeleton (Ivings et al. 2002). During preliminary testing of NCALD-ASOs, we noticed morphological changes in the MNs treated with NCALD-ASO69 and NCALD-ASO89 compared to MNs treated with CTRL-ASO. Indeed, it has been shown that NCALD overexpression has a negative impact in axonal outgrowth (Yamatani et al. 2010), whereas its reduction has the opposite effect (Riessland et al. 2017). In the present work, MNs treated with NCALD-ASOs exhibited wider growth cones compared to MNs treated with CTRL-ASO. Strikingly, MNs treated with NCALD-ASO89 showed shorter axons and non-typical morphology of MNs (Figure 39). Since MN growth cones represent such a critical component of the future synapse with the skeletal muscle, and MN degeneration implies to NMJ pathology (Monani, Coover, and Burghes 2000), we decided to analyze growth cone morphology upon NCALD-ASO69 treatment in more detail.

The interactions between dynamic actin filaments and dynamic microtubules at the growth cone involve their coordinated polymerization and depolymerization (Dent and Kalil 2001), and are crucial for axonal outgrowth, growth cone turning and response to guidance cues for pathfinding (Tamariz and Varela-Echavarria 2015). Actin bundling is important for filopodia formation and extension, force generation and cellular motility. In addition, lamellipodia are sheet-like extensions of cross-linked F-actin meshwork that are not only involved in growth cone protrusion and migration but also in adhesion to the substrate (Small et al. 2002; da Silva and Dotti 2002). First, we quantified the morphology of the MN growth cones using a classification based on actin filament morphology: blunt (collapsed axonal end), filopodia and lamellipodia (Khazaei et al. 2014). The treatment of hiPSC derived MNs with 60 nM of NCALD-ASO69 led to a significant reduction of the number of blunt growth cones and an increase in filopodia and lamellipodial terminal ends, emphasizing that NCALD reduction has a positive impact in growth cone dynamics and decreases the number of neurons with defective axonal outgrowth. As previously mentioned, actin cytoskeleton dynamics are the driving force for neurite extension towards the target, but microtubules are required for maintenance of the axonal elongation and the speed of growth (da Silva and Dotti 2002). During axonal growth, microtubules in the central domain of the growth cone are spread and grow fast, whereas in slow growing axons they form loops, which could lead to the formation of new branches or reorganization into a new axon (Dent and Kalil 2001). In the present work, microtubule morphology was categorized according to the shape in the central domain of the growth cone: bundled (characterized by thin static microtubules), spread or

looped (Berghuis et al. 2007). Excitingly, *NCALD*-ASO69 treatment resulted in significant increase of spread and looped conformations in both healthy and SMA type I hiPSC derived MNs compared to CTRL-ASO treated MN cultures, which goes in line with the findings on actin morphology.

These results are surprising taking into account that no additional SMN-enhancing treatment was administered to the cultures, meaning that the effect observed is due to *NCALD* reduction solely. In addition, this data strongly supports the protective role of *NCALD* reduction at the NMJ level observed in the mouse model.

4.2.3.2 *NCALD*-ASO69 has an impact in neuronal activity

Neuronal activity is crucial for the formation and maintenance of neuronal circuits by shaping synaptic function and axonal plasticity, which contributes to the health of the MNs. Consequently, its imbalance significantly adds to the development of neurodegenerative disorders like ALS and SMA (Simon et al. 2021). Decrease neuronal firing rate is one SMA hallmark which not only affects MNs but the overall neuronal circuits for motor control (Fletcher et al. 2017; Tharaneetharan et al. 2021; Simon et al. 2021; Jablonka et al. 2007), strongly suggesting that an increase in neuronal activity is essential to counteract the progressive neurodegeneration. Indeed, pharmacological increase of neuronal activity has shown neuroprotective effects in ALS (Saxena et al. 2013; Baczyk et al. 2020).

Here, we wanted to determine if *NCALD*-ASO69 treatment alone enhances spontaneous activity of hiPSC derived MNs from healthy and SMA lines. Neuronal activity from hiPSCs derived MN cultures was measured using the multielectrode array. As expected, SMA MNs exhibited reduced spontaneous neuronal activity at day 20 of the differentiation when compared to healthy MNs. Moreover, pharmacological *NCALD* reduction had a significant increase in parameters associated with neuronal activity such as spike count, burst count and percentage of spikes in a burst in SMA and healthy MNs. Moreover, the time between bursts was significantly reduced for the SMA type I line upon *NCALD*-ASO69 treatment. Interestingly, the healthy line WTC11 and the SMA type I line HGK1 line responded better to the treatment than MNs from HUVEC and CS32iSMA. These data emphasize the importance of integrating hiPSC models in the preclinical studies, since hiPSC derived from patients represent the full array of human genetic variability.

In conclusion, *NCALD* reduction in hiPSC derived MNs increases neuronal activity, and supports the results obtained in the preclinical study, where the combination of SMN-ASO and *Ncald*-ASO ameliorate electrophysiological defects in SMA mice.

4.3 Future outlook

To summarize, these are the key findings of the present study:

1) Combinatorial therapy using *SMN*-ASO and *Chp1*-ASO does not ameliorate SMA hallmarks at PND21; 2) Re-injection of *Chp1*-ASO in adult animals does not ameliorate SMA hallmarks at 2 months of age; 3) Re-injection of *Ncald*-ASO in adult animals prolongs amelioration of electrophysiological defects and NMJ denervation in SMA mice; 4) Treatment of hiPSC derived MNs with *NCALD*-ASO69 had an impact in growth cone morphology and increased neuronal activity. Importantly, these findings open new research opportunities:

1) We developed *Chp1*-ASOs that significantly downregulate *CHP1* and cause cerebellar ataxia at certain concentrations, resembling the genetically induced ataxia phenotype. These *Chp1*-ASOs can be used to pharmacologically induce cerebellar ataxia in mice. This could be an interesting approach for future therapeutic studies and to better understand the biology of Purkinje neurons.

2) The re-injections with *Ncald*-ASO helped to maintain the therapeutic effect observed at PND21 by Torres-Benito and collaborators. *NCALD* reduction together with *SMN* enhancement exert a synergistic effect over time. Importantly, *NCALD* protein levels in spinal cord decrease naturally, reaching 50% of reduction at 6 months of age when compared to levels at PND4. Next step would be to test several re-injections of *Ncald*-ASO over time to assess the therapeutic effect for longer period and to determine until when *NCALD* reduction is required to ameliorate SMA phenotype.

3) We studied electrophysiology of the gastrocnemius muscle and NMJs of the transversus abdominis. To have a better insight into the therapeutic effect of *NCALD* reduction, more muscles should be analyzed. In addition, it is suggested that testing compounds in different mouse models, for example the Taiwanese mouse model (used here) and the SMA delta7 mouse, might help to better translate preclinical results to the clinics by incorporating genetic diversity.

4) In line with the previous point, multiple hiPSC derived from patients can be used to determine the therapeutic effect of a compound, incorporating genetic diversity of the “real clinical world”. Thus, increasing the number of hiPSC derived MNs lines treated with *NCALD*-ASO69 would give us a better understanding of the therapeutic potential of *NCALD* reduction.

5) The generation of NMJs on a dish from hiPSC SMA lines, to resemble the motor unit affected in SMA, is a critical next step in the testing of *NCALD*-ASO69 therapy, since *NCALD* reduction seems to play such a critical role in NMJ integrity and functionality.

6) The short-term effect and stability of the designed MOE gapmer ASOs suggests that further optimization of the ASOs may be required in order to effectively prolong the therapeutic effect without needing re-injection.

7) Neurodegenerative disorders often share common pathogenic pathways. Endocytosis and actin dynamics have been shown to be defective in SMA and ALS (Burk and Pasterkamp 2019; Theunissen et al. 2021). It would be of great interest to test if NCALD reduction acts protective across-diseases, for example in ALS, as it has been proven for PLS3, acting protective against SMA and ataxia (Janzen et al. 2019).

5. MATERIALS AND METHODS

5.1 Materials

5.1.1 Laboratory equipment

Instrument	Notation	Manufacturer
Analytical balance	AX2202M	Ohaus
Analytical balance (fine scale)	ARJ 120-4M	Kern
Bioruptor – sonication system	Ultrasonic waterbath 2510 UCD 200	Branson Diagenode
Cell incubators	Heracell™ 150 MCO-170AICUVH	Heraeus PHCBI
Cell culture hood	Herasafe™ KS12	Heraeus
Cell culture shaker for EBs	Mini KM CO2-FL	Edmund Bühler GmbH
Centrifuges	AllegraX22-R 5415R	Beckmann Coulter Eppendorf
Cryostat	CM3050 S	Leica
<u>Electrophoresis chambers</u>		
Agarose gels	MGV-620T SGE-020-02 E-H6	C.B.S & Scientific C.B.S & Scientific Febicon
SDS-PAGE gels	Mini-Protean 3 cell	Bio-Rad
Embedding module	EG1150 H	Leica
Fiber optic light source	KL 1500 LCD	Leica
Gel documentation	Chemidoc MP ChemiDoc XRS	Bio-Rad Bio-Rad
Heating block	Univertemp MT 100	Universal Labortechnik
Heating magnetic stirrer	MR 3001	Heidolph
Horizontal shaker	3011	GFL
Homogenizer	Precellys 24	Peqlab
<u>Microscopes</u>	Axioskop2 AxioImager.M2 Apotome DMIL CKX53 Thunder	Zeiss Zeiss Zeiss Leica Olympus Leica
Microtom	RM2	Leica
Microwave	R-898 (AL)-A	Sharp
Multi-electrode array	MW-HS-20065	Multichannel systems
Neubauer chamber	1100000	LO Laboroptik Ltd
pH meter	inoLab pH Level	WTW
Photometer	Biophotometer NanoDrop 1000	Eppendorf Peqlab

	NanoDrop One	ThermoScientific
Pipettes	2.5/10/200/1000/5000 µl Research Pro (10 µl) Pipete boy 2	Eppendorf Eppendorf Integra Biosciences
Power Supplies	PowerPac™ Basic/HC/1000	Bio-Rad
Rotating wheel	LD 79	Kisker Biotech
Roller mixer	SRT9 RM5	Stuart Hartenstein
Scale	EW 6000-1M Analytical balance (fine)	Beckman Coulter Sartorius
Thermocyclers	C1000 Touch S1000	Bio-Rad Bio-Rad
Tissue processor	ASP300	Leica
Vacuum pump	PM126040-026.3	Biometra
Vortex	444-1372	VWR
Water bath	1083	GFL
<u>Western blot</u> Blotting paper Glasplates Membrane	550 g/m ² 0.75 mm Nitrocellulose	Hartenstein Bio-Rad GE Healthcare

5.1.2 Mouse work equipment

Instrument	Notation	Manufacturer
Beam-walking device	customized	Central Workshop, Biocenter Cologne
Disposal scalpel	147210	Hartenstein
Ear tags	1005-1	National Band & Tag Co.
Ear tag applicator	1005-s1	National Band & Tag Co.
Electrophysiology device	UltraPro S100	Natus Neurology
EP-1 Econo pump	7318142	Bio-Rad
Forceps	BD047R FM002R Dumont #55	Aesculap Aesculap Fine Science Tools
Grip Strength Meter	303500-M/SEN	TSE System
Heating pad	Comfort 10W 76084	Terra Exotica Trixie
<u>Injection needles</u> 30 gauge, Ø-A: 0,31 mm, pst 4 Glass needle	HAMI7803-07 customized	Hamilton Biocenter Cologne
Microdrill	Cordless MicroDrill	KF Technology
Microliter syringe (5 µl)	75 N SYR	Hamilton
Minutien pins	26002-10	Fine Science Tools
Operating scissors	FD012R BC 321 R	Fine Science Tools Aesculap

	BC 341 R	Aesculap
Silicone elastomer	761036-5EA	Sigma-Aldrich
Stereotactic device	DKI940 DKI936 DK5000	Bilaney

5.1.3 Chemicals

Chemical	Manufacturer
2- β -Mercaptoethanol (99 %, p.a.)	AppliChem
2-Propanol (≥ 99.5 %)	AppliChem
Acetic acid	AppliChem
Acetone	AppliChem
Agarose	Sigma-Aldrich
Bovine Serum Albumin (BSA)	Sigma-Aldrich
Bradford solution	AppliChem
Bromphenol blue	AppliChem
Citrate	AppliChem
Coomassie Brilliant Blue R-250	AppliChem
Dimethylpolysiloxane	Sigma-Aldrich
Dimethyl sulfoxide (DMSO)	Sigma-Aldrich
Eosin Y (acidic)	Sigma-Aldrich
Ethanol (≥ 99.5 %, p.a.)	AppliChem
Ethidium bromide (1 % in H ₂ O)	AppliChem
Ethylenediaminetetratic acid (EDTA)	AppliChem
Glycerol (86%, p.a)	AppliChem
Glycine	AppliChem
Hematoxyline	Sigma-Aldrich
Hydrochloric acid (37 %)	AppliChem
Hydroxymethylaminoethane (Tris)	AppliChem
Methanol (≥ 99.9 %, p.a.)	AppliChem
Milk powder (low fat)	AppliChem
Mowiol	Sigma-Aldrich
Paraformaldehyde (PFA)	Sigma-Aldrich
Phenol Red	Sigma-Aldrich
Ponceau S	Sigma-Aldrich
Sodium chloride (p.a.)	AppliChem
Sodium dodecyl sulfate (SDS)	AppliChem
Sucrose	AppliChem
TBE buffer (10 x)	AppliChem
Tetramethylenediamine (TEMED)	AppliChem

Triton X-100	AppliChem
Trizma base	Sigma-Aldrich
Tween-20	AppliChem
Water (HPLC grade)	Sigma-Aldrich

5.1.4 Reagents

5.1.4.1 Reagents used for molecular biology

Reagent	Manufacturer
Ammoniumpersulfate (APS) (AquaPlus Mix)	AppliChem
AquaPlus Mix (40%) (29:1) Acrylamide	AppliChem
Complete Mini Protease Inhibitors	Roche
Cytoseal™ XYL	Thermo Scientific
dNTPs	AppliChem
DNA ladder 2-log (100 bp/ 10 kb)	New England Biolabs
DNA Loading dye	New England Biolabs
Page Ruler Prestained Protein Ladder	Thermo Fisher Scientific
PBS (10 x)	Roche
Prolong Gold antifade reagent with DAPI	Thermo Fisher Scientific
Restore Western Blot Stripping Buffer	Thermo Fisher Scientific
RIPA buffer	Sigma-Aldrich
Super Signal West Pico ECL Substrate	Thermo Fisher Scientific

5.1.4.2 Cell culture reagents, media and plates

Reagent	Manufacturer
1x PBS Dulbecco, w/o Ca ²⁺ , Mg ²⁺	Thermo Fisher Scientific
StemPro™ Accutase™	Thermo Fisher Scientific
Amphotericin B	Thermo Fisher Scientific
Ascorbic acid	Appllichem
B-27 Supplement without vit. A (50 x)	Thermo Fisher Scientific
b-mercaptoethanol	Thermo Fisher Scientific
Brain derived neurotrophic factor (BDNF)	Peprtech
<u>Cell culture plates</u>	
TC-Plate (6 well, 12 well, 24 well)	Sarstedt
TC-Flasks (25 cm ² and 75 cm ² mL)	
25 cm ² / 75 cm ² Flask Ultra-low attachment surface 3815	Corning
24 wells with 12 gold electrodes (electrode Ø 100 µm, electrode spacing 700 µm)	Multichannel systems
35 mm Grid-500 Glass Bottom 81168	Ibidi

Ciliary neurotrophic factor (CNTF)	Peprotech
CHIR99021	Tocris
Collagenase IV	Thermo Fisher Scientific
DAPT	Tocris
DMEM (+ 4.5 g/L D-Glucose, + L-Glutamine, + Pyruvate)	Thermo Fisher Scientific
DMEM/F12 GlutaMAX™	Thermo Fisher Scientific
Essential 6 medium	Thermo Fisher Scientific
F-127	Thermo Fisher Scientific
Fetal calf serum (FCS)	Biochrom AG
Fluo-4, AM	Thermo Fisher Scientific
Glial cell-line derived neurotrophic factor (GDNF)	Peprotech
Horse Serum (HS)	Biochrom AG
KO serum replacement	Thermo Fisher Scientific
Laminin L2020	Sigma-Aldrich
LDN193189	Selleckchem
Lipofectamine® 3000	Thermo Fisher Scientific
Matrigel® matrix hESC-qualified	Corning
mTeSR™1 basal medium	Stemcell Technologies
mTeSR™1 5x supplement	Stemcell Technologies
mTeSR™ Plus	Stemcell Technologies
mTeSR™ Plus 5x supplement	Stemcell Technologies
N2 supplement 100X	Thermo Fisher Scientific
Neurobasal® Medium (1 x) (#21103049)	Thermo Fisher Scientific
OptiMEM® (1 x) (#31985)	Thermo Fisher Scientific
Pasteur glass pipettes	
Penicillin/Streptomycin	Thermo Fisher Scientific
Poly-D-lysine	AppliChem
Poly-L-ornithine	Sigma-Aldrich
Retinoic acid	Sigma-Aldrich
SB431542	Tocris
Smoothened agonist SAG	Merck millipore
Tergazyme®	Alconox
Trypan Blue	Bio-Rad
Trypsin/EDTA	Thermo Fisher Scientific
Trypsin	Worthington
Y27632 (Rock inhibitor)	Selleckchem

5.1.5 Kits

Name	Manufacturer
Vectastain ABC	Vector Laboratories

5.1.6 Enzymes

Enzyme Name	Manufacturer
DNA Polymerase, OneTaq® Quick-Load® Master Mix	New England Biolabs
Proteinase K	AppliChem

5.1.7 Primary antibodies and staining reagents

Dilutions are indicated for each application: westernblot (WB) or immunofluorescence (IF).

Antibody name	Host species/dilution	Manufacturer/catalog #
Anti-ACTB, HRP-conjugated	Mouse - WB 1:10,000	Proteintech; HRP-60008
Anti-ACTB	Mouse - WB 1:10,000	Sigma-Aldrich; A5316
Anti-BASSOON	Mouse – IF 1:200	Enzo Life Science, ADI-VAM-PS003-F
Anti-Calbindin-D28k	Mouse - IF 1:250	Swant; CB300
Anti-ChAT	Goat - IF 1:100	Millipore; AB144P
Anti-CHP1	Rabbit - WB 1:1000; IF 1:100	Thermo Fisher Scientific; PA5-29876
Anti-ISL1	Mouse - WB 1:500; IF 1:20	Hybridoma Bank 39.4D5
Anti-NCALD	Rabbit - WB 1:1000; IF 1:100	Proteintech; 12925-1-AP
Anti-Neurofilament (NF-L), NF	Rabbit - IF 1:250	Cell Signaling; C28E10
Anti-OCT 3/4	Mouse - IF 1:200	Santa Cruz, sc-5279
Anti-PSD95	Mouse – IF 1:200	Biologend
Anti-SMN	Mouse - WB 1:3000, IF 1:250	BD Biosciences; 610646
Anti-SOX2	Mouse - IF 1:200	Santa Cruz, sc-365823
Anti-SV2	Mouse - IF 1:250	Hybridoma Bank; AB2315387
Anti-TUJ1	Rabbit - IF 1:200	Abcam ab18207
Anti-VGLUT1	Rabbit - IF 1:100	Synaptic Systems; 135303
Anti-PSD95	Mouse – IF 1:200	Biologend

5.1.8 Secondary antibodies

Dilutions are indicated for each application: westernblot (WB) or immunofluorescence (IF).

Antibody/Staining name	Host species/dilution	Manufacturer/catalog #
anti-mouse IgG, HRP-conjugated	goat; WB 1:5000	Dianova; 115-035-146
anti-rabbit IgG, HRP-conjugated	goat; WB 1:5000	Cell Signaling; 7074

anti-mouse IgG, AlexaFluor488-conjugated	goat; IF 1:300	Thermo Fisher Scientific; A11001
anti-mouse IgG, AlexaFluor647-conjugated	donkey; IF 1:300	Thermo Fisher Scientific; A31571
anti-rabbit IgG, AlexaFluor488-conjugated	donkey; IF 1:300	Thermo Fisher Scientific; A21206
anti-rabbit IgG, AlexaFluor568-conjugated	donkey; IF 1:300	Thermo Fisher Scientific; A10042
anti-rabbit IgG, AlexaFluor647-conjugated	goat; IF 1:300	Thermo Fisher Scientific; A32733
anti-goat IgG, AlexaFluor568-conjugated	donkey; IF 1:300	Thermo Fisher Scientific; A11057
Bungarotoxin, AlexaFluor555 (BTX)	IF 1:2000	Thermo Fisher Scientific; B35451
Phalloidin, AlexaFluor568	IF 1:100	Thermo Fisher Scientific; A12380

5.1.9 Eukaryotic cell lines

5.1.9.1 PC12 cells

PC12 were first established from a transplantable rat adrenal pheochromocytoma that can undergo neuronal differentiation when treated with nerve growth factor (NGF). Differentiation upon NGF treatment induces branching of neuronal-like processes. *Chp1*-KO PC12 cells were generated in our Lab by Dr. SM Hosseinibarkooie and M. Scharte using CRISPR/Cas8 genome editing tool (Scharte, 2018 thesis).

5.1.9.2 Primary murine embryonic fibroblasts (MEFs)

Primary murine embryonic fibroblast used in this study were isolated from wild type and *Chp1^{vac/vac}* embryos at embryonic day 12.5-13.5, by Dr. Eva Janzen during her doctoral thesis and were cryopreserved in liquid nitrogen.

5.1.9.3 hiPSCs

All hiPSCs lines used in this study were generated by others and/or purchased in different iPSC Core facilities: HUVEC hiPSC line comes from a healthy donor and was a generous gift from the Kurial Lab (Panopoulos et al. 2011). WTC11 line was generated by the Conklin Lab and purchased from Erasmus MC iPSC Core Facility. CS13iSMA and CS32iSMA were purchased from Cedars Sinai iPSC Core Facility. HGK1, HGK4a, HGK13, HGK22, HGK27 were generated in our lab by Dr. Ludwig Heesen (Heesen et al. 2016) and Dr. Garbes (Garbes et al. 2013).

Table 1. hiPSC lines

Cell line	Phenotype	SMN1/SMN2 copies	Sex	Age at sampling	Reprogrammed
HUVEC	Healthy	2/2	male	fetal	Retrovirus
WTC11	Healthy	2/2	male	30 years	Episomal plasmid
HGK1	SMA type I	0/2	female	6 months	Retrovirus
CS32iSMA	SMA type I	0/2	male	7 months	Episomal plasmid
HGK4a	SMA type II	0/3	male	10 years	Retrovirus
CS13iSMA	SMA type II	0/3	male	3 years	Episomal plasmid
HGK13	SMA type III	0/3	male	18 years	Retrovirus
HGK27	SMA type IIIb	0/4	male	26 years	Sendai virus

5.1.10 Mouse inbred strains

A detailed description of the mouse lines is given in section X. For the present study, the following inbred mouse strains were used:

- The Taiwanese SMA mouse model FVB.Cg-Tg(SMN2)2Hung *Smn*^{tm1Hung}/J, purchased from Jackson Laboratory (stock number 005058). We backcrossed this line for > 7 generations with wild type C57BL6/N to obtain a congenic SMA mouse line in C57BL6/N background (Ackermann et al. 2013). An intermediate mouse model was produced by crossing *Smn*^{ko/ko}; *SMN2*^{tg/tg} female on FVB/N background with *Smn*^{ko/wt} male on C57BL6/N background to obtain both SMA (*Smn*^{ko/ko}; *SMN2*^{tg/0}) and the healthy heterozygous (HET) (*Smn*^{ko/wt}; *SMN2*^{tg/0}) mixed 50 litters (50% FVB/N: 50% C57BL6/N) (Riessland et al. 2017). For the experiments, in order to generate SMA mice with a milder phenotype, a suboptimal dose of 30 µg *SMN*-ASO was injected subcutaneously (s.c.) in the skin fold of the neck at PND1 using a microliter syringe (Hamilton) (Hosseinibarkooie et al. 2016).
- For ASO leads testing we used the wild type FVB mouse line.
- To obtain MEFs without CHP1 protein expression, we used the *vacillator* mouse model (B6.Cg-CHP1vac) (Liu et al. 2013).

5.1.11 Solutions and media

5.1.11.1 Routinely used solutions

If not mentioned otherwise, all solutions were stored at room temperature (RT).

Solution name	Composition
Ammonium persulfate (APS)	1% (w/v) in deionized H ₂ O, storage at -20°C
Blocking solution for Western blot	6% (w/v) Milk powder (low fat) in TBS-T
Citrate buffer (for 1 L)	2.1 g Citrate (0.01 M), ad ddH ₂ O to 1 L → adjust pH 6.0
Laemmli buffer (3x)	2.4 ml Tris (1 M, pH 6.8), 3 ml SDS (20%), 3 ml Glycerol, 1.6 ml 2-β-Mercaptoethanol, 0.006 g Bromophenol blue, store at 4°C
Paraformaldehyde	4% (w/v) Paraformaldehyde in 1x PBS (pH 7.4), Paraformaldehyde was solubilized with 1 M NaOH and heating (60°C), aliquoted and stored at -20°C
Ponceau S staining solution	1% (w/v) Ponceau S, 2% (v/v) ml Acetic acid in ddH ₂ O
SDS Electrophoresis buffer (10x, for 1 L)	30.29 g Trizma base, 144.13 g Glycin, 10 g SDS, ad ddH ₂ O to 1000 ml
Resolving gel for SDS PAGE (12%, for 10 ml)	4.85 ml ddH ₂ O, 2.55 ml AquaPlus Mix (29:1) Acrylamide, 2.6 ml Tris (1.5 M, pH 8.8), 0.1 ml SDS (10%), 0.1 ml APS (10%), 40 µl TEMED
Stacking gel for SDS PAGE (5 %, for 4 ml)	2.96 ml ddH ₂ O, 0.52 ml AquaPlus Mix (29:1) Acrylamide, 0.52 ml Tris (1 M, pH 6.8), 40 µl SDS (10%), 40 µl APS (10%), 4 µl TEMED
Tail lysis buffer (for 500 ml)	5 ml EDTA (0.5 M), 20 ml NaCl (5 M), 5 ml SDS (20%), 50 ml Tris/HCl (1 M, pH 8.5), ad ddH ₂ O to 500 ml → adjust pH 7.4, add 200 µg/ml Proteinase K (fresh)
TBS (10x, for 1 L)	12.1 g Tris (0.1 M), 87.7 g NaCl (1.5 M) ad ddH ₂ O to 1 L, adjust pH 7.6 (HCl)
TBS-T (for 5 L)	12.1 g Tris (20 mM), 40 g NaCl (137 Mm), 25 ml Tween 20 (0.5%), in ddH ₂ O → adjust pH 7.56 (HCl)
TE ⁻⁴ buffer (for 100 ml)	1 ml Tris (1 M, pH 8.0), 20 µl EDTA (0.5 M, pH 8.0), ddH ₂ O to 100 ml, add 50 µg/ml RNase A (fresh), stored at 4°C
Transfer buffer (for 2 L)	4.84 g Trizma base, 22.52 g Glycin, 400 ml Methanol, add ddH ₂ O up to 2000 ml

5.1.11.2 Cell culture media

All cell culture media were stored at 4°C for short-term use and at -20°C for long-term storage.

Name	Composition
MEFs culture media	500 ml DMEM, 50 ml FCS (10%), 5 ml Pen/Strep (10 U/ml), 1.25 ml Amphotericin B (250 µg/ml)
PC12 culture media	500 ml DMEM GlutaMAX™, 25 ml FCS (5%), 50 ml HS (10%), 5 ml Pen/Strep, 1.25 ml Amphotericin B
PC12 freezing media	90% PC12 culture media, 10% DMSO → filter

EB formation media	Essential 6, 1% Pen/Strep (10 U/ml), Rock-Inhibitor 10 μ M
Basal motor neuron differentiating media from hiPSC (1L)	500 ml Neurobasal®Medium, 500 ml DMEM/F12 Glutamax, 20 ml B-27 supp. without vit. A (50x), 10 ml N2 supp. (100X), 1 ml b-mercaptoethanol, 500 μ l ascorbic acid (1 mM), 5 ml Pen/Strep (10 U/ml)
hiPSCs pluripotent media	mTeSR1 400 ml + mTeSR supp. (5x) 100 ml, 5 ml Pen/Strep (10 U/ml)
hiPSCs pluripotent media plus	mTeSR Plus 400 ml + mTeSR plus supp. (5x) 100 ml, 5 ml Pen/Strep (10 U/ml)
hiPSCs freezing media	50% KO- serum replacement, 40% KO-DMEM, 10% DMSO, 10 μ M Rock inhibitor
NPCs freezing media	90% KO-serum replacement, 10% DMSO

5.1.12 Primers for genotyping

Primer sequences were designed using SeqBuilder software and purchased from Integrated DNA Technologies (IDT). Lyophilized stocks were reconstituted at a concentration of 100 pmol/ μ l and subsequently diluted to working solutions at a concentration of 10 pmol/ μ l.

Application	Name	Sequence (5' - 3')	Amplicon length [bp]	Annealing temp.
<i>Smn</i> Genotyping	Smn rev	AGCCTGAAGAACGAGATCAGC	KO: 950 WT: 1050	59°C
	Smn WT fw	ATAACACCACCACTCTTACTC		
	Smn KO fw	GTAGCCGTGATGCCATTGTCA		

5.1.13 Antisense oligonucleotides

Antisense oligonucleotides (ASOs) were provided within a collaboration from IONIS Pharmaceuticals (Carlsbad, USA) as lyophilized or diluted stocks. For lyophilized stock preparation, the ASO was resuspended in sterile 1x PBS and the concentration was determined by absorbance measurement at an OD of 260 nm and calculated using Lambert-Beer's law with the following equation: $(A_{260} * \text{dilution factor} * \text{molecular weight}) / (\text{extinction coefficient} * \text{path length} * 1000) = \text{ASO concentration [mg/ml]}$.

5.1.13.1 Antisense oligonucleotides for *in vivo* injections

For *in vivo* injections, lyophilized *SMN*-ASO targeting *SMN2* was reconstituted to a final 10 μ g/ μ l solution in sterile 1x PBS and verified photometrically. The same day of the *in vivo* treatment, concentration was confirmed photometrically. Lyophilized *Chp1*-ASOs and Ctrl-ASO stocks were reconstituted in a range of concentrations (10 – 100 μ g/ μ l) for the dosage testing. Lyophilized *Ncald*-ASO was reconstituted at a final working solution of 100 μ g/ μ l. All the ASOs were aliquoted and stored at -20°C until use.

Table 2. Human and murine ASOs provided by Ionis Pharmaceuticals, for *in vivo* experiments.

Name	IONIS #	Target	Sequence	MW (Da)	Chemistry
SMN-ASO	387954	SMN2	ATTCACCTTCATAATGCTGG	7925,02	Uniform MOE, PS
Chp1-ASO1	1113746	Chp1	GGACAATCTAATTCTTTAGG	7122,83	5-10-5 MOE gapmer w/mixed backbone
Chp1-ASO2	1113751	Chp1	ATTCAGAGTTTTGTGCGAAA	7148,83	5-10-5 MOE gapmer w/mixed backbone
Chp1-ASO3	1113816	Chp1	CCGTAGTTCCTGTACTCCT	7056,84	5-10-5 MOE gapmer w/mixed backbone
Chp1-ASO4	1113826	Chp1	GCATAGTATTAACAGGCAC	7139,88	5-10-5 MOE gapmer w/mixed backbone
Ncald-ASO	673756	Ncald	GTGGTTCTTGTTTTACAGGA	7146,8	5-10-5 MOE gapmer w/mixed backbone
CTRL-ASO i.c.v	676626		GTTTTCAAATACACCTTCAT	7045,82	5-10-5 MOE gapmer w/mixed backbone
CTRL-ASO systemic	141923		CCTTCCCTGAAGGTTCTCC	7152,26	MOE-gapmer, phosphorothioate backbone

5.1.13.2 Antisense oligonucleotides for *in vitro* experiments

For *in vitro* treatment of the hiPSCs derived MNs, ASO concentrations were measured making a dilution of 10:1 in TE pH 8.0 and reading the absorbance at 260 nm. Beer's Law was used to calculate the concentration as follows: $(A_{260} * \text{Dilution factor}) / (\text{extinction coefficient}) = \text{concentration in mM}$. Working solutions were diluted in sterile water to obtain an approximate concentration of 100 μM . All the ASOs were aliquoted and stored at -20°C until use. ASOs were again measured before *in vitro* treatment.

Table 3. Human ASOs provided by Ionis Pharmaceuticals, for *in vitro* experiments.

Name	IONIS #	Target	Sequence	MW (Da)	Chemistry
CHP1-ASO57	1113157	CHP1	AGTGAATTAAGGGTGA	5502,58	kkk-10-kkk
CHP1-ASO59	1113159	CHP1	GTTTATCAAGGTGTTT	5424,53	kkk-10-kkk
CHP1-ASO84	1113084	CHP1	ATATTAGGCACTCCG	5405,58	kkk-10-kkk
NCALD-ASO55	1113355	NCALD	GACAGATATGACTTCC	5414,59	kkk-10-kkk
NCALD-ASO69	1113369	NCALD	CACATAGATTAACCA	5391,61	kkk-10-kkk
NCALD-ASO89	1113389	NCALD	TCTTTTTGGTCTACCA	5362,54	kkk-10-kkk
CTRL-ASO	549144		GGCCAATACGCCGTCA	5428,62	kkk-10-kkk

5.1.14 Software Packages and internet databases

Software	Provider
BioRender	https://biorender.com/
EndNote	Thomson Reuters
Fiji/ImageJ	Open Source
GraphPad Prism	GraphPad Software
Image Lab	Bio-Rad
Microsoft Office	Microsoft
Mausoleum software	Mausoleum
ZEN	Zeiss
Ensembl	http://www.ensembl.org
GeneCards	http://www.genecards.com
NCBI	http://www.ncbi.nlm.nih.gov
OMIM	http://www.ncbi.nlm.nih.gov/omim
SeqBuilder	Dnastar

5.2 Methods

5.2.1 Nucleic acid methods

5.2.1.1 Isolation of DNA from mouse tissue biopsies

In order to perform standard genotyping of the mice, tail or ear tissue samples were lysed in tail lysis buffer freshly supplemented with proteinase K (200 µg/ml) at 55°C overnight until it was completely dissolved. Next, the resultant tissue suspension was centrifuged for 5 min at maximum speed (16,200 x g) to pellet the cells and debris. To precipitate the DNA, the supernatant was then transferred to a new 1.5 ml Eppendorf tube with 500 µl isopropanol, well mixed and centrifuged for 10 min at maximum speed. Supernatant was discarded and DNA pellet was washed with 500 µl of 70% ethanol to remove residual salt and centrifuged again for 5 min at maximum speed. Ethanol was removed and pellets were dried for 10 min in a vacuum concentrator and subsequently resuspended in 80-100 µl of TE⁴⁺ RNase for 1h at 37°C. 1 µl of the isolated DNA was used for genotyping PCR.

5.2.1.2 Polymerase chain reaction (PCR)

To amplify specific DNA fragments for genotyping purpose, the polymerase chain reaction (PCR) was applied. The amplification of a DNA sequence is based on an enzymatic reaction using gene-specific forward and reverse primers flanking the fragment of interest. A thermostable DNA polymerase called *Thermophilusaquaticus* (Taq) DNA polymerase, which synthesizes DNA in 5'-3' direction, is responsible of the DNA amplification. A standard PCR cycle program and the standard PCR reaction composition are listed in (Table 4 and Table 5). For genotyping PCR, the OneTaq Quick-Load Master mix (New England Biolabs) already containing Taq DNA polymerase, dNTPs, MgCl₂, and reaction buffer was used. PCR products were separated and visualized on an agarose gel.

Table 4: Standard thermocycler PCR program.

Step	Duration	Temperature [°C]
1. Initial denaturation	5 min	95
2. Denaturation	30 sec	95
3. Primer annealing	30 sec	Primer dependent, here 53-60°C
4. Elongation	1 min per 1 kb	72
Repeat steps 2-4 for 35x		
5. Final elongation	10 min	72
Cooling	∞	4

Table 5: Components and volumes of genotyping PCR.

	Genotyping PCR
Components	Volume [μl]
10x PCR buffer	10 μl OneTaq Quick-Load Master mix
100 mM of dNTP	
MgCl ₂	
Taq polymerase	
ddH ₂ O	7
Primer fw (10 pmol)	1
Primer rev (10 pmol)	1
Template DNA	1

5.2.1.3 Agarose gel electrophoresis

Agarose gel electrophoresis was used to separate the DNA fragments according to their size by applying an electrical field. DNA is negatively charged thanks to its phosphate backbone, and migrates towards the positively charged pole in the electric field. Routinely, 1.5% agarose gels were prepared by solving the corresponding amounts of agarose in 1x TBE buffer and heating it up in a microwave. When the solution was completely dissolved and cooled down to approximately 50-60 °C, ethidium bromide was added to a final concentration of 1 µg/ml. Next, the solution was poured into a gel chamber with well combs to create pockets to load the PCR product samples, and left to solidify. After complete polymerization of the agarose, the gel was covered with 1x TBE, the combs were removed and PCR samples (with loading dye already included) were loaded into the wells. Time for gel running was 20-30 min at 100-120 V and the separated bands were detected with the ChemiDoc XRS Imaging System (Bio-Rad).

5.2.2 Protein biochemistry methods

All experimental procedures with proteins were carried at 4°C, since proteins tend to degrade and aggregate at high temperatures. Proteins were routinely isolated with RIPA buffer (Sigma-Aldrich) containing protease inhibitors (PIC) to block protease activity.

5.2.2.1 Isolation of proteins from tissues

First, tissue samples were snap-frozen using dry ice immediately after collection, and either processed directly or storage at -80°C. For protein isolation, frozen tissue samples were transferred to 2 ml reaction tubes filled ceramic beads (Peqlab) and an appropriate amount of RIPA buffer and homogenized using the Precellys24 device (Peqlab), for 25 sec at 5500 rpm. Next, the samples were incubated for 10 min on ice followed by a centrifugation step of 20 min at maximum speed at 4°C. The supernatant was collected and the samples were sonicated for 10 min in a water bath at 4 °C. After a final centrifugation step of 20 min at full speed at 4°C, the supernatant was collected in a new Eppendorf tube. Protein lysates were stored at -80°C.

5.2.2.2 Isolation of proteins from cells

For protein isolation from cultured cells, cells were washed with 1x PBS (MEFs and PC12 cells) or KO-DMEM in the case of MN derived from hiPSCs, and an appropriate amount of RIPA buffer supplemented with protease inhibitor was added (usually 60-80 µl were used to lyse one well of a 6-well plate). Cells were collected using cell scrapers, transferred to Eppendorf tubes and subsequently sonicated for 10 min in a water bath. Next, the cell lysate suspension was centrifuged for 20 min at 4°C

at the maximum speed of 16,200x g and the supernatant with soluble proteins was collected and aliquoted into new reaction tubes. Protein lysates were stored at -80°C until usage.

5.2.2.3 Determination of protein concentration with Bradford

Protein concentrations from both tissue and cells were determined by spectrophotometry using the Bradford assay. This colorimetric assay is based on protein binding to the dye Coomassie Brilliant Blue G-250 resulting in a shift of its absorption from 465 nm (red form of the dye) to 595 nm (blue form of the dye). For this assay, the BioPhotometer (Eppendorf) was calibrated using a standard curve of BSA dilutions (0.5-5 µg). Then, 1 µl of the protein lysate was mixed with 499 µl Bradford solution (AppliChem) and incubated for 10 min at room temperature. Sample concentration was determined by measuring the absorption at 595 nm and referring the measured values to the BSA standard curve.

5.2.2.4 Sodium dodecyl polyacrylamide gel electrophoresis (SDS-PAGE)

Sodium dodecyl polyacrylamide gel electrophoresis (SDS-PAGE) was routinely conducted in order to separate proteins according to their molecular weight (MW). Upon heat denaturation in the presence of the reducing compound β-Mercaptoethanol, the SDS detergent (present in Laemmli buffer and polyacrylamide (PAA) gel) binds to the hydrophobic regions of the proteins conferring them a negative charge. Thus, all proteins are separated according to their size independently of their intrinsic charge: low mass proteins travel faster through the gel than those with higher mass. To prepare samples for SDS-PAGE, protein lysates (usually 10-20 µg) were mixed with 3x Laemmli buffer and denatured for 5 min at 95°C.

Discontinuous SDS-PAGE gels were prepared using two different types of agarose in order to generate two phases, the stacking gel and the separating gel. The upper stacking gel (pH 6.8) has a 5% of acrylamide, generating bigger pores that will allow the proteins to easily migrate and concentrate at the border between the two phases of the gel. The lower separating gel (pH 8.8), has a higher acrylamide content (usually 12%) and forms smaller pores that will slow the migration of large mass proteins, that remain in the upper regions of the separating gel, whereas low mass proteins easily migrate to the bottom, separating the protein samples by MW.

The SDS-PAGE gel was located in the electrophoresis container with 1x electrophoresis buffer and the denatured protein lysates were loaded into the wells of the stacking gel. In the lateral well, 10 µl of the protein ladder PAGE Ruler Plus (Thermo Fisher Scientific) was additionally loaded to estimate the relative protein size. Gel Electrophoresis was performed at an initial voltage of 70 V for about 30 min and subsequently increased to 100 V.

5.2.2.5 Western Blot

After SDS-PAGE protein separation, we performed wet blotting to transfer the proteins to a nitrocellulose membrane using a Bio-Rad system. Once the proteins are immobilized on the membrane, specific antibodies can be used for the detection. For protein transfer, the components were equilibrated in transfer buffer (section 5.1.11.1) and arranged in the following order: (negative cathode) a sponge pad, a filter paper, the gel containing the separated proteins, the nitrocellulose membrane, another filter paper, and a sponge pad (positive anode). All components were fixed and covered with transfer buffer inside the transfer chamber. A cooling device was also included in the transfer chamber to prevent overheating. The protein transfer was performed at 4°C at 30 V overnight or at 110 V for 2h. Protein will migrate in the electric field from the cathode due to their negative charge, and will adhere to the membrane by forming hydrophobic interactions. Immediately after the transfer, Ponceau S staining was carried out for 30 seconds to assess the success of the transfer and the equal loading. This compound is an azo-dye that reversibly binds to positively charged amino acid side-chains. To remove the dye to further proceed with the analysis, the membrane was incubated with TBS-T buffer on a shaker for 5 until the red stain was gone (~ 5 min).

5.2.2.6 Detection of proteins on Western blot membranes

First, to avoid non-specific binding to free epitopes, the membrane was blocked for 1h in 6% not fat milk in TBS-T. In order to specifically detect a protein of interest, western blot membrane was incubated with the appropriate concentration of primary antibodies diluted in 2.5% milk overnight at 4°C. Next day, the membrane was washed 3x for 10 min with TBS-T and incubated with the right concentration of secondary antibody conjugated with horseradish peroxidase (HRP) in 2.5% milk at room temperature. The secondary antibody is directed against the species from which the primary antibody was derived. Afterwards, the membrane was washed 3x 10 min with TBS-T and incubated in an enhanced chemiluminescent Substrate for HRP (Super Signal West Pico Chemiluminescent Substrate (Thermo Fisher Scientific) in a 1:1 ratio: Luminol Enhancer Solution + Stable Peroxide Solution for 1-5 min. The enhancer solution contains H₂O₂ and luminol that will be oxidized by the HRP present in the secondary antibodies, thereby generating luminescence that can be detected using the ChemiDoc XRS Imaging System from Bio-Rad. All primary and secondary antibodies with the respective dilutions are listed in section 5.1.7 and 5.1.8, respectively.

In order to detect multiple proteins on the same membrane using different antibodies, the membrane was incubated in Restore Western Blot Stripping Buffer (Thermo Fisher Scientific) for 15-30 min, followed by a wash step with TBS-T. Finally, the membrane can be blocked again with 6% milk in TBS-T for 1h and the same procedure as described above can be followed for a different antibody.

5.2.3 Cell culture

All cell culture procedures were conducted in a laminar flow tissue culture work bench to keep sterile conditions. In order to prevent contamination, cell culture media were supplemented with antibiotics and anti-fungal agents (the last one only for MEFs and PC12 cells), including penicillin, streptomycin and amphotericin B. All cells kept in sterile incubators at 37°C and 5% CO₂ atmosphere. All media was pre-warmed at 37°C before being added to the cells.

5.2.3.1 MEFs and PC12 cells

Murine embryonic fibroblasts (MEFs) were cultured in DMEM supplemented with 10% fetal calf serum (FCS). PC12 cells were grown in DMEM GlutaMAX supplemented with 10% horse serum (HS) and 5% FCS. When confluency reached 80-100%, cells were passaged following this steps: first, old medium was removed and cells were washed with 1x PBS. Trypsin/EDTA for 5 min at 37°C was used for trypsinization, allowing cells to detach from the plate. Enzymatic activity of the peptidase was blocked by applying an equal volume of fresh culture media. Single cells were either transferred to a new flask/plate in a lower density or cryo-conserve.

5.2.3.2 hiPSCs culture

Human iPSCs were routinely cultured in feeder-free conditions using mTeSR1 pluripotent media supplemented with Pen/Strep. On the first day, hiPSCs were seeded in 6-well cell culture plates coated with Matrigel™ using mTeSR1 supplemented with 10 μM Rock inhibitor (Rho kinase inhibitor, Y-27632) to enhance the survival of dissociated cells after passaging or cryopreservation. Every day cells were washed with pre-warmed PBS 1x and fresh pluripotent media (without Rock inhibitor) was added. When cells were 80-90% confluent, were either passaged to a new plate in lower density, cryopreserved or used to start a new MN differentiation. For passage and cryopreservation, cells were treated for 5 min at 37°C with Accutase® which is a cell dissociation reagent with proteolytic and collagenolytic enzymes that allow single cell dissociation. After detachment, reaction was stopped by adding 2x the volume of pre-warmed KO-DMEM media and gently resuspended. Cell suspension was subsequently centrifuged for 3 minutes at 300 x g, the supernatant was discarded and cells were resuspended in the desired media: mTeSR1+Rock inhibitor for passaging or KO-SR+KO-DMEM+DMSO for cryopreservation.

5.2.3.3 hiPSCs differentiation into MNs

We established in our lab a protocol described in (Guo et al. 2017) and added some modifications to differentiate hiPSCs into spinal MNs. When a 6-well of hiPSCs was at 80-90% confluence, cells were washed with 1x PBS and similar size squares (1-2 mm) were generated using a flame-modified Pasteur glass pipette in order to generate the clumps for embryoid body formation. Next, cells were again washed with 1x PBS to remove the floating cells generated during the square formation. Subsequently, hiPSCs were treated with 1ml Collagenase type IV (3 mg/ml) diluted in KO-DMEM media and incubated until detachment of the clumps at 37°C. To block Collagenase IV activity, PBS was added and the solution with the clumps was gently transferred to a 15 ml Falcon tube. After 1 minute, clumps went to the bottom of the flask, and the supernatant was aspirated. Clumps were gently resuspended in EB formation media containing Essential™6 medium supplemented with 10 µM Rock inhibitor and transferred to ultra-low attachment flasks on an horizontal shaker (40 rpm) in the incubator at 37°C, this will be day 0 of the differentiation. Essential™6 medium does not contain bFGF thereby enabling embryoid body formation and directed differentiation. The first two days of the differentiation, neuronal basal medium (DMEM/F12 Glutamax and Neurobasal supplemented with N2 and B27 without vitamin A) was supplemented with 3 µM CHIR99021 (4423, Tocris Bioscience), 0.2 µM LDN-193189 (S2618, Selleckchem), 40 µg SB431542 (1614, Tocris Bioscience), and 5 µM Y-27632 (S1049, Selleckchem). From day 3 on, neuronal basal media was supplemented with 0.1 µM retinoic acid (Sigma) and 500 nM SAG (Merck Millipore). From day 8 on until the end of the differentiation BDNF (10 ng/ml, Peprotech) and GDNF (10 ng/ml, Peprotech) were added to the media. From day 9 to 11 neuronal media was supplemented with 10 µM DAPT (2634, Tocris Bioscience), and from day 12-16 with 20 µM DAPT. Until day 11 included, 100 % media was changed every day. On day 11, clumps with MN progenitors were dissociated into single cells for plating on 20 µg/ml laminin coated wells. Every day, 50% of the media was changed and new 50% of the media was added. From day 17 on, maturation media containing exclusively 10 ng/ml of BDNF, GDNF and CNTF (Peprotech) was added. Every other day media were changed by replacing half of the medium.

Embryoid bodies (EBs) dissociation represents a critical point in the MN differentiation, since many cells die during the process because the EBs are very robust, therefore not all the differentiations will give the same amount of neuronal progenitors (between 5×10^6 – 30×10^6 cells). The EB dissociation protocol consist in:

1. Collect the EBs into a 15 ml falcon tube.
2. Centrifugation for 5 min at 50 x g.
3. Resuspend EBs in 1x PBS and centrifuge again for 5 min at 50 x g.

4. Resuspend the pellet in 1ml Accutase[®] using a p1000 and incubate in the water bath 37°C for ~15 mins. Gently mechanical dissociation can be applied using the p1000, every 4 minutes during the incubation with the Accutase[®]. To avoid long time enzymatic treatments, cells can be gently resuspended and wait for 1 minute until the big clumps sediment at the bottom of the falcon tube and the single cells can be collected from the supernatant.
5. Transfer single cells to a new 15ml falcon tube and block Accutase[®] activity with KO-DMEM supplemented with 10 μ M Rock inhibitor.
6. Count cells using TrypanBlue 1:1 ratio.
7. Centrifuge desired amount for plating or cryopreservation.
8. For plating, resuspend the pellet in MN media day 11.

5.2.3.4 Cell counting

In order to be consistent with the cell number in the experiments, cells were counted and seeded at the desired densities. After enzymatic treatment, cells were resuspended in the corresponding media. Trypan Blue diazo dye was used to quantify cell viability since it only interacts with the cells when membranes are damaged. To count the cells, 10 μ l of cell suspension suspension was transferred to a Neubauer counting chamber. The mean cell number of the four squares was determined by microscopy, multiplied by two because of the Trypan Blue dilution and subsequently multiplied by 1×10^4 to obtain the cell number per ml.

5.2.3.5 Cryo-conservation of cells

For long term storage, cells were processed for cryo-conservation. For that purpose, single cells obtained after their respective enzymatic treatment were centrifuged at 300 x g for 10 min. The cell pellet was resuspended in their respective freezing medium (5.1.11.2), filled into cryotubes and transferred into a cryo-container that will cool down at a rate of -1°C/min in the -80°C freezer. On the next day, cells were stored in the liquid nitrogen tank.

5.2.3.6 Antisense oligonucleotide treatments

Treatment with the ASOs was performed in two ways: free-uptake or using a lipid-based transfection reagent.

5.2.3.6.1 Free-uptake

cEt-ASOs can enter the cells via 'free-uptake' without the need of a delivery reagent that is mediated through dependent endocytic mechanisms. Its internalization depends on the ability of the ASO to bind

the membrane-associated proteins (Linnane et al. 2019). A total of 1.2×10^6 cells were plated in a 6-well plate. For free-uptake treatment of the hiPSCs derived MNs, different concentrations of ASOs (50nM-300nM) were diluted in the MN media at differentiation day 13. Protein lysates were collected 7 days after transfection using RIPA buffer supplemented with PIC.

5.2.3.6.2 Lipofectamine 3000

Cells were plated in a density of 1.2×10^6 cells in 6-well. Next, cells were transfected at day 13 with different concentration of ASOs using Lipofectamine 3000 transfection reagent. Routinely, the transfection was performed according to the manufacturer's protocol. In each well, a total of 3 μ l Lipofectamine 3000 was used for each transfection reaction. Cell lysates were collected 2 or 7 days after transfection.

5.2.3.7 Multielectrode array

Electrophysiological recordings of the hiPSCs derived MNs were measured at day 20 of the differentiation with a multi-electrode array (Multichannels System) using a 24 well plate containing 12 gold electrodes per well. Plates were coated as previously described using Poly-L-ornithine and 20 μ g/ml laminin. At day 11 of the differentiation, after EBs dissociation, a total of 100.000 cells were seeded in each well, diluted in 60 μ L of MN media day 11. Cells were left to settle for 2h before adding 1 mL of the corresponding MN media, in an incubator at 37°C and 5% CO₂. On day 13 of the differentiation, MNs were treated with 60nM CTRL-ASO or *NCALD*-ASO using Lipofectamine 3000. Importantly, measurements at day 20 of the differentiation were taken before media change, since addition of fresh media transiently alters the electrophysiological properties of the MNs. Before each recording, the plate was left for 2 minutes on the recorder. Experimental recordings took place in a non-humidifier incubator at 37°C for 3 minutes. Data acquisition and analysis was performed with the Multi-Channel Suite software (Multichannels system) applying the following parameters: threshold for spike detection $\pm 10 \mu$ V, band pass filter with 100 Hz and 3kHz cut-off frequencies. In order to detect the spikes, an adaptive threshold at 5.5 times the standard deviation of the estimated noise on each electrode was set. Three independent differentiations per line were taken into account for the statistical analysis.

5.2.4 Laboratory mice work

All animals used in this study were housed in the mouse facility of either the Institute of Genetics Cologne or the Center for Molecular Medicine Cologne (University of Cologne). All mouse experiments were approved by the local animal protection committee of the "Landesamt für Natur, Umwelt and

Verbraucherschutz" of Northrhine Westfalia (LANUV NRW) under the reference number: 81–02.04.2019.A138 and 84-02.04.2014.A242.

5.2.4.1 SMA mice: Taiwanese SMA mouse model

The severe Taiwanese SMA mouse model (FVB.Cg-Tg(SMN2)2Hung *Smn*^{1tmHung/J}; stock number 005058) was originally purchased from Jackson laboratory. This model was generated by replacing the exon 7 of the murine *Smn* gene with a hypoxanthine phosphoribosyl-transferase (HPRT) selection cassette, while the rest of the locus remained intact. In contrast to humans, mice only possess one *Smn* gene, thus *Smn* full knockout is embryonically lethal. In order to generate a viable SMA mouse model, two tandem copies of the human *SMN2* transgene were introduced using a bacterial artificial chromosome (BAC) into the *Smn*^{ko/ko} background. The resulting homozygous *Smn*^{ko/ko}; *SMN2*^{tg/tg} mice carry in total four *SMN2* copies. Life span and fertility of the homozygous animals is not compromised, however they develop ear and tail necrosis within a few weeks of life (Hsieh-Li et al. 2000). Purchased homozygous SMA Taiwanese mice were originally on congenic FVB/N background. In the past, we backcrossed the Taiwanese SMA mice > 7 generations to obtain also the model on congenic C57BL6/N background since we know that the background of the animals has a strong effect on the phenotypic outcome. For our experimental breeding, homozygous females on FVB/N background were crossed with male C57BL6/N *Smn*^{ko/wt} to generate the mixed₅₀ SMA mice. This breeding results in a F1 offspring of ~50% severe SMA (*Smn*^{ko/ko}; *SMN2*^{tg/0}) mice and the corresponding healthy HET (*Smn*^{ko/wt}; *SMN2*^{tg/0}) were generated.

5.2.4.2 Subcutaneous injection of antisense oligonucleotides (ASOs)

The *SMN*-ASO (Hua et al. 2011) was prepared as described at a working solution of 10 µg/µl in sterile 1x PBS. In order to generate SMA mice with an intermediate SMA phenotype, *SMN*-ASO was injected subcutaneously (s.c.) at a suboptimal dose of 30 µg on PND1 (Riessland et al. 2017). The s.c. injections were administered in the skin fold of the neck using a microliter syringe. All animals from the offspring of the experimental breeding scheme were injected.

5.2.4.3 i.c.v. injections of ASOs

The blood brain barrier limits the access to the CNS, therefore, administration of therapeutic compounds directly in the CNS system can improve the treatment of neurodegenerative disorders like SMA. In the present study, both neonatal and adult mice received i.c.v. injections with various concentrations of CTRL-ASO, *Chp1*-ASOs or *Ncald*-ASOs.

5.2.4.3.1 i.c.v. injections in neonatal mice

The following protocol is based on the work by (Glascock et al. 2011). Before i.c.v. injection, 30 mins before the cryoanesthesia animals were injected with Buprenorphin (0,025 mg/kg of body weight). Next, local anesthesia was achieved by applying Bupivacain to the skin of the scalp. PND2 pups were immobilized via cryo-anesthesia for 1-2 minutes. Customized glass needles were used for ASO administration. Once the animal was immobilized, the skin of the head was firmly pressed with the left hand. The skin of the neonatal mice is almost transparent, thus the injection point was determined by using the anatomical vascular structures as a guide: perpendicular to the skull surface and 0.25 mm lateral from the sagittal suture and 0.5 mm rostral to the coronary suture, close to the confluence of the sinuses (Figure 47). In total, 1.5 μ l of the respective ASO were injected (1 μ l of ASO and 0.5 μ l of trypan blue). After removing the needle, a bit of pressure was applied in order to avoid possible bleeding. Neonatal mice were monitored for signs of distress for 5 minutes before returning them to the cage.

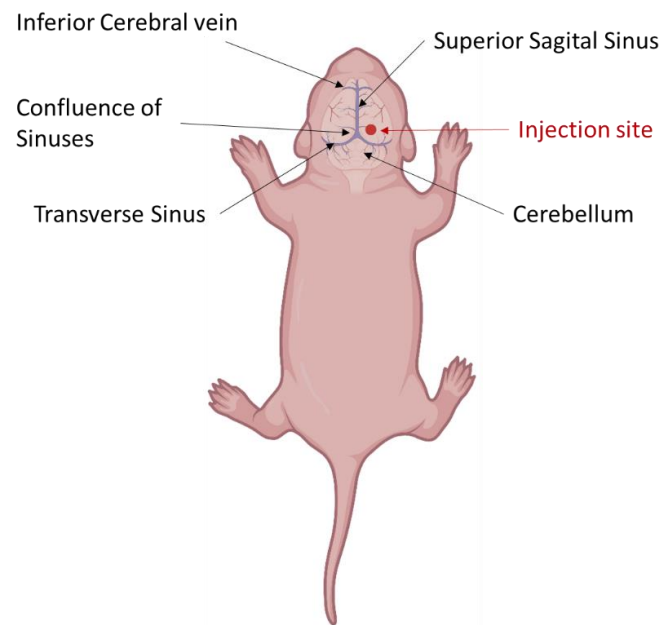


Figure 47. Graphical scheme for neonatal i.c.v. injection.

Neonatal i.c.v. injection of *Chp1*-ASO or *Ncald*-ASO is performed between the confluence of the sinuses marked with a red dot.

5.2.4.3.2 i.c.v. bolus injection in adult mice

Animals were anesthetized using Ketamine (Ketaset 100 mg/ml, Wirtschaftsgenossenschaft deutscher Tierärzte)/Xylazine (2%, Serumwerk Bernburg AG, Bernburg) and placed and fixed in a stereotaxic

instrument (Bilaney) with mouse adaptor and micropositioner (Figure 48). To keep body temperature during all the procedure, a thermostatic warming plate was used. Skin of the head was then sterilized using a cotton pad embedded in EtOH, and a clean cut was performed with a scalpel. Next, injection coordinates were determined from the mouse bregma (for HET: X = 1 mm, Y = 0.3 mm; for SMA X = 0.980 mm, Y = 0.250 mm; in all the Z = range between -1.6 mm and -1.7 mm) (Figure 48) (DeVos and Miller 2013). To drill a hole in the skull we used a microdrill (burr size: 0.8 mm, KF Technology). Finally, a total of 5 μ l of ASO was delivered in different concentrations at a rate of 1 μ l/30 s.

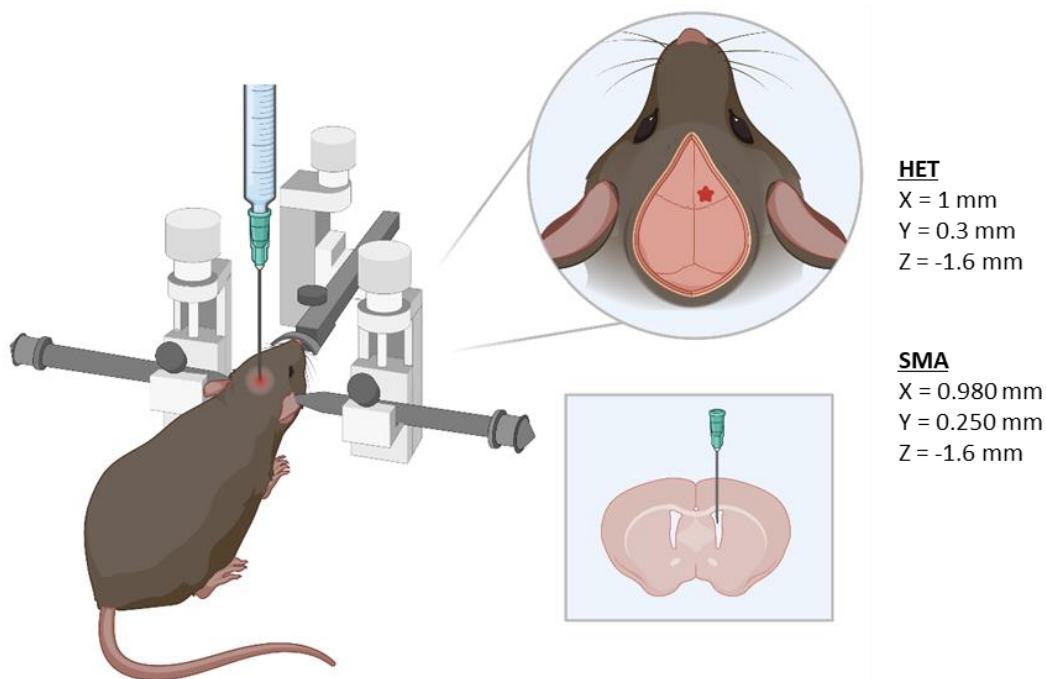


Figure 48. Graphical representation of the i.c.v. bolus injection in adult animals.

Animals are anesthetized and fixed in a stereotaxic equipment. The area on top of the head is sterilized with ethanol 70%. With a surgical scalpel, we performed a small incision of about 1 cm. With the needle already fixed in the equipment, we give the right coordinates to aim the lateral ventricle, and we mark the incision point. We drill a hole using a micro-drill. Previous to the injection, the area is cleaned with PBS to remove small particles of bone. The needle is carefully introduced until the desired Z coordinate. Speed of ASO injection is more or less 1 μ l/30 seconds.

5.2.4.4 Compound muscle action potential (CMAP) and motor unit number estimation (MUNE) measurements in mice

CMAP and MUNE are electrophysiological measures used *in vivo* to monitor the functional status of the motor unit pool, especially relevant in SMA where motor axonal loss occurs. First, mice were anesthetized with inhaled isoflurane (5% induction, 1.5-2% maintenance and 1 L per minute O₂ flow rate). Body temperature was always maintained at 37°C with a thermostatic warming plate. For recordings, sensory needle electrodes (28 gauge, recording area active 2.0 mm²) were used. Upon

supramaximal sciatic nerve stimulation, CMAP response of the gastrocnemius muscle can be recorded as described previously (Arnold et al. 2014; Arnold et al. 2015; Bogdanik et al. 2015). The active (E1) electrode was placed subcutaneously at the proximal region of the *gastrocnemius* muscle of the right hind limb. The reference electrode (E2) was positioned at the metatarsal region of the foot of the same limb. For sciatic nerve stimulation, two insulated monopolar needle electrodes (28 gauge, 0.25 mm diameter) were used: the anode was placed over the sacrum and the cathode was positioned at the sciatic notch, both subcutaneously. The sciatic nerve was stimulated with square-wave pulses of 0.1 ms durations and <10 mA intensity, until the responding CMAP amplitude was saturated (supramaximal). The average CMAP response (peak-to-peak) was determined from six repetitively recorded CMAP responses, for each mouse.

MUNE was calculated as described (Arnold et al. 2015). First, the average single motor unit potential (SMUP) was determined. For that purpose, the initial incremental response (between 0.3 and 0.7 mA) and nine additional increments were recorded by gradually increasing the stimulus intensities. The measured amplitude difference of two subsequent increments was at least 25 μ V. Finally, MUNE was determined the following:

Calculate the single SMUP

SMUP 1= peak-to-peak amplitude of increment 1

SMUP 2= (peak-to-peak amplitude of increment 2) – (peak-to-peak amplitude of increment 1)

Average SMUP and divide by the total number of increments

Calculate MUNE by dividing the maximal CMAP amplitude by the average SMUP

MUNE= CMAP/average SMUP

5.2.4.5 The beam-walking assay

Motor coordination and balance of *Chp1*-ASOs injected mice was measured using the beam-walking assay, in order to detect if *Chp1*-ASO animals displayed an ataxic gait. This test was originally developed to analyze rodent gait, which allows the detection of motor deficits caused by motor cortex injury (Feeney, Gonzalez, and Law 1982) and is proven to be more sensitive than the rotarod test (Stanley et al. 2005). First, mice were trained for a short time period to walk along a ruler (60 cm long, 3 cm wide and 30 cm elevated) towards a goal box. Next, for the experiment, mice were placed on the beam (50 cm long, 8 mm diameter and 30 cm elevated) and the time the mouse needed to cross until the goal

box was measured. In total, three trials were performed for each mouse. The test was first performed on 3-weeks-old and 6-weeks-old mice.

5.2.4.6 Preparation of mouse tissue and organs

For routinely performed tissue and organ collection, mice were sacrificed at PND14, PND21, PND28, 6-weeks or 8-weeks of age by cervical dislocation or with carbon dioxide in an isolated chamber.

Immediately after sacrifice, the mouse head was removed by decapitation with scissors, and the skull was opened in order to isolate the brain. For protein, it was subdivided in the two hemispheres.

The TVA muscle was isolated as described in (Murray et al. 2008). In order to open the mouse, the skin of the abdominal wall was carefully cut from the lower abdomen up to the chest of the animal and gently detached from the muscles by pulling it to the sides. Once the abdominal wall was exposed, a small cut above the bladder was generated, followed by a circular scission towards the laterals of the mouse and going up to the ribcage. Then, the diaphragm was cut and the abdominal muscles together with the ribcage were transferred to a silgard-filled Petri dish and covered with 1x PBS. The abdominal muscles were stretched using forceps and minuten pins and subsequently fixed for 20 min with 4% PFA. In order to study the TVA muscle, the external oblique and internal oblique muscle layers covering the TVA were carefully removed, and the TVA muscle in close proximity to the ribcage was cut and stored in 1x PBS at 4°C until immunohistochemical processing (Section 5.2.5.2).

Next, liver and tibialis anterior and gastrocnemius muscles were isolated. The collected tissues were either snap-frozen on dry ice for protein isolation or placed in embedding chambers and fixed overnight in 4% PFA for paraffin sectioning and stainings (section 5.2.5.5).

Finally, the spinal cord was isolated from the vertebral column by pushing it out manually in the case of the P14 animals, or with the help of a syringe flushing out 1x PBS for older mice. The spinal cord was either directly snap-frozen for protein isolation or fixed overnight in 4% PFA for subsequent cryo-sectioning and stainings (Section 5.2.5.3).

5.2.4.7 Transcardial perfusion of mice

Transcardial perfusion is a way to euthanize the animals that allows organ structure preservation and blood removal for paraffin- or cryo-sectioning. First of all, mice were anesthetized using 0.1 ml/10 g Ketamine/Xylazine solution in 0.9% NaCl. As soon as the animal reached the surgical plane of anesthesia, it was fixed on a styrofoam plate and the abdomen and the diaphragm were cut. Next, the rib cage was carefully opened and fixed to the sides to expose the heart and the lungs. Subsequently,

the tip of a 27 gauge needle connected with a tube to the perfusion pump was carefully introduced in the left ventricle of the beating heart. Additionally, a small hole was made in the atrium of the right ventricle using a 20 gauge needle. Initially, 1x PBS was pumped through the body with a steady flow of 10 ml/min, allowing the removal of the blood from the organs. The color of the tongue was used as an indicator for blood clearance. Next, 4% PFA solution was applied to the pump before the heart stopped beating, thus the organs are fixed. After perfusion, the mouse brain was carefully isolated. The head was removed by decapitation and the skull was cleared of residual muscle tissue and laterally cut on both sides. Finally, the lid of the skull was removed and the exposed brain was carefully collected and transferred into 4% PFA solution for further fixation overnight at 4°C. Afterwards, the brain was processed either for paraffin-sectioning (Section 5.2.5.5).

5.2.5 Histological methods

For all immunohistological staining, a humid dark chamber was routinely used.

5.2.5.1 Immunofluorescent staining of cells

Immunofluorescent stainings of cells were conducted using a standard protocol. First, cells were washed with 1x PBS in the case of hiPSCs and PC12 cells or KO-DMEM for MNs derived from hiPSCs to avoid detachment of the cells. Next, hiPSCs and PC12 cells were fixed in 4% PFA, and MNs were fixed with 4% PFA supplemented with 4% sucrose to preserve dendritic and axonal structures for 10-15 min at room temperature. After fixation, cells were washed 3x with 1x PBS and permeabilized in 1x PBS containing 0.2% Tween20 (PBS-T) for 20 min. Subsequently, cells were blocked for 1h in blocking solution (PBS-T with 5% BSA and 5% FCS, filtered) in order to avoid nonspecific antibody binding. Primary antibodies were diluted in blocking solution and fixated cells were incubated overnight at 4°C. On the next day, cells were washed 3x with 1x PBS, and incubated with the secondary fluorescent antibodies diluted in blocking solution for 1h at room temperature. To stain F-actin, conjugated Phalloidin was used at the same time as the secondary fluorescent antibodies. Afterwards, cells were again washed 3x with 1x PBS. Finally, coverslips were mounted with ProLong antifade reagent with DAPI to stain nuclei, on microscope slides. The stainings were stored at 4°C until imaging. All primary and secondary antibodies with the respective dilutions were listed in section 5.1.7 and 5.1.8

5.2.5.2 Immunofluorescent staining of the TVA

In order to analyze the NMJs, we performed the staining of TVA muscles. For this purpose, following fixation we pulled the abdominal muscles until we only had the TVA. Muscles were washed 3x with 1x PBS, permeabilized for 30 min with permeabilization solution (1x PBS containing 2% Triton X-100) and

blocked for 1h with filtered blocking solution (1x PBS supplemented with 1% Triton X-100, 5% BSA and 5% FCS) at room temperature. Next, TVAs were incubated overnight at 4°C with the primary antibody diluted in blocking solution. NF was used to visualize the presynaptic site and the nerve. On the next day, the muscles were washed 6x for 10 min with 1x PBS and subsequently stained with AlexaFluor555-conjugated Bungarotoxin (BTX) and the secondary fluorescent antibody at room temperature for 2h. BTX is a toxin derived from snakes that binds to the acetylcholine receptors and can be used when conjugated with a fluorophore to visualize the post-synapse of the NMJ. Afterwards, the muscles were washed 5x with 1x PBS, and mounted with Prolong Gold antifade reagent on microscope slides. Prolong Gold antifade reagent was used to conserve the fluorescent signal during long exposure times. The stainings were stored at 4°C until microscope imaging and analyses.

5.2.5.3 Immunofluorescent staining of spinal cord sections

For immunofluorescence stainings, the lumbar region was isolated from the spinal cords. In order to process the tissue for cryoprotection after fixation, spinal cords were washed with 1x PBS and incubated with 20% and 30% sucrose in 1x PBS at 4°C on the subsequent nights, respectively. Next, the samples were embedded in Tissue-Tec medium (Sakura) and immediately stored at -20°C. A cryostat device was used to cut 40 µm thick sections that were collected in a reaction tube and permeabilized in 1x PBS supplemented with 2% Triton X-100 for 30 min at room temperature on a rotating wheel. Then, the sections were blocked for 1h with blocking solution (1x PBS supplemented with 1% Triton X-100, 5% BSA and 5% FCS, filtered) at room temperature and incubated overnight on a rotating wheel at 4°C with primary antibodies diluted in blocking solution. Primary anti-ChAT and anti-VGLUT1 antibodies were used to allow the visualization of the MN soma and the glutamatergic synapses, respectively. On the next day, the sections were washed 5x 10 min with 1x PBS and incubated with the secondary fluorescent antibodies diluted in 1x PBS for 2h at room temperature on the rotating wheel. Afterwards, the sections were washed again 5x 10 min with 1x PBS, and mounted with Prolong Gold antifade reagent on microscope slides. The stainings were stored at 4°C until microscope imaging and analysis.

5.2.5.5 Hematoxylin and eosin staining of muscle paraffin sections

The Hematoxylin and eosin (H&E) staining is commonly used in histology: Hematoxylin stains the nuclei in dark blue and Eosin the cytoplasmic proteins in red/pink. We used this technique to determine the muscle fiber size from tibialis anterior and gastrocnemius muscle. For histological analysis, the tissues were processed as described in section 5.2.5.9. After overnight fixation, the tissue samples were dehydrated using a fully-enclosed tissue processor and embedded in paraffin using a heated paraffin

embedding module. Next, we cut 10 μm thick sections using a microtome. The staining of the paraffin sections was performed according to a standard H&E staining protocol listed in Table 4.

Table 6. H&E staining protocol.

Step	Procedure	Duration [min]
1.	Deparaffinization in Xylene	2x 15
Rehydration in EtOH series		
2.	100% EtOH	2
3.	96% EtOH	2
4.	70% EtOH	2
5.	1x PBS	1
6.	water	1
7.	Filtered Hematoxylin	6
8.	short rinse in water	
9.	water	15
10.	short rinse in ddH ₂ O	
11.	Eosin	1
12.	short rinse 6-7x in water	
Dehydration in EtOH series		
13.	70%	1
14.	96%	1
15.	100%	1
16.	Xylene	1
17.	Mounting in Cytoseal™ XYL mounting medium	

5.2.5.6 Immunostaining of cerebellum paraffin sections

To perform the immunostaining, paraffin-embedded sections were collected during sectioning on Superfrost Plus microscope slides (Thermo Fisher Scientific) to secure the attachment. The sections were first deparaffinized for 2x 15 min in Xylene and rehydrated using decreasing concentrations of EtOH for 1 min (2x 100% EtOH, 96% EtOH and 70% EtOH, respectively) followed by 10 min incubation in ddH₂O. Next, a retrieval step was performed to increase epitope accessibility by boiling the sections 3x in citrate buffer for 5 min at 600 W using a microwave. After, the sections were incubated in citrate buffer for 45 min at room temperature. Following antigen retrieval, the sections were washed for 5 min in 1x TBS and incubated for 1h in blocking solution (1x TBS supplemented with 1.5% goat serum) at room temperature. Next, the sections were washed 1x 5 min with 1x TBS and incubated overnight with anti-calbindin-D28k antibody diluted in blocking solution at 4°C. On the next day, sections were 3x washed for 5 min with 1x TBS. Sections were then incubated for 30 min at room temperature with

biotinylated secondary antibody diluted in blocking solution followed by 3x 5 min washes with 1x TBS. In order to couple avidin-conjugated peroxidase to the biotinylated secondary antibody, Vectastain Avidin-Biotin Complex (ABC) reagent was added and incubated for 30 min at room temperature. Subsequently, samples were washed (3x 5 min with TBS) and incubated with diaminobezidine (DAB) staining solution for 5 min at room temperature. The peroxidase oxidize DAB in the presence of H₂O₂ resulting in the production of a brown precipitate. Next, samples were rinsed for 5 min in water, followed by a 5 min wash with 1x TBS. Finally, the sections were rehydrated and mounted.

5.2.6 Microscopic image acquisition and analysis

All images were acquired using either the fluorescent AxioImager.M2 equipped with an AxioCam 503 mono camera and an ApoTome 2.0 (Zeiss) device for optical sectioning or the bright field microscope Axioskop2 with an AxioCam ICc1 camera (Zeiss).

5.2.6.1 NMJ analysis

In order to measure NMJ size and innervation, TVA muscle triangles were prepared as previously described in section 5.2.5.2. All images were acquired as z-stacks using the same exposure time and the 20x objective of the AxioImager.M2. Z-stacks of 10-20 slices at a 0.5 µm interval were acquired and analyzed using the maximum intensity projections of the z-stacks. For quantification purposes, only NMJs that were oriented parallel to the slide were considered. The NMJ area was determined using the Fiji software by applying the Li's Minimum Cross Entropy thresholding method. NMJ innervation was categorized according to the percentage of NF that innervates each end plate (BTX-positive). Equal or more than 80% was considered fully innervated, between 15% and 79% was counted as partially innervated and less than 15% denervated.

5.2.6.2 Proprioceptive inputs per MN soma

Spinal cord sectioning of the lumbar region and subsequent staining was performed as previously described in section 5.2.5.3. For the quantifications, z-stacks of 30-50 slices at a 0.5 µm interval were acquired using a fixed exposure time and the 40x objective of the AxioImager.M2. VGLUT1⁺ number per MN soma was analyzed using the Fiji 3D viewer extension and a customized macro developed by Peter Zentis (Imaging facility, CECAD). The macro splits the images into two channels, one for ChAT⁺ MN soma and another for VGLUT⁺ inputs to allow the following quantification. Next, the separated channel images were smoothed: for the ChAT⁺ image, each pixel was replaced with the median of its 6x6x4 neighborhood and an automatic background removal was performed by Li's Minimum Cross

Entropy thresholding method. For the VGLUT1⁺ image, each pixel was replaced with the median of its 16x16x16 neighborhood and the inputs were automatically segmented using the 3D simple segmentation function of the 3D ImageJ Suite (Ollion et al. 2013). Additionally, the following criteria were applied: the threshold intensity was obtained by applying the Otsu's threshold clustering algorithm to the stack histogram. Moreover, 20 voxel was considered as a minimum size criterion. After image preprocessing, the experimenter selected in the smoothed ChAT⁺ image single non-overlapping MN soma and drew the smallest possible cuboids around it. Further segmentation was performed automatically within the cuboids using the Otsu method to obtain input values for a 3D hysteresis thresholding. The resultant mask was widened by four voxels and holes within the mask were filled. After selection of all suitable MN somas within an image, the macro processed each 3D selection, again using functions of the 3D ImageJ suite. For the final quantification, first all VGLUT1⁺ inputs within the selection were determined. Finally, from this only those relevant for a given MN soma within 2 μm distance were calculated. Additionally, the MN surface area and the volume were determined.

5.2.6.3 Muscle fiber size analysis

The *tibialis anterior* and *gastrocnemius* muscle cross-sections were stained with an H&E staining as described in section 5.2.6.5. For this, the muscle fiber areas were delineated using the contour tool of the ZEN imaging software to quantify the area. In total, 100 muscle fibers per animal were quantified.

5.2.7 Experimental design

All offspring of each litter were blinded-injected and processed by randomized numbering. The experimenter was blinded regarding genotypes of the mice at all steps until final statistical analysis. Experimented was blinded regarding cell line genotypes during image acquisition, recordings and statistical analysis. We conducted all experiments at least in triplicates. All experiments with hiPSCs correspond to at least three independent differentiations, each of them with at least three technical replicates. Blinding was performed by randomized numbering by an independent person. To avoid pseudo replication, the mean value per animal and mean value of technical replicates was applied for statistical analysis.

5.2.8 Statistical Analysis

Statistical analysis was performed using the software programs MS Excel 2013 (Microsoft) and GraphPad Prism 9 (GraphPad Software). For the comparison of two means unpaired and paired two-tailed Student's t-test were applied for equal variances. To compare categories (NMJ innervation and

growth cone analysis) χ^2 test was performed, and for more than two comparisons, for normalization the p value was multiplied by the total number of comparisons. For multiple comparisons, we performed one-way ANOVA statistics tests with Tukey posthoc test. Mice survival was graphically represented by the Kaplan-Meier method applying a log-rank test. The following three levels of statistical significance were distinguished: *p <0.05, **p <0.01, and ***p <0.001. The figure legends depict the specific statistical test used, sample size and p-values, respectively.

5.3 Storage of materials and data

All data presented in this PhD thesis can be found in the server of the Institute of Human Genetics of Cologne: Institute>crypto>wall>AG wirth>Anixa

All cell lines used in the PhD thesis are kept in the liquid nitrogen tank of the Institute of Human Genetics, 4th floor, CMMC. In tower 12, in boxes labeled as “Anixa hiPSCs”, “Anixa hiPSCs 2”, “Anixa NPCs”.

All proteins and organs collected during this PhD thesis are kept in the -80°C freezer, 4th floor, CMMC, in boxes labelled as “Anixa Chp1-project” or “Anixa Ncald-project”

Images of muscles, spinal cord and NMJs from this thesis are stored in the hard-drive of the Institute of Human Genetics, which is kept by the Technical Assistant Roman Rombo.

6. PUBLICATIONS AND SCIENTIFIC COMMUNICATIONS

Publications

Muinos-Bühl A, Rombo R, Janzen E, Ling KK, Hupperich K, Rigo F, Bennet CF, Wirth B. 2022. Combinatorial ASO-mediated therapy with low dose SMN and the protective modifier Chp1 is not sufficient to ameliorate SMA pathology hallmarks. *Neurobiology of disease*. doi: 10.1016/j.nbd.2022.105795. Epub 2022 Jun 18.

Delle Vedove, A., Natarajan, J., Zanni, G., Eckenweiler, M., **Muinos-Bühl, A.**, Storbeck, M., Guillen Boixet, J., Barresi, S., Pizzi, S., Hölker, I., Körber, F., Franzmann, T., Bertini, E., Kirschner, J., Alberti, S., Tartaglia, M., Wirth, B. 2022. CAPRIN1P512L causes aberrant protein aggregation and associates with early-onset ataxia. *Cell. Mol. Life Sci.* 79, 526. <https://doi.org/10.1007/s00018-022-04544-3>

Muinos-Bühl A, Rombo R, Ling KK, Rigo F, Bennet CF, Wirth B. 2023. Long-term SMN- and Ncald-ASO combinatorial therapy in SMA mice and NCALD-ASO treatment in hiPSC-derived motoneurons. Manuscript in preparation

Fortuna, T., Kour, S., Chimata, A., **Muinos-Bühl, A.**, Anderson, E., Ward, C., Chauhan, O., O'Brian, C., Rajasundaram, D., Rajan, D., Wirth, B., Singh, A., Pandey, U.B. SMN regulates GEMIN5 expression via the Tudor domain and modulates GEMIN5-mediated disease. 2023. *Brain*. Under revision.

Oral presentation

RTG-NCA Retreat 2020 – Germany

Anixa Muinos-Bühl, Roman Rombo, Eva Janzen, Karen K. Ling, Frank Rigo, C. Frank Bennett, and Brunhilde Wirth. Molecular and therapeutical investigation of SMA modifiers

Human Genetics Symposium 2021 – Cologne (Germany)

Anixa Muinos-Bühl, Roman Rombo, Eva Janzen, Andrea Delle Vedove, Johanna Bihler, Karen K. Ling, Frank Rigo, C. Frank Bennett, and Brunhilde Wirth. Targeting SMA genetic modifiers with ASO based combinatorial therapies.

RTG-NCA Retreat 2022 – Germany

Anixa Muinos-Bühl, Roman Rombo, Andrea Delle Vedove, Karen K. Ling, Frank Rigo, C. Frank Bennett, and Brunhilde Wirth. Long-term SMN- and Ncald-ASO combinatorial therapy in SMA mice and NCALD-ASO treatment in hiPSC-derived motoneurons

Poster presentations

Cure SMA 2019 – Anaheim, CA (USA)

Anixa Muiños-Bühl, Karen K.Y. Ling, Frank Rigo, Min Jeong Kye, C. Frank Bennett, Brunhilde Wirth. SMN-ASO and CHP1-ASO combinatorial therapy in hiPSC derived motor neurons

Ernst Klenk symposium 2019 – Cologne (Germany)

A. Muiños-Bühl, E. Janzen, K. K. Ling, Hupperich, R. Rombo, F. Rigo, M. J. Kye, C. F. Bennett, B. Wirth. ASO-based combinatorial therapy aimed to increase SMN and decrease CHP1 in Spinal Muscular Atrophy

SMA Europe 2020 – Evry (France)

Anixa Muiños-Bühl, Eva Janzen, Karen K. Ling, Roman Rombo, Kristina Hupperich, Frank Rigo, Frank C. Bennett and Brunhilde Wirth. ASO-based combinatorial therapy in mice aimed to increase SMN and decrease CHP1 two protective genetic modifiers of SMA

Cure SMA 2021 – Online conference

Anixa Muiños-Bühl, Roman Rombo, Eva Janzen, Andrea Delle Vedove, Marlen Lauffer, Karen K. Ling, Frank Rigo, C. Frank Bennett, and Brunhilde Wirth. Targeting SMA genetic modifiers with ASO-based combinatorial therapies

CMMC Retreat 2021 – Cologne (Germany)

A. Muiños-Bühl, E. Janzen, K. K. Ling, Hupperich, R. Rombo, F. Rigo, M. J. Kye, C. F. Bennett, B. Wirth. Molecular and therapeutical investigation of SMA modifiers

SMA Europe 2022 – Barcelona (Spain)

Anixa Muiños-Bühl, Roman Rombo, Karen K. Ling, Frank Rigo, C. Frank Bennett, and Brunhilde Wirth. Long-term *SMN*- and *Ncald*-ASO combinatorial therapy in SMA mice and *NCALD*-ASO treatment in hiPSC-derived motorneurons

Awards

CMMC Annual Retreat 2021, Cologne (Germany) - Best poster award

7. REFERENCES

- Abati, E., A. Manini, G. P. Comi, and S. Corti. 2022. 'Inhibition of myostatin and related signaling pathways for the treatment of muscle atrophy in motor neuron diseases', *Cell Mol Life Sci*, 79: 374.
- Ackermann, B., S. Krober, L. Torres-Benito, A. Borgmann, M. Peters, S. M. Hosseini Barkooie, R. Tejero, M. Jakubik, J. Schreml, J. Milbradt, T. F. Wunderlich, M. Riessland, L. Tabares, and B. Wirth. 2013. 'Plastin 3 ameliorates spinal muscular atrophy via delayed axon pruning and improves neuromuscular junction functionality', *Hum Mol Genet*, 22: 1328-47.
- Al Dakhoul, S. 2017. 'Very severe spinal muscular atrophy (Type 0)', *Avicenna J Med*, 7: 32-33.
- Ames, J. B., and S. Lim. 2012. 'Molecular structure and target recognition of neuronal calcium sensor proteins', *Biochim Biophys Acta*, 1820: 1205-13.
- Ando, S., M. Funato, K. Ohuchi, S. Inagaki, A. Sato, J. Seki, C. Kawase, T. Saito, H. Nishio, S. Nakamura, M. Shimazawa, H. Kaneko, and H. Hara. 2019. 'The Protective Effects of Levetiracetam on a Human iPSCs-Derived Spinal Muscular Atrophy Model', *Neurochem Res*, 44: 1773-79.
- Ando, S., M. Funato, K. Ohuchi, T. Kameyama, S. Inagaki, J. Seki, C. Kawase, K. Tsuruma, M. Shimazawa, H. Kaneko, and H. Hara. 2017. 'Edaravone is a candidate agent for spinal muscular atrophy: In vitro analysis using a human induced pluripotent stem cells-derived disease model', *Eur J Pharmacol*, 814: 161-68.
- Andrade, J., S. T. Pearce, H. Zhao, and M. Barroso. 2004. 'Interactions among p22, glyceraldehyde-3-phosphate dehydrogenase and microtubules', *Biochem J*, 384: 327-36.
- Andreassi, C., C. Angelozzi, F. D. Tiziano, T. Vitali, E. De Vincenzi, A. Boninsegna, M. Villanova, E. Bertini, A. Pini, G. Neri, and C. Brahe. 2004. 'Phenylbutyrate increases SMN expression in vitro: relevance for treatment of spinal muscular atrophy', *Eur J Hum Genet*, 12: 59-65.
- Andrews, M. G., and A. R. Kriegstein. 2022. 'Challenges of Organoid Research', *Annu Rev Neurosci*, 45: 23-39.
- Arnold, W. D., P. N. Porensky, V. L. McGovern, C. C. Iyer, S. Duque, X. Li, K. Meyer, L. Schmelzer, B. K. Kaspar, S. J. Kolb, J. T. Kissel, and A. H. Burghes. 2014. 'Electrophysiological Biomarkers in Spinal Muscular Atrophy: Preclinical Proof of Concept', *Ann Clin Transl Neurol*, 1: 34-44.
- Arnold, W. D., K. A. Sheth, C. G. Wier, J. T. Kissel, A. H. Burghes, and S. J. Kolb. 2015. 'Electrophysiological Motor Unit Number Estimation (MUNE) Measuring Compound Muscle Action Potential (CMAP) in Mouse Hindlimb Muscles', *J Vis Exp*.
- Avila, A. M., B. G. Burnett, A. A. Taye, F. Gabanella, M. A. Knight, P. Hartenstein, Z. Cizman, N. A. Di Prospero, L. Pellizzoni, K. H. Fischbeck, and C. J. Sumner. 2007. 'Trichostatin A increases SMN expression and survival in a mouse model of spinal muscular atrophy', *J Clin Invest*, 117: 659-71.
- Baczyk, M., N. O. Alami, N. Delestree, C. Martinot, L. Tang, B. Commisso, D. Bayer, N. Doisne, W. Frankel, M. Manuel, F. Roselli, and D. Zytnicki. 2020. 'Synaptic restoration by cAMP/PKA drives activity-dependent neuroprotection to motoneurons in ALS', *J Exp Med*, 217.
- Baksheeva, V. E., P. O. Tsvetkov, A. O. Zalevsky, V. I. Vladimirov, N. V. Gorokhovets, D. V. Zinchenko, S. E. Permyakov, F. Devred, and E. Y. Zernii. 2022. 'Zinc Modulation of Neuronal Calcium Sensor Proteins: Three Modes of Interaction with Different Structural Outcomes', *Biomolecules*, 12.
- Baranello, G., B. T. Darras, J. W. Day, N. Deconinck, A. Klein, R. Masson, E. Mercuri, K. Rose, M. El-Khairi, M. Gerber, K. Gorni, O. Khwaja, H. Kletzl, R. S. Scalco, T. Seabrook, P. Fontoura, L. Servais, and Firefish Working Group. 2021. 'Risdiplam in Type 1 Spinal Muscular Atrophy', *N Engl J Med*, 384: 915-23.
- Baranello, G., K. Gorni, M. Daigl, A. Kotzeva, R. Evans, N. Hawkins, D. A. Scott, A. Mahajan, F. Muntoni, and L. Servais. 2021. 'Prognostic Factors and Treatment-Effect Modifiers in Spinal Muscular Atrophy', *Clin Pharmacol Ther*, 110: 1435-54.
- Barroso, M. R., K. K. Bernd, N. D. DeWitt, A. Chang, K. Mills, and E. S. Sztul. 1996. 'A novel Ca²⁺-binding protein, p22, is required for constitutive membrane traffic', *J Biol Chem*, 271: 10183-7.

- Battaglia, G., A. Princivalle, F. Forti, C. Lizier, and M. Zeviani. 1997. 'Expression of the SMN gene, the spinal muscular atrophy determining gene, in the mammalian central nervous system', *Hum Mol Genet*, 6: 1961-71.
- Ben-Shushan, E., E. Feldman, and B. E. Reubinoff. 2015. 'Notch signaling regulates motor neuron differentiation of human embryonic stem cells', *Stem Cells*, 33: 403-15.
- Bennett, C. F., A. R. Krainer, and D. W. Cleveland. 2019. 'Antisense Oligonucleotide Therapies for Neurodegenerative Diseases', *Annu Rev Neurosci*, 42: 385-406.
- Berghuis, P., A. M. Rajnicek, Y. M. Morozov, R. A. Ross, J. Mulder, G. M. Urban, K. Monory, G. Marsicano, M. Matteoli, A. Canty, A. J. Irving, I. Katona, Y. Yanagawa, P. Rakic, B. Lutz, K. Mackie, and T. Harkany. 2007. 'Hardwiring the brain: endocannabinoids shape neuronal connectivity', *Science*, 316: 1212-6.
- Bernabo, P., T. Tebaldi, E. J. N. Groen, F. M. Lane, E. Perenthaler, F. Mattedi, H. J. Newbery, H. Zhou, P. Zuccotti, V. Potrich, H. K. Shorrock, F. Muntoni, A. Quattrone, T. H. Gillingwater, and G. Viero. 2017. 'In Vivo Translatome Profiling in Spinal Muscular Atrophy Reveals a Role for SMN Protein in Ribosome Biology', *Cell Rep*, 21: 953-65.
- Bogdanik, L. P., M. A. Osborne, C. Davis, W. P. Martin, A. Austin, F. Rigo, C. F. Bennett, and C. M. Lutz. 2015. 'Systemic, postsymptomatic antisense oligonucleotide rescues motor unit maturation delay in a new mouse model for type II/III spinal muscular atrophy', *Proc Natl Acad Sci U S A*, 112: E5863-72.
- Bordet, T., P. Berna, J. L. Abitbol, and R. M. Pruss. 2010. 'Olesoxime (TRO19622): A Novel Mitochondrial-Targeted Neuroprotective Compound', *Pharmaceuticals (Basel)*, 3: 345-68.
- Bowerman, M., C. L. Anderson, A. Beauvais, P. P. Boyl, W. Witke, and R. Kothary. 2009. 'SMN, profilin IIa and plastin 3: a link between the deregulation of actin dynamics and SMA pathogenesis', *Mol Cell Neurosci*, 42: 66-74.
- Bowerman, M., A. Beauvais, C. L. Anderson, and R. Kothary. 2010. 'Rho-kinase inactivation prolongs survival of an intermediate SMA mouse model', *Hum Mol Genet*, 19: 1468-78.
- Bowerman, M., C. G. Becker, R. J. Yanez-Munoz, K. Ning, M. J. A. Wood, T. H. Gillingwater, K. Talbot, and Uk Sma Research Consortium. 2017. 'Therapeutic strategies for spinal muscular atrophy: SMN and beyond', *Dis Model Mech*, 10: 943-54.
- Bowerman, M., L. M. Murray, A. Beauvais, B. Pinheiro, and R. Kothary. 2012. 'A critical smn threshold in mice dictates onset of an intermediate spinal muscular atrophy phenotype associated with a distinct neuromuscular junction pathology', *Neuromuscul Disord*, 22: 263-76.
- Bowerman, M., L. M. Murray, J. G. Boyer, C. L. Anderson, and R. Kothary. 2012. 'Fasudil improves survival and promotes skeletal muscle development in a mouse model of spinal muscular atrophy', *BMC Med*, 10: 24.
- Bowerman, M., D. Shafey, and R. Kothary. 2007. 'Smn depletion alters profilin II expression and leads to upregulation of the RhoA/ROCK pathway and defects in neuronal integrity', *J Mol Neurosci*, 32: 120-31.
- Boyd, P.J., Gillingwater, T.H. 2017. 'Axonal and Neuromuscular Junction Pathology in Spinal Muscular Atrophy.' in C. J. Sumner, Paushkin, S., Ko, C.P. (ed.), *Spinal Muscular Atrophy: Disease Mechanisms and Therapy* (Academic Press).
- Braunewell, K. H., and A. J. Klein-Szanto. 2009. 'Visinin-like proteins (VSNLs): interaction partners and emerging functions in signal transduction of a subfamily of neuronal Ca²⁺ -sensor proteins', *Cell Tissue Res*, 335: 301-16.
- Brichta, L., Y. Hofmann, E. Hahnen, F. A. Siebzehrubl, H. Raschke, I. Blumcke, I. Y. Eyupoglu, and B. Wirth. 2003. 'Valproic acid increases the SMN2 protein level: a well-known drug as a potential therapy for spinal muscular atrophy', *Hum Mol Genet*, 12: 2481-9.
- Briese, M., B. Esmaeili, S. Fraboulet, E. C. Burt, S. Christodoulou, P. R. Towers, K. E. Davies, and D. B. Sattelle. 2009. 'Deletion of smn-1, the Caenorhabditis elegans ortholog of the spinal muscular atrophy gene, results in locomotor dysfunction and reduced lifespan', *Hum Mol Genet*, 18: 97-104.

- Burghes, A. H., Didonato, C.J., McGovern, V.L., Arnold, W.D.,. 2017. 'Mammalian Models of Spinal Muscular Atrophy.' in C.J Sumner, Paushkin, S., Ko, C.P. (ed.), *Spinal Muscular Atrophy: Disease Mechanisms and Therapy* (Academic Press).
- Burgoyne, R. D. 2007. 'Neuronal calcium sensor proteins: generating diversity in neuronal Ca²⁺ signalling', *Nat Rev Neurosci*, 8: 182-93.
- Burgoyne, R. D., and L. P. Haynes. 2012. 'Understanding the physiological roles of the neuronal calcium sensor proteins', *Mol Brain*, 5: 2.
- Burk, K., and R. J. Pasterkamp. 2019. 'Disrupted neuronal trafficking in amyotrophic lateral sclerosis', *Acta Neuropathol*, 137: 859-77.
- Cartegni, L., and A. R. Krainer. 2002. 'Disruption of an SF2/ASF-dependent exonic splicing enhancer in SMN2 causes spinal muscular atrophy in the absence of SMN1', *Nat Genet*, 30: 377-84.
- Casey, J. R., S. Grinstein, and J. Orłowski. 2010. 'Sensors and regulators of intracellular pH', *Nat Rev Mol Cell Biol*, 11: 50-61.
- Chan, Y. B., I. Miguel-Aliaga, C. Franks, N. Thomas, B. Trulzsch, D. B. Sattelle, K. E. Davies, and M. van den Heuvel. 2003. 'Neuromuscular defects in a *Drosophila* survival motor neuron gene mutant', *Hum Mol Genet*, 12: 1367-76.
- Chang, H. C., D. N. Dimlich, T. Yokokura, A. Mukherjee, M. W. Kankel, A. Sen, V. Sridhar, T. A. Fulga, A. C. Hart, D. Van Vactor, and S. Artavanis-Tsakonas. 2008. 'Modeling spinal muscular atrophy in *Drosophila*', *PLoS One*, 3: e3209.
- Chang, H. C., W. C. Hung, Y. J. Chuang, and Y. J. Jong. 2004. 'Degradation of survival motor neuron (SMN) protein is mediated via the ubiquitin/proteasome pathway', *Neurochem Int*, 45: 1107-12.
- Chang, J. G., H. M. Hsieh-Li, Y. J. Jong, N. M. Wang, C. H. Tsai, and H. Li. 2001. 'Treatment of spinal muscular atrophy by sodium butyrate', *Proc Natl Acad Sci U S A*, 98: 9808-13.
- Chang, W. F., T. Y. Lin, M. Peng, C. C. Chang, J. Xu, H. M. Hsieh-Li, J. L. Liu, and L. Y. Sung. 2022. 'Survival Motor Neuron Enhances Pluripotent Gene Expression and Facilitates Cell Reprogramming', *Stem Cells Dev*, 31: 696-705.
- Chaytow, H., Y. T. Huang, T. H. Gillingwater, and K. M. E. Faller. 2018. 'The role of survival motor neuron protein (SMN) in protein homeostasis', *Cell Mol Life Sci*, 75: 3877-94.
- Cherry, J. J., E. Y. Osman, M. C. Evans, S. Choi, X. Xing, G. D. Cuny, M. A. Glicksman, C. L. Lorson, and E. J. Androphy. 2013. 'Enhancement of SMN protein levels in a mouse model of spinal muscular atrophy using novel drug-like compounds', *EMBO Mol Med*, 5: 1103-18.
- Cifuentes-Diaz, C., T. Frugier, F. D. Tiziano, E. Lacene, N. Roblot, V. Joshi, M. H. Moreau, and J. Melki. 2001. 'Deletion of murine SMN exon 7 directed to skeletal muscle leads to severe muscular dystrophy', *J Cell Biol*, 152: 1107-14.
- Coovert, D. D., T. T. Le, P. E. McAndrew, J. Strasswimmer, T. O. Crawford, J. R. Mendell, S. E. Coulson, E. J. Androphy, T. W. Prior, and A. H. Burghes. 1997. 'The survival motor neuron protein in spinal muscular atrophy', *Hum Mol Genet*, 6: 1205-14.
- Corti, S., M. Nizzardo, C. Simone, M. Falcone, M. Nardini, D. Ronchi, C. Donadoni, S. Salani, G. Riboldi, F. Magri, G. Menozzi, C. Bonaglia, F. Rizzo, N. Bresolin, and G. P. Comi. 2012. 'Genetic correction of human induced pluripotent stem cells from patients with spinal muscular atrophy', *Sci Transl Med*, 4: 165ra62.
- Crooke, S. T., B. F. Baker, R. M. Crooke, and X. H. Liang. 2021. 'Antisense technology: an overview and prospectus', *Nat Rev Drug Discov*, 20: 427-53.
- Crooke, S. T., S. Wang, T. A. Vickers, W. Shen, and X. H. Liang. 2017. 'Cellular uptake and trafficking of antisense oligonucleotides', *Nat Biotechnol*, 35: 230-37.
- Crooke, S. T., J. L. Witztum, C. F. Bennett, and B. F. Baker. 2018. 'RNA-Targeted Therapeutics', *Cell Metab*, 27: 714-39.
- Cui, L., H. Li, Y. Xi, Q. Hu, H. Liu, J. Fan, Y. Xiang, X. Zhang, W. Shui, and Y. Lai. 2022. 'Vesicle trafficking and vesicle fusion: mechanisms, biological functions, and their implications for potential disease therapy', *Mol Biomed*, 3: 29.
- da Silva, J. S., and C. G. Dotti. 2002. 'Breaking the neuronal sphere: regulation of the actin cytoskeleton in neuritogenesis', *Nat Rev Neurosci*, 3: 694-704.

- Darras, B. T., C. A. Chiriboga, S. T. Iannaccone, K. J. Swoboda, J. Montes, L. Mignon, S. Xia, C. F. Bennett, K. M. Bishop, J. M. Shefner, A. M. Green, P. Sun, I. Bhan, S. Gheuens, E. Schneider, W. Farwell, D. C. De Vivo, and Isis-Cs Isis-Cs Study Groups. 2019. 'Nusinersen in later-onset spinal muscular atrophy: Long-term results from the phase 1/2 studies', *Neurology*, 92: e2492-e506.
- Darras, B. T., T. O. Crawford, R. S. Finkel, E. Mercuri, D. C. De Vivo, M. Oskoui, E. F. Tizzano, M. M. Ryan, F. Muntoni, G. Zhao, J. Staropoli, A. McCampbell, M. Petrillo, C. Stebbins, S. Fradette, W. Farwell, and C. J. Sumner. 2019. 'Neurofilament as a potential biomarker for spinal muscular atrophy', *Ann Clin Transl Neurol*, 6: 932-44.
- Darras, B. T., R. Masson, M. Mazurkiewicz-Beldzinska, K. Rose, H. Xiong, E. Zanoteli, G. Baranello, C. Bruno, D. Vlodayets, Y. Wang, M. El-Khairi, M. Gerber, K. Gorni, O. Khwaja, H. Kletzl, R. S. Scalco, P. Fontoura, L. Servais, and Firefish Working Group. 2021. 'Risdiplam-Treated Infants with Type 1 Spinal Muscular Atrophy versus Historical Controls', *N Engl J Med*, 385: 427-35.
- Day, J. W., R. S. Finkel, C. A. Chiriboga, A. M. Connolly, T. O. Crawford, B. T. Darras, S. T. Iannaccone, N. L. Kuntz, L. D. M. Pena, P. B. Shieh, E. C. Smith, J. M. Kwon, C. M. Zaidman, M. Schultz, D. E. Feltner, S. Tauscher-Wisniewski, H. Ouyang, D. H. Chand, D. M. Sproule, T. A. Macek, and J. R. Mendell. 2021. 'Onasemnogene abeparvovec gene therapy for symptomatic infantile-onset spinal muscular atrophy in patients with two copies of SMN2 (STR1VE): an open-label, single-arm, multicentre, phase 3 trial', *Lancet Neurol*, 20: 284-93.
- De Vivo, D. C., E. Bertini, K. J. Swoboda, W. L. Hwu, T. O. Crawford, R. S. Finkel, J. Kirschner, N. L. Kuntz, J. A. Parsons, M. M. Ryan, R. J. Butterfield, H. Topaloglu, T. Ben-Omran, V. A. Sansone, Y. J. Jong, F. Shu, J. F. Staropoli, D. Kerr, A. W. Sandrock, C. Stebbins, M. Petrillo, G. Braley, K. Johnson, R. Foster, S. Gheuens, I. Bhan, S. P. Reyna, S. Fradette, W. Farwell, and Nurture Study Group. 2019. 'Nusinersen initiated in infants during the presymptomatic stage of spinal muscular atrophy: Interim efficacy and safety results from the Phase 2 NURTURE study', *Neuromuscul Disord*, 29: 842-56.
- Delle Vedove, A., J. Natarajan, G. Zanni, M. Eckenweiler, A. Muinos-Buhl, M. Storbeck, J. Guillen Boixet, S. Barresi, S. Pizzi, I. Holker, F. Korber, T. M. Franzmann, E. S. Bertini, J. Kirschner, S. Alberti, M. Tartaglia, and B. Wirth. 2022. 'CAPRIN1(P512L) causes aberrant protein aggregation and associates with early-onset ataxia', *Cell Mol Life Sci*, 79: 526.
- Dent, E. W., and K. Kalil. 2001. 'Axon branching requires interactions between dynamic microtubules and actin filaments', *J Neurosci*, 21: 9757-69.
- DeVos, S. L., and T. M. Miller. 2013. 'Direct intraventricular delivery of drugs to the rodent central nervous system', *J Vis Exp*: e50326.
- Di Sole, F., K. Vadnagara, O. W. Moe, and V. Babich. 2012. 'Calcineurin homologous protein: a multifunctional Ca²⁺-binding protein family', *Am J Physiol Renal Physiol*, 303: F165-79.
- Dimitriadi, M., J. N. Sleight, A. Walker, H. C. Chang, A. Sen, G. Kalloo, J. Harris, T. Barsby, M. B. Walsh, J. S. Satterlee, C. Li, D. Van Vactor, S. Artavanis-Tsakonas, and A. C. Hart. 2010. 'Conserved genes act as modifiers of invertebrate SMN loss of function defects', *PLoS Genet*, 6: e1001172.
- Duque, S. I., W. D. Arnold, P. Odermatt, X. Li, P. N. Porensky, L. Schmelzer, K. Meyer, S. J. Kolb, D. Schumperli, B. K. Kaspar, and A. H. Burghes. 2015. 'A large animal model of spinal muscular atrophy and correction of phenotype', *Ann Neurol*, 77: 399-414.
- Duque, S., B. Joussemet, C. Riviere, T. Marais, L. Dubreil, A. M. Douar, J. Fyfe, P. Moullier, M. A. Colle, and M. Barkats. 2009. 'Intravenous administration of self-complementary AAV9 enables transgene delivery to adult motor neurons', *Mol Ther*, 17: 1187-96.
- Ebert, A. D., J. Yu, F. F. Rose, Jr., V. B. Mattis, C. L. Lorson, J. A. Thomson, and C. N. Svendsen. 2009. 'Induced pluripotent stem cells from a spinal muscular atrophy patient', *Nature*, 457: 277-80.
- El Marabti, E., and O. Abdel-Wahab. 2021. 'Therapeutic Modulation of RNA Splicing in Malignant and Non-Malignant Disease', *Trends Mol Med*, 27: 643-59.
- Eshraghi, M., E. McFall, S. Gibeault, and R. Kothary. 2016. 'Effect of genetic background on the phenotype of the Smn2B^{-/-} mouse model of spinal muscular atrophy', *Hum Mol Genet*, 25: 4494-506.
- Fallini, C., G. J. Bassell, and W. Rossoll. 2010. 'High-efficiency transfection of cultured primary motor neurons to study protein localization, trafficking, and function', *Mol Neurodegener*, 5: 17.

- . 2012. 'Spinal muscular atrophy: the role of SMN in axonal mRNA regulation', *Brain Res*, 1462: 81-92.
- Fallini, C., P. G. Donlin-Asp, J. P. Rouanet, G. J. Bassell, and W. Rossoll. 2016. 'Deficiency of the Survival of Motor Neuron Protein Impairs mRNA Localization and Local Translation in the Growth Cone of Motor Neurons', *J Neurosci*, 36: 3811-20.
- Fallini, C., J. P. Rouanet, P. G. Donlin-Asp, P. Guo, H. Zhang, R. H. Singer, W. Rossoll, and G. J. Bassell. 2014. 'Dynamics of survival of motor neuron (SMN) protein interaction with the mRNA-binding protein IMP1 facilitates its trafficking into motor neuron axons', *Dev Neurobiol*, 74: 319-32.
- Fallini, C., H. Zhang, Y. Su, V. Silani, R. H. Singer, W. Rossoll, and G. J. Bassell. 2011. 'The survival of motor neuron (SMN) protein interacts with the mRNA-binding protein HuD and regulates localization of poly(A) mRNA in primary motor neuron axons', *J Neurosci*, 31: 3914-25.
- Fan, L., and L. R. Simard. 2002. 'Survival motor neuron (SMN) protein: role in neurite outgrowth and neuromuscular maturation during neuronal differentiation and development', *Hum Mol Genet*, 11: 1605-14.
- Feeney, D. M., A. Gonzalez, and W. A. Law. 1982. 'Amphetamine, haloperidol, and experience interact to affect rate of recovery after motor cortex injury', *Science*, 217: 855-7.
- Feldkotter, M., V. Schwarzer, R. Wirth, T. F. Wienker, and B. Wirth. 2002. 'Quantitative analyses of SMN1 and SMN2 based on real-time lightCycler PCR: fast and highly reliable carrier testing and prediction of severity of spinal muscular atrophy', *Am J Hum Genet*, 70: 358-68.
- Finkel, R. S., C. A. Chiriboga, J. Vajsar, J. W. Day, J. Montes, D. C. De Vivo, M. Yamashita, F. Rigo, G. Hung, E. Schneider, D. A. Norris, S. Xia, C. F. Bennett, and K. M. Bishop. 2016. 'Treatment of infantile-onset spinal muscular atrophy with nusinersen: a phase 2, open-label, dose-escalation study', *Lancet*, 388: 3017-26.
- Finkel, R. S., E. Mercuri, B. T. Darras, A. M. Connolly, N. L. Kuntz, J. Kirschner, C. A. Chiriboga, K. Saito, L. Servais, E. Tizzano, H. Topaloglu, M. Tulinius, J. Montes, A. M. Glanzman, K. Bishop, Z. J. Zhong, S. Gheuens, C. F. Bennett, E. Schneider, W. Farwell, D. C. De Vivo, and Endear Study Group. 2017. 'Nusinersen versus Sham Control in Infantile-Onset Spinal Muscular Atrophy', *N Engl J Med*, 377: 1723-32.
- Fletcher, E. V., C. M. Simon, J. G. Pagiazitis, J. I. Chalif, A. Vukojicic, E. Drobac, X. Wang, and G. Z. Mentis. 2017. 'Reduced sensory synaptic excitation impairs motor neuron function via Kv2.1 in spinal muscular atrophy', *Nat Neurosci*, 20: 905-16.
- Foran, E., D. Y. Kwon, J. H. Nofziger, E. S. Arnold, M. D. Hall, K. H. Fischbeck, and B. G. Burnett. 2016. 'CNS uptake of bortezomib is enhanced by P-glycoprotein inhibition: implications for spinal muscular atrophy', *Neurobiol Dis*, 88: 118-24.
- Foust, K. D., E. Nurre, C. L. Montgomery, A. Hernandez, C. M. Chan, and B. K. Kaspar. 2009. 'Intravascular AAV9 preferentially targets neonatal neurons and adult astrocytes', *Nat Biotechnol*, 27: 59-65.
- Foust, K. D., X. Wang, V. L. McGovern, L. Braun, A. K. Bevan, A. M. Haidet, T. T. Le, P. R. Morales, M. M. Rich, A. H. Burghes, and B. K. Kaspar. 2010. 'Rescue of the spinal muscular atrophy phenotype in a mouse model by early postnatal delivery of SMN', *Nat Biotechnol*, 28: 271-4.
- Gabanella, F., M. E. Butchbach, L. Saieva, C. Carissimi, A. H. Burghes, and L. Pellizzoni. 2007. 'Ribonucleoprotein assembly defects correlate with spinal muscular atrophy severity and preferentially affect a subset of spliceosomal snRNPs', *PLoS One*, 2: e921.
- Garbes, L., L. Heesen, I. Holker, T. Bauer, J. Schreml, K. Zimmermann, M. Thoenes, M. Walter, J. Dimos, M. Peitz, O. Brustle, R. Heller, and B. Wirth. 2013. 'VPA response in SMA is suppressed by the fatty acid translocase CD36', *Hum Mol Genet*, 22: 398-407.
- Garbes, L., M. Riessland, I. Holker, R. Heller, J. Hauke, C. Trankle, R. Coras, I. Blumcke, E. Hahnen, and B. Wirth. 2009. 'LBH589 induces up to 10-fold SMN protein levels by several independent mechanisms and is effective even in cells from SMA patients non-responsive to valproate', *Hum Mol Genet*, 18: 3645-58.
- Giganti, A., J. Plastino, B. Janji, M. Van Troys, D. Lentz, C. Ampe, C. Sykes, and E. Friederich. 2005. 'Actin-filament cross-linking protein T-plastin increases Arp2/3-mediated actin-based movement', *J Cell Sci*, 118: 1255-65.

- Gilhus, N. E., S. Tzartos, A. Evoli, J. Palace, T. M. Burns, and Jgm Verschuuren. 2019. 'Myasthenia gravis', *Nat Rev Dis Primers*, 5: 30.
- Gilliam, T. C., L. M. Brzustowicz, L. H. Castilla, T. Lehner, G. K. Penchaszadeh, R. J. Daniels, B. C. Byth, J. Knowles, J. E. Hislop, Y. Shapira, and et al. 1990. 'Genetic homogeneity between acute and chronic forms of spinal muscular atrophy', *Nature*, 345: 823-5.
- Girard, F., J. Venail, B. Schwaller, and M. R. Celio. 2015. 'The EF-hand Ca(2+)-binding protein superfamily: a genome-wide analysis of gene expression patterns in the adult mouse brain', *Neuroscience*, 294: 116-55.
- Gluscock, J. J., E. Y. Osman, T. H. Coady, F. F. Rose, M. Shababi, and C. L. Lorson. 2011. 'Delivery of therapeutic agents through intracerebroventricular (ICV) and intravenous (IV) injection in mice', *J Vis Exp*.
- Gogliotti, R. G., K. A. Quinlan, C. B. Barlow, C. R. Heier, C. J. Heckman, and C. J. Didonato. 2012. 'Motor neuron rescue in spinal muscular atrophy mice demonstrates that sensory-motor defects are a consequence, not a cause, of motor neuron dysfunction', *J Neurosci*, 32: 3818-29.
- Graef, I. A., F. Wang, F. Charron, L. Chen, J. Neilson, M. Tessier-Lavigne, and G. R. Crabtree. 2003. 'Neurotrophins and netrins require calcineurin/NFAT signaling to stimulate outgrowth of embryonic axons', *Cell*, 113: 657-70.
- Greensmith, L., and G. Vrbova. 1997. 'Disturbances of neuromuscular interaction may contribute to muscle weakness in spinal muscular atrophy', *Neuromuscul Disord*, 7: 369-72.
- Groen, E. J. N., E. Perenthaler, N. L. Courtney, C. Y. Jordan, H. K. Shorrock, D. van der Hoorn, Y. T. Huang, L. M. Murray, G. Viero, and T. H. Gillingwater. 2018. 'Temporal and tissue-specific variability of SMN protein levels in mouse models of spinal muscular atrophy', *Hum Mol Genet*, 27: 2851-62.
- Gromova, A., and A. R. La Spada. 2020. 'Harmony Lost: Cell-Cell Communication at the Neuromuscular Junction in Motor Neuron Disease', *Trends Neurosci*, 43: 709-24.
- Gubitza, A. K., W. Feng, and G. Dreyfuss. 2004. 'The SMN complex', *Exp Cell Res*, 296: 51-6.
- Guo, W., M. Naujock, L. Fumagalli, T. Vandoorne, P. Baatsen, R. Boon, L. Ordovas, A. Patel, M. Welters, T. Vanwelden, N. Geens, T. Tricot, V. Benoy, J. Steyaert, C. Lefebvre-Omar, W. Boesmans, M. Jarpe, J. Sternecker, F. Wegner, S. Petri, D. Bohl, P. Vanden Berghe, W. Robberecht, P. Van Damme, C. Verfaillie, and L. Van Den Bosch. 2017. 'HDAC6 inhibition reverses axonal transport defects in motor neurons derived from FUS-ALS patients', *Nat Commun*, 8: 861.
- Hamilton, G., and T. H. Gillingwater. 2013. 'Spinal muscular atrophy: going beyond the motor neuron', *Trends Mol Med*, 19: 40-50.
- Hao le, T., M. Wolman, M. Granato, and C. E. Beattie. 2012. 'Survival motor neuron affects plastin 3 protein levels leading to motor defects', *J Neurosci*, 32: 5074-84.
- Harada, Y., V. K. Rao, K. Arya, N. L. Kuntz, C. J. DiDonato, G. Napchan-Pomerantz, A. Agarwal, V. Stefans, M. Katsuno, and A. Veerapandiyani. 2020. 'Combination molecular therapies for type 1 spinal muscular atrophy', *Muscle Nerve*, 62: 550-54.
- Harding, B. N., S. Kariya, U. R. Monani, W. K. Chung, M. Benton, S. W. Yum, G. Tennekoon, and R. S. Finkel. 2015. 'Spectrum of neuropathophysiology in spinal muscular atrophy type I', *J Neuropathol Exp Neurol*, 74: 15-24.
- Heesen, L., M. Peitz, L. Torres-Benito, I. Holker, K. Hupperich, K. Dobrindt, J. Jungverdorben, S. Ritzenhofen, B. Weykopf, D. Eckert, S. M. Hosseini-Barkooie, M. Storbeck, N. Fusaki, R. Lonigro, R. Heller, M. J. Kye, O. Brustle, and B. Wirth. 2016. 'Plastin 3 is upregulated in iPSC-derived motoneurons from asymptomatic SMN1-deleted individuals', *Cell Mol Life Sci*, 73: 2089-104.
- Hensel, N., and P. Claus. 2018. 'The Actin Cytoskeleton in SMA and ALS: How Does It Contribute to Motoneuron Degeneration?', *Neuroscientist*, 24: 54-72.
- Hofmann, Y., C. L. Lorson, S. Stamm, E. J. Androphy, and B. Wirth. 2000. 'Htra2-beta 1 stimulates an exonic splicing enhancer and can restore full-length SMN expression to survival motor neuron 2 (SMN2)', *Proc Natl Acad Sci U S A*, 97: 9618-23.
- Hosoyama, T., J. V. McGivern, J. M. Van Dyke, A. D. Ebert, and M. Suzuki. 2014. 'Derivation of myogenic progenitors directly from human pluripotent stem cells using a sphere-based culture', *Stem Cells Transl Med*, 3: 564-74.

- HosseiniBarkooie, S., M. Peters, L. Torres-Benito, R. H. Rastetter, K. Hupperich, A. Hoffmann, N. Mendoza-Ferreira, A. Kaczmarek, E. Janzen, J. Milbradt, T. Lamkemeyer, F. Rigo, C. F. Bennett, C. Guschlbauer, A. Buschges, M. Hammerschmidt, M. Riessland, M. J. Kye, C. S. Clemen, and B. Wirth. 2016. 'The Power of Human Protective Modifiers: PLS3 and CORO1C Unravel Impaired Endocytosis in Spinal Muscular Atrophy and Rescue SMA Phenotype', *Am J Hum Genet*, 99: 647-65.
- Hsieh-Li, H. M., J. G. Chang, Y. J. Jong, M. H. Wu, N. M. Wang, C. H. Tsai, and H. Li. 2000. 'A mouse model for spinal muscular atrophy', *Nat Genet*, 24: 66-70.
- Hua, Y., K. Sahashi, G. Hung, F. Rigo, M. A. Passini, C. F. Bennett, and A. R. Krainer. 2010. 'Antisense correction of SMN2 splicing in the CNS rescues necrosis in a type III SMA mouse model', *Genes Dev*, 24: 1634-44.
- Hua, Y., K. Sahashi, F. Rigo, G. Hung, G. Horev, C. F. Bennett, and A. R. Krainer. 2011. 'Peripheral SMN restoration is essential for long-term rescue of a severe spinal muscular atrophy mouse model', *Nature*, 478: 123-6.
- Hua, Y., T. A. Vickers, H. L. Okunola, C. F. Bennett, and A. R. Krainer. 2008. 'Antisense masking of an hnRNP A1/A2 intronic splicing silencer corrects SMN2 splicing in transgenic mice', *Am J Hum Genet*, 82: 834-48.
- Hua, Y., and J. Zhou. 2004. 'Survival motor neuron protein facilitates assembly of stress granules', *FEBS Lett*, 572: 69-74.
- Iino, S., S. Kobayashi, and H. Hidaka. 1998. 'Neurocalcin-immunopositive nerve terminals in the muscle spindle, Golgi tendon organ and motor endplate', *Brain Res*, 808: 294-9.
- Ivings, L., S. R. Pennington, R. Jenkins, J. L. Weiss, and R. D. Burgoyne. 2002. 'Identification of Ca²⁺-dependent binding partners for the neuronal calcium sensor protein neurocalcin delta: interaction with actin, clathrin and tubulin', *Biochem J*, 363: 599-608.
- Jablonka, S., M. Beck, B. D. Lechner, C. Mayer, and M. Sendtner. 2007. 'Defective Ca²⁺ channel clustering in axon terminals disturbs excitability in motoneurons in spinal muscular atrophy', *J Cell Biol*, 179: 139-49.
- Jablonka, S., K. Karle, B. Sandner, C. Andreassi, K. von Au, and M. Sendtner. 2006. 'Distinct and overlapping alterations in motor and sensory neurons in a mouse model of spinal muscular atrophy', *Hum Mol Genet*, 15: 511-8.
- Jafar-Nejad, P., B. Powers, A. Soriano, H. Zhao, D. A. Norris, J. Matson, B. DeBrosse-Serra, J. Watson, P. Narayanan, S. J. Chun, C. Mazur, H. Kordasiewicz, E. E. Swayze, and F. Rigo. 2021. 'The atlas of RNase H antisense oligonucleotide distribution and activity in the CNS of rodents and non-human primates following central administration', *Nucleic Acids Res*, 49: 657-73.
- Janzen, E., N. Mendoza-Ferreira, S. Hosseinibarkooie, S. Schneider, K. Hupperich, T. Tschanz, V. Grysko, M. Riessland, M. Hammerschmidt, F. Rigo, C. F. Bennett, M. J. Kye, L. Torres-Benito, and B. Wirth. 2018. 'CHP1 reduction ameliorates spinal muscular atrophy pathology by restoring calcineurin activity and endocytosis', *Brain*, 141: 2343-61.
- Janzen, E., L. Wolff, N. Mendoza-Ferreira, K. Hupperich, A. Delle Vedove, S. Hosseinibarkooie, M. J. Kye, and B. Wirth. 2019. 'PLS3 Overexpression Delays Ataxia in Chp1 Mutant Mice', *Front Neurosci*, 13: 993.
- Jeong, J., S. Pandey, Y. Li, J. D. Badger, 2nd, W. Lu, and K. W. Roche. 2019. 'PSD-95 binding dynamically regulates NLGN1 trafficking and function', *Proc Natl Acad Sci U S A*, 116: 12035-44.
- Jimenez-Vidal, M., J. Srivastava, L. K. Putney, and D. L. Barber. 2010. 'Nuclear-localized calcineurin homologous protein CHP1 interacts with upstream binding factor and inhibits ribosomal RNA synthesis', *J Biol Chem*, 285: 36260-6.
- Kaifer, K. A., E. Villalon, E. Y. Osman, J. J. Glascock, L. L. Arnold, D. D. W. Cornelison, and C. L. Lorson. 2017. 'Plastin-3 extends survival and reduces severity in mouse models of spinal muscular atrophy', *JCI Insight*, 2: e89970.
- Kariya, S., T. Obis, C. Garone, T. Akay, F. Sera, S. Iwata, S. Homma, and U. R. Monani. 2014. 'Requirement of enhanced Survival Motoneuron protein imposed during neuromuscular junction maturation', *J Clin Invest*, 124: 785-800.

- Kariya, S., G. H. Park, Y. Maeno-Hikichi, O. Leykekhman, C. Lutz, M. S. Arkovitz, L. T. Landmesser, and U. R. Monani. 2008. 'Reduced SMN protein impairs maturation of the neuromuscular junctions in mouse models of spinal muscular atrophy', *Hum Mol Genet*, 17: 2552-69.
- Kariyawasam, D., A. D'Silva, J. Howells, K. Herbert, P. Geelan-Small, C. S. Lin, and M. A. Farrar. 2020. 'Motor unit changes in children with symptomatic spinal muscular atrophy treated with nusinersen', *J Neurol Neurosurg Psychiatry*, 92: 78-85.
- Kashima, T., and J. L. Manley. 2003. 'A negative element in SMN2 exon 7 inhibits splicing in spinal muscular atrophy', *Nat Genet*, 34: 460-3.
- Khayrullina, G., Z. A. Alipio-Gloria, M. O. Deguise, S. Gagnon, L. Chehade, M. Stinson, N. Belous, E. M. Bergman, F. W. Lischka, J. Rotty, C. L. Dalgard, R. Kothary, K. A. Johnson, and B. G. Burnett. 2022. 'Survival motor neuron protein deficiency alters microglia reactivity', *Glia*, 70: 1337-58.
- Khayrullina, G., K. E. Moritz, J. F. Schooley, N. Fatima, C. Viollet, N. M. McCormack, J. T. Smyth, M. L. Doughty, C. L. Dalgard, T. P. Flagg, and B. G. Burnett. 2020. 'SMN-deficiency disrupts SERCA2 expression and intracellular Ca(2+) signaling in cardiomyocytes from SMA mice and patient-derived iPSCs', *Skelet Muscle*, 10: 16.
- Khazaei, M. R., M. P. Girouard, R. Alchini, S. Ong Tone, T. Shimada, S. Bechstedt, M. Cowan, D. Guillet, P. W. Wiseman, G. Brouhard, J. F. Cloutier, and A. E. Fournier. 2014. 'Collapsin response mediator protein 4 regulates growth cone dynamics through the actin and microtubule cytoskeleton', *J Biol Chem*, 289: 30133-43.
- Kingdom, R., and C. F. Wright. 2022. 'Incomplete Penetrance and Variable Expressivity: From Clinical Studies to Population Cohorts', *Front Genet*, 13: 920390.
- Kong, L., X. Wang, D. W. Choe, M. Polley, B. G. Burnett, M. Bosch-Marce, J. W. Griffin, M. M. Rich, and C. J. Sumner. 2009. 'Impaired synaptic vesicle release and immaturity of neuromuscular junctions in spinal muscular atrophy mice', *J Neurosci*, 29: 842-51.
- Kordasiewicz, H. B., L. M. Stanek, E. V. Wancewicz, C. Mazur, M. M. McAlonis, K. A. Pytel, J. W. Artates, A. Weiss, S. H. Cheng, L. S. Shihabuddin, G. Hung, C. F. Bennett, and D. W. Cleveland. 2012. 'Sustained therapeutic reversal of Huntington's disease by transient repression of huntingtin synthesis', *Neuron*, 74: 1031-44.
- Krishnan, A., V. Venkataraman, E. Fik-Rymarkiewicz, T. Duda, and R. K. Sharma. 2004. 'Structural, biochemical, and functional characterization of the calcium sensor neurocalcin delta in the inner retinal neurons and its linkage with the rod outer segment membrane guanylate cyclase transduction system', *Biochemistry*, 43: 2708-23.
- Kwon, D. Y., W. W. Motley, K. H. Fischbeck, and B. G. Burnett. 2011. 'Increasing expression and decreasing degradation of SMN ameliorate the spinal muscular atrophy phenotype in mice', *Hum Mol Genet*, 20: 3667-77.
- Kwon, S. E., and E. R. Chapman. 2011. 'Synaptophysin regulates the kinetics of synaptic vesicle endocytosis in central neurons', *Neuron*, 70: 847-54.
- Lauria, F., P. Bernabo, T. Tebaldi, E. J. N. Groen, E. Perenthaler, F. Maniscalco, A. Rossi, D. Donzel, M. Clamer, M. Marchioretto, N. Omersa, J. Orri, M. Dalla Serra, G. Anderluh, A. Quattrone, A. Inga, T. H. Gillingwater, and G. Viero. 2020. 'SMN-primed ribosomes modulate the translation of transcripts related to spinal muscular atrophy', *Nat Cell Biol*, 22: 1239-51.
- Le, T. T., L. T. Pham, M. E. Butchbach, H. L. Zhang, U. R. Monani, D. D. Coovert, T. O. Gavrulina, L. Xing, G. J. Bassell, and A. H. Burghes. 2005. 'SMNDelta7, the major product of the centromeric survival motor neuron (SMN2) gene, extends survival in mice with spinal muscular atrophy and associates with full-length SMN', *Hum Mol Genet*, 14: 845-57.
- Lefebvre, S., L. Burglen, S. Reboullet, O. Clermont, P. Bulet, L. Viollet, B. Benichou, C. Cruaud, P. Millasseau, M. Zeviani, and et al. 1995. 'Identification and characterization of a spinal muscular atrophy-determining gene', *Cell*, 80: 155-65.
- Lefebvre, S., P. Bulet, Q. Liu, S. Bertrand, O. Clermont, A. Munnich, G. Dreyfuss, and J. Melki. 1997. 'Correlation between severity and SMN protein level in spinal muscular atrophy', *Nat Genet*, 16: 265-9.
- Lewelt, A., K. J. Krosschell, C. Scott, A. Sakonju, J. T. Kissel, T. O. Crawford, G. Acsadi, G. D'Anjou, B. Elsheikh, S. P. Reyna, M. K. Schroth, J. A. Maczulski, G. J. Stoddard, E. Elovic, and K. J. Swoboda.

2010. 'Compound muscle action potential and motor function in children with spinal muscular atrophy', *Muscle Nerve*, 42: 703-8.
- Liang, X., M. R. Song, Z. Xu, G. M. Lanuza, Y. Liu, T. Zhuang, Y. Chen, S. L. Pfaff, S. M. Evans, and Y. Sun. 2011. 'Isl1 is required for multiple aspects of motor neuron development', *Mol Cell Neurosci*, 47: 215-22.
- Lin, C. S., W. Shen, Z. P. Chen, Y. H. Tu, and P. Matsudaira. 1994. 'Identification of I-plastin, a human fimbrin isoform expressed in intestine and kidney', *Mol Cell Biol*, 14: 2457-67.
- Lin, X., and D. L. Barber. 1996. 'A calcineurin homologous protein inhibits GTPase-stimulated Na-H exchange', *Proc Natl Acad Sci U S A*, 93: 12631-6.
- Lin, X., J. J. Li, W. J. Qian, Q. J. Zhang, Z. F. Wang, Y. Q. Lu, E. L. Dong, J. He, N. Wang, L. X. Ma, and W. J. Chen. 2017. 'Modeling the differential phenotypes of spinal muscular atrophy with high-yield generation of motor neurons from human induced pluripotent stem cells', *Oncotarget*, 8: 42030-42.
- Lin, X., R. A. Sikkink, F. Rusnak, and D. L. Barber. 1999. 'Inhibition of calcineurin phosphatase activity by a calcineurin B homologous protein', *J Biol Chem*, 274: 36125-31.
- Ling, K. K., R. M. Gibbs, Z. Feng, and C. P. Ko. 2012. 'Severe neuromuscular denervation of clinically relevant muscles in a mouse model of spinal muscular atrophy', *Hum Mol Genet*, 21: 185-95.
- Ling, K. K., M. Y. Lin, B. Zingg, Z. Feng, and C. P. Ko. 2010. 'Synaptic defects in the spinal and neuromuscular circuitry in a mouse model of spinal muscular atrophy', *PLoS One*, 5: e15457.
- Linnane, E., P. Davey, P. Zhang, S. Puri, M. Edbrooke, E. Chiarparin, A. S. Revenko, A. R. Macleod, J. C. Norman, and S. J. Ross. 2019. 'Differential uptake, kinetics and mechanisms of intracellular trafficking of next-generation antisense oligonucleotides across human cancer cell lines', *Nucleic Acids Res*, 47: 4375-92.
- Liu, H., J. Lu, H. Chen, Z. Du, X. J. Li, and S. C. Zhang. 2015. 'Spinal muscular atrophy patient-derived motor neurons exhibit hyperexcitability', *Sci Rep*, 5: 12189.
- Liu, Q., and G. Dreyfuss. 1996. 'A novel nuclear structure containing the survival of motor neurons protein', *EMBO J*, 15: 3555-65.
- Liu, Q., U. Fischer, F. Wang, and G. Dreyfuss. 1997. 'The spinal muscular atrophy disease gene product, SMN, and its associated protein SIP1 are in a complex with spliceosomal snRNP proteins', *Cell*, 90: 1013-21.
- Liu, Y., H. C. Zaun, J. Orłowski, and S. L. Ackerman. 2013. 'CHP1-mediated NHE1 biosynthetic maturation is required for Purkinje cell axon homeostasis', *J Neurosci*, 33: 12656-69.
- Loeblich, S. 2014. 'The role of F-actin in modulating Clathrin-mediated endocytosis: Lessons from neurons in health and neuropsychiatric disorder', *Commun Integr Biol*, 7: e28740.
- Lorson, C. L., and E. J. Androphy. 2000. 'An exonic enhancer is required for inclusion of an essential exon in the SMA-determining gene SMN', *Hum Mol Genet*, 9: 259-65.
- Lorson, C. L., E. Hahnen, E. J. Androphy, and B. Wirth. 1999. 'A single nucleotide in the SMN gene regulates splicing and is responsible for spinal muscular atrophy', *Proc Natl Acad Sci U S A*, 96: 6307-11.
- Lunn, M. R., and C. H. Wang. 2008. 'Spinal muscular atrophy', *Lancet*, 371: 2120-33.
- Luu, K. T., D. A. Norris, R. Gunawan, S. Henry, R. Geary, and Y. Wang. 2017. 'Population Pharmacokinetics of Nusinersen in the Cerebral Spinal Fluid and Plasma of Pediatric Patients With Spinal Muscular Atrophy Following Intrathecal Administrations', *J Clin Pharmacol*, 57: 1031-41.
- Mailman, M. D., J. W. Heinz, A. C. Papp, P. J. Snyder, M. S. Sedra, B. Wirth, A. H. Burghes, and T. W. Prior. 2002. 'Molecular analysis of spinal muscular atrophy and modification of the phenotype by SMN2', *Genet Med*, 4: 20-6.
- Makhortova, N. R., M. Hayhurst, A. Cerqueira, A. D. Sinor-Anderson, W. N. Zhao, P. W. Heiser, A. C. Arvanites, L. S. Davidow, Z. O. Waldon, J. A. Steen, K. Lam, H. D. Ngo, and L. L. Rubin. 2011. 'A screen for regulators of survival of motor neuron protein levels', *Nat Chem Biol*, 7: 544-52.
- Martin, J. E., T. T. Nguyen, C. Grunseich, J. H. Nofziger, P. R. Lee, D. Fields, K. H. Fischbeck, and E. Foran. 2017. 'Decreased Motor Neuron Support by SMA Astrocytes due to Diminished MCP1 Secretion', *J Neurosci*, 37: 5309-18.

- Martinez-Hernandez, R., C. Soler-Botija, E. Also, L. Alias, L. Caselles, I. Gich, S. Bernal, and E. F. Tizzano. 2009. 'The developmental pattern of myotubes in spinal muscular atrophy indicates prenatal delay of muscle maturation', *J Neuropathol Exp Neurol*, 68: 474-81.
- McWhorter, M. L., U. R. Monani, A. H. Burghes, and C. E. Beattie. 2003. 'Knockdown of the survival motor neuron (Smn) protein in zebrafish causes defects in motor axon outgrowth and pathfinding', *J Cell Biol*, 162: 919-31.
- Meister, G., C. Eggert, and U. Fischer. 2002. 'SMN-mediated assembly of RNPs: a complex story', *Trends Cell Biol*, 12: 472-8.
- Melki, J., P. Sheth, S. Abdelhak, P. Burlet, M. F. Bachelot, M. G. Lathrop, J. Frezal, and A. Munnich. 1990. 'Mapping of acute (type I) spinal muscular atrophy to chromosome 5q12-q14. The French Spinal Muscular Atrophy Investigators', *Lancet*, 336: 271-3.
- Mendell, J. R., S. A. Al-Zaidy, K. J. Lehman, M. McColly, L. P. Lowes, L. N. Alfano, N. F. Reash, M. A. Iammarino, K. R. Church, A. Kleyn, M. N. Meriggioli, and R. Shell. 2021. 'Five-Year Extension Results of the Phase 1 START Trial of Onasemnogene Apeparvovec in Spinal Muscular Atrophy', *JAMA Neurol*, 78: 834-41.
- Mendell, J. R., S. Al-Zaidy, R. Shell, W. D. Arnold, L. R. Rodino-Klapac, T. W. Prior, L. Lowes, L. Alfano, K. Berry, K. Church, J. T. Kissel, S. Nagendran, J. L'Italien, D. M. Sproule, C. Wells, J. A. Cardenas, M. D. Heitzer, A. Kaspar, S. Corcoran, L. Braun, S. Likhite, C. Miranda, K. Meyer, K. D. Foust, A. H. M. Burghes, and B. K. Kaspar. 2017. 'Single-Dose Gene-Replacement Therapy for Spinal Muscular Atrophy', *N Engl J Med*, 377: 1713-22.
- Mendoza-Ferreira, N., M. Coutelier, E. Janzen, S. Hosseinibarkooie, H. Lohr, S. Schneider, J. Milbradt, M. Karakaya, M. Riessland, C. Pichlo, L. Torres-Benito, A. Singleton, S. Zuchner, A. Brice, A. Durr, M. Hammerschmidt, G. Stevanin, and B. Wirth. 2018. 'Biallelic CHP1 mutation causes human autosomal recessive ataxia by impairing NHE1 function', *Neurol Genet*, 4: e209.
- Mentis, G. Z., D. Blivis, W. Liu, E. Drobac, M. E. Crowder, L. Kong, F. J. Alvarez, C. J. Sumner, and M. J. O'Donovan. 2011. 'Early functional impairment of sensory-motor connectivity in a mouse model of spinal muscular atrophy', *Neuron*, 69: 453-67.
- Mercuri, E., G. Baranello, O. Boespflug-Tanguy, L. De Waele, N. Goemans, J. Kirschner, R. Masson, E. S. Mazzone, A. Pechmann, M. C. Pera, C. Vuillerot, S. Bader-Weder, M. Gerber, K. Gorni, J. Hoffart, H. Kletzl, C. Martin, T. McIver, R. S. Scalco, W. Y. Yeung, L. Servais, and Sunfish Working Group. 2022. 'Risdiplam in types 2 and 3 spinal muscular atrophy: A randomised, placebo-controlled, dose-finding trial followed by 24 months of treatment', *Eur J Neurol*.
- Mercuri, E., B. T. Darras, C. A. Chiriboga, J. W. Day, C. Campbell, A. M. Connolly, S. T. Iannaccone, J. Kirschner, N. L. Kuntz, K. Saito, P. B. Shieh, M. Tulinius, E. S. Mazzone, J. Montes, K. M. Bishop, Q. Yang, R. Foster, S. Gheuens, C. F. Bennett, W. Farwell, E. Schneider, D. C. De Vivo, R. S. Finkel, and Cherish Study Group. 2018. 'Nusinersen versus Sham Control in Later-Onset Spinal Muscular Atrophy', *N Engl J Med*, 378: 625-35.
- Mirea, A., E. S. Shelby, M. Axente, M. Badina, L. Padure, M. Leanca, V. Dima, and C. Sporea. 2021. 'Combination Therapy with Nusinersen and Onasemnogene Apeparvovec-xioi in Spinal Muscular Atrophy Type I', *J Clin Med*, 10.
- Monani, U. R., D. D. Coovert, and A. H. Burghes. 2000. 'Animal models of spinal muscular atrophy', *Hum Mol Genet*, 9: 2451-7.
- Moradi, M., R. Sivadasan, L. Saal, P. Luningschror, B. Dombert, R. J. Rathod, D. C. Dieterich, R. Blum, and M. Sendtner. 2017. 'Differential roles of alpha-, beta-, and gamma-actin in axon growth and collateral branch formation in motoneurons', *J Cell Biol*, 216: 793-814.
- Muinos-Buhl, A., R. Rombo, E. Janzen, K. K. Ling, K. Hupperich, F. Rigo, C. F. Bennett, and B. Wirth. 2022. 'Combinatorial ASO-mediated therapy with low dose SMN and the protective modifier Chp1 is not sufficient to ameliorate SMA pathology hallmarks', *Neurobiol Dis*, 171: 105795.
- Mullard, A. 2015. 'Stem-cell discovery platforms yield first clinical candidates', *Nat Rev Drug Discov*, 14: 589-91.
- Munsat, T. L., and K. E. Davies. 1992. 'International SMA consortium meeting. (26-28 June 1992, Bonn, Germany)', *Neuromuscul Disord*, 2: 423-8.

- Muntoni, F., E. Bertini, G. Comi, J. Kirschner, A. Lusakowska, E. Mercuri, M. Scoto, W. L. van der Pol, C. Vuillerot, A. Burdeska, M. El-Khairi, P. Fontoura, J. Ives, K. Gorni, C. Reid, S. Fuerst-Recktenwald, and Oleos Study Group. 2020. 'Long-term follow-up of patients with type 2 and non-ambulant type 3 spinal muscular atrophy (SMA) treated with olesoxime in the OLEOS trial', *Neuromuscul Disord*, 30: 959-69.
- Muramatsu, H., T. Kuramochi, H. Katada, A. Ueyama, Y. Ruike, K. Ohmine, M. Shida-Kawazoe, R. Miyano-Nishizawa, Y. Shimizu, M. Okuda, Y. Hori, M. Hayashi, K. Haraya, N. Ban, T. Nonaka, M. Honda, H. Kitamura, K. Hattori, T. Kitazawa, T. Igawa, Y. Kawabe, and J. Nezu. 2021. 'Novel myostatin-specific antibody enhances muscle strength in muscle disease models', *Sci Rep*, 11: 2160.
- Murray, L. M., L. H. Comley, D. Thomson, N. Parkinson, K. Talbot, and T. H. Gillingwater. 2008. 'Selective vulnerability of motor neurons and dissociation of pre- and post-synaptic pathology at the neuromuscular junction in mouse models of spinal muscular atrophy', *Hum Mol Genet*, 17: 949-62.
- Nakamura, N., Y. Miyake, M. Matsushita, S. Tanaka, H. Inoue, and H. Kanazawa. 2002. 'KIF1Bbeta2, capable of interacting with CHP, is localized to synaptic vesicles', *J Biochem*, 132: 483-91.
- Naoe, Y., K. Arita, H. Hashimoto, H. Kanazawa, M. Sato, and T. Shimizu. 2005. 'Structural characterization of calcineurin B homologous protein 1', *J Biol Chem*, 280: 32372-8.
- Naryshkin, N. A., M. Weetall, A. Dakka, J. Narasimhan, X. Zhao, Z. Feng, K. K. Ling, G. M. Karp, H. Qi, M. G. Woll, G. Chen, N. Zhang, V. Gabbeta, P. Vazirani, A. Bhattacharyya, B. Furia, N. Risher, J. Sheedy, R. Kong, J. Ma, A. Turpoff, C. S. Lee, X. Zhang, Y. C. Moon, P. Trifillis, E. M. Welch, J. M. Colacino, J. Babiak, N. G. Almstead, S. W. Peltz, L. A. Eng, K. S. Chen, J. L. Mull, M. S. Lynes, L. L. Rubin, P. Fontoura, L. Santarelli, D. Haehnke, K. D. McCarthy, R. Schmucki, M. Ebeling, M. Sivaramakrishnan, C. P. Ko, S. V. Paushkin, H. Ratni, I. Gerlach, A. Ghosh, and F. Metzger. 2014. 'Motor neuron disease. SMN2 splicing modifiers improve motor function and longevity in mice with spinal muscular atrophy', *Science*, 345: 688-93.
- Ng, S. Y., B. S. Soh, N. Rodriguez-Muela, D. G. Hendrickson, F. Price, J. L. Rinn, and L. L. Rubin. 2015. 'Genome-wide RNA-Seq of Human Motor Neurons Implicates Selective ER Stress Activation in Spinal Muscular Atrophy', *Cell Stem Cell*, 17: 569-84.
- Nolle, A., A. Zeug, J. van Bergeijk, L. Tonges, R. Gerhard, H. Brinkmann, S. Al Rayes, N. Hensel, Y. Schill, D. Apkhazava, S. Jablonka, J. O'Mer, R. K. Srivastav, A. Baasner, P. Lingor, B. Wirth, E. Ponimaskin, R. Niedenthal, C. Grothe, and P. Claus. 2011. 'The spinal muscular atrophy disease protein SMN is linked to the Rho-kinase pathway via profilin', *Hum Mol Genet*, 20: 4865-78.
- Odorico, J. S., D. S. Kaufman, and J. A. Thomson. 2001. 'Multilineage differentiation from human embryonic stem cell lines', *Stem Cells*, 19: 193-204.
- Oikawa, K., S. Kimura, N. Aoki, Y. Atsuta, Y. Takiyama, T. Nagato, M. Yanai, H. Kobayashi, K. Sato, T. Sasajima, and M. Tateno. 2004. 'Neuronal calcium sensor protein visinin-like protein-3 interacts with microsomal cytochrome b5 in a Ca²⁺-dependent manner', *J Biol Chem*, 279: 15142-52.
- Oikawa, K., G. L. Odero, S. Nafez, N. Ge, D. Zhang, H. Kobayashi, K. Sate, S. Kimura, M. Tateno, and B. C. Albensi. 2016. 'Visinin-Like Protein-3 Modulates the Interaction Between Cytochrome b (5) and NADH-Cytochrome b (5) Reductase in a Ca²⁺-Dependent Manner', *Cell Biochem Biophys*, 74: 449-57.
- Okano, H., D. Yasuda, K. Fujimori, S. Morimoto, and S. Takahashi. 2020. 'Ropinirole, a New ALS Drug Candidate Developed Using iPSCs', *Trends Pharmacol Sci*, 41: 99-109.
- Ollion, J., J. Cochennec, F. Loll, C. Escude, and T. Boudier. 2013. 'TANGO: a generic tool for high-throughput 3D image analysis for studying nuclear organization', *Bioinformatics*, 29: 1840-1.
- Oprea, G. E., S. Krober, M. L. McWhorter, W. Rossoll, S. Muller, M. Krawczak, G. J. Bassell, C. E. Beattie, and B. Wirth. 2008. 'Plastin 3 is a protective modifier of autosomal recessive spinal muscular atrophy', *Science*, 320: 524-7.
- Oskoui, M., Darras, B.T., De Vivo, D.C. 2017. 'Spinal Muscular Atrophy:125 Years Later and on the Verge of a Cure.' in C. J. Sumner, Paushkin, S., Ko, C.P. (ed.), *Spinal Muscular Atrophy: Disease Mechanisms and Therapy* (Academic Press).

- Pang, T., T. Hisamitsu, H. Mori, M. Shigekawa, and S. Wakabayashi. 2004. 'Role of calcineurin B homologous protein in pH regulation by the Na⁺/H⁺ exchanger 1: tightly bound Ca²⁺ ions as important structural elements', *Biochemistry*, 43: 3628-36.
- Panopoulos, A. D., S. Ruiz, F. Yi, A. Herrerias, E. M. Batchelder, and J. C. Izpisua Belmonte. 2011. 'Rapid and highly efficient generation of induced pluripotent stem cells from human umbilical vein endothelial cells', *PLoS One*, 6: e19743.
- Paterlini, M., V. Revilla, A. L. Grant, and W. Wisden. 2000. 'Expression of the neuronal calcium sensor protein family in the rat brain', *Neuroscience*, 99: 205-16.
- Patitucci, T. N., and A. D. Ebert. 2016. 'SMN deficiency does not induce oxidative stress in SMA iPSC-derived astrocytes or motor neurons', *Hum Mol Genet*, 25: 514-23.
- Pchitskaya, E., E. Popugaeva, and I. Bezprozvanny. 2018. 'Calcium signaling and molecular mechanisms underlying neurodegenerative diseases', *Cell Calcium*, 70: 87-94.
- Pechmann, A., M. Behrens, K. Dornbrack, A. Tassoni, S. Stein, S. Vogt, D. Zoller, G. Bernert, T. Hagenacker, U. Schara-Schmidt, I. Schwersenz, M. C. Walter, M. Baumann, M. Baumgartner, M. Deschauer, A. Eisenkolbl, M. Flotats-Bastardas, A. Hahn, V. Horber, R. A. Husain, S. Illsinger, J. Johannsen, C. Kohler, H. Kolbel, M. Muller, A. von Moers, K. Schlachter, G. Schreiber, O. Schwartz, M. Smitka, E. Steiner, E. Stogmann, R. Trollmann, K. Vill, C. Weiss, G. Wiegand, A. Ziegler, H. Lochmuller, J. Kirschner, and S. MArtCARE study group. 2022. 'Effect of nusinersen on motor, respiratory and bulbar function in early-onset spinal muscular atrophy', *Brain*.
- Pellizzoni, L. 2007. 'Chaperoning ribonucleoprotein biogenesis in health and disease', *EMBO Rep*, 8: 340-5.
- Pellizzoni, L., B. Charroux, and G. Dreyfuss. 1999. 'SMN mutants of spinal muscular atrophy patients are defective in binding to snRNP proteins', *Proc Natl Acad Sci U S A*, 96: 11167-72.
- Rahit, Kmth, and M. Tarailo-Graovac. 2020. 'Genetic Modifiers and Rare Mendelian Disease', *Genes (Basel)*, 11.
- Rajendra, T. K., G. B. Gonsalvez, M. P. Walker, K. B. Shpargel, H. K. Salz, and A. G. Matera. 2007. 'A *Drosophila melanogaster* model of spinal muscular atrophy reveals a function for SMN in striated muscle', *J Cell Biol*, 176: 831-41.
- Ramos, D. M., C. d'Ydewalle, V. Gabbeta, A. Dakka, S. K. Klein, D. A. Norris, J. Matson, S. J. Taylor, P. G. Zaworski, T. W. Prior, P. J. Snyder, D. Valdivia, C. L. Hatem, I. Waters, N. Gupte, K. J. Swoboda, F. Rigo, C. F. Bennett, N. Naryshkin, S. Paushkin, T. O. Crawford, and C. J. Sumner. 2019. 'Age-dependent SMN expression in disease-relevant tissue and implications for SMA treatment', *J Clin Invest*, 129: 4817-31.
- Ratni, H., M. Ebeling, J. Baird, S. Bendels, J. Bylund, K. S. Chen, N. Denk, Z. Feng, L. Green, M. Guerard, P. Jablonski, B. Jacobsen, O. Khwaja, H. Kletzl, C. P. Ko, S. Kustermann, A. Marquet, F. Metzger, B. Mueller, N. A. Naryshkin, S. V. Paushkin, E. Pinard, A. Poirier, M. Reutlinger, M. Weetall, A. Zeller, X. Zhao, and L. Mueller. 2018. 'Discovery of Risdiplam, a Selective Survival of Motor Neuron-2 (SMN2) Gene Splicing Modifier for the Treatment of Spinal Muscular Atrophy (SMA)', *J Med Chem*, 61: 6501-17.
- Riessland, M., B. Ackermann, A. Forster, M. Jakubik, J. Hauke, L. Garbes, I. Fritzsche, Y. Mende, I. Blumcke, E. Hahnen, and B. Wirth. 2010. 'SAHA ameliorates the SMA phenotype in two mouse models for spinal muscular atrophy', *Hum Mol Genet*, 19: 1492-506.
- Riessland, M., A. Kaczmarek, S. Schneider, K. J. Swoboda, H. Lohr, C. Bradler, V. Grysko, M. Dimitriadi, S. Hosseinibarkooie, L. Torres-Benito, M. Peters, A. Upadhyay, N. Biglari, S. Krober, I. Holker, L. Garbes, C. Gilissen, A. Hoischen, G. Nurnberg, P. Nurnberg, M. Walter, F. Rigo, C. F. Bennett, M. J. Kye, A. C. Hart, M. Hammerschmidt, P. Kloppenburg, and B. Wirth. 2017. 'Neurocalcin Delta Suppression Protects against Spinal Muscular Atrophy in Humans and across Species by Restoring Impaired Endocytosis', *Am J Hum Genet*, 100: 297-315.
- Rigo, F., S. J. Chun, D. A. Norris, G. Hung, S. Lee, J. Matson, R. A. Fey, H. Gaus, Y. Hua, J. S. Grundy, A. R. Krainer, S. P. Henry, and C. F. Bennett. 2014. 'Pharmacology of a central nervous system delivered 2'-O-methoxyethyl-modified survival of motor neuron splicing oligonucleotide in mice and nonhuman primates', *J Pharmacol Exp Ther*, 350: 46-55.

- Rindt, H., Z. Feng, C. Mazzasette, J. J. Glascock, D. Valdivia, N. Pyles, T. O. Crawford, K. J. Swoboda, T. N. Patitucci, A. D. Ebert, C. J. Sumner, C. P. Ko, and C. L. Lorson. 2015. 'Astrocytes influence the severity of spinal muscular atrophy', *Hum Mol Genet*, 24: 4094-102.
- Rochette, C. F., N. Gilbert, and L. R. Simard. 2001. 'SMN gene duplication and the emergence of the SMN2 gene occurred in distinct hominids: SMN2 is unique to Homo sapiens', *Hum Genet*, 108: 255-66.
- Rossoll, W., S. Jablonka, C. Andreassi, A. K. Kroning, K. Karle, U. R. Monani, and M. Sendtner. 2003. 'Smn, the spinal muscular atrophy-determining gene product, modulates axon growth and localization of beta-actin mRNA in growth cones of motoneurons', *J Cell Biol*, 163: 801-12.
- Rossoll, W., A. K. Kroning, U. M. Ohndorf, C. Steegborn, S. Jablonka, and M. Sendtner. 2002. 'Specific interaction of Smn, the spinal muscular atrophy determining gene product, with hnRNP-R and gry-rbp/hnRNP-Q: a role for Smn in RNA processing in motor axons?', *Hum Mol Genet*, 11: 93-105.
- Rudnicki, S. A., J. A. Andrews, T. Duong, B. M. Cockroft, F. I. Malik, L. Meng, J. Wei, A. A. Wolff, A. Genge, N. E. Johnson, C. Tesi-Rocha, A. M. Connolly, B. T. Darras, K. Felice, R. S. Finkel, P. B. Shieh, J. K. Mah, J. Statland, C. Campbell, A. A. Habib, N. L. Kuntz, M. Oskoui, and J. W. Day. 2021. 'Reldesemtiv in Patients with Spinal Muscular Atrophy: a Phase 2 Hypothesis-Generating Study', *Neurotherapeutics*, 18: 1127-36.
- Rudnik-Schoneborn, S., R. Heller, C. Berg, C. Betzler, T. Grimm, T. Eggermann, K. Eggermann, R. Wirth, B. Wirth, and K. Zerres. 2008. 'Congenital heart disease is a feature of severe infantile spinal muscular atrophy', *J Med Genet*, 45: 635-8.
- Rudnik-Schoneborn, S., S. Vogelgesang, S. Armbrust, L. Graul-Neumann, C. Fusch, and K. Zerres. 2010. 'Digital necroses and vascular thrombosis in severe spinal muscular atrophy', *Muscle Nerve*, 42: 144-7.
- Ruiz, R., J. J. Casanas, L. Torres-Benito, R. Cano, and L. Tabares. 2010. 'Altered intracellular Ca²⁺ homeostasis in nerve terminals of severe spinal muscular atrophy mice', *J Neurosci*, 30: 849-57.
- Saal, L., M. Briese, S. Kneitz, M. Glinka, and M. Sendtner. 2014. 'Subcellular transcriptome alterations in a cell culture model of spinal muscular atrophy point to widespread defects in axonal growth and presynaptic differentiation', *RNA*, 20: 1789-802.
- Sahu, G., and R. W. Turner. 2021. 'The Molecular Basis for the Calcium-Dependent Slow Afterhyperpolarization in CA1 Hippocampal Pyramidal Neurons', *Front Physiol*, 12: 759707.
- Saito, R., N. Hara, M. Tada, Y. Honma, A. Miyashita, O. Onodera, T. Ikeuchi, and A. Kakita. 2020. 'Novel CHP1 mutation in autosomal-recessive cerebellar ataxia: autopsy features of two siblings', *Acta Neuropathol Commun*, 8: 134.
- Sanchez, G., A. Y. Dury, L. M. Murray, O. Biondi, H. Tadesse, R. El Fatimy, R. Kothary, F. Charbonnier, E. W. Khandjian, and J. Cote. 2013. 'A novel function for the survival motoneuron protein as a translational regulator', *Hum Mol Genet*, 22: 668-84.
- Saxena, S., F. Roselli, K. Singh, K. Leptien, J. P. Julien, F. Gros-Louis, and P. Caroni. 2013. 'Neuroprotection through excitability and mTOR required in ALS motoneurons to delay disease and extend survival', *Neuron*, 80: 80-96.
- Schrank, B., R. Gotz, J. M. Gunnensen, J. M. Ure, K. V. Toyka, A. G. Smith, and M. Sendtner. 1997. 'Inactivation of the survival motor neuron gene, a candidate gene for human spinal muscular atrophy, leads to massive cell death in early mouse embryos', *Proc Natl Acad Sci U S A*, 94: 9920-5.
- Schreml, J., M. Riessland, M. Paterno, L. Garbes, K. Rossbach, B. Ackermann, J. Kramer, E. Somers, S. H. Parson, R. Heller, A. Berkessel, A. Sterner-Kock, and B. Wirth. 2013. 'Severe SMA mice show organ impairment that cannot be rescued by therapy with the HDACi JNJ-26481585', *Eur J Hum Genet*, 21: 643-52.
- Shababi, M., C. L. Lorson, and S. S. Rudnik-Schoneborn. 2014. 'Spinal muscular atrophy: a motor neuron disorder or a multi-organ disease?', *J Anat*, 224: 15-28.
- Sharma, A., A. Lambrechts, T. Hao le, T. T. Le, C. A. Sewry, C. Ampe, A. H. Burghes, and G. E. Morris. 2005. 'A role for complexes of survival of motor neurons (SMN) protein with gemins and

- profilin in neurite-like cytoplasmic extensions of cultured nerve cells', *Exp Cell Res*, 309: 185-97.
- Sharma, A., S. Sances, M. J. Workman, and C. N. Svendsen. 2020. 'Multi-lineage Human iPSC-Derived Platforms for Disease Modeling and Drug Discovery', *Cell Stem Cell*, 26: 309-29.
- Shen, X., and D. R. Corey. 2018. 'Chemistry, mechanism and clinical status of antisense oligonucleotides and duplex RNAs', *Nucleic Acids Res*, 46: 1584-600.
- Shi, Y., H. Inoue, J. C. Wu, and S. Yamanaka. 2017. 'Induced pluripotent stem cell technology: a decade of progress', *Nat Rev Drug Discov*, 16: 115-30.
- Shorrock, H. K., T. H. Gillingwater, and E. J. N. Groen. 2019. 'Molecular Mechanisms Underlying Sensory-Motor Circuit Dysfunction in SMA', *Front Mol Neurosci*, 12: 59.
- Simon, C. M., B. Blanco-Redondo, J. M. Buettner, J. G. Pagiazitis, E. V. Fletcher, J. K. Sime Longang, and G. Z. Mentis. 2021. 'Chronic Pharmacological Increase of Neuronal Activity Improves Sensory-Motor Dysfunction in Spinal Muscular Atrophy Mice', *J Neurosci*, 41: 376-89.
- Singh, A., P. Dalal, J. Singh, and P. Tripathi. 2018. 'Type 0 Spinal Muscular Atrophy in rare association with congenital Contracture and generalized osteopenia', *Iran J Child Neurol*, 12: 105-08.
- Singh, R. N., M. D. Howell, E. W. Ottesen, and N. N. Singh. 2017. 'Diverse role of survival motor neuron protein', *Biochim Biophys Acta Gene Regul Mech*, 1860: 299-315.
- Sivaramakrishnan, M., K. D. McCarthy, S. Campagne, S. Huber, S. Meier, A. Augustin, T. Heckel, H. Meistermann, M. N. Hug, P. Birrer, A. Moursy, S. Khawaja, R. Schmucki, N. Berntenis, N. Giroud, S. Golling, M. Tzouros, B. Banfai, G. Duran-Pacheco, J. Lamerz, Y. Hsiu Liu, T. Luebbers, H. Ratni, M. Ebeling, A. Clery, S. Paushkin, A. R. Krainer, F. H. Allain, and F. Metzger. 2017. 'Binding to SMN2 pre-mRNA-protein complex elicits specificity for small molecule splicing modifiers', *Nat Commun*, 8: 1476.
- Sleigh, J. N., S. D. Buckingham, B. Esmaeili, M. Viswanathan, E. Cuppen, B. M. Westlund, and D. B. Sattelle. 2011. 'A novel *Caenorhabditis elegans* allele, *smn-1(cb131)*, mimicking a mild form of spinal muscular atrophy, provides a convenient drug screening platform highlighting new and pre-approved compounds', *Hum Mol Genet*, 20: 245-60.
- Small, J. V., T. Stradal, E. Vignal, and K. Rottner. 2002. 'The lamellipodium: where motility begins', *Trends Cell Biol*, 12: 112-20.
- Smith, R. A., T. M. Miller, K. Yamanaka, B. P. Monia, T. P. Condon, G. Hung, C. S. Lobsiger, C. M. Ward, M. McAlonis-Downes, H. Wei, E. V. Wancewicz, C. F. Bennett, and D. W. Cleveland. 2006. 'Antisense oligonucleotide therapy for neurodegenerative disease', *J Clin Invest*, 116: 2290-6.
- Stanley, J. L., R. J. Lincoln, T. A. Brown, L. M. McDonald, G. R. Dawson, and D. S. Reynolds. 2005. 'The mouse beam walking assay offers improved sensitivity over the mouse rotarod in determining motor coordination deficits induced by benzodiazepines', *J Psychopharmacol*, 19: 221-7.
- Stoklund Dittlau, K., E. N. Krasnow, L. Fumagalli, T. Vandoorne, P. Baatsen, A. Kerstens, G. Giacomazzi, B. Pavie, E. Rossaert, J. Beckers, M. Sampaolesi, P. Van Damme, and L. Van Den Bosch. 2021a. 'Generation of Human Motor Units with Functional Neuromuscular Junctions in Microfluidic Devices', *J Vis Exp*.
- . 2021b. 'Human motor units in microfluidic devices are impaired by FUS mutations and improved by HDAC6 inhibition', *Stem Cell Reports*, 16: 2213-27.
- Strauss, K. A., M. A. Farrar, F. Muntoni, K. Saito, J. R. Mendell, L. Servais, H. J. McMillan, R. S. Finkel, K. J. Swoboda, J. M. Kwon, C. M. Zaidman, C. A. Chiriboga, S. T. Iannaccone, J. M. Krueger, J. A. Parsons, P. B. Shieh, S. Kavanagh, S. Tauscher-Wisniewski, B. E. McGill, and T. A. Macek. 2022. 'Onasemnogene abeparvovec for presymptomatic infants with two copies of SMN2 at risk for spinal muscular atrophy type 1: the Phase III SPR1NT trial', *Nat Med*, 28: 1381-89.
- Strauss, K. A., M. A. Farrar, F. Muntoni, K. Saito, J. R. Mendell, L. Servais, H. J. McMillan, R. S. Finkel, K. J. Swoboda, J. M. Kwon, C. M. Zaidman, C. A. Chiriboga, S. T. Iannaccone, J. M. Krueger, J. A. Parsons, P. B. Shieh, S. Kavanagh, M. Wigderson, S. Tauscher-Wisniewski, B. E. McGill, and T. A. Macek. 2022. 'Onasemnogene abeparvovec for presymptomatic infants with three copies of SMN2 at risk for spinal muscular atrophy: the Phase III SPR1NT trial', *Nat Med*, 28: 1390-97.
- Sugarman, E. A., N. Nagan, H. Zhu, V. R. Akmaev, Z. Zhou, E. M. Rohlf, K. Flynn, B. C. Hendrickson, T. Scholl, D. A. Sirko-Osadsa, and B. A. Allitto. 2012. 'Pan-ethnic carrier screening and prenatal

- diagnosis for spinal muscular atrophy: clinical laboratory analysis of >72,400 specimens', *Eur J Hum Genet*, 20: 27-32.
- Sumner, C. J., T. N. Huynh, J. A. Markowitz, J. S. Perhac, B. Hill, D. D. Coovert, K. Schussler, X. Chen, J. Jarecki, A. H. Burghes, J. P. Taylor, and K. H. Fischbeck. 2003. 'Valproic acid increases SMN levels in spinal muscular atrophy patient cells', *Ann Neurol*, 54: 647-54.
- Swoboda, K. J., T. W. Prior, C. B. Scott, T. P. McNaught, M. C. Wride, S. P. Reyna, and M. B. Bromberg. 2005. 'Natural history of denervation in SMA: relation to age, SMN2 copy number, and function', *Ann Neurol*, 57: 704-12.
- Takahashi, K., K. Tanabe, M. Ohnuki, M. Narita, T. Ichisaka, K. Tomoda, and S. Yamanaka. 2007. 'Induction of pluripotent stem cells from adult human fibroblasts by defined factors', *Cell*, 131: 861-72.
- Takahashi, K., and S. Yamanaka. 2006. 'Induction of pluripotent stem cells from mouse embryonic and adult fibroblast cultures by defined factors', *Cell*, 126: 663-76.
- Tamariz, E., and A. Varela-Echavarria. 2015. 'The discovery of the growth cone and its influence on the study of axon guidance', *Front Neuroanat*, 9: 51.
- Tharaneetharan, A., M. Cole, B. Norman, N. C. Romero, J. R. A. Woollorton, M. A. Harrington, and J. Sun. 2021. 'Functional Abnormalities of Cerebellum and Motor Cortex in Spinal Muscular Atrophy Mice', *Neuroscience*, 452: 78-97.
- Theunissen, F., P. K. West, S. Brennan, B. Petrovic, K. Hooshmand, P. A. Akkari, M. Keon, and B. Guennewig. 2021. 'New perspectives on cytoskeletal dysregulation and mitochondrial mislocalization in amyotrophic lateral sclerosis', *Transl Neurodegener*, 10: 46.
- Tisdale, S., M. Van Alstyne, C. M. Simon, G. Z. Mentis, and L. Pellizzoni. 2022. 'SMN controls neuromuscular junction integrity through U7 snRNP', *Cell Rep*, 40: 111393.
- Torres-Benito, L., M. F. Neher, R. Cano, R. Ruiz, and L. Tabares. 2011. 'SMN requirement for synaptic vesicle, active zone and microtubule postnatal organization in motor nerve terminals', *PLoS One*, 6: e26164.
- Torres-Benito, L., S. Schneider, R. Rombo, K. K. Ling, V. Grysko, A. Upadhyay, N. L. Kononenko, F. Rigo, C. F. Bennett, and B. Wirth. 2019. 'NCALD Antisense Oligonucleotide Therapy in Addition to Nusinersen further Ameliorates Spinal Muscular Atrophy in Mice', *Am J Hum Genet*, 105: 221-30.
- Towfighi, J., R. S. Young, and R. M. Ward. 1985. 'Is Werdnig-Hoffmann disease a pure lower motor neuron disorder?', *Acta Neuropathol*, 65: 270-80.
- Upadhyay, A., S. Hosseinibarkooie, S. Schneider, A. Kaczmarek, L. Torres-Benito, N. Mendoza-Ferreira, M. Overhoff, R. Rombo, V. Grysko, M. J. Kye, N. L. Kononenko, and B. Wirth. 2019. 'Neurocalcin Delta Knockout Impairs Adult Neurogenesis Whereas Half Reduction Is Not Pathological', *Front Mol Neurosci*, 12: 19.
- Valadez-Barba, V., A. Cota-Coronado, O. R. Hernandez-Perez, P. H. Lugo-Fabres, E. Padilla-Camberos, N. F. Diaz, and N. E. Diaz-Martinez. 2020. 'iPSC for modeling neurodegenerative disorders', *Regen Ther*, 15: 332-39.
- Van Alstyne, M., I. Tattoli, N. Delestree, Y. Recinos, E. Workman, L. S. Shihabuddin, C. Zhang, G. Z. Mentis, and L. Pellizzoni. 2021. 'Gain of toxic function by long-term AAV9-mediated SMN overexpression in the sensorimotor circuit', *Nat Neurosci*, 24: 930-40.
- Varderidou-Minasian, S., B. M. Verheijen, O. Harschnitz, S. Kling, H. Karst, W. L. van der Pol, R. J. Pasterkamp, and M. Altelaar. 2021. 'Spinal Muscular Atrophy Patient iPSC-Derived Motor Neurons Display Altered Proteomes at Early Stages of Differentiation', *ACS Omega*, 6: 35375-88.
- Vill, K., O. Schwartz, A. Blaschek, D. Glaser, U. Nennstiel, B. Wirth, S. Burggraf, W. Roschinger, M. Becker, L. Cibere, J. Durner, K. Eggermann, B. Olgemoller, E. Harms, U. Schara, H. Kolbel, and W. Muller-Felber. 2021. 'Newborn screening for spinal muscular atrophy in Germany: clinical results after 2 years', *Orphanet J Rare Dis*, 16: 153.
- Villalobos, C., and R. Andrade. 2010. 'Visinin-like neuronal calcium sensor proteins regulate the slow calcium-activated afterhyperpolarizing current in the rat cerebral cortex', *J Neurosci*, 30: 14361-5.

- Wen, H. L., C. H. Ting, H. C. Liu, H. Li, and S. Lin-Chao. 2013. 'Decreased stathmin expression ameliorates neuromuscular defects but fails to prolong survival in a mouse model of spinal muscular atrophy', *Neurobiol Dis*, 52: 94-103.
- Wirth, B., L. Brichta, and E. Hahnen. 2006. 'Spinal muscular atrophy: from gene to therapy', *Semin Pediatr Neurol*, 13: 121-31.
- Wirth, B., L. Garbes, and M. Riessland. 2013. 'How genetic modifiers influence the phenotype of spinal muscular atrophy and suggest future therapeutic approaches', *Curr Opin Genet Dev*, 23: 330-8.
- Wirth, B., M. Karakaya, M. J. Kye, and N. Mendoza-Ferreira. 2020. 'Twenty-Five Years of Spinal Muscular Atrophy Research: From Phenotype to Genotype to Therapy, and What Comes Next', *Annu Rev Genomics Hum Genet*, 21: 231-61.
- Wirth, B., Mendoza-Ferreira, N., Torres-Benito, L. 2017. 'Spinal Muscular Atrophy Disease Modifiers.' in C. J. Sumner, Paushkin, S., Ko, C.P. (ed.), *Spinal Muscular Atrophy: Disease Mechanisms and Therapy* (Academic Press).
- Woschitz, V., I. Mei, E. Hedlund, and L. M. Murray. 2022. 'Mouse models of SMA show divergent patterns of neuronal vulnerability and resilience', *Skelet Muscle*, 12: 22.
- Yamatani, H., T. Kawasaki, S. Mita, N. Inagaki, and T. Hirata. 2010. 'Proteomics analysis of the temporal changes in axonal proteins during maturation', *Dev Neurobiol*, 70: 523-37.
- Yeo, C. J. J., and B. T. Darras. 2021. 'Yeo and Darras: Extraneuronal Phenotypes of Spinal Muscular Atrophy', *Ann Neurol*, 89: 24-26.
- Yoshida, M., S. Kitaoka, N. Egawa, M. Yamane, R. Ikeda, K. Tsukita, N. Amano, A. Watanabe, M. Morimoto, J. Takahashi, H. Hosoi, T. Nakahata, H. Inoue, and M. K. Saito. 2015. 'Modeling the early phenotype at the neuromuscular junction of spinal muscular atrophy using patient-derived iPSCs', *Stem Cell Reports*, 4: 561-8.
- Yu, J., M. A. Vodyanik, K. Smuga-Otto, J. Antosiewicz-Bourget, J. L. Frane, S. Tian, J. Nie, G. A. Jonsdottir, V. Ruotti, R. Stewart, Slukvin, II, and J. A. Thomson. 2007. 'Induced pluripotent stem cell lines derived from human somatic cells', *Science*, 318: 1917-20.
- Zhang, H., L. Xing, W. Rossoll, H. Wichterle, R. H. Singer, and G. J. Bassell. 2006. 'Multiprotein complexes of the survival of motor neuron protein SMN with Gemins traffic to neuronal processes and growth cones of motor neurons', *J Neurosci*, 26: 8622-32.
- Zhang, X. T., Y. Zhang, Y. X. Zhang, Z. Y. Jiang, H. Yang, L. Jiang, B. Yang, and J. C. Tong. 2021. 'Helicid Reverses the Effect of Overexpressing NCALD, Which Blocks the sGC/cGMP/PKG Signaling Pathway in the CUMS-Induced Rat Model', *J Healthc Eng*, 2021: 7168397.
- Zhang, Z., F. Lotti, K. Dittmar, I. Younis, L. Wan, M. Kasim, and G. Dreyfuss. 2008. 'SMN deficiency causes tissue-specific perturbations in the repertoire of snRNAs and widespread defects in splicing', *Cell*, 133: 585-600.
- Zhang, Z., A. M. Pinto, L. Wan, W. Wang, M. G. Berg, I. Oliva, L. N. Singh, C. Dengler, Z. Wei, and G. Dreyfuss. 2013. 'Dysregulation of synaptogenesis genes antecedes motor neuron pathology in spinal muscular atrophy', *Proc Natl Acad Sci U S A*, 110: 19348-53.
- Zhao, X., Z. Feng, N. Risher, A. Mollin, J. Sheedy, K. K. Y. Ling, J. Narasimhan, A. Dakka, J. D. Baird, H. Ratni, C. Lutz, K. S. Chen, N. A. Naryshkin, C. P. Ko, E. Welch, F. Metzger, and M. Weetall. 2021. 'SMN protein is required throughout life to prevent spinal muscular atrophy disease progression', *Hum Mol Genet*, 31: 82-96.
- Zhuri, D., H. Gurkan, D. Eker, Y. Karal, S. Yalcintepe, E. Atli, S. Demir, and E. I. Atli. 2022. 'Investigation on the Effects of Modifying Genes on the Spinal Muscular Atrophy Phenotype', *Glob Med Genet*, 9: 226-36.

ACKNOWLEDGEMENTS

First of all, I would like to thank my supervisor Prof. Dr. Brunhilde Wirth for giving me the opportunity to work in her group, where I could work in the development of therapies which has always been my dream as a scientist.

I thank Prof. Dr. Elena Rugarli for kindly agreeing to correct and to review my PhD thesis. I also thank Prof. Dr David Vilchez for agreeing in reviewing my thesis, Prof. Dr. Ansgar Büschges for taking the chair of the exam committee, and Dr. Katerina Vlantis agreeing on taking the minutes.

I would like to thank my lab mates for all the support I have received from them since the moment I started this PhD, you made this experience much better. Andre, you were my first real friend in the lab and one of my best friends in life. I really thank you for everything you did to help me scientifically and personally. I will never forget our time together here and I am sooo excited for what is waiting for both of us out there. I will miss you, a lot. Tamasito, of course I will miss you too. I will miss how grumpy you can be =), our “vamos a fumar”. I am sorry I could not find you a girl friend during this time, however I am happy you found one yourself! I will miss to be the three of us, but I will always carry you in my heart. I want to thank Roman, for being always there and for make this work possible, I will miss our deep talks while prepping mice or injecting animals =). To my little Ele, I am so happy I got to know you and count you as my friend, thank you for everything, I am very proud of you and I know you will become an amazing scientist. Jorgito, gracias por todas las risas que nos echamos que han hecho mas llevadero este ultimo año y medio. Me ha hecho muy feliz conocerte y te deseo lo mejor de lo mejor para este doctorado, se que eres muy capaz de todo lo que te propongas. To the office girls, Ilka, Lisa and Nur, thanks for everything, for listening to me everytime I went to the office, you were always there for the good and the bad, I will miss you and I wish you all the very very best for your PhDs, you are smart and hard workers. To Sofia, thanks for bringing a bit of craziness to this lab, I always had good laughs with you! I know you will go places girl =). I also want to thank Valentina, not only for your feedback but also for all the advices you gave me! I want to thank Irmgard and Sebastian for their work to keep the lab in order! I want to thank Laura for teaching me many of the techniques I used in this PhD working with animals, it was hard when you left but I am very happy that I got to know you and become your friend! Moreover, I want to thank Eva, which was there to teach me how to start the Chp1 project, I learnt a lot from you, thank you so much! I also want to thank AG Zempel members for the scientific advice and the fun times playing the black stories card game =). A special thank goes to many of the former members of AG Wirth: Natalia, Mosi, Janine, Marlen, Bryony, Aaradhita, Svenja, Charly and AG Kye: Ines, Max, Wiebke. I also want to thank Leo for his help with the hiPSCs (I don't know where I would be now without you), scientific input and for all the good moments together.

My gratitude goes to our collaborators from Ionis Pharmaceuticals, who have always generously provided us with SMN-ASO and generated *Chp1/CHP1*-ASOs and *Ncald/NCALD*-ASOs. My work has also been greatly supported by the animal caretakers from the Genetics animal facility.

I would also like to thank Katerina Vlantis, for all the support I received during my PhD, I cannot put into words how happy I am that you were always there to help me, no matter when or at what time, you are just amazing. Also I am very thankful for Kathy Joergens, you were always super helpful with all the travel documents.

Las siguientes palabras son para mi familia y amigos. Papá, mamá, gracias por creer en mi y apoyarme en todo momento, habeis estado siempre ahí para animarme cuando más lo he necesitado. Os he echado de menos cada día y os prometo que volveré a España pronto, os quiero. Sin duda a la persona que más he echado de menos en el mundo es a mi abu (y a abuelo también), que siempre ha estado ahí para mí y me ha querido incondicionalmente como a una hija, estar lejos de ti ha sido lo más difícil. Quiero darle las gracias también a mis tios Eugenio y Guille, a mis primos Chiki, Javi y Niki, y a mi tío/hermano Cho, a mi tía Mar y a mis primos Xoán y Sabeliña y a mi madrastra Esther ;), por animarme siempre con el doctorado! Y gracias a mi tío Andi por ayudarme a encontrar doctorado y a empezar mi vida en Colonia. A mi amiga Miri, gracias gracias y gracias por estar siempre ahí, por creer en mí, por escucharme y por darme tan buenos consejos, ojala ahora podamos vernos más! A mis amigos de Colonia, que me habeis hecho sentir como en casa y me habeis escuchado y visto llorar por este doctorado... y también me habeis sacado de fiesta para ayudarme a olvidarlo jajaja, gracias. Por último pero no por ello menos importante... Lucas, gracias por estar ahí siempre, por tirar de mí cuando yo no podía, por creer en mí más que yo misma. Gracias por todo lo que has hecho y haces por mí cada día, por hacerme crecer y sacar lo mejor de mí, y por hacerme reír tanto. Eres mi compañero de vida. T'estime.

ERKLÄRUNG ZUM GESUCH UM ZULASSUNG ZUR PROMOTION

Erklärung zur Dissertation
gemäß der Promotionsordnung vom 12. März 2020

Diese Erklärung muss in der Dissertation enthalten sein.
(This version must be included in the doctoral thesis)

„Hiermit versichere ich an Eides statt, dass ich die vorliegende Dissertation selbstständig und ohne die Benutzung anderer als der angegebenen Hilfsmittel und Literatur angefertigt habe. Alle Stellen, die wörtlich oder sinngemäß aus veröffentlichten und nicht veröffentlichten Werken dem Wortlaut oder dem Sinn nach entnommen wurden, sind als solche kenntlich gemacht. Ich versichere an Eides statt, dass diese Dissertation noch keiner anderen Fakultät oder Universität zur Prüfung vorgelegen hat; dass sie - abgesehen von unten angegebenen Teilpublikationen und eingebundenen Artikeln und Manuskripten - noch nicht veröffentlicht worden ist sowie, dass ich eine Veröffentlichung der Dissertation vor Abschluss der Promotion nicht ohne Genehmigung des Promotionsausschusses vornehmen werde. Die Bestimmungen dieser Ordnung sind mir bekannt. Darüber hinaus erkläre ich hiermit, dass ich die Ordnung zur Sicherung guter wissenschaftlicher Praxis und zum Umgang mit wissenschaftlichem Fehlverhalten der Universität zu Köln gelesen und sie bei der Durchführung der Dissertation zugrundeliegenden Arbeiten und der schriftlich verfassten Dissertation beachtet habe und verpflichte mich hiermit, die dort genannten Vorgaben bei allen wissenschaftlichen Tätigkeiten zu beachten und umzusetzen. Ich versichere, dass die eingereichte elektronische Fassung der eingereichten Druckfassung vollständig entspricht.“

Teilpublikationen: Sind in Kapitel 6 angegeben



01.12.2022, Anixa Muiños Bühl

Datum, Name und Unterschrift

Declaration for the doctoral thesis (dissertation)
according to the doctoral regulations published 12th March 2020

Non-official English translation of the "Erklärung zur Dissertation"
(The German version must be included in the doctoral thesis)

"I hereby declare that I have completed the present dissertation independently and without the use of any aids or literature other than those referred to. All passages that have been taken, either literally or in sense, from published and unpublished works, are marked as such. I declare that this dissertation has not been submitted to any other faculty or university; that - apart from the partial publications and included articles and manuscripts listed below - it has not yet been published, and that I will not publish the dissertation before completing my doctorate without the permission of the PhD Committee. I am aware of the terms of the doctoral regulations. In addition, I hereby declare that I am aware of the "Regulations for Safeguarding Good Scientific Practice and Dealing with Scientific Misconduct" of the University of Cologne, and that I have observed them during the work on the thesis project and the written doctoral thesis. I hereby commit myself to observe and implement the guidelines mentioned there in all scientific activities. I assure that the submitted electronic version is identical to the submitted printed version".

Partial publications of the thesis: are given in Chapter 6 of the thesis



01.12.2022, Anixa Muiños Bühl

Date, name, and signature

Erklärung zum Gesuch um Zulassung zur Promotion
gemäß der Promotionsordnung vom 12. März 2020

1. Zugänglichkeit von Daten und Materialien

Die Dissertation beinhaltet die Gewinnung von Primärdaten oder die Analyse solcher Daten oder die Reproduzierbarkeit der in der Dissertation dargestellten Ergebnisse setzt die Verfügbarkeit von Datenanalysen, Versuchsprotokollen oder Probenmaterial voraus.

- Trifft nicht zu
 Trifft zu.

In der Dissertation ist dargelegt wie diese Daten und Materialien gesichert und zugänglich sind (entsprechend den Vorgaben des Fachgebiets beziehungsweise der Betreuerin oder des Betreuers).

2. Frühere Promotionsverfahren

Ich habe bereits einen Dokortitel erworben oder ehrenhalber verliehen bekommen.

Oder: Für mich ist an einer anderen Fakultät oder Universität ein Promotionsverfahren eröffnet worden, aber noch nicht abgeschlossen.

Oder: Ich bin in einem Promotionsverfahren gescheitert.

- Trifft nicht zu
 Zutreffend
Erläuterung:

3. Straftat

Ich bin nicht zu einer vorsätzlichen Straftat verurteilt worden, bei deren Vorbereitung oder Begehung der Status einer Doktorandin oder eines Doktoranden missbraucht wurde.

Ich versichere, alle Angaben wahrheitsgemäß gemacht zu haben.

01.12.2022
Datum

Anixa Muiños Bühl
Name


Unterschrift

Declaration on the application for admission to the doctoral examinations
according to the doctoral regulations published 12th March 2020

1. Accessibility of data and materials

The dissertation involves the acquisition of primary data or the analysis of such data or the reproducibility of the results presented in the dissertation requires the availability of data analyses, experimental protocols or sample material.

not applicable

applicable

I have described in the dissertation how these data and materials are secured and accessible (according to the specifications of the subject area or supervisor).

2. Previous doctoral examinations

I have already obtained a doctorate or been awarded an honorary doctoral degree.

Or: A doctoral examination has been opened at another faculty or university, but not yet completed.

Or: I have failed in a doctoral examination.

not applicable

applicable

explanatory note:

3. Criminal offense

I have not been convicted of a deliberate criminal offence in the preparation or commission of which the status as a doctoral candidate was abused.

I declare that all information provided is truthful.

01.12.2022

Date

Anixa Muiños Bühl

Name



Signature

CURRICULUM VITAE

Personal information

Name: Anixa Muiños Bühl

Date of birth: 29.08.1991

Place of birth: Redondela (Spain)

Nationality: Spanish

University Education

2009-2015 (B.Sc) Bachelor in Biotechnology.

Universidad Francisco de Vitoria

2014-2015 Master in Business, Biotechnology

ALITER, International Business School

2015-2017 (M.Sc) Master in Advanced Therapies and Biotechnological Innovation

Universidad Francisco de Vitoria

From 2017 Promotionsstudium (Dr.rer.nat) in Genetics

University of Cologne

Professional experience

2014-2016 Internship at the Animal breeding and Genetics Department

Institute Nacional de Investigacion Agraria y Alimentaria (INIA)

2016-2017 Internship at The New York Stem Cell Foundation

Since 2017 PhD student at the Institute of Human Genetics Cologne

